On the assessment of blood velocity and wall shear rate in arteries with Doppler ultrasound: a validation study

James R Blake

A thesis submitted for the degree of Doctor of Philosophy.
The University of Edinburgh.
April 2008

Abstract

Cardiovascular disease, mostly atherosclerosis, is responsible for one third of all deaths globally, rising to more than 50% in the Western World. Risk factors include smoking, diet, and familial history. Doppler ultrasound can provide estimates of blood velocity and wall shear rate. Clinically, maximum velocity is used to categorise patients for surgery, although Doppler velocity measurement is prone to errors and in need of validation. Wall shear stress—which can be derived from wall shear rate—plays a role in disease initiation and progression, although its clinical utility is unclear due to difficulties associated with its measurement.

This thesis investigates the use of Doppler ultrasound as a tool to estimate blood velocity and wall shear rate. A simplified method for estimation of wall shear rate in healthy arteries is developed that uses spectral Doppler ultrasound. This method is based upon the theory of oscillatory flow in rigid pipes, requiring two measurements that are readily available with clinical ultrasound machines. This method is compared to a similar method based on colour flow imaging. The spectral Doppler method underestimated the theoretic value of wall shear rate by between 7 and 22%, with results varying between phantoms. Errors for the colour method were on average 35% greater. Test measurements from one healthy volunteer demonstrated that this method can be applied in-vivo.

In more advanced stages of disease, peak velocity distal to a stenosis is of clinical interest and the simplified method for wall shear rate estimation is invalid. Steady flow in a series of simplified stenosis geometries was studied using a dual-beam Doppler system to obtain velocity vectors. These measurements were compared with data from an equivalent system that used particle image velocimetry (PIV) and was considered the gold standard. For Reynolds numbers at the stenosis throat of less than 800, flow remained laminar over the region studied, although distal flow separation did occur. For higher throat Reynolds numbers—corresponding to more severe stenoses or increased flow rates—asymmetric recirculation regions developed; the transition to turbulence occurred more proximally, with a corresponding reduction in stenotic jet and recirculation length.

Qualitative agreement was observed in the velocity profile shapes measured using ultrasound and PIV at throat Reynolds numbers less than 800. Above this threshold the qualitative agreement between the velocity profiles became poorer as both downstream distance and the degree of stenosis increased. Peak axial velocity distal to the stenosis was underestimated, on average, by 15% in the ultrasound system. Estimation of shear rate remained difficult with both experimental techniques. Under a Newtonian approximation, the normalised wall shear stresses agree qualitatively. Under pulsatile flow conditions using an idealised flow waveform, superior qualitative agreement was observed in the velocity profiles at diastole than at systole. Similar to the steady flow behaviour, this agreement deteriorated with stenosis severity.

The current generation of clinical ultrasound machines are capable of estimating the wall shear rate in healthy arteries. In the presence of significant arterial disease, errors in the peak velocity may result in mis-selection of patients for surgery, while estimation of the wall shear stress remains extremely problematic; particularly with identifying the wall location and measuring velocities close to the wall.

Declaration of originality

I hereby declare that the research recorded in this thesis, and the thesis itself, was composed and originated entirely by myself in the Department of Medical Physics, and the Institute of Materials and Processes, at The University of Edinburgh.

James R. Blake

Acknowledgements

I'd like to thank my supervisors, Pete and Bill, for all the help, advice and support (however blunt, you were usually right), and for providing access to the PIV equipment. Without their input, this thesis would be much, much slimmer, if it existed at all.

I must also thank the Engineering and Physical Sciences Research Council (EPSRC), who funded the majority of this work.

Casting the net wider, I have to thank several of the Broom Cupboard inhabitants, past and present. Kate, for the conversations regarding all things fluidic and ultrasonic, and for establishing the cake cult, thanks. Dr B, an ever present source of distraction and technical savoir-faire; and Dr B, a fine cake maker and source sanity; thanks for the help proof-reading, among other things. Robin, your encyclopædic knowledge of all things Doppler so often distinguished the wood from the trees. Siobhan, thanks for teaching me some of the darker secrets of the arcane art of phantom making. Steven, your eternal optimism was an inspiration. Thanks to Ben and David, for boosting morale when it was even lower than usual. Thanks to Norman, for his ultrasound advice and for the occasional dram. And, of course, an enormous thanks to the most popular name in the cake box, for keeping track of everything from orders, repairs, returns, and just generally for looking after me, Irene.

Beyond the BC, I have to thank Jon, for his excellent reference manager and endless LaTeX hints. Mingxiu, Jason and William all provided valuable help and advice regarding stenoses, computing and physics. Anis and Dave, thanks for the time spent and headaches acquired in the dark, dark, room. I must also thank Bobby Hogg at the engineering workshop, his technical help solved innumerable problems. There's also been the odd memorable (or not!) night with too many people to thank here, you know who you were.

I want to thank Mum and Dad, for their constant support, encouragement and advice, and Michael, for keeping my feet on the ground. And finally, I want to thank Jen; her patience, understanding and care kept me sane, especially in the later stages—I don't know if I could have done it without you.

Epigram

"The average Ph.D thesis is nothing but the transference of bones from one graveyard to another."

Frank J Dobbie, *A Texan in England*, 1945.

Contents

List of figures

List of tables

Acronyms and abbreviations

A-mode	Amplitude mode
BMF	Blood mimicking fluid
B-mode	Brightness mode
CCD	Charge coupled device
CFD	Computational fluid dynamics
CFI	Colour flow images
CVD	Cardiovascular disease
CW	Continuous wave (Doppler)
EC	Endothelial cell
ECST	European carotid surgery trial
IA	Interrogation area
LDA	Laser Doppler anemometry
M-mode	Motion mode
MRI	Magnetic resonance imaging
NASCET	North America symptomatic carotid endarterectomy trial
Nd:YAG	Neodymium-doped yttrium aluminium garnet
PC	Personal computer
PIV	Particle image velocimetry
PRF	Pulse repetition frequency
PSV	Peak systolic velocity
PW	Pulsed wave (Doppler)
SMC	Smooth muscle cell
SRES	Shear rate estimation system
TIA	Transient ischæmic attack
TMM	Tissue mimicking material
TTL	Transistor-transitor logic
WSR	Wall shear rate
WSS	Wall shear stress

Nomenclature

α	Womersley parameter (normalised frequency)
α_k	Womersley parameter for the k-th harmonic
κ	Degree of stenosis, in percent
γ_w	Wall shear rate
ω	Angular frequency [s^{-1}]
τ_w	Wall shear stress [Pa]
$\hat{\tau_w}$	Normalised wall shear stress
η	Development index
ρ	Density [$kg \cdot m^{-3}$]
μ	Dynamic viscosity [$Pa \cdot s$]
ν	Kinematic viscosity [$m^2 \cdot s^{-1}$]
A	Vessel cross-sectional area [m^2]
Q	Flow rate [$m^3 \cdot s^{-1}$]
D	Vessel diameter [D]
R	Vessel radius [m]
Re	Reynolds number
$\bar{v}$	Mean cross-sectional velocity [$m \cdot s^{-1}$]
$\hat{v}$	Normalised velocity

Chapter 1
Introduction

Cardiovascular disease (CVD) is responsible for approximately 30% of mortality globally, and over 50% of annual deaths in Western Europe and Northern America (Beaglehole et al., 2004). The umbrella of CVD includes diseases such as hypertensive heart disease, ischæmic heart disease, cerebrovascular disease and inflammatory heart disease, which primarily manifest themselves in the form of atherosclerosis, arteriosclerosis and aneurysms. Ultimately, CVD can lead to stroke, myocardial infarction and transient ischæmic attacks (TIA), all of which can prove fatal or severely damage the patient's quality of life.

This chapter will provide an overview of the development and clinical managment of arterial disease. It will discuss the hypothesised role played by a potentially important biomechanical factor—the wall shear stress—on the development of atherosclerosis, and ways that it may be measured. The clinical use of Doppler ultrasound as a patient management tool is discussed, as are the problems of the current approach. Gaps in the scientific literature are identified that are in need of attention; based on some of these gaps, the aims of this thesis are defined. Finally, some background concepts fundamental to this thesis are reviewed.

1.1 The cardiovascular system

1.1.1 The healthy system

The arterial system transports essential nutrients and removes waste products to and from cells in the body. Without adequate blood supply cells die, with severe consequences for the body as a whole if these cells are from the myocardium or in the brain.

Blood vessels in the body range in diameter from around 2.5 cm for the largest vessel, the aorta, to tens of microns for the smallest capillaries. All large arcteries—vessels with a diameter greater than 200μm—consist of a heterogeneous wall (Fig. 1.1), which confines the blood to the lumen. The arterial wall is built from three primary layers: the inner layer, known as the intima, consists of a single layer of endothelial cells; the following layer, the media is primarily

a series of approximately circumferentially orientated smooth muscle cells (SMCs); the final, adventitial layer is made of collagen fibres with some elastin, nerves and fibroplasts added (Humphrey, 2002).

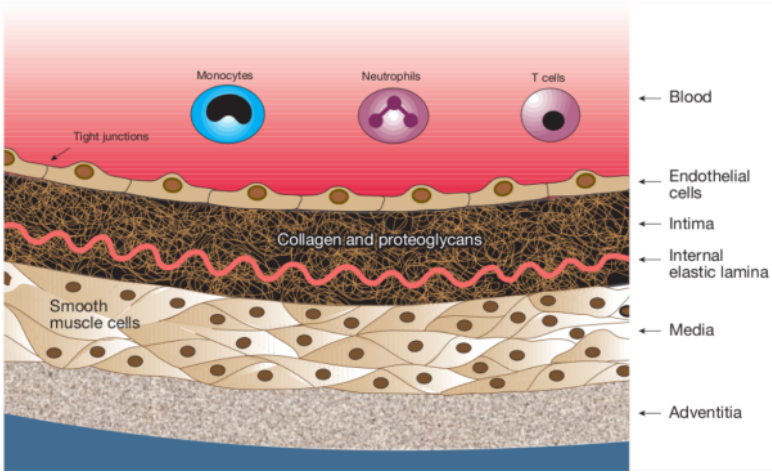

Figure 1.1: *The healthy artery wall. (Reprinted by permission from Macmillan Publishers Ltd: Nature, AJ Lusis, Atherosclerosis, 407: 233–241. Copyright (2000).)*

Each layer of the artery wall adds functionality to arterial behaviour. The intima is the direct interface between the moving blood and the wall—it contains endothelial cells (ECs) that sense blood motion through the wall shear stress (WSS). The ECs react to changes in WSS by modifying production of vasoactive mediators, the principal component of which is nitric oxide, such that blood flow is modulated as required (Kamiya & Togawa, 1980; Koller & Kaley, 1990; Koller et al., 1993). Smooth muscle cells in the media add a degree of elasticity and can be used to regulate arterial diameter. The adventitial layer of the artery wall, being mostly collagen, serves to prevent overdilation of vessels, and also anchors the artery to surrounding tissue.

The healthy artery must be able to repair itself from injury. In case of injury, the high shear stresses in the blood activate platelets in the blood (given the presence of factors such as the von Willebrand factor and Ca^{2+}), and adhesion of the platelets to the injured site occurs quickly (Wootton & Ku, 1999).

1.1.2 Diseases of the cardiovascular system

Cardiovascular disease can exist in many forms, however, the most common diseases are hypertension, aneurysm and atherosclerosis. Hypertension is a consistent elevation of blood pressure;

aneurysm is a ballooning of the arteries as the walls weaken, usually in the abdominal aorta but also in the cerebrovascular circulation; and atherosclerosis is a broad term encompassing the development of localised plaques and the narrowing of arterial lumen that can be responsible, for example, for myocardial infarct and stroke.

Atherosclerosis is found at sites in the circulatory where flow is complex, such as bifurcations and arches. At these sites, the wall shear stress is lower than that maintained elsewhere and, in the presence of risk factors such as smoking, a diet high in low density lipoprotein (LDL), and familial history, the development of plaques may be initiated (Slager et al., 2005*a*). LDL molecules stimulate the accumulation and inflammation of monocytes between the intima and media layers of the artery wall. The monocytes absorb LDL and are modified into foam cells, which proliferate and form the initial fatty streaks (Steinberg, 2002). As the lesions grow, any restriction of the arterial lumen increases the WSS locally. During the early stages of disease, the vessel reacts to the increased shear stress, and remodels to maintain a healthy lumen (Giddens et al., 1993); beyond a certain limit, the remodelling ceases. Any further increase in plaque size can cause stenosis.

The progression of disease from fatty streaks to occlusive plaques is not fully understood. Mechanisms for plaque growth include elevated levels of angiotensin-converting enzyme and increased expression of adhesion molecules such as E-selectin by endothelial cells (Slager et al., 2005*a*). Angiotensin-converting enzyme inhibits production of nitric oxide (NO), a powerful antiproliferation, antithrombotic and antiatherogenic agent, while E-selectin encourages recruitment and proliferation of white blood cells (leukocytes and monocytes), stimulating the inflammatory response (Richardson, 2002). The repeated healing response leads to the development of scar tissue, forming a fibrous cap consisting mostly of collagen with some smooth muscle cells at the site of the injury. Underneath the cap, the high concentration of foam cells forms a lipid pool. As the foam cells die, a necrotic core may develop inside the plaque (Lusis, 2000).

Symptoms may arise from advanced stenosis even without plaque rupture (Richardson, 2002). Typically, such symptoms will present themselves initially during exercise, where the degree of lumen reduction is so severe that the required blood flow cannot be maintained. If the disease progresses, such that symptoms are present at rest, tissue death and gangrene may occur. Should the plaque rupture—which is as a result of tissue, rather than shear, stresses—consequences tend both to be more immediate and severe. Depending on the location of the

offending plaque, angina, myocardial infarction and stroke are all possible outcomes. The rupture releases thrombotic material from the core of the plaque into the bloodstream which stimulates four clotting mechanisms—adhesion, activation, aggregation and coagulation (Wootton & Ku, 1999)—which can occlude the vessel at the site of injury, or travel downstream and block smaller arteries. The first two mechanisms are the normal vascular response to injury, but the aggregating and coagulating functions provide feedback that stimulates further thrombosis. It should be noted that plaque rupture need not be fatal or lead to complete occlusion of vessels. Clinical reports suggest that in stenoses with a 50% or more diameter reduction, 70% of plaques show evidence of previous disruption, raising the concept of the stable and the vulnerable plaque (Richardson, 2002).

1.1.3 Clinical management of atherosclerosis

The concept of vulnerable plaques has become the dominant focus in the clinical management of stenosis (Libby & Aikawa, 2002). If a plaque is deemed stable, then the most common treatments include a reduced fat diet, weight loss and moderate exercise. Medical approaches may also be adopted, such as treatment with blood thinning or cholesterol lowering drugs (Steinberg, 2002).

The difficulty with treatment of stenosis lies in correctly identifying the unstable plaque. Between two-thirds and three-quarters of acute myocardial infarctions occur due to the rupture of atherosclerotic plaque (Libby & Aikawa, 2002), but identification of these plaques is difficult, not least, since they may not be visible on an angiogram due to vascular remodelling (Richardson, 2002). Indeed, evidence suggests that plaques which remodel in a positive manner to maintain the lumen have larger lipid cores and contain more macrophages, and are hence more likely to fall into the unstable category (Richardson, 2002).

Plaque growth that does not result in remodelling can lead to chronic stenosis, with the risk of ischæmia in tissue downstream of the blockage. To assess the value of surgery in carotid stenosis, two major randomised clinical trials investigated which patient groups would benefit from intervention (ECST collaborators, 1998; Barnett et al., 1998). The conclusions of both studies were that surgery only benefits the severest cases ($> 70\%$ diameter reduction). ECST collaborators (1998) concluded that for such patients, surgery yielded an absolute reduction in the risk of stroke within three years of 11.6%, that is, 116 major strokes or deaths from any cause might be prevented for every 1000 patients undergoing surgery. Barnett et al. (1998) con-

cluded that to prevent one stroke after five years, fifteen interventions are needed (in equivalent figures to ECST, 67 strokes would be prevented for every 1000 patients). In both studies, the proportion of control patients without stroke after five years was around 75%, providing further firm evidence that differentiating between stable and vulnerable plaques is hard.

For severe stenosis or complete occlusion of arteries, surgery is usually necessary. Balloon angioplasty involves delivering an inflatable balloon to the occluded site via a catheter and inflating it to reestablish the vessel lumen. Stenting is performed in parallel to reinforce the artery walls after the balloon is removed. More invasive surgical options include endarterectomy and bypass grafts. During endarterectomy, plaque is removed from inside the vessel, restoring the lumen. Bypass grafts can be used to bypass completely occluded vessels using segments of healthy arteries and veins from another part of the patient. Cardiovascular surgery risks include thrombosis, which may lead to infarction and stroke. Typically, the risk associated with endarterectomy is 2–7% (ECST collaborators, 1998; Barnett et al., 1998); for bypass surgery, perioperative risk is between 1 and 4% (Mackey et al., 1996; Yusuf et al., 1994).

1.1.4 Imaging of cardiovascular disease

An important tool in efficient management of CVD is the availability of reliable diagnostic tools. Typically, disease progression is monitored with one of the three following modalities: X-ray angiograpy, magnetic resonance angiography and ultrasonography. Of these three methods, X-ray angiography is considered the current gold standard.

1.1.4.1 X-ray angiography

X-ray angiography is considered the current gold standard for carotid artery stenosis definition having been used as the reference standard in both the large scale clinical trials (Barnett et al., 1998; ECST collaborators, 1998). The technique produces images that clearly show arterial geometry, although no information about the arterial wall can be gathered (Fig. 1.2a). Contrast can be improved through the use of digital subtract angiography (DSA) which is now widespread. Interpretation of the images is non-trivial, since the projection of a 3D vessel into two dimensions necessarily introduces some error. This problem is alleviated by using biplanar techniques or fully 3D methods (which required computed tomography), although many facilities do not have access to these methods.

The technique involves catheterisation, usually through the femoral artery, and a subsequent release of a bolus of contrast agent. The technique is normally reserved for planning surgical procedures, as the catheter represents a stroke risk, either by dislodging plaques, stimulating thrombosis at the catheter tip or by damaging the vessel wall. The risk of permanent neurological complications is between 1 and 4% (Davies & Humphrey, 1993; Hankey et al., 1990).

(a) X-ray angiography of carotid stenosis.

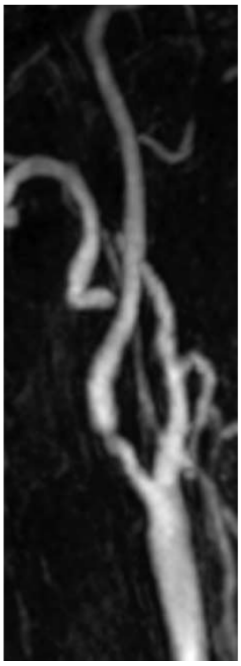

(b) Magnetic resonance angiography of the same vasculature.

Figure 1.2: *Angiography of the vasculature. Springer and European Radiology Supplements,* ***15****–5, (2005),* E11–E16*, SA Thurnher, Fig. 1; with kind permission from Springer Science and Business Media.*

1.1.4.2 Magnetic resonance imaging

Magnetic resonance imaging is a non-invasive modality capable of providing high resolution images (0.5–1.0 mm). Magnetic resonance angiography (MRA) provides contrast enhanced images of the vasculature similar to X-ray angiography by delivering contrast agent to the patient (Fig. 1.2b), although images may be obtained without contrast using time-of-flight sequences (Gerber et al., 2004). The brightness of the image is proportional to the blood velocity. MRAs commonly have a large field of view. This is an advantage compared to X-ray angiograms, as it allows clinicians to quickly detect any previously unknown disease.

Contrast enhanced MRA is considered superior to time-of-flight methods since images can be acquired in less time and with superior depiction of vessel edges (Cloft et al., 1996). Typical acquisitions last around five minutes, compared to around 11 minutes for time-of-flight techniques. The major problem with contrast enhanced MRA involves timing the acquisition to coincide with optimum delivery of the agent inside the vasculature, otherwise image quality is variable (Gerber et al., 2004). Unlike conventional X-ray angiography, MRA can provide some information about the artery wall; the development of quantitative image processing techniques will make MRI an invaluable tool for determining plaque stability (Richardson, 2002). A recent review of the diagnostic potential of MRA concluded that the pooled sensitivity and specificity (ie, true positive diagnosis and true negative diagnosis respectively) both exceed 90% when compared with DSA (Nederkoorn et al., 2003).

MR angiography can suffer from signal loss if retrograde flowing blood re-enters the sample volume. This can spuriously increase the apparent stenosis severity, with severe clinical consequences (Culebras et al., 1997). The use of contrast enhancement does not entirely alleviate this problem. Other issues with MRA include blurring due to patient movement and patient claustrophobia which may increase anxiety. MR remains incompatible with cardiac pacemakers, rendering the technique completely unsuitable for some patients. MR angiography is also relatively expensive.

1.1.4.3 Ultrasonography

Ultrasonography is the most widely used imaging technique, principally because it is real-time, non-invasive, portable and cheap (Gerber et al., 2004). When imaging CVD, three modes of ultrasound are generally used: brightness mode (B-mode) shows the returned intensity of sound (Fig. 1.3a); colour flow imaging (CFI) depicts the spatial variation in velocity (Fig. 1.3b); and spectral Doppler, which shows the variation of velocity from one sample volume over time (Fig. 1.3c). Only spectral Doppler is used to make quantitative measurements.

In arterial disease, B-mode imaging is not used to assess the degree of stenosis, since ultrasound's resolution has been historically poor. Shadowing from calcified plaques also degrades image quality, which is further compounded by being limited to a 2D plane. Colour flow imaging is used primarily to locate the fastest flowing jet of blood. Having accomplished this task, the clinician can estimate the degree of stenosis by positioning the spectral Doppler sample

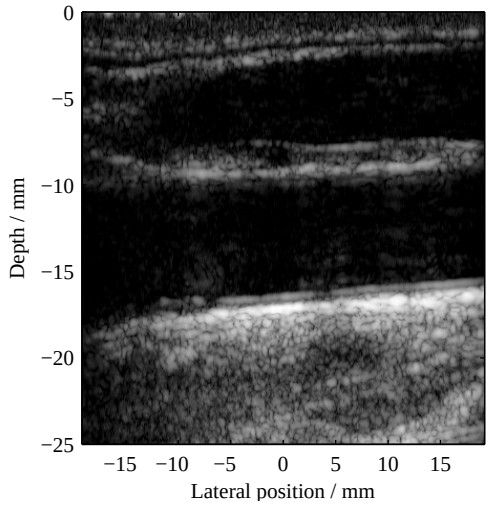

(a) B-mode imaging of the common carotid artery.

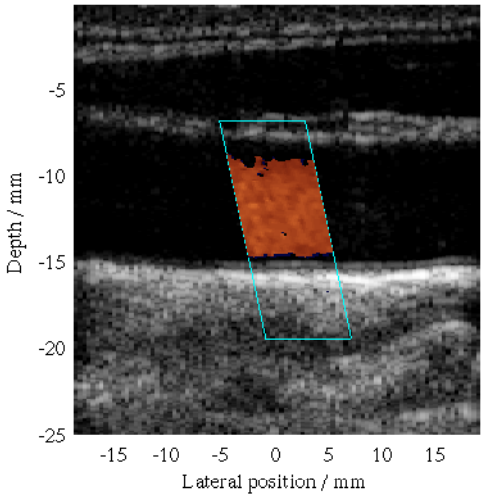

(b) Colour flow imaging in the common carotid artery.

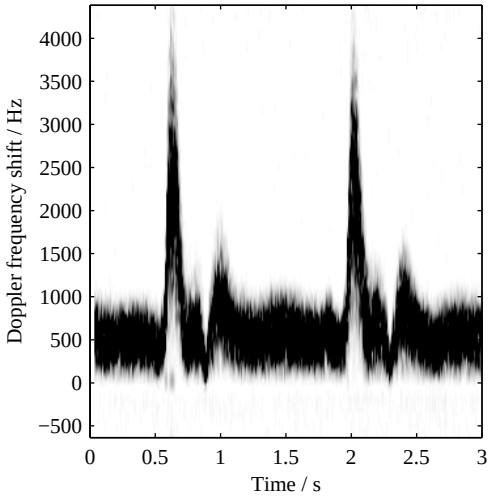

(c) A spectral Doppler trace obtained from the CCA.

Figure 1.3: B*-mode and colour flow imaging in the common carotid artery.*

volume in the jet (Fig. 1.4). The stenosis measurement is derived from the maximum velocity (Bluth et al., 1988; Robinson et al., 1988).

Ultrasound can also be used to visualise arterial from within arteries. Intra-vascular ultrasound (IVUS) provides extremely high resolution images of the arterial wall, and can be used to assess the vulnerability of plaques (Richardson, 2002). Plaque eccentricity and composition can both be assessed and provide information not available on conventional angiograms (di Mario et al., 1999). Ultimately quantification both of the vessel wall and plaque is possible, with such high resolution that running computer simulations of blood flow based on the vessel geometry is feasible (Steinman, 2002). However, the improved functionality of this modality is offset

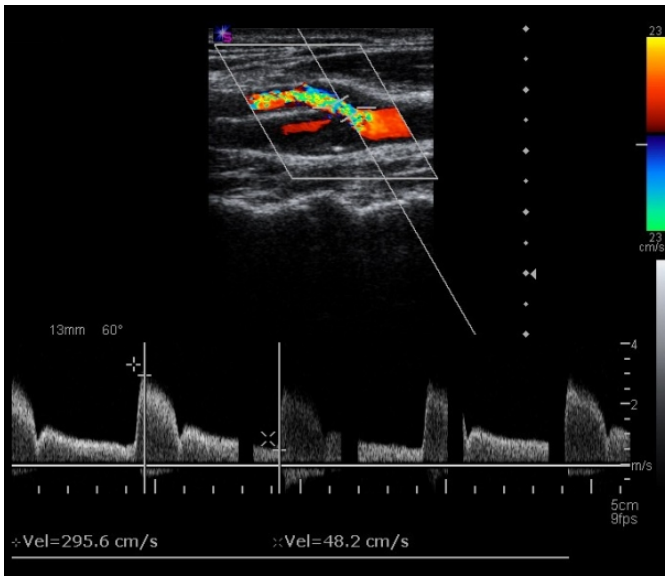

Figure 1.4: *Duplex ultrasound: the small, combined* B*-mode and* CFI *display is used to guide the positioning of the spectral Doppler sample volume.*

by the invasive nature of the catheter, which must be even closer to the stenosis than catheters used to inject contrast with X-ray and MR angiography. Thus, because of the increased risk associated with catherisation, IVUS is typically reserved for assessing outcomes of surgery, such as angioplasty and stenting.

1.1.5 Diagnosis of carotid stenosis with Doppler ultrasound

As stated in Sect. 1.1.4.3, the peak systolic velocity measured by Doppler ultrasound is used to diagnose carotid disease. However, some caution should be exercised when converting maximum velocity to the degree of stenosis. Several different indices are used, such as the peak systolic velocity (PSV) and the peak end diastolic velocity (PEDV); both measurements are located at the point of maximum stenosis. Further derived indices exist, such as the ratio of the PSV at the site of maximum stenosis to the PSV in the common carotid artery (Evans & McDicken, 2000; Hoskins, 1990). Robinson et al. (1988) suggested that only the peak systolic velocity be used; both for the sake of simplicity and that the reliability was not significantly different to other measurements.

The literature regarding the clinical measurement of stenosis using Doppler ultrasound is extensive, frequently contradictory, and consequently in need of a thorough review. Numerous studies have established relationships between PSV and the degree of stenosis estimated via

Author	% diameter reduction	PSV threshold / cm·s^{-1}
Alexandrov et al. (1997)	>70	250, 140†
Bluth et al. (1988)	60–79	130
	80–99	250
Elgersma et al. (1998)	≥70	210‡, 270*
Fillinger et al. (1996)	>60	190–240§
Heijenbrok-Kal et al. (2006)	50–99	125
	70–99	220
Hunink et al. (1993)	≥70	230
Kuntz et al. (1997)	70–99	229[1], 340[2]
Nederkoorn et al. (2002)	70–99	270
Robinson et al. (1988)	>50	150
	>70	225

Table 1.1: *Categorisation of stenosis by Doppler ultrasound.* †PSV *threshold and a combination of* PEDV*, or velocity ratio, or* B*-mode diameter reduction;* ‡*July 1992–February 1994; *October 1996–August 1997;* §*Machine specific threshold;* [1]*Laboratory* A*;* [2]*Laboratory* B.

X-ray angiography. On the basis of these data, many PSV thresholds have been recommended, above which severe carotid stenosis (>70% by diameter) is diagnosed (Table 1.1).

There is a range of PSV thresholds used in different laboratories to categorise patients for carotid surgery (Table 1.1). Values, even in the same institute, do not remain constant, and should be updated frequently (Elgersma et al., 1998). Thresholds used in one clinic yield poorer results at another (Alexandrov et al., 1997; Kuntz et al., 1997). The inevitable confusion due to the proliferation of recommendations is evident in the UK ultrasound community (Walker & Naylor, 2006). Different centres defined stenosis differently, with the PSV threshold varying from 140–240 cm·s^{-1}. Furthermore, confusion existed in the gold standard (DSA) definition; 26% of respondents reported using the NASCET definition of stenosis; 31% reported using the ECST method; the remaining 43% did not know what definition their centre used to categorise stenosis severity.

Of the many reasons for the confusion in the PSV threshold, poor study design has attracted critical attention (Rothwell et al., 2000). Of 40 studies reviewed, only two thirds were retrospective, 55% failed to study randomised or consecutive patients and 62% did not present any data on reproducibility. Potential flaws in basic study design included: quoting reproducibility data for mild stenosis; publishing data from young, healthy individuals, rather than patients; and, in a substantial number of studies, selection bias, where patients are imaged by one modality first, for example Hunink et al. (1993), before being recommended a subsequent scan with the test

modality. Selection bias is extremely difficult to avoid, given that recommending patients for a further unnecessary test with a known risk (such as a DSA) on the basis of a negative previous result is unethical (Nederkoorn et al., 2002). Other issues of concern regarded blind assessment of images and stenosis definition (ie, ECST or NASCET criteria, studies after 1990 were much better at this). Specific criticism was reserved for sample sizes; none of the reviewed studies were of sufficient statistical weight to allow the authors to draw robust conclusions.

Other than poor design, systematic errors have been identified in methodologies used to diagnose severe stenosis. Among the more obvious reasons, operator experience, different equipment and even differences in cardiac output are at least partly responsible for some variability (Alexandrov et al., 1997; Elgersma et al., 1998; Fillinger et al., 1996; Kuntz et al., 1997). The purposes of the ultrasound investigation are also reasonable for some degree of ambiguity. If US is used to select patients for X-ray angiography, then diagnosing a false negative (FN) is potentially more serious than a false positive (FP) (Alexandrov et al., 1997; Elgersma et al., 1998; Heijenbrok-Kal et al., 2006; Kuntz et al., 1997), since a FN removes a patient from further study, with associated risk of stroke, but a FP yields only a DSA (assuming the misdiagnosis is corrected). The consequence of favouring FPs over FNs is therefore a reduction in the PSV threshold. If the study objective is to maximise accuracy, rather than the minimisation of stroke risk, the gravity of FPs and FNs is equal, thus a more accurate PSV threshold may ultimately be set.

Of the issues discussed in the literature, specific instrumentation issues are mostly overlooked. Methodologies mostly ensure that the beam-to-flow (BTF) angle is less than 60°. In complex flow, as occurs in the vicinity of a stenosis, the direction of flow is not known. Consequently, a substantial error will be present in the BTF angle, which propagates through to the velocity measurement. Based on an in-vitro study, an uncertainty in the BTF angle of 5–10° results in velocity errors of 15–30% for beam-vessel angles of less than 60° (Hoskins, 1997).

Quantifying the *peak* systolic velocity also introduces further errors. Considering the finite size of the Doppler aperture on the transducer reveals that a range of BTF angles are present (Fig. 1.5), rather than just one (Daigle et al., 1990; Hoskins, 1999). Consequently, a geometric broadening effect is introduced into the measured Doppler spectrum, with the maximum broadening arising from the acutest angle subtended at the Doppler aperture. Errors introduced via this method are inevitably geometry dependent, but typically range from 15–40%.

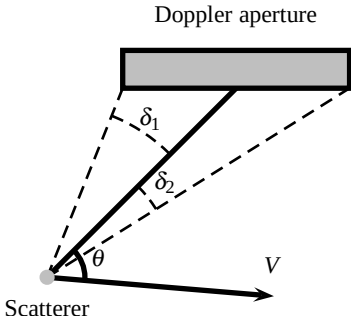

Figure 1.5: *Geometric spectral broadening in Doppler ultrasound.*

Despite the range of thresholds and the systematic errors due to spectral broadening, Doppler ultrasound is successful at diagnosing stenosis. With appropriately set velocities, typical values for sensitivity and specificity can exceed 90% (Alexandrov et al., 1997; Elgersma et al., 1998; Fillinger et al., 1996; Kuntz et al., 1997), although further improvement of one performance indicator usually comes at the expense of another. In clinical practise, Doppler ultrasound is typically used to pre-screen patients for X-ray angiography, thus PSV threshold are set at a clinically useful level (which minimises false negative diagnosis), rather than a threshold that necessarily maximises accuracy.

1.1.6 Summary

X-ray angiography, MRA and Doppler ultrasound are accurate modalities that allow clinical diagnosis of stenosis. The relative newcomer, MRA, is rapidly gaining ground on the established gold standard, digital subtraction angiography (Forsting & Wanke, 2003), but the cost-effectiveness and real-time nature of DUS mean that it will remain the primary clinical tool for the initial diagnosis of carotid stenosis. Choosing the appropriate threshold for the peak systolic velocity remains an imprecise science; recommendations abound in the literature, although the most useful advice would appear to regularly test and update the thresholds locally (Elgersma et al., 1998; Kuntz et al., 1997), while greater clinical appreciation of application (Alexandrov et al., 1997; Kuntz et al., 1997) and instrumentation errors (Daigle et al., 1990; Hoskins, 1999) would help.

1.2 The role of biomechanics in arteries

1.2.1 Biomechanical forces in arteries

Mechanical forces acting on the artery wall affect its pathology. Two forces dominate: the outward pressure (known as the transmural pressure) exerted by the constrained blood pushing radially outwards; and the wall shear stress (WSS) which is a shearing force that acts on the inner-most layer of the artery. The magnitude of the transmural pressure is on the order of 10^4 Pa; the magnitude of the WSS is around 1 Pa. The wall shear stress is the product of the blood viscosity and the velocity gradient at the vessel wall,

$$\tau_{\mathrm{w}} = -\mu \left.\frac{\partial v}{\partial r}\right|_{\mathrm{r=R}}, \tag{1.1}$$

where τ_{w} is the wall shear stress, μ is the dynamic viscosity and $\left.{}^{\partial v}/_{\partial r}\right|_{\mathrm{r=R}}$ the velocity gradient (shear rate) at the artery wall. The velocity field is a 3D entity. Flow through relatively straight arteries is mostly orientated along the vessel axis; however, at curves and vessel branches, the circumferential component of velocity may result in significant deviations between the direction of the WSS vector and the axis.

The distribution of shear stress varies throughout the circulatory system, according to the local hæmodynamic forces. According to the principle of minimum work (Murray, 1926), some degree of consensus emerged assuming that values of wall shear stress should be approximately equal across species and throughout the arterial tree. However, evidence supporting this argument is scarce. Recently, evidence rendering this hypothesis null has emerged (Cheng et al., 2007; Dammers et al., 2002; Wu et al., 2004), and the consensus is that mean WSS is not constant throughout the vasculature (Reneman et al., 2006).

The transmural pressure acts radially, distending the artery wall. The artery resists this force with a tension (a hoop stress) acting in the circumferential direction of the order of 10^5 Pa. The hoop stress may be calculated via Laplace's law (Nichols & O'Rourke, 1990),

$$T = \frac{PR}{h}, \tag{1.2}$$

where T is the circumferential stress, P the distending pressure, R the radius and h is the thickness of the vessel wall. Laplace's law assumes a circular geometry and that the vessel wall is thin, while it ignores effects due to dynamic pressure. The variation of the transmural pressure throughout the arterial tree less localised than the WSS distribution, since blood pressure is predominantly a systemic property. In healthy vasculature, the primary pressure drop occurs across the smallest vessels (the capillaries), such that pressure in the large arteries is approximately constant.

1.2.2 Biomechanical factors in arteries

Endothelials cells sense flow in vessels as the wall shear stress acts directly upon them. The exact nature of the mechanotransduction remains unknown; under shearing forces, the luminal side of the cell is stretched and this load is transmitted throughout the cell and to other cells via the cellular matrix (Reneman et al., 2006). Thus, it is at the point of attachment to the matrix that the cells are able to detect the shearing stress. Another suggestion is that a layer of proteins that cover ECs may, in fact, detect fluid dynamic forces and convert them into tensile stress (Smith et al., 2003). Under this hypothesis, the EC would not actually sense the shearing stress; however, it would remain the catalyst to any response.

Under increased shear stress, which usually results from increased blood flow, ECs produce vaso-active endothelial-derived relaxing factors—principally nitric oxide but others exist—which results in vaso-dilation (Davies, 1995; Koller et al., 1993). This mechanism functions both in-vivo and in-vitro. Typically, vaso-dilation is a short term response to elevated levels of wall shear stress. Long term elevations in WSS trigger arterial remodelling (Bendick et al., 1997; Kamiya & Togawa, 1980; Zarins et al., 1987); the hypothesis is that the vessel will dilate until normal levels of shear stress are restored. Similarly, sustained reduction of blood flow results in permanent vaso-constriction (Langille & O'Donnell, 1986). That the ECs play a major role in this process is without doubt; removal of the endothelium before altering the flow rate results in no remodelling (Davies, 1995; Koller et al., 1993; Langille & O'Donnell, 1986).

The shearing force that acts on ECs stimulates not only vaso-dilation, but also encourages the cells to change their mounting on the extra-cellular matrix. In the aortas of dogs, Flaherty et al. (1972) observed that in uniform segments, the ECs were aligned with the direction of flow had an elongated structure; close to vessel branches and curves, the cells had non-axial alignments, with much less elongation in cell structure. Upon removing a section of artery wall from regions

of stable flow and replacing it, having rotated it through ninety degrees, the endothelial cells had realigned with the flow in less than ten days. Similar results have been obtained from in-vitro studies; comparing a bed of endothelial cells exposed to laminar flow for 24 hours with cells in a static culture, Barbee et al. (1994) observed that under flow conditions, the ECs had aligned in the direction of flow and developed and elongated structure.

1.2.3 Biomechanical factors in arterial disease

Atherosclerosis is a focal disease that affects the branching points and curves of the major vessels. A significant body of work exists that correlates the locations of plaque development with low and oscillating values of wall shear stress (Caro et al., 1971; Moore & Ku, 1994; Ku et al., 1985*a*,*b*; Pedersen et al., 1997; Zarins et al., 1983). Low values typically imply a time averaged magnitude inferior to 0.5 Pa; oscillatory shear stress implies that the direction of the shear stress vector changes through the cardiac cycle. Similarly, the thickness of the intima-media layer of the artery wall have been found to correlate with low values of wall shear stress (Friedman et al., 1981, 1986).

The correlation between low wall shear stresses and plaques does not explain why lesions develop. The current hypothesis is that low wall shear stress induces a range of biological responses. Specifically, low WSS increases the expression and activity of angiotensin-converting enzyme, and also the expression of E-selectin and cell adhesion molecules by endothelial cells (Slager et al., 2005*a*). These changes ultimately reduce production of nitric oxide and increase recruitment of monocytes, respectively (see Sect. 1.1.2).

As vascular lesions develop from fatty streaks to plaques, arterial remodelling is hypothesised to be responsible for maintaining the prevailing conditions of low wall shear stress (Slager et al., 2005*a*). As a plaque develops at a site of low WSS, the lumen is locally reduced, leading to increased shear stress. The plaque free (healthy) part of the vessel remodels, ultimately restoring the previous status-quo, and, in effect, promoting further plaque development. Vascular remodelling is known to be functionally dependent upon endothelial cells (Koller et al., 1993; Langille & O'Donnell, 1986). Consequently, the failure of vessels to remodel beyond a particular threshold is believed to indicate that, locally, the region of plaque free walls containing healthy ECs capable of promoting vascular remodelling is minimal (Slager et al., 2005*a*). This leads to a reduction of the lumen, via a mechanism considered a normal response to shear stress.

Once remodelling ceases and lumen narrowing begins, the proximal side of the stenosis is subjected to increased WSS; distally, a region of reduced WSS forms. Examinations of excised, ruptured plaques, indicate that the structure of the cap changes along the length of the lesion. Proximally, the cap is thinner, with more evidence of rupturing and high concentrations of macrophages. In the low WSS region downstream of the stenosis throat, smooth muscle cells dominate (Slager et al., 2005*b*). The increased frequency of ruptured plaques upstream suggests that high WSS may destabilise the fibrous caps; distally, the low values of wall shear stress encourage further development of atherosclerosis.

Potential mechanisms that weaken the upstream cap are likely due to increased production of NO by endothelial cells in response to raised levels of WSS. High levels of nitric oxide can promote smooth muscle cell apoptosis, potentially leading to tissue reduction in the cap (Slager et al., 2005*b*). High shear stress encourages ECs to reduce inflammation. The endothelial cells thus upregulate transforming growth factor-β, which reduces proliferation of SMCs (Slager et al., 2005*b*). Together, these responses to increased shear stress, which would normally be construed to be vaso-protective, may contribute to the destabilisation of plaques.

As noted in Sect. 1.1.2, it is tissue stresses that are responsible for plaque rupture, not shearing stresses. Maximum stress occurs at plaque shoulders, where the plaque merges with healthy vessel wall laterally (Slager et al., 2005*b*). The actual distribution of stresses in the plaque is sensitive to the structure of the plaque; the thinner the fibrous cap, the higher the stresses (Loree et al., 1992). Thus, the cap thinning action hypothesised to be due to elevated wall shear stress not only weakens plaques, but increases the stresses within them. Thus the transformation from a stable to a vulnerable plaque would be complete.

1.2.4 Summary

The wall shear stress is believed to play an important role in initiating the development of atherosclerosis in the presence of known risk factors. Arterial remodelling maintains conditions favourable to atherogenesis. Repeated injury and repair to plaques increases the size of the fibrous cap. As vascular remodelling ceases, the lumen reduces, increasing the proximal wall shear stress. This weakens the cap, rendering the plaque vulnerable to rupture under increased tissue stresses that may result from exertion or sudden increases in blood pressure.

1.3 Estimation of blood velocities and wall shear stress

Sect. 1.1.5 discussed the importance of Doppler ultrasound when selecting patients for vascular surgery and some of the difficulties associated with accurate measurement of maximum velocity. To improve patient categorisation, a better appreciation of the performance of Doppler ultrasound velocity measurements, particularly in complex geometries, is required. Sect. 1.2 discussed the relevance of biomechanical factors in arterial disease. To learn more about the role WSS plays in atherosclerosis, it will be useful to measure the shearing force, both in-vivo and in models of arteries. This section reviews non-invasive measurement of blood velocity and wall shear stress with Doppler ultrasound.

1.3.1 Velocity estimation with Doppler ultrasound

1.3.1.1 In-vivo estimation of blood velocities

Although many in-vivo imaging methods exist, relatively few are suitable for quantitative analysis. X-ray angiography, for example, is capable of delineating arterial lumen (Sect. 1.1.4.1), but analysis of blood velocities is not possible. Similarly, although methods such as hot-wire anemometry exist, they are invasive, and may cause extreme trauma to patients. The exact value of invasive measurements is not clear; by their very use, they modify the local flow dynamics, such that the data collected may not represent the undisturbed regime. In effect, only two non-invasive and direct methods exist for velocity estimation in-vivo: MRI and Doppler ultrasound. In this section, velocity measurements made with Doppler ultrasound are reviewed.

One of the first in-vivo measurements of blood flow using Doppler ultrasound studied aortic flow with continuous wave (CW) ultrasound (Franklin et al., 1961). A transmitting and receiving element were invasively attached to opposite sides of a dog's aorta, and the received frequency shift produced physiologic waveforms. The device was not capable of determining flow direction, but in in-vitro calibration tests, the instrument's response to velocity was confirmed to be linear.

Pulsed wave (PW) Doppler devices are capable of estimating velocity and an axial co-ordinate; an important advantage over CW designs. (Baker, 1970) described one of the first pulsed instruments, illustrating how it could be used to provide estimates of volume flow rate non-invasively.

The authors raised the difficulty of specifying the beam-to-flow (BTF) angle, although without any solution.

The potential of Doppler ultrasound to supersede X-ray angiography was determined by Keller et al. (1976*a*). Using a CW device in the carotid artery, and determining flow direction by distally applying pressure to the facial arteries, they established that in the majority of cases Doppler ultrasound yielded positive results confirmed by angiograms. Classification of disease was based on waveform shape, particularly on the presence of reverse flow. With a PW device, the same group also demonstrated the feasibility of measuring velocity profiles in the carotid artery, for both the healthy and diseased case (Keller et al., 1976*b*). The difficulty of specifying the BTF angle was again highlighted.

Some of the first efforts to validate in-vivo blood velocity measurements compared Doppler ultrasound and magnetic resonance based velocity measurements (Maier et al., 1989; Vieli et al., 1989). To avoid disturbing the hæmodynamics, healthy volunteers were scanned within 30 minutes using both modalities, and moved between facilities on beds. The results showed a high degree of linearity between velocities measured in the centre of the aorta by both modalities, and good qualitative agreement in velocity profile shapes with the main differences close to the vessel wall. The authors acknowledged that specifying the beam-to-flow angle was a problem; indeed, in one paper they acknowledge that "a postcorrection of the angle of incidence was carried out based on the [MR] image" (Vieli et al., 1989). The value of this correction is unclear, given that the MR scan was not carried out at the same time, and it may actually bias the data towards better agreement, rather than better measurement accuracy. Finally, Doppler ultrasound itself is prone to large errors (Hoskins, 1999) and should not be relied on as a gold standard.

Estimation of velocities in arteries requires accurate quantification of the Doppler frequency shift (for PW devices, strictly the phase shift of the received signal) and knowledge of the BTF angle. The frequency shift along the line of sight can be measured accurately, however, specifying the BTF is complex (Sect. 1.1.4.3). The angular problem can be solved by simultaneously measuring two components of velocity, a technique known as vector Doppler (Hoskins et al., 1994; Overbeck et al., 1992; Steel et al., 2003). Unfortunately, implementation of vector techniques is not widespread, with potentially serious implications for patient selection (Hoskins et al., 1999).

Ultrasound measurements of blood flow have not been restricted to the longitudinal plane. Although in straight vessels, flow is predominantly aligned with the vessel axis, at sites prone to atherosclerosis, blood flow is complex, and can have considerable secondary velocities. Hoskins (1994*a*) observed significant spiral flow in the femoral artery using vector Doppler, while flow in the common carotid artery has also been found to be skewed, suggesting the presence of secondary flow (Brands et al., 1995; Tortoli et al., 2003). Both vessels are often considered straight; that is, it is enough to measure one component of velocity to fully describe the hæmodynamics. Such evidence suggests that this may not be the case.

1.3.1.2 In-vitro estimation of velocities with Doppler ultrasound

The simplest flow phantoms consist of straight tubes, through which steady flow passes. McDicken (1986) used heat shrink tubing and a glycerol/water mixture to demonstrate a linear increase in the flow rate estimated by the Doppler signal. The linearity persisted until turbulence affected the measured velocity. More sophisticated in-vitro test objects can produce oscillatory flow using computer controlled pumps (Holdsworth et al., 1991; Hoskins et al., 1989; Shortland & Cochrane, 1989).

Hoskins (1997) studied flow through a simplified stenosis using a dual-beam Doppler system. Angle independent velocities were obtained by compounding colour flow data from Doppler beams steered in different directions, without any assumptions about the direction of flow. Estimated errors at the site of maximum velocity using conventional single component spectral Doppler increased with angle, ranging from 10–20% at 50° to 24–46% at 70°. The clinical importance of these data was not overlooked, the author suggesting that the technique may improve categorisation of patients with carotid stenosis by removing the need to correct for the beam-to-flow angle.

Velocity variability for steady flow through simplified symmetric and asymmetric stenoses has been studied by Steel et al. (2003) using a prototype dual beam system. Over a range of beam to vessel angles (40–80°), the mean variability of the velocity magnitude was less than 8%, applying a novel algorithm reduced this to 5%. Despite the improvement in velocity fluctuation, the vector method is not widely implemented.

A realistic carotid bifurcation suitable for Doppler ultrasound studies was created by Poepping et al. (2002). Idealised stenoses ranging from 30–80% based upon the NASCET criteria were

added to the internal carotid artery, in an asymmetric and concentric manner. However, obtaining the upper limit of flow rates in these models is limited by the strength of the tissue mimicking material, which ruptures when tissue stresses exceed the yield stress.

Refinement of the tissue mimic produced a stronger phantom, which in principle would allow validation of velocity measurements made using separate modalities (Meagher et al., 2007; Watts et al., 2007). Two geometrically identical phantoms were made, one suitable for acoustic measurements, and another using optically clear silicone rubber, based on idealised anatomic geometries of the carotid bifurcation obtained by MR angiography. At present, no further data has been published comparing velocities from the dual phantom approach.

1.3.2 Estimation of wall shear stress with Doppler ultrasound

1.3.2.1 In-vivo estimation of wall shear stress

One of the first studies to estimate the wall shear stress in-vivo combined the Poiseuille solution for steady flow with ultrasound derived measurements of arterial diameter and maximum velocity (Gnasso et al., 1996). Although widely cited, this study used a flawed method to estimate wall shear stress, hence its results should be treated with caution. The mean WSS is likely to be an acceptable estimate, but for a pulsatile flow, even in a straight, rigid pipe, the instantaneous velocity profiles are distinctly not parabolic, thus all other shear stress estimates will have systematic flaws in them. Despite this error, the reported values of wall shear stress agree well with other published values (Table 1.2).

The parabolic approximation formed the basis of a study investigating flow mediated dilation of the brachial artery (Mitchell et al., 2004). The authors report values of WSS in men and women at end diastole (Table 1.2). Despite flow conditions at diastole being the most Poiseuille-like (quasi steady with little wall movement), values of WSS reported are lower than other mean values for the brachial artery. This is not surprising, as the mean value will be substantially affected by the systolic peak.

The first system capable of estimating the wall shear rate—the authors were careful to differentiate between the velocity gradient and the force—with Doppler ultrasound was described by Brands et al. (1995); Hoeks et al. (1995). In essence, the Shear Rate Estimation System (SRES) is a high frequency, multi-gate pulsed-wave Doppler system that stores acquired radio-frequency data in a large buffer. These are data analysed off-line using a personal computer.

Authors	Vessel	Modality	Max WSS / Pa	Mean WSS / Pa
Oshinski et al. (1995)	Supra-renal aorta	MRI	5.0 (0.9)	1.0 (0.3)
	Infra-renal aorta	MRI	3.2 (0.9)	0.5 (0.3)
Oyre et al. (1997)	Supra-renal aorta	MRI	4.1 (0.5)	0.6 (<0.1)
	Infra-renal aorta	MRI	2.7 (0.2)	0.3 (<0.1)
Taylor et al. (2002)	Supra-celiac aorta	MRI	—	0.4 (0.1)
	Infra-renal aorta	MRI	—	0.1 (0.1)
Dammers et al. (2003)	Brachial	US	3.9 (0.8)	0.5 (0.2)
Mitchell et al. (2004)	Brachial	US	—	0.1 (0.3)†‡
	Brachial	US	—	0.0 (0.3)†*
Silber et al. (2005)	Brachial	MRI	1.2 (0.4)§	—
Wu et al. (2004)	Brachial	MRI	3.7 (0.8)[1]	0.8 (0.4)[1]
Brands et al. (1995)	CCA	US	2.9 (0.8)[1]	—
Dammers et al. (2003)	CCA	US	3.4 (0.8)	1.2 (0.2)
Forsberg et al. (2000)	CCA	US	—	1.7 (0.6)[1]
Gnasso et al. (1996)	CCA	US	3.0 (0.8)	1.2 (0.3)
Hoeks et al. (1995)	CCA	US	2.6 (0.3)[1],[2]	0.8 (0.1)[1],[2]
	CCA	US	1.8 (0.3)[1],[3]	0.8 (0.1)[1],[3]
Oyre et al. (1998*b*)	CCA	MRI	2.6 (0.1)	1.0 (<0.1)
Samijo et al. (1998)	CCA	US	4.3 (1.3)‡	1.3 (0.3)‡
	CCA	US	3.3 (0.7)*	1.2 (0.2)*
Tortoli et al. (2006)	CCA	US	3.6 (0.7)[1]	1.2 (0.3)[1]
Wu et al. (2004)	CCA	MRI	3.8 (0.5)[1]	1.3 (0.2)[1]
Kornet et al. (2000)	Common femoral	US	—	0.4 (0.2)
	Superficial femoral	US	—	0.5 (0.2)
Silber et al. (2005)	Femoral	MRI	1.3 (0.3)§	—
Wu et al. (2004)	Superficial femoral	MRI	2.9 (0.6)[1]	0.5 (0.2)[1]

Table 1.2: *In-vivo values of wall shear stress reported in the literature.* †*Diastolic* WSS*;* ‡*measured in males;* **measured in females;* §*systolic* WSS*;* [1]WSR *measured, converted to* WSS *assuming* $\mu = 4\text{mPa}\cdot\text{s}$*;* [2]*age range 20–30;* [3]*age range 60–70.*

Thus, the SRES is capable of measuring the velocity distribution and consequently velocity gradient as a function of depth and time. Estimates of wall shear rate produced using the SRES fit within hypothesised "healthy" 1–2 Pa (Table 1.2).

Although the SRES represented a significant development, and has been used to investigate WSR in a number of studies (Dammers et al., 2003; Kornet et al., 2000; Samijo et al., 1997, 1998), it suffers from two significant issues. Its use is limited to relatively straight arteries where the direction of flow can be assumed. Secondly, the device assumes that the maximum velocity gradient is necessarily the velocity gradient at the vessel wall. For steady flow, this is a reasonable assumption; but for pulsatile flow, velocity profiles are often triphasic, thus the

maximum velocity gradient may arise from the central flow node rather than from flow next to the vessel wall.

A device similar to the SRES that also returns wall motion and the range of velocities at each depth represents the current state of the art in Doppler ultrasound (Bambi et al., 2004). This instrument can estimate the WSR, but it maintains the assumption that peak velocity gradient is equivalent to the WSR. Further development enabled the system to optimise the alignment of the transducer (Tortoli et al., 2006), removing some of the angular dependency, although this is not true vector Doppler, and it is questionable how well this mechanism would perform in the case of flow separation.

The only attempt to estimate the wall shear rate with a clinical ultrasound machine used colour flow imaging to estimate the velocity profile across the lumen (Forsberg et al., 2000). The results agree remarkably well with other systems based on non-standard hardware despite the difficulty associated with CFI (Table 1.2). In patients with carotid stenosis, WSR increased significantly (from 414 s^{-1} to 687 s^{-1}).

1.3.2.2 In-vitro estimation of wall shear stress with Doppler ultrasound

In-vitro studies of hæmodynamics and fluid flow are particularly useful. Many vessels are difficult to image with non-invasive modalities because they are too tortuous, or turbulent flow prevents accurate velocity measurement. Validation of in-vivo measurements remains difficult. Studying flow in simplified vascular models also uncovers the general fluid behaviour characteristic to certain geometries—such as stenoses and aneurysms—and can provide much needed validation for the instrumentation used.

Some of the first measurements to estimate wall shear rate using Doppler ultrasound attempted to correct for the size of the sample volume (Hughes & How, 1993, 1994). Using a 20 MHz Doppler system, they studied flow through a rigid, straight pipe. Under steady flow, errors in the measured WSR fell from 46% to 12%; under pulsative (Womersley) flow, errors in the mean and peak-to-peak ranged from 21–35% and 8–14% respectively.

The wall shear rate estimated using the Shear Rate Estimation System validated initial measurements using laser Doppler anemometry (LDA) (Brands et al., 1995). Sinusoidal flow in a distensible pipe was measured using LDA and the SRES. The difference between the two systems was around 11%. To explain this, the authors surprisingly conclude that the velocities

measured by with LDA were inaccurate close to the vessel wall, since the system struggled to resolve signals due to slowly moving fluid from the slowly moving wall.

1.3.2.3 Challenges regarding the measurement of wall shear stress

At present, measurement of the WSR/WSS is of academic interest, rather than of clinical interest, despite the hypothesised biomechanical importance. Only one system in the world has even a small, let alone clinically relevant, body of literature to support what normal values of WSR/WSS are (Brands et al., 1995; Dammers et al., 2003; Hoeks et al., 1995; Samijo et al., 1997, 1998). The Shear Rate Estimation System is the only system in the world that measures the velocity gradient, rather than fitting curves to velocity data in the boundary layer (Oyre et al., 1997, 1998*b*; Taylor et al., 1998; Wu et al., 2004).

The SRES is a high resolution device, capable of measuring velocities within 300 μm from the vessel wall. Comparable nearest wall measurements for MRI are between 500 and 1000 μm (Reneman et al., 2006). Even with laser Doppler anemometry, measurements close to the vessel wall are prone to large errors below 500 μm (Fatemi & Rittgers, 1994). Measurements of shear rate far from the vessel wall are, in general, biased to lower values, so the nearer to the wall the velocity measurement may be made, the better the accuracy of the WSR measurement (Fig. 1.6a). (If flow reversal is present, then these measurements may just be completely wrong (Fig. 1.6b).) With Doppler ultrasound, despite its high resolution (at high frequencies), signals very close to the vessel wall contain a low amplitude but fast moving signal from blood, but also a high amplitude (approximately 100 times larger), slow moving signal originating from the wall. Separation of the signals is essential, but removal of the slow moving component due to the vessel wall also removes any signal from slow moving blood next to the wall. Consequently, progression to ever higher frequencies will not necessarily enable measurement of velocities immediately next to the wall.

To offset the bias introduced by limited resolution, the SRES measures the velocity gradient across the entire vessel; the local maxima near to each vessel wall is considered the shear rate at each wall. (This approach has been implemented by other groups, notably (Tortoli et al., 2006).) Although this method produces values broadly in line with the literature—which is, to a large extent, inevitable, since much of the work in the literature uses this assumption—and is, as a consequence considered acceptable, there is no physical reason to justify the use of maximum shear rate as a substitute for the wall shear rate. The only attempt to quantify

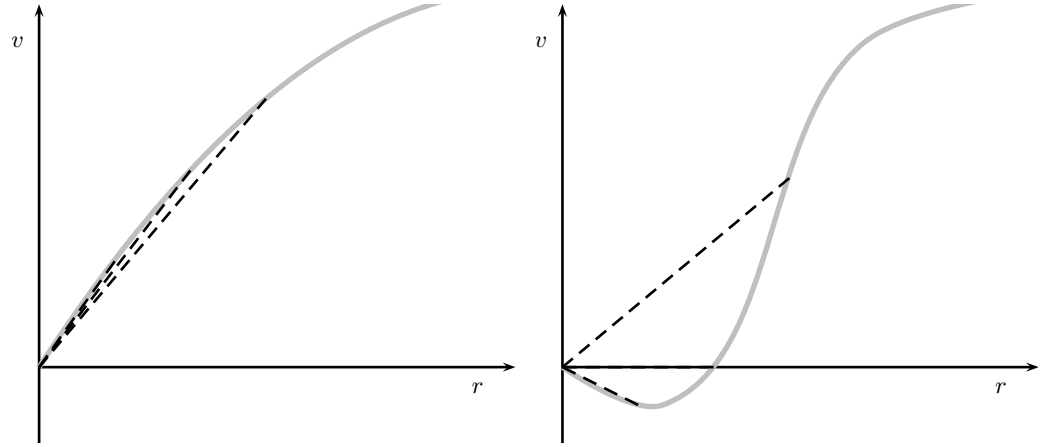

(a) WSR estimation in steady flow. The boundary layer affects the entire velocity profile.

(b) WSR estimation in the presence of reverse flow. The boundary layer ranges only from the wall to the first turning point.

Figure 1.6: *Linear estimation of wall shear rate. Poorer resolution biases the actual* WSR *towards zero; velocity points measured beyond the boundary layer introduce large errors, both in the magnitude and the sign.*

the effect of this assumption (Brands et al., 1995), concluded that the differences between the validation measurements and the SRES measurements were on the order of 11%, and primarily as a result of inaccuracies of the laser Doppler system.

Fitting curves to velocity points measured in the boundary layer has attracted lots of attention (Cheng et al., 2002; Oyre et al., 1997, 1998*b*,*a*; Taylor et al., 2002; Köhler et al., 2001), primarily based on theoretical work (Fatemi & Rittgers, 1994; Lou et al., 1993). However, no physical theory states that a parabola is more suitable for modelling oscillatory flow than a linear method (with the obvious exception of steady flow). Higher order polynomials have also been used, although the reliability decreases as the order of the polynomial increases (Cheng et al., 2002; Fatemi & Rittgers, 1994; Köhler et al., 2001). In general, however many points are used to extrapolate the wall shear rate, they must all lie within the boundary layer of the fluid, otherwise estimates of the WSR may be completely wrong (Fig. 1.6b).

Practical issues also affect the wider study of wall shear stress. Equipment capable of measuring WSR is not widely available in the clinical environment. The SRES system and the Tortoli et al. (2006) are custom built systems, restricting their application to research driven environments. Although some methods have used a clinical scanner to estimate WSR, these studies either assumed Poiseuille flow (Gnasso et al., 1996) or maintained the maximum shear rate assumption (Forsberg et al., 2000).

The restricted availability of machines capable of estimating wall shear rate also presents a problem with population studies. Before a wider study of WSR can be conducted, the methodology must first be validated or at least accepted as valid by the peer review process. In the initial stages, this will typically involve presenting in-vitro and in-vivo data, typically from a small number of assumed healthy volunteers. However, any method that produces values considered outwith the established literature risks being rejected. This rejection is not necessarily valid, since, with the exception of the Mitchell et al. (2004) who presented diastolic values of WSS based on parabolic flow, all healthy WSS values presented by the literature are based on extremely small sample sizes (5–54). Consequently, there is an incentive to develop an elaborate method such that the methodology will be approved by referees, but this may come at the expense of clinical applicability. In turn, this prevents large scale studies of wall shear rate being adopted, so the knowledge base remains small.

One of the intractable problems with estimating the wall shear stress concerns converting the wall shear rate into the shear stress (Eq. (1.1)). Blood viscosity is a function of the blood plasma viscosity and the contribution from the hæmatocrit; it is not constant, depending strongly on the shear rate (Nichols & O'Rourke, 1990). At high values of shear, the viscosity tends to an asymptotic limit (around 4 mPa·s at shear rates >100 s^{-1}). However, at low shear rates, the blood viscosity increases markedly (by a factor of approximately 15 from the asymptotic limit at shear rates around 1 s^{-1}). Consequently, when converting wall shear rate into WSS, the value of μ is not known. Although models of blood viscosity do exist (Weaver et al., 1969), and have been combined with measurements of hæmatocrit and WSR (Dammers et al., 2003; Samijo et al., 1997), the individual's viscosity/shear rate curves were not measured, so the validity of the shear stress measurement is unknown.

The final major problem with WSS estimation concerns the 3D nature of blood flow. Arteries are not planar, so blood flowing through them has three components of velocity. For relatively straight vessels, such as the common carotid artery, the dominating component will be orientated axially. This explains why the majority of studies (particularly those based on ultrasound techniques) have looked at flow in straight vessels (Table 1.2). However, even if one disregards the diseased case, atherosclerosis preferentially develops at bifurcations and curves, sites where geometries and flow are inherently three-dimensional. Study of the circumferential velocities is therefore important, but accomplishing this with existing imaging techniques is difficult. At present, only MRI can measure 3D velocity fields non-invasively, but its limited res-

olution means that it is hard to measure velocities within the boundary layer and the acquisition times for studies are long, making it expensive and susceptible to patient movement. The preferred model for measuring the circumferential component of WSS is now using computational methods. Obtaining realistic vascular geometries and boundary conditions is possible. Unfortunately, CFD typically requires laborious manual segmentation and is largely unvalidated if turbulence is present. Considering the number of machine hours required for such simulations to converge—on the order of 50 or more—means that the method is still several steps away from clinical adoption. Thus, the non-axial component of wall shear stress remains largely beyond the means of current studies.

1.3.3 Summary

Non-invasive velocity measurement effectively means choosing Doppler ultrasound or MRI based techniques. Although velocity estimation with Doppler ultrasound is a well established clinical technique, relatively little work has examined the accuracy of these measurements. Qualitatively, velocities measured in-vivo with MRI and Doppler ultrasound show a linear relationship. However, at critical locations, such as the vessel wall, significant differences occur, predominantly due to partial volume effects, although some contribution is due to the ultrasound clutter filter.

In-vitro experiments have established that in straight vessels, the maximum velocity measured with Doppler ultrasound is directly proportional to the mean flow rate while the flow remains laminar. However, despite advances such as angle independent vector Doppler, studies of the velocity field in complex geometries are absent from the literature, perhaps in part due to difficulties in fabricating suitable test objects. Consequently, the accuracy of Doppler ultrasound derived velocity measurements in the presence of complex fields is unknown.

In-vivo estimation of wall shear stress is difficult, and is principally affected by three problems. Firstly, with conventional imaging techniques, specifying the wall location remains problematic. Secondly, measuring the velocity gradient at the wall is complex; the required resolution is a function of the boundary layer thickness, and measurements close to the wall are affected by clutter filters and partial volume effects. Finally, converting shear rates into shear stresses is a non-trivial process, although models of blood viscosity exist, there is no definitive solution in the literature. The most successful approaches to WSS estimation have relied on assumptions: the maximum shear stress is equivalent to the WSR; that the boundary layer has a parabolic

profile; or that blood is a Newtonian fluid. Of these assumptions, the first two have no physical basis, while the final one is only reasonable at high shear rates (>100 s^{-1}).

1.4 Critical gaps in the literature

Sect. 1.2 and 1.3 discussed the role of biomechanical forces in healthy and diseased arteries, and how relevant parameters have been measured. Accurate measurement of maximum velocity is important, otherwise some patients will have unnecessary surgery, while others will be overlooked potentially beneficial interventions. The prevailing hypothesis, that the wall shear stress is responsible for the sustained progression of atherosclerosis and ultimately for weakening stable plaques, suggests that a more readily applicable technique is needed to monitor WSS in patients, and especially in diseased vessels. Without appropriate measuring tools, it will be impossible to collect data of the required accuracy to refine or ultimately reject the hypothesis.

It is clear that non-invasive measurement of biomechanical parameters is difficult. Limited resolution of instrumentation, difficulties measuring velocities in the vicinity of vessel walls, and uncertainties in flow direction all make velocity measurement in-vivo highly problematic; measuring velocity gradients with any degree of confidence, particularly at the edge of the fluid domain, is consequently even harder. This section highlights important problems in the literature; these problems form the basis of the work presented in this thesis.

1.4.1 Validation of velocities estimated by Doppler ultrasound

In-vivo measurements have compared MRI data with Doppler data in healthy aortas (Maier et al., 1989; Vieli et al., 1989) and found good agreement between modalities, and in-vitro studies under steady flow have found good agreement between peak velocity and measured flow (McDicken, 1986). However, no study compares velocities estimated with Doppler ultrasound and another technique in complex geometries, where a range of velocity magnitudes and beam to flow angles are present.

1.4.2 Estimation of wall shear rate in a clinically acceptable manner

No large scale study has established a range of normal values of wall shear stress in man. Until measurements of WSS can routinely be performed in the clinical environment, using certified

and standard instrumentation, population studies of useful magnitudes will remain unfeasible. Thus, there is a need for a technique that can accurately estimate the WSR using conventional clinical equipment.

1.4.3 Estimation of wall shear rate in diseased arteries

In the presence of vascular disease, only one study has presented estimates of the wall shear rate with non-invasive imaging (Forsberg et al., 2000). However, this paper is short, providing little detail and no validation. All other WSR studies are from healthy vessels. No data exist that show independent WSR measurements obtained from the same complex geometries. Thus, there is a need to establish whether it is possible to estimate values of WSR in complex geometries with Doppler ultrasound, and to validate these measurements using an independent experimental technique.

1.5 Thesis outline

1.5.1 Aims of thesis

Having reviewed the literature regarding the clinical application of Doppler ultrasound in arterial disease, it is evident that the accuracy of maximum velocity measurements is in question. The hypothetical role of the wall shear stress in the development of atherosclerosis has proved difficult to test, not least because of difficulties associated with its measurement, even in healthy arteries. This thesis addresses these two issues. As such, the aims of this thesis are:

- To quantify the accuracy of maximum velocity measurements made with Doppler ultrasound in complex geometries;
- To develop a clinically acceptable method for the estimation of wall shear stress in healthy arteries;
- To assess whether Doppler ultrasound is capable of estimating the wall shear stress in the presence of disturbed flow.

1.5.2 Structure of thesis

Chapt. 1 has introduced arterial biomechanics and discussed the role Doppler ultrasound plays in the management of atherosclerosis and the importance of the wall shear stress.

Chapt. 2 briefly introduces the concepts and techniques used in this thesis. Core ideas from fluid mechanics, in particular dimensionless parameters, are introduced, and simple methods for modelling hæmodynamics are described. This chapter also briefly describes some of the technical aspects of Doppler ultrasound and particle image velocimetry.

Chapt. 3 develops and validates a clinically acceptable method for estimating the wall shear rate in healthy arteries. A clinical ultrasound machine acquires centreline velocities and arterial diameters which are combined to produce time dependent wall shear rate profiles.

Chapt. 4 develops a new working fluid for use in optically transparent models. This fluid has the same refractive index as the surrounding media, reducing refractive errors that occur at interfaces and allowing the use of PIV to study flow through the models.

Chapt. 5 develops a dual flow validation system that allows velocities measured with Doppler ultrasound to be compared with equivalent measurements acquired using particle image velocimetry. The similarity between the dual systems is assessed, and the accuracy of maximum velocity and wall shear rate measurements is characterised.

Chapt. 6 uses the dual validation system to study steady flow through a series of idealised stenoses, at physiologic Reynolds numbers. The distal velocity profiles and wall shear rates measured by both techniques are compared as a function of stenosis severity and flow rate.

Chapt. 7 uses the dual flow system to study oscillatory flow through the same stenosis models. Results are compared at peak systole and end diastole under an idealised flow waveform.

Chapter 2
Essential theoretical considerations

This chapter provides an overview of the essential theory used in this thesis. It briefly introduces concepts from fluid mechanics, in particular the importance of dimensionless parameters. Some of the theoretic aspects of Doppler ultrasound are introduced, and finally the validatory technique used in Chapt. 6 and Chapt. 7, particle image velocimetry (PIV), is covered. With an understanding of these three fields, the data presented in this thesis can readily be tackled.

2.1 Relevant concepts from fluid mechanics

2.1.1 Introduction

This section provides an overview of some concepts in fluid mechanics that are important in this thesis. It describes dimensional analysis and introduces some relevant dimensionless numbers. Simple methods for modelling blood flow are considered, focussing on those that are particularly suited to hæmodynamics.

2.1.2 Dimensionless parameters

Dimensionless numbers are useful in fluid mechanics as they describe fluids that behave in the same way, although they may have completely different values of viscosity, for example. If two fluids have different viscosities, and flow through differently sized pipes (but similar geometries) at different speeds, it is not necessarily apparent that the behaviour of both systems can be compared by studying only one parameter. However, if both fluids are Newtonian, and the geometries and flow rates are time independent, then the dynamics of each system is defined only by the Reynolds number (Sect. 2.1.2.1), which can be considered as the normalised flow rate through vessel. This concept of similarity extends to many diverse parameters, such as frequency, curvature and vortex shedding.

2.1.2.1 Reynolds number

The Reynolds number is an example of a dimensionless parameter, and one of the most important concepts in fluid mechanics, as it determines the nature of the flow regime. The Reynolds number, Re is calculated using Eq. (2.1):

$$\mathrm{Re} = \frac{\rho \bar{v} L}{\mu}, \tag{2.1}$$

where ρ is the density of the fluid, μ is the dynamic viscosity, $\bar{v}$ is the mean velocity and L is a characteristic length, known as the hydraulic diameter. For cylindrical pipes, L is equal to the vessel diameter (Schlichting, 1987). Eq. (2.1) is often written in terms of the kinematic viscosity, ν, defined in Eq. (2.2),

$$\nu = \frac{\rho}{\mu}. \tag{2.2}$$

Substituting Eq. (2.2) into Eq. (2.1) yields

$$\mathrm{Re} = \frac{\bar{v} L}{\nu}; \tag{2.3}$$

which expresses the Reynolds number in terms of the kinematic viscosity. For blood, ν is approximately 3.5×10^{-6} m^2·s^{-1}, under high shear conditions. Typically, healthy arteries range from 100 μm to 25 mm in diameter, with maximum velocities less than 1 m·s^{-1}, so maximum Reynolds numbers are usually around 2000. Flow described by Reynolds numbers in this range is laminar; that is, layers moving at different speeds slide past one another in a smooth manner, with minimal inter-layer mixing.

2.1.2.2 Womersley parameter

All oscillatory flows have periodicity associated with them, and therefore some frequency. In a manner similar to normalising the flow rate, the frequency of a flow may also be normalised. Womersley (1955) derived an expression for the normalised frequency parameter, α, in long, rigid-walled, cylindrical pipes:

$$\alpha = R\sqrt{\frac{\omega}{\nu}}, \tag{2.4}$$

where R is the vessel radius, ω is the angular frequency and ν is the kinematic viscosity. This parameter is of great importance in arterial blood flow, as it allows some degree of theoretical prediction of the velocity profiles (Sect. 2.1.4.4), under certain assumptions.

To specify typical values of the Womersley parameter, it is necessary to know the frequency content of the flow waveform, which is not, in general, available. However, considering the minimum frequency present in the arterial system, that of the heart at 1 Hz, and ω_{min} is therefore around 2π s^{-1}. Arterial waveforms tend not to contain frequencies greater than 20–30 Hz, so ω_{max} is on the order of 150 s^{-1}. Considering typical artery sizes provides estimates for the normalised frequency parameter: 16–80 in the aorta and 4–20 for the common carotid.

2.1.2.3 Dynamic similarity

If the fluid flow in two separate experiments is to be dynamically similar, the dimensionless quantities must be constant across both systems. To ensure similarity in an ideal system with parameters $\{\text{Re}_1, \overline{u}_1, L_1, \nu_1\}$ and an analogue system with $\{\text{Re}_2, \overline{u}_2, L_2, \nu_2\}$, the following condition must hold:

$$\begin{aligned} \text{Re}_1 &= \text{Re}_2, \\ \Rightarrow \frac{\overline{u}_1 L_1}{\nu_1} &= \frac{\overline{u}_2 L_2}{\nu_2}. \end{aligned} \tag{2.5}$$

From Eq. (2.5), it is relatively simple to maintain dynamic similarity when an analogue fluid has a different kinematic viscosity ν_2 to that of the idealised fluid ν_1. If the geometries are the same (ie, $L_1 = L_2$) then ensuring similarity is even simpler; all one must do is scale the mean velocity by the ratio of the viscosities (typically achieved by varying the flow rate Eq. (2.8)). If the two systems contain an oscillatory element—and are rigid walled cylinders—then the normalised frequencies, α_1 and α_2, must also match in each system:

$$\begin{aligned} \alpha_1 &= \alpha_2, \\ \Rightarrow R_1 \sqrt{\frac{\omega_1}{\nu_1}} &= R_2 \sqrt{\frac{\omega_2}{\nu_2}}. \end{aligned} \tag{2.6}$$

Again, if the systems have identical geometries (ie, $R_1 = R_2$), then ensuring similarity is quite simple. The frequency content of the analogue system must be scaled by the ratio of the kinematic viscosities such that

$$\omega_2 = \omega_1 \frac{\nu_2}{\nu_1}. \tag{2.7}$$

Ensuring dynamic similarity between two pulsatile flow systems which have very similar geometries requires appropriate changes to only two parameters: the mean flow rate and the frequency content of the waveform. This concept is exploited in Chapt. 6 and Chapt. 7.

2.1.2.4 Normalised velocity

A convenient way to express the mean velocity, $\overline{v}$, is as the ratio of the flow rate Q to the area of the vesssel A:

$$\overline{v} = \frac{Q}{A}. \tag{2.8}$$

This simple expression allows accurate calculation of the mean velocity, provided that suitable methods exist to measure the flow rate and arterial diameter. For in-vitro experimental flow studies, such measurements can readily be performed, either with a graduated cylinder and stopwatch, or with in-line flow sensors; however, measurement of Q is non-trivial for the in-vivo case. With an accurate measurement of mean velocity (Eq. (2.8)), it is convenient to present data as normalised velocities, $\hat{v}$, (ie, in multiples of the mean velocity),

$$\hat{v} = \frac{v}{\overline{v}}, \tag{2.9}$$

since this allows comparison of velocity data between experiments that may have been performed in scale models.

2.1.2.5 Normalised wall shear stress

Much as it is convenient to consider normalised velocities, considering normalised—dimensionless–values of the wall shear stress allows comparison between experiments performed in scale models or with different working fluids. To normalise the WSS, it is divided by the density and mean

velocity of the working fluid, yielding

$$\hat{\tau_{\mathrm{w}}} = \frac{\tau_{\mathrm{w}}}{\rho \bar{v}^2}, \tag{2.10}$$

where $\hat{\tau_{\mathrm{w}}}$ is the normalised WSS, τ_{w} is the (dimensional) WSS and ρ is the density of the fluid.

2.1.2.6 Summary

Two of the most important dimensionless parameters have been introduced and their relevance explained. The Reynolds number describes the fluid regime and, for the healthy cardivascular system, is always below 2000, implying that blood flows through arteries in a laminar manner. The Womersley parameter describes the fluid behaviour under periodic conditions by acting as a normalised frequency parameter. The inertia present due to the fluids density acts like an inductor in an electrical circuit; at low values of α, velocity profiles are highly affected by viscous effects, but for high values the inertia dominates the viscosity and velocity profiles flatten out. For flow conditions when several frequencies are present, the final velocity profile is represented by the sum of the profiles for each discrete frequency harmonic.

There are many other dimensionless parameters—for example the Strouhal and Duke number—but for brevity only the parameters most significant to this thesis have been introduced. From the perspective of experimental fluid dynamics, one of the most important consequences of normalised flow rate and frequencies is that equivalent experiments may be conducted in scale models or with different working fluids. The use of dimensional analysis, as this process is known, is widespread and provides an important tool for the experimental scientist.

2.1.3 Turbulence

Considering Eq. (2.1), the Reynolds number can be considered as the ratio of inertial to viscous forces. For Reynolds numbers greater than 2300, the fluid regime is dominated by inertial effects, and tends to be unstable (Schlichting, 1987). Flow in this condition is considered turbulent. In turbulence, inertial forces dominate, and packets of fluid move in structures—known as eddies—rather than in a laminar manner. This results in the efficient exchange of momentum between the fluid layers. Eddy sizes range from the size of the system down to a limit governed by the Reynolds number of the flow; higher Reynolds numbers imply that smaller vortices will exist in the fluid domain (Schlichting, 1987). Large eddies break down

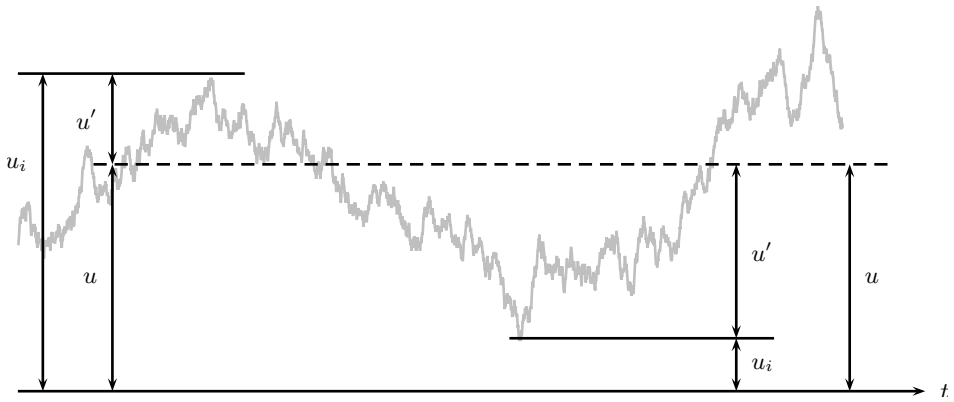

Figure 2.1: *Turbulent velocity fluctuations about a mean velocity. (Adapted from Pao (1961).)*

into smaller structures in a cascading manner until the viscosity is able to dominate the smallest vortices and damp them out. For lower Reynolds numbers, the fluid regime is laminar, and viscous forces dominate the fluid behaviour; layers of fluid with different velocities slide past each other smoothly, with minimal inter-layer mixing.

No implicit theory of turbulence exists, but successful working approaches exist based on statistics (Pao, 1961). Experiments have shown that at any fixed point in the velocity field, the instantaneous velocity fluctuates about a mean value (Fig. 2.1). Breaking the velocity vector into cartesian co-ordinates produces three instantaneous velocities, u_i, v_i, and w_i, which are comprised of their time averaged components u, v and w, and the fluctuations u', v' and w':

$$u_i = u + u'; \tag{2.11}$$

$$v_i = v + v'; \tag{2.12}$$

$$w_i = w + w'. \tag{2.13}$$

From the velocity fluctuations about the mean velocity, estimates of the level of turbulence may be obtained (Schlichting, 1987). The turbulence intensity, T, can be calculated as:

$$T = \frac{\sqrt{1/3\left(\overline{u'^2} + \overline{v'^2} + \overline{w'^2}\right)}}{\overline{v}}, \tag{2.14}$$

where $\overline{v}$ is the mean velocity (rather than the time averaged v component). Far from surfaces and structures, the turbulence can be isotropic, such that the fluctuations in each velocity component

are equal:

$$\overline{u'^2} = \overline{v'^2} = \overline{w'^2}; \tag{2.15}$$

in this case, the level of turbulence may be calculated from one velocity component only:

$$T = \frac{\sqrt{\overline{u'^2}}}{\overline{v}}. \tag{2.16}$$

In practice, the isotropic definition of turbulence intensity is often used, even though the structures are not isotropic, such as in wind tunnels. The wind tunnel is essentially the same fluid structure as an artery, so in this thesis, values of turbulence intensity are calculated using Eq. (2.16).

2.1.4 Simple methods used to model hæmodynamics

2.1.4.1 Introduction

Modelling flow in arteries is useful as it can provide estimates for relevant biomechanical factors, including the wall shear stress and peak blood velocity. Many different models have been studied, ranging from the simplest, known as lumped parameter models (Zamir, 2005), to four dimensional techniques that attempt to simulate both blood flow and tissue stresses (Li, 2006; Fraser, 2007). This section briefly covers some of the techniques that have been used to study arterial flow, and highlights the methods most relevant to this thesis.

2.1.4.2 Lumped parameter models

Lumped parameter models are the simplest models that have been used to study blood flow. The name is derived from the methodology: all of the properties of the arterial tree are lumped together to isolate the effect of a handful of parameters. This is usually done by constructing an electrical analogy to the arterial system: viscosity is effectively resistance, compliance can be considered as capacitance, and inertia is treated as inductance. Current flowing in the model is analogous to blood flow. The potential difference between two sites is equivalent to the pressure drop in arteries. It is even possible to ignore the inertial effects using these models. The Windkessel, a successful model that can provide estimates of cardiac output consists only of a resistor and capacitor in parallel (Nichols & O'Rourke, 1990).

Lumped parameter models cannot, by their nature, provide an information about biomechanical factors in individual arteries. Distributed models treat the vasculature as a series of wires (known as transmission lines) stemming from an origin (the heart) that bifurcate in a manner similar to arteries (Avolio, 1980). Each element has different properties (ie, resistance, capacitance and inductance), and the effect of wave propagation, reflection and damping in the system allows values of blood velocity and wall shear rate to be estimated in each artery (Stroev et al., 2007).

2.1.4.3 One dimensional models

One dimensional models attempt to solve the Navier-Stokes equations that govern fluid flow (Zamir, 2005). In these models, flow through a cylinder is constrained such that the only wall motion is radial, the velocity field is symmetric around the vessel axis and the major velocity component is oriented axially. To successfully calibrate these models, measurements of artery length and radius are required—hence 1D models. When initialised with good quality data, estimated flow rates from 1D models have been shown to agree well with directly measured flow by MRI (Olufsen et al., 2000).

2.1.4.4 Flow in rigid pipes

Progression from simple lumped parameter and 1D electrical models of blood is usually to the plumbing analogy. In this type of model, arteries are considered as straight tubes with rigid walls. Flow is parallel to the the vessel axis and the effects of branching and wave reflection are omitted, since the vessels are usually treated in isolation.

Steady flow in tubes was studied by Jean Louis Marie Poiseuille in the 1830–40s. He established that the flow rate is directly proportional to the pressure drop across the ends of the pipe—this has come to be referred to as the Hagen-Poiseuille law (Nichols & O'Rourke, 1990). The flow rate, Q, in a cylinder of radius R and of length Δx, driven by a pressure difference ΔP is

$$Q = \frac{\Delta P \pi R^4}{8 \mu \Delta x}, \tag{2.17}$$

where μ is the dynamic viscosity of the fluid. As the fluid flows through the pipe, the viscous effects permeate from the wall towards the centre (the free stream) of the tube. This is known

as the boundary layer. Fluid next to the wall is believed to move at the same speed as the vessel wall, if the wall is fixed, then the layer of fluid next to the wall is stationary (Schlichting, 1987). This is a central tenet of fluid mechanics—known as the no-slip condition—although it is unproven. Progressing inward from the wall, each layer of fluid is slowed by the outer layer, until, at the vessel centre, the maximum velocity occurs. If the fluid flows sufficiently far through the pipe (a distance called the inlet length), the viscous effects reach the centre of the pipe. At this point, the velocity profile no longer changes with axial displacement. This condition is often referred to as fully developed (steady) flow.

To derive these equations, one considers a layer of the fluid. The viscous force acting on the layer, F_μ, is equal to the difference between the retarding force on the outer side and the accelerating drag on the inside. This is expressed as the change in the product of the velocity gradient $\partial v/\partial r$, the viscosity, and the area of the fluid body (a cylinder) exposed to the wall, $2\pi r\Delta x$, over the thickness of the fluid layer, δr,

$$F_\mu = -\frac{\partial}{\partial r}\left(2\pi r\mu\Delta x\frac{\partial v}{\partial r}\right)\delta r.$$

Under steady conditions, this retarding force opposes the force due to the pressure drop, $F_{\Delta P}$, which is the product of the pressure drop and the cross-sectional area of the layer, such that

$$F_{\Delta P} = 2\pi r\delta r\Delta P.$$

Under steady flow, the sum of these two forces produces no net force, so

$$\begin{aligned} F_{\Delta P} + F_\mu &= 0, \\ 2\pi r\delta r\Delta P &= -\frac{\partial}{\partial r}\left(2\pi r\mu\Delta x\frac{\partial v}{\partial r}\right)\delta r, \\ \Rightarrow \frac{\partial}{\partial r}\left(r\frac{\partial v}{\partial r}\right) &= -\frac{r\Delta P}{\mu\Delta x}. \end{aligned}$$

Integrating this expression yields:

$$\begin{aligned} r\frac{\partial v}{\partial r} &= -\frac{r^2\Delta P}{2\mu\Delta x} + C, \\ \Rightarrow \frac{\partial v}{\partial r} &= -\frac{r\Delta P}{2\mu\Delta x} + \frac{C}{r}. \end{aligned}$$

For symmetric velocity profiles, the velocity gradient must be zero at $r = 0$, hence the integration constant, C, must also be equal to zero and we have

$$\frac{\partial v}{\partial r} = -\frac{r\Delta P}{2\mu\Delta x}. \tag{2.18}$$

Further integration of Eq. (2.18) yields,

$$v(r) = -\frac{r^2\Delta P}{4\mu\Delta x} + C', \tag{2.19}$$

where C' is another integration constant. Considering the no-slip condition, the velocity must be zero at the boundary wall, ie, $v = 0$ at $r = R$, therefore

$$C' = \frac{R^2\Delta P}{4\mu\Delta x}. \tag{2.20}$$

Combining Eq. (2.19) and Eq. (2.20) yields the final form of the velocity profile:

$$\begin{aligned} v(r) &= \frac{\Delta P}{4\mu\Delta x}(R^2 - r^2) \\ &= \frac{R^2\Delta P}{4\mu\Delta x}\left(1 - \frac{r^2}{R^2}\right) \\ &= v_0\left(1 - \frac{r^2}{R^2}\right). \end{aligned} \tag{2.21}$$

From Eq. (2.21), in which v_0 is the centre line velocity, it is clear that the velocity profile is parabolic, ranging from a maximum at ($r = 0$) to zero at the wall ($r = R$). In practice, the velocity profile is not always parabolic under steady flow; the boundary layer requires an inlet length (ie, a minimum Δx) to become established, and this length is a function of the Reynolds number and the vessel diameter (Schlichting, 1987). Confirmation of the Eq. (2.17) is obtained by integrating the Eq. (2.21) around the axis of the cylinder:

$$\begin{aligned} Q &= \int_0^R v(r)2\pi r\mathrm{d}r \\ &= \frac{\pi R^2\Delta P}{2\mu\Delta x}\int_0^R r(R^2 - r^2)\mathrm{d}r \\ &= \frac{\Delta P\pi R^4}{8\mu\Delta x}. \end{aligned} \tag{2.22}$$

The wall shear stress under Poiseuille flow is calculated by substituting Eq. (2.18) at $r = R$ into Eq. (1.1):

$$\begin{aligned} \tau_{\mathrm{w}} &= -\mu \frac{-R\Delta P}{2\mu\Delta x} \\ \tau_{\mathrm{w}} &= \frac{R\Delta P}{2\Delta x} \end{aligned} \tag{2.23}$$

Eq. (2.23) can be expressed in a number of other, more convenient forms, including:

$$\tau_{\mathrm{w}} = \frac{4\mu Q}{\pi R^3} = \frac{2\mu v_0}{R}. \tag{2.24}$$

The Hagen-Poiseuille law is more suited to venous, rather than arterial, flow, since flow in arteries is much more pulsatile in its nature. The solution for flow driven by an oscillating pressure gradient ($\partial p/\partial z = A^* \mathrm{e}^{\mathrm{i}\omega \mathrm{t}}$) in rigid walled, long cylinders, was derived by Womersley (1955):

$$v(y,t) = \frac{A^* R^2}{i\mu\alpha^2}\left[1 - \frac{J_0(\alpha y i^{3/2})}{J_0(\alpha i^{3/2})}\right]\mathrm{e}^{\mathrm{i}\omega \mathrm{t}}. \tag{2.25}$$

Where Eq. (2.25) $y = r/R$, the normalised radial co-ordinate, $i = \sqrt{-1}$ and J_0 is a zeroth order Bessel function of the first kind. The normalised frequency parameter, α, which was defined in Eq. (2.4) features prominently in this expression, explaining why it is often referred to as the Womersley number. Womersley flow is considered fully developed (oscillatory) flow, since the velocity profile is not a function of the axial co-ordinate.

Eq. (2.25) is an extremely importance expression in hæmodynamics. It is used widely in computational studies (Fraser, 2007) and can be used to characterise flow waveforms in arteries (Fraser et al., 2008; Holdsworth et al., 1999). As the equation stands, it is structured to calculate the velocity profile from only one frequency, making it unsuitable for use with arterial waveforms which contain energy from a range of frequencies. If the arterial system can be considered a linear system, then the individual frequency harmonics may be treated separately and the final waveform is the cumulative sum of each harmonic (Nichols & O'Rourke, 1990). Eq. (2.25) was rewritten by Evans (1982) as the linear sum over the frequency components, after

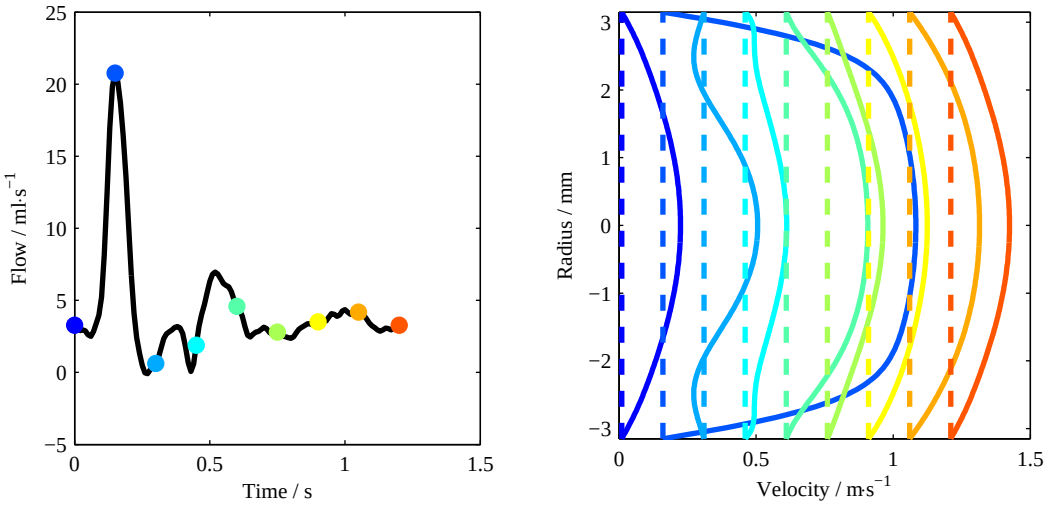

(a) Estimated carotid flow from a healthy male, after Holdsworth et al. (1999).

(b) The corresponding velocity profiles for the time points in Fig. 2.2a.

Figure 2.2: *Womersley flow and velocity profiles.*

having expressed the equation in terms of the mean velocity rather than the pressure gradient:

$$v(y,t) = \sum_{k=0}^{\infty} \mathrm{Re}\left\{ \mathrm{V_{mean,k}} e^{\mathrm{j(k\omega t-\psi_k)}} \left[\frac{\mathrm{J_0(\beta_k) - J_0(\beta_k y)}}{\mathrm{J_0(\beta_k) - 2J_1(\beta_k)/\beta_k}} \right] \right\}. \tag{2.26}$$

Where Re$\{.\}$ represents the real part of a complex function, J_1 is a first order Bessel function of the first kind and $\beta_k = \alpha_k i^{3/2}$. α is defined in Eq. (2.4), but in this case it must be defined for each harmonic,

$$\alpha_k = R\sqrt{\frac{k\omega}{\nu}}. \tag{2.27}$$

The subscript k refers to individual frequency harmonics, the phase of each is indicated by ψ_k. For $k = 0$, Eq. (2.26) refers to steady flow, for which the velocity profile is parabolic. The final velocity profile is just the superposition of all of the individual frequency harmonics (Fig. 2.2b).

2.1.4.5 Computional fluid dynamics

In complex geometries such as arteries, analytic solutions are not, in general, available. Computational fluid dynamics (CFD) is an approach that solves the Navier-Stokes equations the govern fluid behaviour numerically, subject to certain boundary conditions. CFD is a very powerful technique, as it allows exact control of each experimental parameter. As a consequence it

has become very popular for studying hæmodynamics, particularly in the presence of vascular disease, such as stenosis (Li, 2006) and abdominal aortic aneurysm (Fraser, 2007). However, despite recent advances in computing power, CFD remains time consuming, and is largely unvalidated in the presence of turbulence.

2.1.4.6 Summary

Many different approaches have been used to model blood flow in arteries. These approaches range in complexity from simple zero and 1D methods that yield less information, but do so very quickly, to four dimensional numerical solutions via CFD. In the context of this thesis, the most relevant models are the steady Poiseuille model and the time varying Womersley solutions. These two models are used extensively, often to provide theoretic validation of experimental results.

2.1.5 Summary

Some essential concepts of fluid mechanics have been introduced. In particular, the importance of dimensionless variables such as the Reynolds number has been emphasised, since they allow the comparison between data acquired from different flow systems. A simple but useful statistical approach to turbulence was introduced, and finally, different methods used to model hæmodynamics were compared.

2.2 Doppler ultrasound

2.2.1 Introduction

Acoustic waves are longitudinal waves, creating zones of oscillating pressure in the direction of travel (Fishbane et al., 1996). Consequently, ultrasound waves exhibit all of the behaviour observed in acoustic waves—reflection, refraction, scattering, diffraction and interference, for example. Acoustic waves must exist inside a medium, characterised by particular parameters such as the acoustic impedance, speed of sound and rate at which the energy of the wave is attenuated. In medical ultrasound, typical frequencies are on the order 1–10 megahertz. Clinical ultrasound scanners assume a constant speed of sound of 1540 $\mathrm{m{\cdot}s^{-1}}$, which is the average

velocity of sound in soft biological tissue (Gerber et al., 2004), resulting in wavelengths and consequently limits of resolution that are on the order of 0.15–1.5 mm.

The different phenomena of waves are used to varying extents in the medical applications of ultrasound. To a large extent, the refraction, diffraction and interference of the ultrasound beam is ignored. This is a consequence of the natural variation of acoustic properties within soft tissue, which is, from a practical perspective, unquantifiable in real time. Image formation relies heavily on scattering and reflection, while velocity estimation relies almost exclusively upon the scattering by the medium, allowing useful information to be obtained despite the difficulties associated with medium variation.

Medical ultrasound is used to form images by emitting ultrasound and detecting the returned echo. The returning echoes are created by reflections at interfaces in the media and by scattering due to the presence of small particles—for example, cells—that are present in the medium. Typically, one transducer (although technically transceiver would be more accurate terminology) is used to transmit the pulses of ultrasound before switching to receive mode to listen for the returning echo. However, in older systems it was common for two different devices to perform the tasks separately.

2.2.2 Velocity estimation with Doppler ultrasound

Velocity estimation is an important diagnostic tool in medical ultrasound. As discussed in Sect. 1.3, it is extensively used to screen patients for carotid angiography (Bluth et al., 1988; Spencer & Reid, 1979) and it is an important factor for assessing fœtal development during pregnancy. With continuous wave (CW) devices, velocity estimation with ultrasound is based upon the Doppler effect. For the case where the source is moving at velocity v, with the wave propagating at c, and with carrier frequency f_0, the apparent frequency of the wave as measured by the observer, $f^{'}$, is given by Eq. (2.28),

$$f^{'} = f_0 \frac{1}{1 + \frac{v}{c}\cos\theta}, \tag{2.28}$$

where $\cos\theta$ has been introduced in the denominator to account for geometry (Fig. 2.3). If it is the observer and not the source which is moving, the effect of the motion is subtly different, as

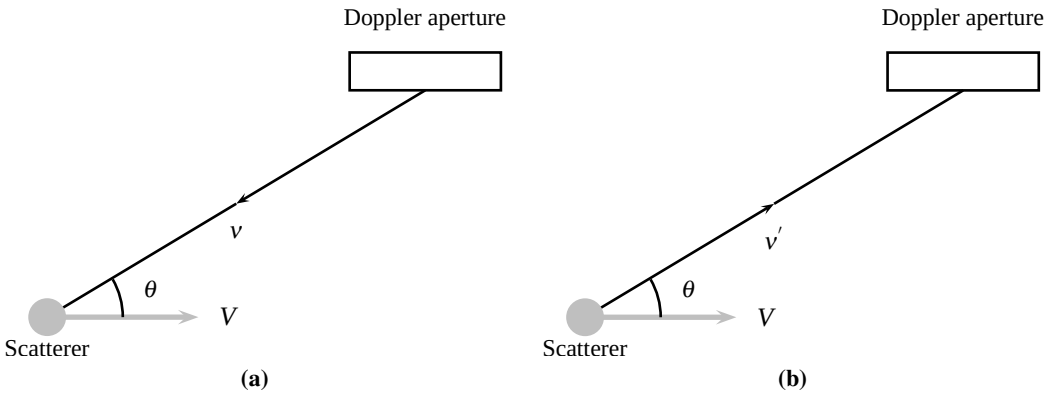

Figure 2.3: *The Doppler effect in medical ultrasound. The transmitted pulse undergoes two Doppler shifts: once when it is scattered by the moving particle, and once when the moving particle acts as a moving source.*

shown in equation Eq. (2.29).

$$f^{'} = f_0(1 - \frac{v}{c}\cos\theta). \tag{2.29}$$

Considering this effect in the context of medical ultrasound, it is clear the ultrasound wave is subject to a Doppler shift from both methods. Initially, scatterers in the body act as moving observers, and Eq. (2.29) applies. Thus, the ultrasound which is scattered travels with a new carrier frequency, $f^{'}$. As the ultrasound is received by the transducer, the situation is reversed; the scatterers now act as a moving source. In this case, Eq. (2.28) applies, and the transducer observes the carrier frequency to be $f^{''}$. The difference between the transmitted and received frequencies is known as the Doppler frequency, f_{D}, and is given by Eq. (2.30),

$$f_{\mathrm{D}} = f_0 - f^{''} \tag{2.30}$$

A more convenient expression for f_{D} can be obtained by expanding $f^{''}$ using the binomial theorem to the first order:

$$\begin{aligned} f^{''} &= \frac{f^{'}}{1 + v/c\cos\theta}; & (2.31)\\ &= f_0\frac{1 - v/c\cos\theta}{1 + v/c\cos\theta}; & (2.32)\\ &\approx f_0(1 - 2v/c\cos\theta). & (2.33) \end{aligned}$$

Substituting Eq. (2.33) into Eq. (2.30) yields a final expression for the frequency shift that arises due to the motion of the scatterers:

$$f_{\mathrm{D}} = 2\frac{v}{c} f_0 \cos\theta. \tag{2.34}$$

It is this frequency shift, f_{D}, which is measured by CW Doppler ultrasound devices. With knowledge of the speed of sound, the velocity of the scattering particles can be estimated. From Eq. (2.34), the angle dependence can clearly be seen. Should the angle between the velocity and ultrasound beam tend to a right angle, then no velocity will be measured. Consequently, the beam is frequently steered to create a more convenient angle between the beam and direction of flow.

2.2.2.1 Continuous wave Doppler systems

Ultrasonic Doppler devices work in one of two ways; either the transducer contains two elements to transmit and receive the ultrasound beam simultaneously—known as continuous wave (CW)—or the transducer transmits an ultrasound pulse, and subsequently switches to receive mode to measure the returned echo, these machines are known as pulsed wave (PW). CW devices are, in general, simpler than PW ones (Evans & McDicken, 2000), since they need only remove the transmitted signal (f_0 in Eq. (2.30)) from the returned signal (f''). However, CW devices have one major restriction—no information is available regarding the depth of the received echo. Since the signal is constantly transmitted, even with knowledge of the speed of sound, it is impossible to determine where echoes return from. For this reason, CW Doppler devices are often regarded as less useful than PW devices, and have largely been superceded by them. In this thesis, CW Doppler was not used; general references to Doppler ultrasound refer specifically to pulsed wave devices.

2.2.2.2 Pulsed wave Doppler systems

Pulsed wave Doppler ultrasound systems are capable of measuring blood and tissue velocities from a finite sample volume, a known range (time) from the transducer face. This is the main advantage of pulsed systems over continuous wave systems—the extra information about the position of a scatterer. In order that PW systems can do this, the ultrasound pulse is transmitted in short bursts, similar to conventional B-mode imaging, and the system then switches to receive

mode. The time between the transmitted and received echo is then converted into a distance with knowledge of the speed of sound. The rate at which pulses are sent is known at the pulse repetition frequency (PRF).

The major drawback that arises with PW Doppler, which is inherent, and not a result of discretization for digital analysis, is that these systems can only unambiguously resolve frequency shifts below the Nyquist limit. Formally, pulsed wave Doppler does not measure frequency shift using the Doppler technique, since only continuous waves are subject to Doppler shifts. Consequently, PW systems emit several consecutive pulses, and the change of phase (or time) in the received signals is used to estimate the Doppler frequency. Typically, 8–32 pulses are sent; the trade off is between temporal resolution (it takes longer to send more pulses) and accuracy (more pulses allow a more reliable estimate). Although the use of higher PRFs can improve the temporal resolution, this is often precluded by the depth of the sample volume, which imposes a maximum threshold that may be calculated by considering the time it takes to transmit and receive an echo from a particular depth:

$$f_{0,\mathrm{PRF}} = \frac{1}{t} = \frac{c}{2d}; \tag{2.35}$$

where $f_{0,\mathrm{PRF}}$ is the maximum achievable PRF for a certain depth. Estimated frequency shifts measured using PW Doppler are almost identical to the frequency shift due to the Doppler effect with CW systems (Evans & McDicken, 2000).

2.2.2.3 Estimation of pulsed Doppler spectra

Pulsed wave Doppler spectra show the energy present in frequency bins for frequencies up to the Nyquist frequency (Fig. 2.4). Negative frequencies imply that motion is away from the transducer, while positive frequencies indicate motion towards the transducer. Jensen (1996, p 155–194) authoritatively described the implementation of PW systems and calculation of the spectrogram.

Energy in PW Doppler spectrograms is rarely concentrated to narrow frequency bands, even for the cases of very short sample volumes (such that velocity gradients in the blood are very small) or carefully designed test objects such as the string phantom (Hoskins, 1994*b*). A number of phenomena are responsible for the smearing of energy (known as broadening) across frequencies. The sample volume cannot be made infinitely small, so the presence of velocity gradients

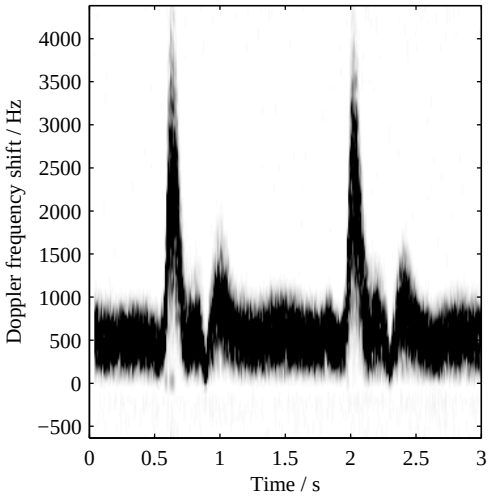

Figure 2.4: *A spectrogram obtained from the common carotid artery of a healthy male.*

will always introduce some broadening. Even for the case of a string phantom, the shearing force will drag some fluid with the moving string, such that a velocity gradient is created. Attempting to minimise broadening due to velocity gradients by using a shorter sample volume does not necessarily reduce the signal bandwidth, since the product of the signal length (which defines the size of the range gate) and its bandwidth is constant (Evans & McDicken, 2000). As an example, a continuous wave instrument that necessarily has a very long sample volume due to the absence of any depth information will, for the same experimental setup as a PW device, have a much narrower Doppler bandwidth, by virtue of the much lower frequency content of the receiving window. Non-stationarity (ie, the acceleration of blood) within the sample volume between successive pulses also broadens the Doppler spectrum (Fish, 1991). However, among the major sources of broadening are geometric spectral broadening (Daigle et al., 1990), which arises from the finite size of the Doppler aperture (and the finite size of the sample volume), amplitude modulation and frequency modulation (Ata & Fish, 1991; Hoeks et al., 1991).

2.2.2.4 Estimation of the mean Doppler frequency

Although the most complete way to display all of the information obtained using PW Doppler is via the spectrogram, it is often useful to display a reduced amount of information. Colour flow imaging (CFI) is a widely implemented technique that displays the mean Doppler frequency for each sample volume as in an image. This is useful in clinical environments, as it can guide the sonographer's positioning of the Doppler sample volume to obtain the maximum velocity

estimate (Fig. 1.4). Estimation of the mean frequency in the Doppler spectrum can be carried out using Eq. (2.36),

$$\overline{f_D} = \frac{\int_f P(f) f \mathrm{d}f}{\int_f P(f) \mathrm{d}f}, \tag{2.36}$$

where $\overline{f_D}$ is the mean Doppler frequency, $P(f)$ is the received Doppler power spectrum, and f is frequency. (In practice, modern systems would first digitally sample the power spectrum, such that the integral is replaced by a discrete sum over all of the measured frequency bins.) While this method is the most robust way to obtain the mean Doppler frequency, it does require that the whole spectrum is sampled at every point. In turn, this requires the use of long pulse sequences, which would result in poor frame rates. Consequently, to maintain adequate frame rates with CFI the length of the Doppler pulse sequence is reduced, typically, to around 4–8 pulses. Short pulse sequences are unable to reliably measure the full spectrum of Doppler frequencies present in each sample volume, so alternative algorithms to Eq. (2.36) must be used.

The most widely used mean frequency estimators in clinical ultrasound scanners are based on one of two methods: auto-correlation (Kasai et al., 1985) and cross-correlation (Bonnefous & Pesqué, 1986). The auto-correlator method estimates the mean Doppler shift based on the phase shift between successive pulses; the cross-correlator forms its estimate based on the time shift between each pulse. The major limitation of the phase shift approach lies in the restricted range of frequency shifts that can unambiguously be determined—this is limited to $\pm f_{\mathrm{PRF}}$—although this has a subsequent depth restriction too, that arises from Eq. (2.35) (Jensen, 1993). Methods that rely on the time shift approach, however, do not suffer from this ambiguity. In principle, since the shift that occurs between successive pulses is time, not frequency derived, cross-correlation methods have no limitations on their range that derive from the algorithm used (Jensen, 1993). In practice, however, the ability of the cross-correlation algorithm to correctly determine the peak that corresponds to the true velocity of a scatterer is a probabalistic process—in order to increase detection rates above 70%, the velocity range is typically restricted; the limited range is exactly equivalent to the range of velocities that can be measured using the phase based techniques (Jensen, 1993).

2.2.3 Summary

Some of the basic concepts regarding velocity estimation with Doppler ultrasound have been introduced. The advantages of PW devices over CW devices were discussed, and some of the sources of broadening of Doppler spectra considered. Finally, two widely implemented algorithms for estimating the mean Doppler frequency in CFI were introduced, and some of their main advantages and limitations were considered.

2.3 Particle image velocimetry

Particle image velocimetry is an optical technique that offers a good compromise between visualising velocity fields and accurate measurements. It is capable of measuring a wide range of velocities with an accuracy of around 2% (Westerweel, 1997). Although this precision is poorer than that of LDA, the benefits of whole field velocity measurement outweight those of increased accuracy. This section introduces theoretical and technical aspects of particle image velocimetry.

2.3.1 Introduction

Particle image velocimetry is a simple and non-invasive optical technique that can measure the whole flow field with only two laser pulses. It uses tracer particles to infer the fluid velocity at a point; in its simplest form, one can imagine leaves floating on a stream, providing an observer with an estimate of the surface velocity of the water. In a modern scientific setting, PIV is typically used to obtain velocity vector maps of complex fluid behaviour, such as flow over aircraft wings or flow in three dimensional geometries, such as models of human arteries.

PIV offers a qualitative description of the flow field, while retaining an adequate amount of quantitative information to extract velocity profiles and shear rates. With most modern lasers, PIV is capable of studying a wide range of velocities, allowing measurement of flows containing boundary layers and small scale spatial structures. The versatility and accuracy offered by PIV make it an ideal gold standard technique for validating measurements made using Doppler ultrasound. This section discusses only the basic principles of PIV. A fuller description of PIV, including its extension to three dimensions, either through the use of holography or stereoscopy

is given by a number of authors (Adrian, 1991, 2005; Raffel et al., 1998; Westerweel, 1993, 1997).

2.3.2 Theory

2.3.2.1 PIV principle

Particle image velocimetry requires three core elements: a light sheet, usually produced by a laser and some optics; a flow seeded with particles that scatter the light; and a device to record images of the scattered light, typically a digital camera (Fig. 2.5). The light sheet is pulsed twice. In the duration between flashes, Δt, the seeding particles move. From the stored locations of the particles, the velocity field can be deduced if the particle displacements are calculated and the time between each light pulse is known. Most modern PIV systems capture digital images rather than film images, and employ digital analysis methods instead of optical ones. As such, this technique is strictly known as *digital* PIV (*d*PIV).

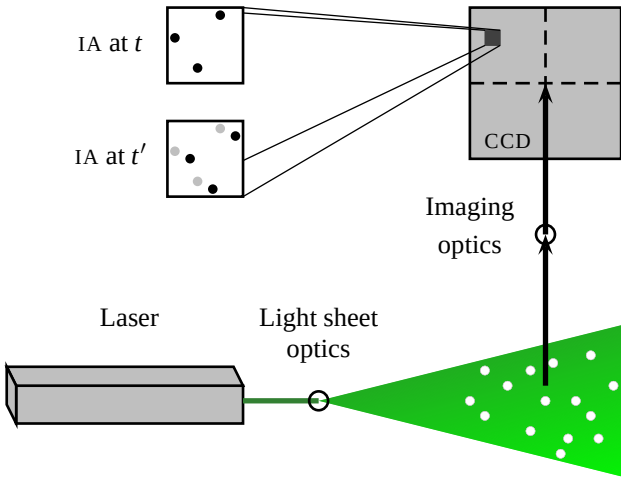

Figure 2.5: *Schematic diagram of a* PIV *setup. The laser beam is converted into a light sheet. Tracer particles in the fluid scatter the light, and images are stored using the* CCD *at times t and t'. The displacement of the particles in each interrogation area is used to calculate the local velocity.*

2.3.2.2 Seeding particles

PIV relies on particles in the fluid to scatter light, if the fluid does not naturally contain any suitable particles, they must be added. The tracer particles must satisfy two conditions (Prasad, 2000): they must faithfully follow the local fluid motion; and they must scatter light efficiently.

As an aside to the first condition, in order that the particles accurately represent the fluid dynamics, the particles themselves must not interact. This implies that PIV—when used to study the motion of fluids—can only represent Newtonian behaviour. Should one wish to study the behaviour of a particle/fluid suspension, some independent means is necessary to decouple the particle motion from that of the fluid. A fuller description of the properties required for tracer particles is given by Melling (1997).

A simple way to assess whether the tracer particles satisfy the first condition is to calculate the settling velocity of the particles due to gravity. Below this velocity threshold, the particles will sink, clearly violating the condition. Considering a spherical scatterer and that particle motion is due entirely to viscous (Stokes) drag, the settling velocity u_∞ is given by

$$u_\infty = \frac{g d_p^2 (\rho_p - \rho_f)}{18\mu}, \tag{2.37}$$

where g is the acceleration due to gravity, d_p is the particle diameter, ρ_p and ρ_f are the mean densities of the particles and fluid, respectively, and μ is the kinematic viscosity of the fluid. If the fluid velocity is much greater than u_∞, then the particles are suitable for use with PIV. However, if the fluid velocities vary across the fluid domain, such that in some region velocities tend towards the settling velocity—as might occur in the vicinity of a vessel boundary—then care needs to be taken to minimise the difference in densities between the fluid and the tracer particles. In the study of liquids, plastic and polystyrene materials tend to minimise the density difference, while for application to air flows, very fine oil droplets produced by an atomiser are frequently used.

The tracer particles must also efficiently scatter light. In this context, the intensity of scattered light reaching the camera sensor must be enough to maintain an adequate signal to noise ratio. For particles larger than the wavelength of the incident light, Mie scattering governs the distribution of the scattered light (van der Hulst, 1981). Mie scattering is not homogeneous—the scattering has a large degree of angular dependence—but is strongly dependent on the size of the particles. Thus, a facile way to ensure adequate scattering is to use larger tracer particles, however, care must be taken not to break the former condition in an effort to satisfy the latter.

The seeding density is also important. Too little seeding, and the data points are sparsely locately, too much seeding and the laser light is unable to penetrate far beyond the surface due to the high number of scatterers. For optimal image quality, the tracer particles should

be distributed homogenously—this fact manifests itself further in the analysis of PIV images (Sect. 2.3.2.4)—such that no structures can be discerned from the seeding density distribution. In practice, this can be difficult to achieve in flows with boundary layer separation, since particles may become trapped in regions of recirculation, leading to a local increase in the seeding density.

2.3.2.3 Imaging optics

The imaging system used in particle image velocimetry amounts to nothing more fundamental than an extremely high powered, fast, flash gun and a high speed camera. Lasers are typically used because they are capable of producing exceptionally bright, yet short, pulses of light, typically on the order of nanoseconds. The short pulse duration prevents motion blur which would reduce the quality of the image. The development of dual cavity, pulsed lasers enabled PIV's use with a range of extremely wide range of velocities. Before their existence, light pulses were tied to the repetition rate of the particular laser—typically 30–50 kHz—restricting the velocity range that a particular laser could be used to study.

Lasers can produce intense beams of light. However, for the purposes of PIV, the beam of light must be converted into a light sheet. This can be done with several lenses, depending on the nature of the light beam produced by the laser, but the fundamental optical component is usually a cylindrical lens—this is a lens that focusses only in one plane—with a negative focal length, which causes the light beam to diverge into a light sheet (Fig. 2.6). In practice, more than one lens is usually required to produce a thin light sheet. The light sheet must be narrower than the depth of field of the camera, otherwise particles outwith the interrogation volume will scatter light, forming blurred images at the camera sensor and subsequently reducing image quality. Fig. 2.6 shows a second—converging—cylindrical lens that reduces the thickness of the light sheet by focussing the laser beam in the vertical plane.

To form an image of the scattered light, a lens is placed in front of the camera. To calculate the distance that the lens must be from the light sheet and from the camera CCD sensor, the thin lens equation is used (Fishbane et al., 1996),

$$\frac{1}{f} = \frac{1}{s_1} + \frac{1}{s_2}. \tag{2.38}$$

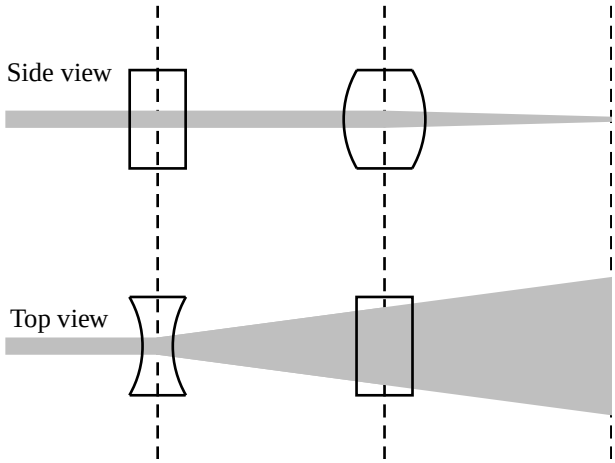

Figure 2.6: *Creation of a focussed light sheet from a beam of light using two cylindrical lenses. The incoming laser beam is shown on the left hand side, and is incident on a cylindrical lens. This diverges the light beam in one plane, without altering the path of the light in the perpendicular plane.*

In Eq. (2.38), f is the focal length of the lens, with s_1 and s_2 the distance from the lens to the scatterer and from the lens to the CCD, respectively. The lens quality need not be excessively high—an ordinary 50 mm lens designed for use with 35 mm photographic film is perfectly adequate for *d*PIV. An important factor that should be considered when selecting a lens, is the f-number, $f^{\#}$, defined in Eq. (2.39),

$$f^{\#} = \frac{f}{D}, \tag{2.39}$$

which is the ratio of the focal length of the lens, f, to the aperture diameter, D. The f-number determines the minimum size of particle images in the image plane—this is an artifact of diffraction through the lens aperture, and is actually the diameter of the Airy diffraction disk d_{Airy}, which is defined in Eq. (2.40),

$$d_{\text{Airy}} = 2.44 f^{\#}(M+1)\lambda. \tag{2.40}$$

In Eq. (2.40), M is the magnification of the optical arrangement and λ is the wavelength of light. For a typical camera lens, the Airy disk is on the order of a few microns, however, if significant magnification is present in the optical arrangement, the diffraction limited spot size can increase rapidly. The magnification of the system is set by s_1 and s_2:

$$M = \frac{s_2}{s_1} \tag{2.41}$$

The final size of the particle images is a function of the magnification and of the diffraction of the optical system,

$$d_{\mathrm{i}} = \sqrt{(Md_{\mathrm{p}})^2 + d_{\mathrm{Airy}}^2}, \tag{2.42}$$

where d_{i} is the particle diameter in the image, and d_{p} the diameter of the scatterers. To prevent blurring of the image due to the optics, the depth of field (ie, the region where scattered light is focussed to a point) must be narrower than the light sheet thickness. The depth of field, δz, is calculated by

$$\delta z = 4(1 + M^{-1})^2 f^{\#^2} \lambda. \tag{2.43}$$

Cameras designed for modern, *d*PIV, usually have a double buffer storage facility that allows extremely rapid read out from the charge-coupled device (CCD) sensor. The speed of data transfer from the CCD to computer memory is limited by the bandwidth of the system. For typical studies with Δt on the order of 1–100 μs, this would prevent the use of dual exposure PIV since some charge acquired during first exposure would remain on the CCD for the second frame. By temporarily storing the first frame in a hardware buffer, the CCD can be prepared for a second measurement, after which both frames are conventionally transfered to computer memory before the next pair of images are acquired. After the successful acquistion of each pair of images, the two frames are transferred to a secondary medium, typically computer memory, although this process takes substantially longer than the temporary transfer to the buffer. This speed of the data transfer is such that modern PIV systems are typically capable of capturing 10–20 image pairs per second.

2.3.2.4 Image analysis

In order to obtain quantitative information about the velocity field, each image is divided up into small regions of interest, referred to as interrogation areas (IAs). Typically, each IA is of the order 32×32 pixels in size. Square IAs are common ($N \times N$), but for flows with a particularly large velocity component in one direction, it is sometimes more useful to use interrogation areas of size $M \times N$ square pixels. To optimise the algorithms used, the sides of the IAs are usually restricted to power-of-two lengths. Having divided up each frame of the image pair into interrogation areas, the next, and most important task, is to calculate the mean displacement

of the tracer particles between the two frames, for each IA. This is directly proportional to the mean velocity, so obtaining the displacements is tantamount to obtaining the velocity vector field for each image pair.

The mean displacement of the tracer particles in each IA is the distance that the first IA must be moved in order to minimise the differences between the frames. Given that calculation of the mean displacement for each interrogation area is fundamental to obtaining the velocity for each IA, the algorithm used must be accurate, and, to strike a balance with usability, especially when large number of vectors are involved, it must be efficient. The most accurate way to minimise the difference between the two interrogation areas is by directly calculating the sum of the squared differences, χ, and finding the resulting displacement $(\delta x, \delta y)$ which minimises it

$$\chi(x,y,\delta x,\delta y)^2 = \sum_{i=0}^{W_x-1}\sum_{j=0}^{W_y-1}\left(F(x+i,y+j)-G(x+i+\delta x,y+j+\delta y)\right)^2, \tag{2.44}$$

where $\chi(x,y,\delta x,\delta y)^2$ is the sum of the squared differences between the interrogation areas, $W_x \times W_y$ are the dimensions of the interrogation area, (x,y) is the position of lower left corner of the IA, and F and G are the first and second frames of the image pair respectively. The displacement $(\delta x, \delta y)$ which minimises $\chi(x,y,\delta x,\delta y)^2$ is considered to be the true displacement. Eq. (2.44) is extremely accurate, but it does not strike a balance with usability in terms of computing time. Fortunately, the algorithm is readily optimised; expanding the least squares function in Eq. (2.44) yields,

$$\begin{aligned}\chi(x,y,\delta x,\delta y)^2 \quad = \quad & \sum_{i=0}^{W_x-1}\sum_{j=0}^{W_y-1} F^2(x+i,y+j) \\ & + \sum_{i=0}^{W_x-1}\sum_{j=0}^{W_y-1} G^2(x+i+\delta x,y+j+\delta y) \\ & -2\sum_{i=0}^{W_x-1}\sum_{j=0}^{W_y-1} F(x+i,y+j)G(x+i+\delta x,y+j+\delta j).\end{aligned} \tag{2.45}$$

This first term on the right hand size of Eq. (2.45) contains neither δx nor δy, and consequently cannot contribute to the minimum of the least squares. The second term is merely a sum of the intensity in the second IA; if $G(x,y)$ is homogeneous, then it will not contribute significantly to

the minimum. This leaves only the final term

$$\chi'(x,y,\delta x,\delta y)^2 = \sum_{i=0}^{W_x-1}\sum_{j=0}^{W_y-1} F(x+i,y+j)G(x+i+\delta x,y+j+\delta j), \tag{2.46}$$

where $\chi'(x,y,\delta x,\delta)^2$ is the approximated sum of the squared differences between the each interrogation area. The right hand side of Eq. (2.46) is known as the cross-correlation function; as it stands, it remains computationally expensive. However, the convolution theorem states that

$$\mathscr{F}\{f\star g\} = \mathscr{F}\{f\}\mathscr{F}\{g\}. \tag{2.47}$$

Where $\mathscr{F}$ is the the Fourier transform of a function, f and g are functions, and $\star$ represents the convolution of two functions. One can use Eq. (2.47) to efficiently computate the difference between the two interrogation areas through the use of the fast Fourier transform algorithm:

$$\chi'^2 = \mathscr{F}^{-1}\{\mathscr{F}(F)\mathscr{F}(G)\}, \tag{2.48}$$

where $\mathscr{F}^{-1}$ denotes the inverse Fourier transform of a function, and the subscripts have been dropped for clarity.

Having calculated the cross-correlation between the two interrogation areas, the location of the maximum corresponds to the displacements, δx and δy (in pixels), that minimise the difference between the images of the interrogation areas, that is, the similiarities between the IAs are maximised. It is worth bearing in mind that this is only the mean displacement—the presence of velocity gradients within the IA will reduce the signal to noise ratio, but otherwise cannot be observed inside the region of interest.

The correlation peak calculated in Eq. (2.46), χ'^2, is actually a biased estimate of displacement that minimises the differences between the two interrogation areas. It contains within it the product of the spatial cross-correlation of the two windowing functions and the cross-correlation of the discretised images. The cross-correlation of the windowing functions introduces a bias towards smaller displacements (Westerweel, 1997), however, this may be removed by dividing χ'^2 by the bias function (Fig. 2.7).

The position of the maxima in the correlation plane, $(\delta x,\delta y)$, can only be located to $\pm 1/2$ pixel. For typical interrogation area sizes of 32×32 pixels squared, the maximum detectable pixel

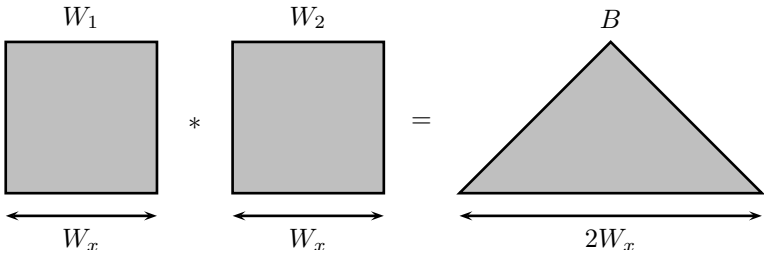

Figure 2.7: *The biasing effect of top hat windowing functions, shown in 1*D*. This effect may be removed by dividing the function in the correlation plane by the spatial correlation of the two windows.*

displacement is on the order of 8 pixels. The uncertainty in locating the peak in the correlation plane thus leads to a precision of around 6%; for many applications this is insufficient.

Provided that the correlation peak is wider than one pixel—as is normally the case for optimised PIV—the accuracy of the measurement can be improved using interpolation. The interpolation method used is important, which points the curve is fitted to less so, since most of the information is contained in the point corresponding to the peak in the correlation plane and those immediately adjacent to it. Most other points fall below the noise threshold of the correlation plane. Consequently, the interpolation schemes that have been developed are known as three point estimators (Raffel et al., 1998).

Two commonly used three point estimators use Gaussian interpolation and centroid interpolation. The performance of these estimators varies widely, with Gaussian interpolation showing little bias, whilst the centroid estimator tends to bias displacements towards the nearest integer value in pixels, a phenomenon known as pixel-locking (Fig. 2.8). The Gaussian based estimator performance is greatly superior bias since the peak in the correlation plane has, approximately, a Gaussian shape—this convenient fact can be explained by considering the image intensity of a spherical particle at the CCD sensor, which is governed by the shape of the Airy disk (Sect. 2.3.2.3). Convolving a Gaussian with another Gaussian yields a further Gaussian, so, around the maxima of the correlation plane, the shape can be approximated by a Gaussian (Westerweel, 1997).

2.3.2.5 Optimisation

Calculation of the mean displacement is dependent on the tracer particles. To contribute meaningful information to the cross-correlation function, a particle must be present in the interroga-

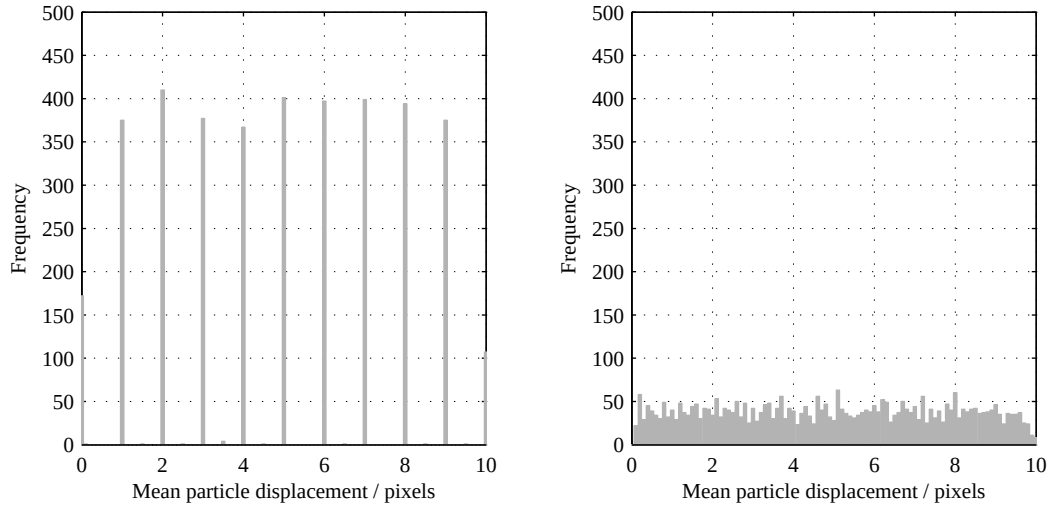

(a) Extreme pixel-locking due to the use of the centroid three point estimator.

(b) Improved sub-pixel performance with a Gaussian estimator.

Figure 2.8: *Pixel-locking in synthesised* PIV *images. A series of synthesised image pairs were analysed using the centroid three point estimator and a Gaussian three point estimator. The images contain an equal number of vectors with displacements ranging from 0 pixels to 10 pixels in step sizes of 0.05 pixels.*

tion area in both images. Although all particles correlate with other particles and contribute to the background noise level (grey lines in Fig. 2.9), paired particles also contribute to the signal (black lines). Unpaired particles (ie, particles moving out of or entering into the IA) reduce the signal to noise ratio as they contribute to the noise level, but do not increase the level of the signal. It can be seen in Fig. 2.9 that increasing the maximum displacement of the particles reduces the proportion of the IA that contains paired particles and hence reduces the SNR. The optimum displacement for each IA has been shown to be one quarter of the size of the interrogation area (Westerweel, 1997).

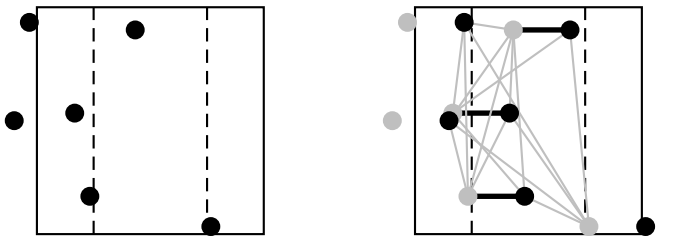

Figure 2.9: *Optimisation of* PIV *minimises the number of unpaired particles and maximises the numbers of paired particles, since only paired particles can contribute to the signal (black lines). If particles move into or out of the* IA *during the time separation, they only contribute to the noise level (grey lines).*

Similarly, velocity gradients inside the IA affect the signal to noise ratio of the cross-correlation function. If a particle moves by δx, it will contribute towards a maximum in the cross-correlation function at δx; however, a second particle may move by $\delta x'$, producing a maximum at a different location in the correlation plane. This broadens the peak of the correlation function, in effect increasing the uncertainty in the location of the maxima and hence increasing the likelihood that the calculated mean displacement may be spurious.

2.3.2.6 Post processing

Outliers inevitably occur with PIV due to the technique's statistical nature. As discussed in Sect. 2.3.2.5, the reliability of the velocity measurement may be controlled by optimal seeding concentration, but in practice, some post-processing is always needed. This post-processing can be based on nearest-neighbour validation techniques (Westerweel, 1993), although more sophisticated methods have also been developed that use concepts such as local coherence (Nogueira et al., 1997). Ultimately, the aim of post-processing is to remove the necessary but tedious process of manual outlier detection and replace it by a robust, statistical procedure.

2.3.3 Summary

Particle image velocimetry is a powerful technique that is capable of providing quantitative information about velocities over the full field of view. Although its precision is limited compared to other optical techniques such as laser Doppler anenometry, it compares favourably to Doppler ultrasound which commonly suffers from errors of up to 50%. From a validation perspective, PIV is therefore a particularly useful tool for estimating errors in velocity measurement with experimental flow models.

2.4 Conclusion

This chapter has provided a basic overview of the concepts and techniques used in this thesis. It has reviewed the concepts from fluid mechanics that are particularly relevant to this thesis, in particular, dimensional analysis and methods used to model flow in straight tubes. Two experimental techniques for studying flow, Doppler ultrasound and particle image velocimetry, were introduced, and some of the theory regarding their correct implementation was explained.

This chapter has not attempted to provide an exhaustive review of the material contained within it, rather, it is included to allow the reader to familiarise themselves with the diverse range of topics used in this thesis.

Chapter 3
A simple method to estimate wall shear rate using ultrasound

To fully understand the role wall shear stress plays in the development of atherosclerosis, a reliable method for estimating shear stress is required. If this method is suited for widespread clinical adoption, then the necessary body of evidence to support any conclusions can be established. Existing systems that estimate wall shear stress in-vivo usually require customised hardware that is of limited availability. This chapter aims to develop an approach that can estimate the wall shear rate using commonly availability clinical ultrasound machines.

This chapter has been accepted in another form for publication in the journal *Ultrasound in Medicine and Biology*.

3.1 Introduction

Measurement of the wall shear stress requires three pieces of information: the wall location, the velocity gradient at the wall, and the dynamic viscosity of the fluid adjacent to the vessel wall. With existing instruments, these measurements are difficult, indeed, since obtaining the velocity gradient requires extrapolation, the wall location/velocity gradient may remain an intractable problem. Furthermore, the dynamic viscosity is a function of the local velocity gradient (Nichols & O'Rourke, 1990), although at shear rates typical of large arteries, the viscosity of blood behaves asymptotically (Weaver et al., 1969). Consequently, this chapter will consider the Newtonian approximation and assume a linear relationship between wall shear stress and wall shear rate (WSR). This issue will be explored further in the discussion.

Most ultrasound studies estimate shear rate from velocity profile data, and assume that the maximum shear rate is equal to the shear rate at the wall (Brands et al., 1995; Samijo et al., 1997, 1998; Tortoli et al., 2006). Some studies have used deconvolution in an attempt to correct for the effect of the finite sample volume (Hughes & How, 1993; Flaud et al., 1997), observing

noticeable improvement after application of the technique. However, there is no theoretical basis for assuming that the maximum shear rate is equal to the wall shear rate, and all of these systems require equipment that is non-standard in the clinical environment, restricting the widespread application of these techniques.

Attempts to estimate WSR with standard clinical machines have been limited thus far. Forsberg et al. (2000) estimated wall shear rate from the time averaged velocity profile (hence assuming the Hagen-Poiseuille condition, yielding parabolic profiles) obtained using colour M-mode, in Doppler phantoms, healthy volunteers and patients. The wall shear rate quoted was, in fact, the maximum shear rate measured from the averaged velocity profile. Struijk et al. (2005) carried out a study of wall shear rate, attempting to account for both pulsatile flow and to estimate the shear rate at the wall, rather than the maximal shear rate, based on the theory of fully developed pipe flow (Womersley, 1955). This method used colour flow imaging to obtain an estimate of the flow rate, which subsequently was used as an input to the Womersley solutions.

Struijk et al. (2005) used colour flow imaging to estimate the wall shear rate. This raises the issue; is it possible to modify the method to use spectral Doppler ultrasound? Consequently, the aim of this chapter is to develop and validate a clinically acceptable, ultrasound based technique to estimate wall shear rate in healthy arteries and to compare the results with those estimated using the colour flow method.

3.2 Materials and methods

3.2.1 Theory

3.2.1.1 Estimation of wall shear rate with colour flow

The data presented in this chapter are based on the analytic solutions for fluid flow in rigid pipes developed by Womersley (1955). Struijk et al. (2005) used this theory to estimate wall shear stress in the fœtal aorta using colour Doppler ultrasound. Briefly, this procedure consists of: acquisition and storage of several cardiac cycles worth of colour Doppler information with the transducer in a longitudinal orientation; estimation of the beam-vessel angle, and subsequent angle correction of the colour data; calculation of the flow rate in each frame by assuming rotational symmetry about the vessel axis; ensemble averaging of the flow waveform; measurement of the vessel diameter from B-mode images; and calculation of the velocity profiles by applying

Eq. (2.26) with the flow rate and mean diameter as input data. Having obtained the temporally and spatially varying velocity distribution, extraction of the wall shear rate can be carried out with the second term of Eq. (1.1).

3.2.1.2 Estimation of wall shear rate with spectral Doppler

An alternative method presented in this chapter uses spectral Doppler and a B-mode diameter measurement to generate the Womersley solutions. This method consists of: recording a spectral Doppler trace for several cardiac cycles with the sample volume in the centre of the vessel and the angle correction set parallel to the vessel wall; recording a B-mode cineloop of the artery with the transducer in a longitudinal orientation; isolation and correction of the peak frequency shift in the Doppler spectrum with a string phantom (Hoskins, 1999); calculation of the ensemble average peak velocity waveform; assessment of the mean arterial diameter from the B-mode images; production of the Womersley profiles using the ensemble average peak velocity waveform and mean diameter as boundary conditions using Eq. (3.2).

Holdsworth et al. (1999), after Evans (1982), derived a relationship between the Fourier components of the centreline velocity (which they called peak velocity), and the Fourier components of the mean velocity,

$$V_{\mathrm{mean,k}} e^{-\mathrm{j}\psi_{\mathrm{k}}} = \mathrm{V}_{\mathrm{centre,k}} e^{-\mathrm{j}\phi_{\mathrm{k}}} \left[\frac{\mathrm{J}_0(\beta_{\mathrm{k}}) - 2\mathrm{J}_1(\beta_{\mathrm{k}})/\beta_{\mathrm{k}}}{\mathrm{J}_0(\beta_{\mathrm{k}}) - 1} \right]. \tag{3.1}$$

Inserting Eq. (3.1) into Eq. (2.26) yields an expression relating the centre line velocity directly to the velocity profiles,

$$v(y,t) = \sum_{k=0}^{\infty} \mathrm{Re} \left\{ \mathrm{V}_{\mathrm{centre,k}} e^{\mathrm{j}(\mathrm{k}\omega\mathrm{t}-\phi_{\mathrm{k}})} \left[\frac{\mathrm{J}_0(\beta_{\mathrm{k}}) - \mathrm{J}_0(\beta_{\mathrm{k}}\mathrm{y})}{\mathrm{J}_0(\beta_{\mathrm{k}}) - 1} \right] \right\}. \tag{3.2}$$

The wall shear rate, γ_w, can subsequently be calculated using Eq. (3.5).

$$\gamma_w = \left.\frac{\partial v}{\partial r}\right|_{r=R} \tag{3.3}$$

3.2.2 Flow phantom fabrication

Walled vascular phantoms with different lumen diameters were used to mimic the physiologic conditions for a range of arteries. (Table 3.1.) The vascular phantoms were constructed from acoustically equivalent tissue mimicking material (TMM) (Teirlinck et al., 1998) with a vessel mimicking material made from C-flex tubing (Cole-Parmer, London, UK). To prepare the tissue mimicking material, the necessary ingredients were measured out into beakers in the appropriate proportions (Table 3.2). Benzalkonium-chloride is a preservative added to increase the working life of the TMM. The ingredients were mixed thoroughly in a steel container with a balloon whisk, then placed under a vacuum bell at a pressure of around 160 mmHg (21 kPa) (creating a vacuum of approximately 600 mmHg) for around five minutes to remove air dissolved in the mixing process. The steel container was then placed in a heat bath set to 95 °C with a lid covering the beaker to minimise evaporation. An electric stirrer continually mixed the agar solution during heating, stirring at approximately 1–2 Hertz. After at least one hour at 95 °C, by which point the agar had melted thoroughly, the thermostat was set to 42 °C. On reaching the required temperature, the liquid TMM was poured into prepared perspex boxes.

To test the acoustic properties of each batch of TMM, spare tissue mimic was poured into a sample dish. Upon setting, the speed of sound and attenuation were measured using a scanning acoustic macroscope (Ultrasonic Sciences Limited, Aldershot, UK). If the properties fell outwith the prescribed limits—speed of sound 1550 ± 15 m·s^{-1}, attenuation 0.50 ± 0.05 dB· cm^{-1}·MHz^{-1}—the batch of TMM was rejected.

Artery	Depth to centre of lumen / mm	Diameter / mm	Wall thickness / mm
Brachial	12, 25, 32	3.18	0.79
Common carotid	21, 26, 39	6.35	1.59
Superficial femoral	33, 44, 53	7.94	1.59
Fœtal aorta	41, 86, 106	4.76	0.79

Table 3.1: *The properties of each vascular phantom used in this study.*

Ingredient	Percentage by mass / %
Glycerol	11.0
Benzalkonium-chloride	0.5
Silicon carbide, 400 grain	0.5
Aluminium oxide, 3.0 mm	1.0
Aluminium oxide, 0.3 mm	1.0
Agar	3.0
Demi-water	83.0

Table 3.2: *Ingredients used in agar tissue mimicking material (Teirlinck et al., 1998).*

Perspex boxes of dimensions 30 cm × 10 cm × 10 cm (L×W×D) (Mike Bisset Plastics, Livingston, UK) were used to build the phantoms (Fig. 3.1a). Stainless steel rods of the appropriate diameter (RS Components, Corby, UK) were pushed through the tubing, which was subsequently pushed through the sides of the boxes and sealed with silicone (Fig. 3.1b). The liquid agar TMM was poured into the boxes. When the agar had set, the stainless steel rods were withdrawn, creating the arterial lumen inside the vessel mimic. When not in use, the phantoms were stored with a layer of 9% by volume glycerol/water solution on the surface, sealed under cling film. This prevented evaporation and preserved the acoustic properties of the tissue mimic.

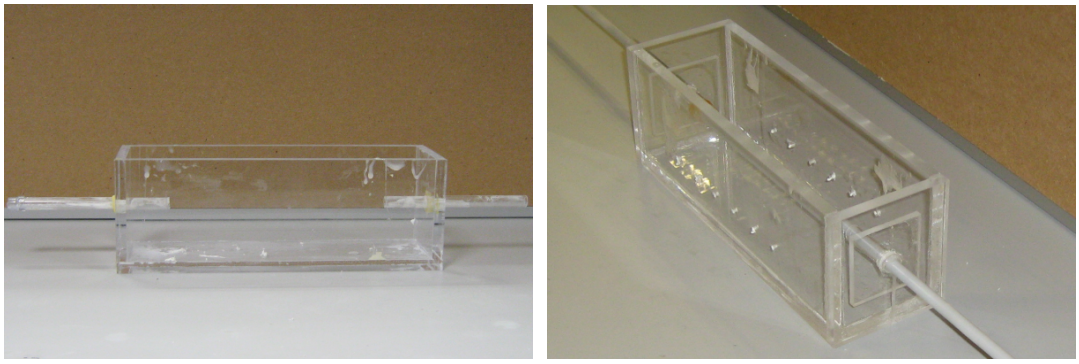

(a) A perspex box used to create ultrasonic vascular flow phantoms.

(b) A vascular phantom with a vessel mimic made of C-flex tubing ready to cast with agar TMM.

Figure 3.1: *Photographs of vascular phantoms in various stages of production.*

Each vascular phantom was connected into a flow loop driven by a gear pump (Micropump model 132, Michael Smith Engineers Ltd., Surrey, UK) powered by an electric motor (M586TE, McLennan Servo Supplies Ltd., Surrey, UK) and an external amplifier (4020-LS, Aerotech Ltd., Berkshire, UK). The amplifier and motor were assembled by the mechanical workshop at the School of Electronics and Engineering of the University of Edinburgh. For the brachial and fœtal aorta phantoms, the working fluid was acoustically equivalent to human blood (Ramnarine

et al., 1998) with kinematic viscosity of 3.3 $mm^2 \cdot s^{-1}$ and a density of 1033 $kg \cdot m^{-3}$. For the carotid and femoral phantoms, a similar fluid was used, except that the orgasol concentration was increased by a factor of four in order to strengthen the acoustic backscatter from the fluid, due to increased attenuation by the thicker vessel mimic—this increased the fluid viscosity to 4.3 $mm^2 \cdot s^{-1}$. The density of this fluid was 1035 $kg \cdot m^{-3}$.

To prepare the blood mimicking fluid, the ingredients were measured out into individual beakers in the required quantities (Table 3.3). The ingredients were then added to one beaker and stirred continuously for 3–4 hours using a magnetic stirrer. After stirring, the BMF was filtered through a 30 μm sieve to remove larger clumps of orgasol, then placed under a degassing bell to a vacuum of 600 mmHg to remove air bubbles introduced by the filtering. To test the acoustic properties, a small sample of the BMF was tested using a scanning acoustic macroscope (Ultrasonic Sciences Limited, Aldershot, UK). If the acoustic properties were outwith prescribed limits—speed of sound 1550 ± 15 $m \cdot s^{-1}$, attenuation 0.05 ± 0.01 $dB \cdot cm^{-1} \cdot MHz^{-1}$—the batch of BMF was rejected. Similarly, the density and kinematic viscosity were measured using a graduated cylinder and scales, and a Cannon-Fenske viscometer (Fisher Scientific UK Limited, Loughborough, UK) respectively. The viscometer was capillary based, and its correct usage is set out in British Standard BS188. If the density was not within 1040 ± 10 $kg \cdot m^{-3}$ or the kinematic viscosity different to 3.5 ± 0.1 mPa·s, the batch was rejected. When not in use, the BMF was stored with a cling film seal to prevent evaporation and changes to the physical properties.

Ingredient	Percentage by mass / %
Glycerol	10.3
Orgasol, 5μm diameter	1.8
Dextran 185000D	3.4
Synperonic N	0.9
Demi-water	85.4

Table 3.3: *Ingredients used in blood mimicking fluid (Ramnarine et al., 1998).*

The flow loop is show schematically in Fig. 3.2. For validation purposes, a calibrated time of flight ultrasonic flow-meter (TS410 with ME10PXN, Transonic Systems Inc., NY, USA) was used to measure the instantaneous flow rate. The flow meter was calibrated using a graduating cylinder and stopwatch; it produced a signal linearly dependent on the flow rate, although the fit was forced through zero to remove zero errors. The probes were positioned at the inlet and outlet of the vascular phantoms and the mean of the aligned signals was used as an estimate of the true flow rate inside the phantom. An interface program written in Labview 7.1 (National

Instruments, Austin, TX, USA) running on a PC running Microsoft Windows (Microsoft Corp., Redmond, WA, USA) allowed the generation and recording of arbitrary waveforms at sampling frequencies up to 10 $kS \cdot s^{-1}$.

The interface program controlled a PCI interface card (PCI6024E, National Instruments, Austin, TX, USA) which carried out the signal generation and acquisition. A text file containing appropriately scaled values of the desired waveform is loaded into memory. On commencement of the data acquisition, the output signal is written to the buffer at the specified frequency (1 $kS \cdot s^{-1}$) and up to 16 input signals may be recorded. Although the interface card has only one analogue-to-digital converter and one digital-to-analogue chip, and hence must process signals in series, the maximum frequency (200 $kS \cdot s^{-1}$) of the ADC/DAC is far greater than the sampling rate, so minimal phase shift was introduced. The signal was passed through the amplifier and on to the pump, resulting in the production of realistic spectral Doppler waveforms in each arterial model. Realistic spectral Doppler (Fig. 3.3) and flow waveforms (Fig. 3.4) were measured in each phantom. To avoid artefacts due to the initiation of flow, data from the first five cycles were discarded.

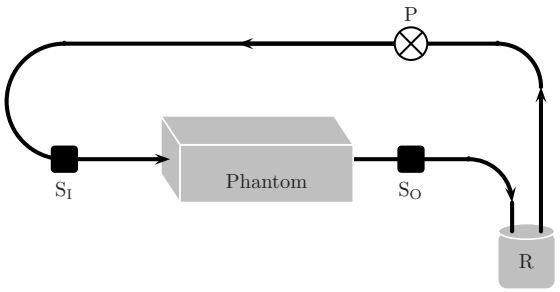

Figure 3.2: *Schematic diagram of the flow circuit used in this chapter:* S_I *and* S_O *are pressure and flow transducers positioned at the inlet and outlet of the phantom; P is a gear pump; and R is the blood mimic reservoir.*

3.2.3 Ultrasound acquisition

The data were recorded with a clinical ATL HDI5000 ultrasound machine (ATL Ultrasound, Bothell, WA, USA) and transferred via the Researchlink option to a PC for off-line analysis. The machine settings were optimised for vascular applications using a linear array transducer (L12–5 38, central B-mode frequency, 12 MHz, central Doppler frequency, 5 MHz), and, for obstetrics, using a curvilinear array (C5–2, central B-mode frequency, 5 MHz, central Doppler frequency, 2.5 MHz).

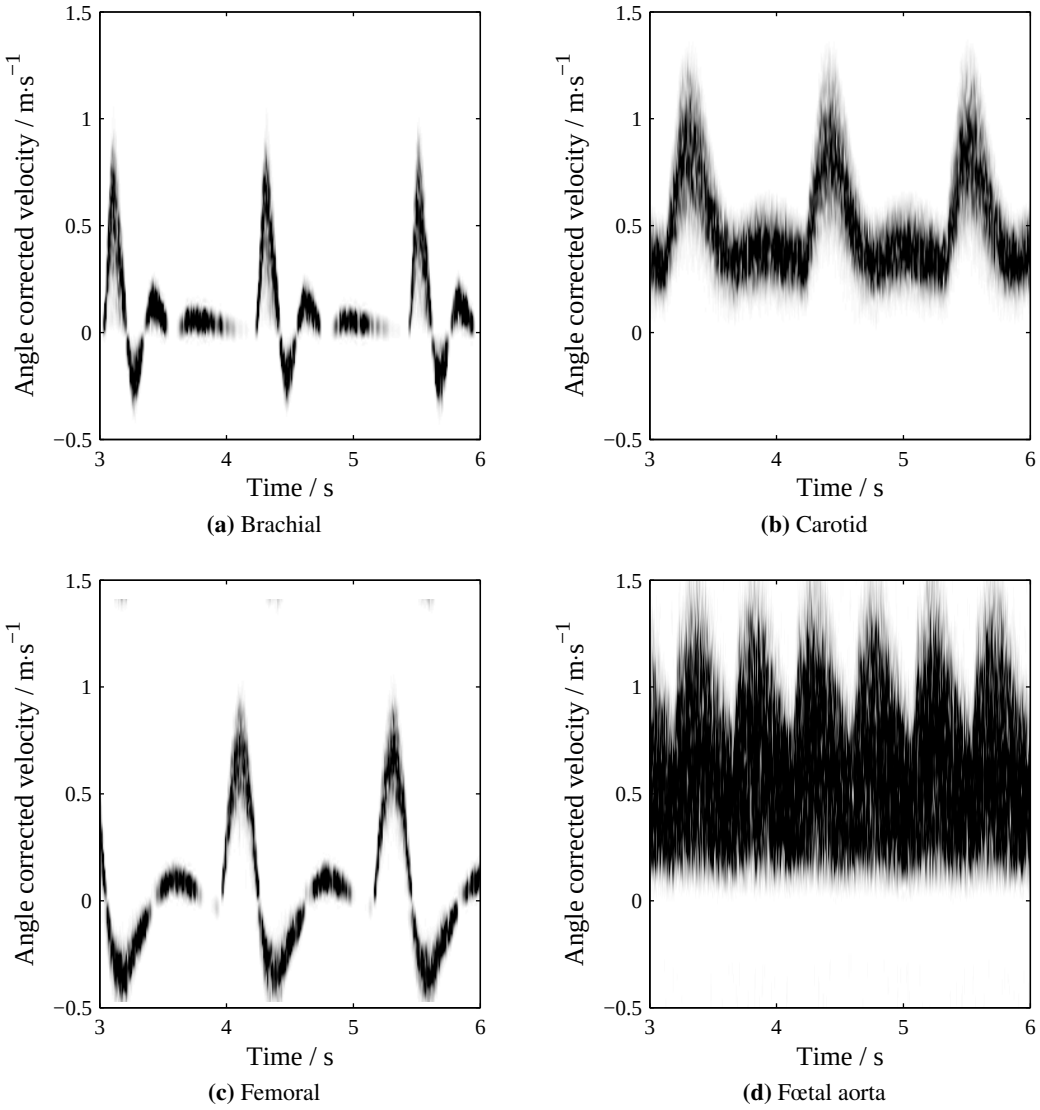

(a) Brachial **(b)** Carotid

(c) Femoral **(d)** Fœtal aorta

Figure 3.3: *Spectral Doppler waveforms obtained from the vascular phantoms.*

Measurements in the study were repeated three times. Each spectral Doppler measurement consisted of a spectral Doppler waveform with at least five complete cardiac cycles and one B-mode recording of the artery lumen in a longitudinal orientation. To allow comparison with the procedure described by Struijk et al. (2005), a colour Doppler cineloop was also recorded as part of each measurement. The length of the B-mode and colour recordings were long enough to fill up the buffer on the ultrasound machine—this was usually enough for six or more complete cycles. For the fœtal aorta, a second colour Doppler recording was acquired with a linear array transducer to obtain an estimate for the development index, η, as set out in Eq. (3.9) and Eq. (3.10).

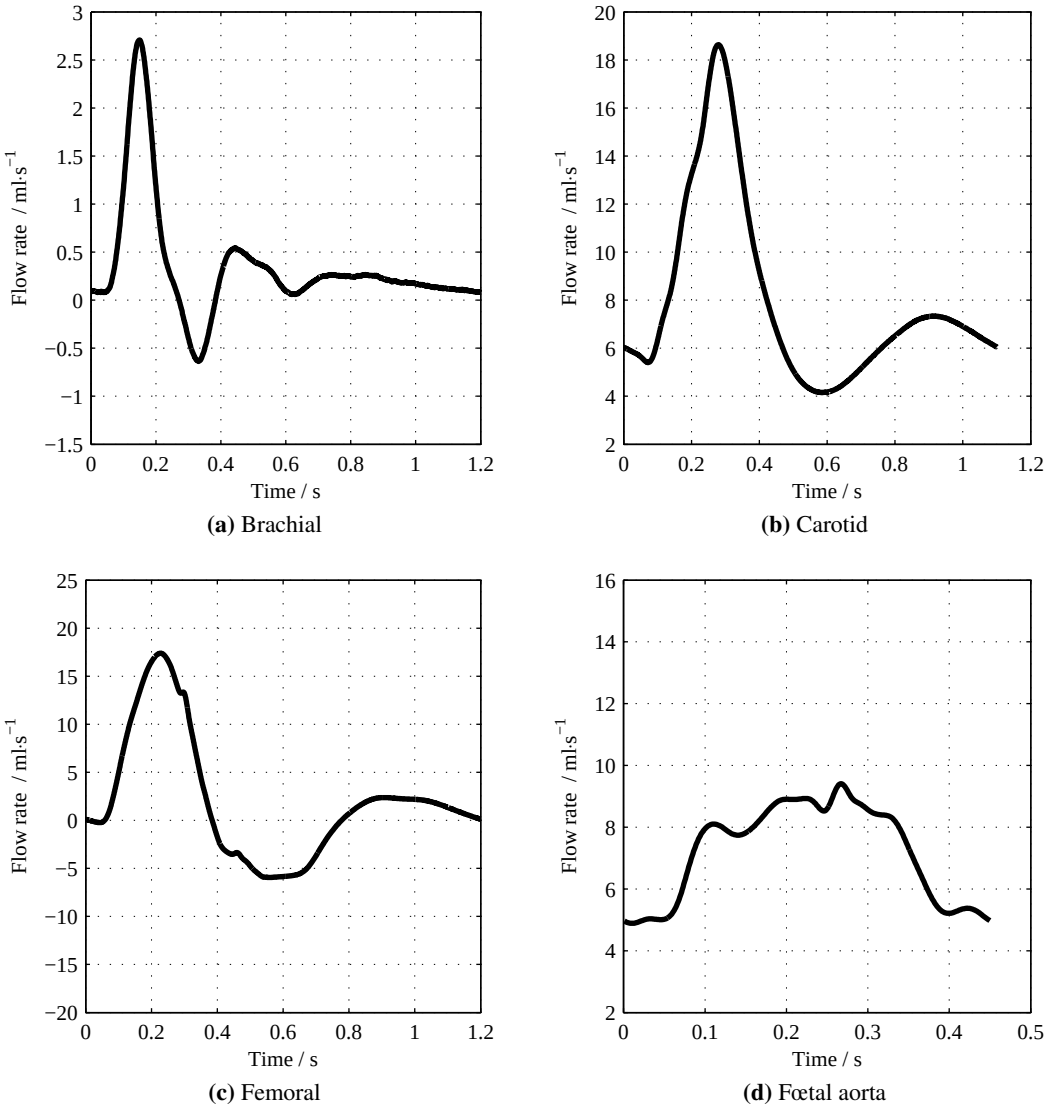

Figure 3.4: *Flow rates in the vascular phantoms measured by ultrasonic time of flight probes.*

To optimise the image quality, the transducer was used in a longitudinal orientation, providing a clear view of the intima-media layer of both the near and far walls. For spectral Doppler, the sample volume was positioned in the centre of the lumen to ensure that the centreline velocity was measured. Typically, for a 6 mm diameter vessel, the sample volume length was 2 mm—this reduced the possibility of measuring larger velocities that do not necessarily lie on the centre line (Loudon & Tordesillas, 1998). The angle correction was aligned with the artery wall. After the spectral waveform had been stored, a B-mode cineloop was also recorded with persistence turned off. The transducer was then removed and replaced to take repeat measurements. When colour Doppler measurements were required, the colour Doppler cineloop was

recorded before removal of the transducer. The colour box was small enough to maintain an adequate frame rate. The line-density was set to C, yielding one Doppler line in the data file for every 0.2 mm with the linear array, or for every 0.3° for the curvilinear transducer. Other colour settings are listed in Table 3.4. The beam widths varied from 2.4–3.9 mm. Machine options defined by the manufacturer were selected based on the particular vascular phantom/artery under investigation (Table 3.5).

Setting	Value
Persistence	Off
Smoothing	Off
Sensitivity	Medium
Wall-filter	Low
DMD	Off

Table 3.4: *Colour settings used on the* HDI*5000 for each artery in this study.*

Artery	Transducer	Primary option	Secondary option
Brachial	L12–5	Peripheral vasculature	Arterial
Common carotid	L12–5	Cerebrovascular	Carotid
Superficial femoral	L12–5	Peripheral vasculature	Arterial
Foetal aorta	C5–2	Obstetrics	General

Table 3.5: *Machine options used on the* HDI*5000 for each artery in this study. (*L*: linear array.* C*: curvilinear array.)*

3.2.4 Ultrasound processing

The ultrasound recordings were analysed in Matlab R2006a (The Mathworks, Natick, MA, USA). The xiftoolbox v0.4.2, an in-house custom written Matlab toolbox for analysing Researchlink files (freely available from the Matlab File Exchange), was used to process all the data recordings.

3.2.4.1 Spectral Doppler processing

Each separate spectral Doppler recording consisted of at least five repeated waveforms. The peak frequency shift in the Doppler power spectrum was automatically extracted using a threshold by the ultrasound scanner. This corresponded to the centreline velocity under Womersley (1955) flow. All subsequent processing was carried out using the centreline velocity alone.

Doppler ultrasound suffers from a number of sources of spectral broadening, leading to an overestimate of the peak frequency shift in the Doppler spectrum (Daigle et al., 1990; Hoskins et al., 1999). The broadening can be split into two components: a range of frequencies is present in the spectrum due to the presence of a range of scatterer velocities in the sample volume; the second component of broadening is due to the instrumentation itself, distorting the ideal spectrum, this is known as geometric spectral broadening (GSB). To remove the error due to GSB, measurements were taken using a string phantom (BBS string phantom, BBS Medical Electronic, Hagersten, Sweden) at the same depth and angle correction as each Doppler recording in the subjects and phantoms. This correction typically reduced the peak frequency in the Doppler spectra by 30–50%. This corrected peak frequency shift was converted to a velocity using the Doppler equation, Eq. (2.34),

$$f_{\mathrm{D}} = 2\frac{v}{c} f_0 \cos\theta,$$

where v is the scatterer velocity along the line of sight, c is the machine calibrated speed of sound in tissue (1540 $\mathrm{m{\cdot}s^{-1}}$), f_{D} is the Doppler frequency shift, and f_0 the carrier frequency of the ultrasound beam.

To calculate an ensemble average from the corrected centreline velocity waveform, each individual cycle must first be isolated, aligned and then averaged. The beginning of each cycle was determined using a gradient threshold. The resulting cycles were aligned by crosscorrelating each cycle with the first (considered a reference waveform), and shifted in time by the resulting correlation peak. Although this process has minimal effect with a computer driven pump, alignment of each cycle is necessary when analysing in-vivo data. Finally, the mean of the aligned signals was calculated; the length of the average cycle was taken as the median of the lengths of the individual cycles.

3.2.4.2 Colour Doppler recordings

To obtain the wall shear rate from the colour Doppler recordings, the procedure described by Struijk et al. (2005) was implemented. For each scan line, an estimate of the flow rate was obtained by integrating of the velocity distribution across the vessel lumen (corrected for

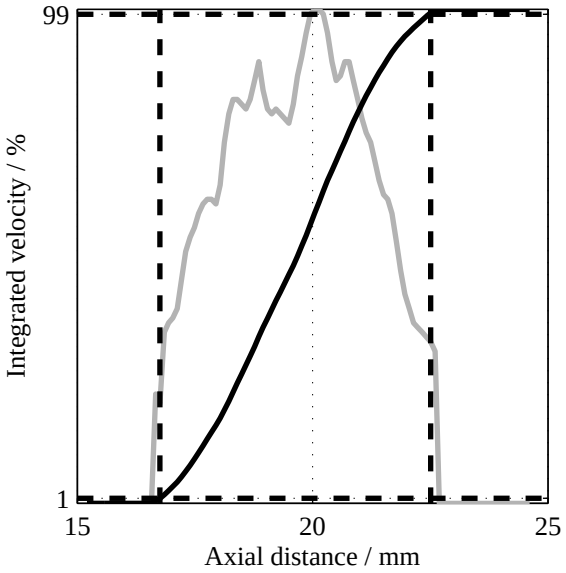

Figure 3.5: *Truncation of the velocity data at 1% and 99% of the cumulative velocity profile to correct for the finite sample volume. (Adapted from Struijk et al. (2005).) The velocity profile is shown in grey, the integrated profile in black.*

beam-vessel angle) around the vessel axis and assuming rotational symmetry. This is shown in Eq. (3.4), taken from Struijk et al. (2005)

$$q(t) = \pi \int_{-R}^{R} r \cdot v(r,t) \mathrm{d}r, \tag{3.4}$$

where $q(t)$ is the flow rate as a function of time, R is the vessel radius, r is the radial distance from the vessel axis, $v(r,t)$ is the spatially and temporally dependent velocity distribution and t is the time variable. To reduce velocity overestimation at the vessel walls due to finite sample volumes, the velocity data for each scanline were truncated at 1% and 99% of the cumulative sum in the same manner as Struijk et al. (2005). To obtain a value for the flow rate for the whole frame, the arithmetic mean of the individual flow rate estimates from each scanline was calculated. Having obtained the flow rate from each frame, the ensemble average waveform was calculated as described previously.

3.2.4.3 Measurement of arterial diameter

B-mode ultrasound recordings were used to measure the diameter of the arteries under study. A line was marked by hand across the lumen of each vessel (Fig. 3.6a). The intensity profile along the line was displayed, and Gaussian curves were fitted to the intima-media layer of the artery walls between limits specified by the user (Fig. 3.6b). The diameter was calculated for every frame in the ultrasound recording; the mean of the distension waveform was considered to be the arterial diameter. The diameter for both the spectral and colour Doppler methods were estimated using the B-mode images.

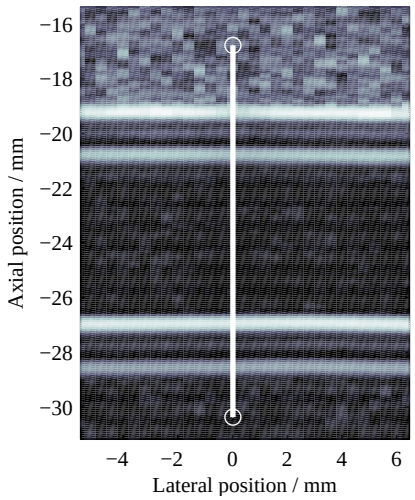

(a) The profile marked across the B-mode image.

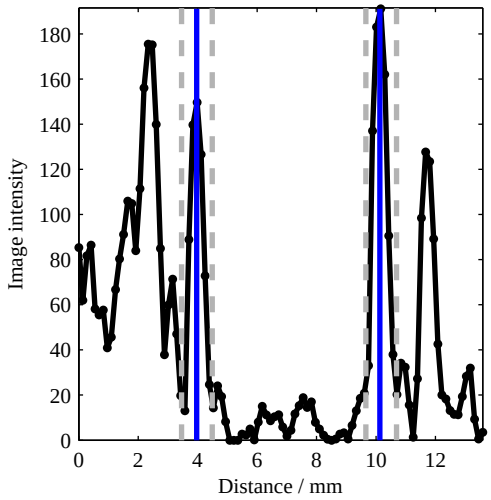

(b) B-mode intensity across the marked profile for one frame. Gaussian curves were fitted to each peak between the grey dashed lines.

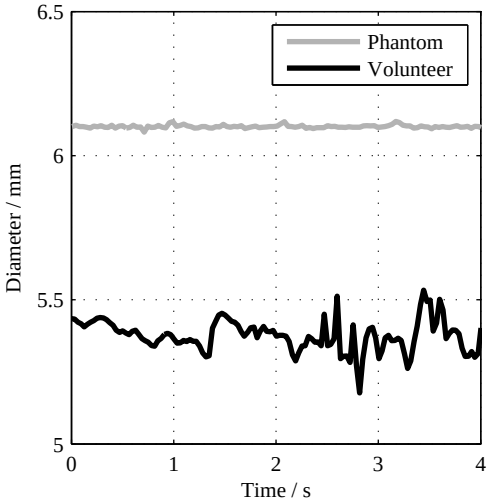

(c) Arterial diameter against time in the carotid phantom and the common carotid of a healthy volunteer.

Figure 3.6: *Calculation of arterial diameter.*

3.2.5 Calculation of Womersley profiles and wall shear rate

For the spectral Doppler measurements, the ensemble averaged centre-line velocity waveform was used with the arterial diameter measurement to generate the Womersley profiles as shown in Eq. (3.2). Using colour Doppler ultrasound, the velocity profiles were obtained using the flow rate, instead of the peak velocity waveform, and eqn (2.26). Eq. (2.26) requires the mean velocity as an input, rather than the flow rate; this was corrected by dividing the flow rate waveform by the area of the lumen.

Having obtained the ensemble averaged Womersley profiles, it is trivial to obtain an estimate for the wall shear rate (WSR), γ_w, using Eq. (3.5).

$$\gamma_w = \left.\frac{\partial v}{\partial r}\right|_{r=R} \tag{3.5}$$

3.2.6 Oscillatory shear index

A measure of the unidirectionality of the WSR is provided by the oscillatory shear index (OSI) (Ku et al., 1985*b*). Considering WSR in only one dimension, the OSI in a particular artery is given by Eq. (3.6),

$$\mathrm{OSI} = \frac{\int_0^T |\gamma_w^*| \mathrm{dt}}{\int_0^T |\gamma_w| \mathrm{dt}}. \tag{3.6}$$

Where γ_w is the wall shear rate, and γ_w^* is the part of the wall shear rate waveform in which the shear rate is in the opposite direction to the time averaged WSR. Unidirectional wall shear manifests itself with OSI $= 0$, whilst highly oscillatory flows (for example, a sinusoid with zero offset) can have a maximum OSI of 0.5.

3.2.7 Subjects

To demonstrate the feasibility of collecting data in humans, an assumed healthy volunteer was scanned in the morning, having not taken caffeine or alcohol that day. Ethical approval was

granted for the recruitment and scanning of a healthy volunteer by a local ethics board. A stabilisation period of thirty minutes was implemented before the examination. Scanning was performed with the volunteer in the supine position and three sets of repeated measurements were obtained from the brachial, common carotid and superficial femoral arteries. The recordings consisted of: a B-mode recording of the artery diameter; a colour Doppler recording; and a spectral Doppler trace from the approximate centre of the artery. Machine settings were the same as used in the vascular phantoms.

3.2.8 Validation of the Womersley conditions

Both variants of the technique depend on the assumptions inherent in the Womersley solutions (Nichols & O'Rourke, 1990, p 136–137). Specifically, these assumptions are: that the flow is laminar; that the fluid behaviour is independent of the axial co-ordinate, depending only on the radial position; that the fluid is homogeneous and Newtonian; that the containing vessel is cylindrical, with rigid walls; that the system can be described by linear systems theory, allowing separate consideration of each frequency component; and that the fluid velocity is zero at the vessel wall.

Of these assumptions, the largest potential source of error in this work concerned the second item—effects introduced by the limited size of the system—commonly termed "inlet length". To test that this condition is satisfied in-vivo, the inlet length, L, for each artery in question was calculated using Eq. (3.7) (Schlichting, 1987, p 186).

$$L = 0.04\frac{\overline{v}D^2}{\nu}, \tag{3.7}$$

where $\overline{v}$ is the mean velocity, D the artery diameter and ν is the kinematic viscosity of blood—for this study, a value of 3.6×10^{-6} $\mathrm{m^2{\cdot}s^{-1}}$ was used for adult blood (Nichols & O'Rourke, 1990) and 4.3×10^{-6} $\mathrm{m^2{\cdot}s^{-1}}$ for fœtal blood (Struijk et al., 2005). Typical geometric values for the arteries studied are listed in Table 3.6. If L is on the order of the arterial length, and the artery is relatively straight, then we can assume that the flow is fully developed.

Eq. (3.7) applies only to the mean—that is, steady—component of flow. Arterial flow is unsteady, but the Womersley conditions assume that all frequency harmonics are separable, allow-

Artery	Peak flow $\mathrm{ml \cdot s^{-1}}$	Mean flow / $\mathrm{ml \cdot s^{-1}}$	Diameter / mm	Length / cm
Brachial	6.3*	0.6*, 1.2†	5.6*, 4.5†, 5.9‡	43*, 22‡
Carotid	30.2*, 11.9§, 24.0[1]	8.0*, 6.2§, 6.0[1]	5.7*, 7.4‡, 6.3[1]	18*, 20‡
Femoral	44.0*, 25.1[2]	5.8*, 3.3[2], 2.5[3]	7.7*, 4.8‡, 6.4[3]	44*, 26‡
Foetal aorta	10.0[4]	6.7[4], 4.9[5]	5.0[4], 4.9[5]	8

Table 3.6: *Typical values for mean velocity, diameter and length of arteries in this study. (Figures for the fœtal aorta are at 30 weeks gestation.) Values taken from †Arnold et al. (1991), ‡Avolio (1980), *Olufsen et al. (2000), §Marshall et al. (2004), [1]Holdsworth et al. (1999), [2]Steinman et al. (1993), [3]Evans & McDicken (2000), [4]Struijk et al. (2005), [5]Brodszki et al. (1998).*

ing the isolation of the steady and oscillatory components. Thus, the observed velocity profile for an oscillatory flow can be considered as a series of higher frequency harmonics superimposed on a mean, steady, velocity profile. Treating these frequency harmonics separately, the inlet length, L_k, has been found experimentally (Caro et al., 1978, p 321–322),

$$L_k = 3.4\frac{v}{\omega_k}, \tag{3.8}$$

where v is the core (centreline) velocity and ω_k is the angular frequency of each harmonic. The core velocity is the largest velocity due to each oscillatory component. From Eq. (3.8), it is clear that the inlet length reduces with frequency, such that the longest inlet length occurs for the lowest harmonic, which is, in general, shorter than the inlet length for steady flow. However, comparison of inlet lengths reported by different authors requires knowledge of the Fourier components of the measured flow wave, which are in general, not available, which can restrict the applicability this method.

To assess whether the collected data in each flow phantom were fully developed, velocity profiles were measured using colour Doppler ultrasound, and the temporal mean velocity profile calculated. This mean velocity profile, was used to obtain a figure of merit, n, that minimised the squared differences, χ^2, between the measured and fitted velocity profiles. This is shown in Eq. (3.9),

$$\chi^2 = \sum_{i=1}^{i=N} \left(\frac{v(r_i)}{v_0} - \left\{ 1 - \left[\frac{r_i}{R} \right]^n \right\} \right)^2, \tag{3.9}$$

Artery	Length / cm	Steady inlet length / cm	Oscillatory inlet length / cm
Brachial	33	2	5
Common carotid	19	10	12
Femoral	35	6	26
Fœtal aorta	8	6	—

Table 3.7: *Estimated inlet length for arteries in-vivo, compared with their approximate lengths. Values are calculated from the mean of data in Table 3.6, using Eq.* (3.7) *and Eq.* (3.8)*. For the fœtal aorta, no waveform has been published, thus no estimate for the oscillatory inlet length can be obtained used Eq.* (3.8)*.*

where R is the artery radius, v_0 is the maximum measured velocity and $v(r_i)$ the measured velocity as a function of discretised radius. A value of $n = 2$ corresponded to a parabolic flow profile, implying that the flow was fully developed. To normalise the figure of merit, we introduce the development index

$$\eta = \frac{2}{n}, \tag{3.10}$$

such that η runs from 0 for plug flow, to 1, corresponding to fully developed flow. The presence of turbulence would also render the Womersley conditions invalid. Turbulent flow is known to occur in the advanced stages of disease, but in healthy arteries its existence is rare. The Reynolds number—defined in Eq. (2.1)—is a dimensionless entity that compares the relative importance of inertial and viscous forces, for very low values, viscous forces dominate, but for high numbers, the inertial forces are most significant. Flow in a cylinder is laminar for Reynolds numbers below 2300 (Schlichting, 1987, p 39). To test for the presence of turbulence in the phantoms, the peak Reynolds number was calculated for each phantom studied.

3.3 Results

3.3.1 Validation of Womersley technique

For the arteries considered in this study, typical inlet lengths in-vivo (Table 3.7) are shorter than the total vessel lengths (Table 3.6). This validates the assumption that flow inside these vessels may be considered developed. The entrance length for each phantom used in this study was at least as long as the corresponding largest length quoted in Table 3.7.

For the B-mode and colour Doppler images obtained from the vascular phantoms, the frame rates ranged from 18–39 Hz for the linear array transducer (L12—5), and from 10–27 Hz for the C5—2 transducer. Values of the development index obtained from the phantoms, with the exception of the fœtal aorta, were all close to unity, while peak Reynolds numbers in all the models were below transitional regime (Table 3.8).

Phantom	Development index	Peak Reynolds number
Brachial	1.17 (0.10)	290 (3)
Common carotid	1.04 (0.10)	984 (2)
Femoral	0.94 (0.17)	740 (3)
Fœtal aorta	0.94 (0.01)	663 (5)

Table 3.8: *Values of the development index and peak Reynolds number for the vascular phantoms used in this study. The figures are presented as mean (standard deviation).*

With the exception of the fœtal aortic phantom using the colour Doppler technique, estimates of the flow waveforms reconstructed (and aligned) using both methodologies qualitatively agree with the measured flow rate (Fig. 3.7). Flow rate estimated with the colour technique showed a general reduction with depth; comparing the mean flow rate with the time-averaged value from the Transonic probes reveals that this variation affects both techniques, although the bias and variability of the colour method far exceeds that of the spectral Doppler method (Fig. 3.8a and Table 3.9).

Comparing mean wall shear rate calculated by both techniques for each vessel with the time averaged WSR provides some estimate of the validity of each method (Fig. 3.8b). The bias and variability of the colour Doppler method exceed those of the spectral Doppler method in all vessels, with similar magnitudes to the flow estimates (Table 3.9).

Phantom	% difference (flow)		% difference (WSR)	
	Colour	Spectral	Colour	Spectral
Brachial	–62 (8)	–6 (3)	–62 (8)	–9 (1)
Carotid	–10 (11)	–7 (3)	–10 (8)	–7 (1)
Femoral	–57 (18)	–22 (7)	–82 (8)	–22 (4)
Fœtal aorta	+66 (3)	–19 (9)	+70 (4)	–17 (10)

Table 3.9: *Percentage difference from the mean flow and wall shear rate for each phantom in this study. Results are presented as mean (standard deviation).*

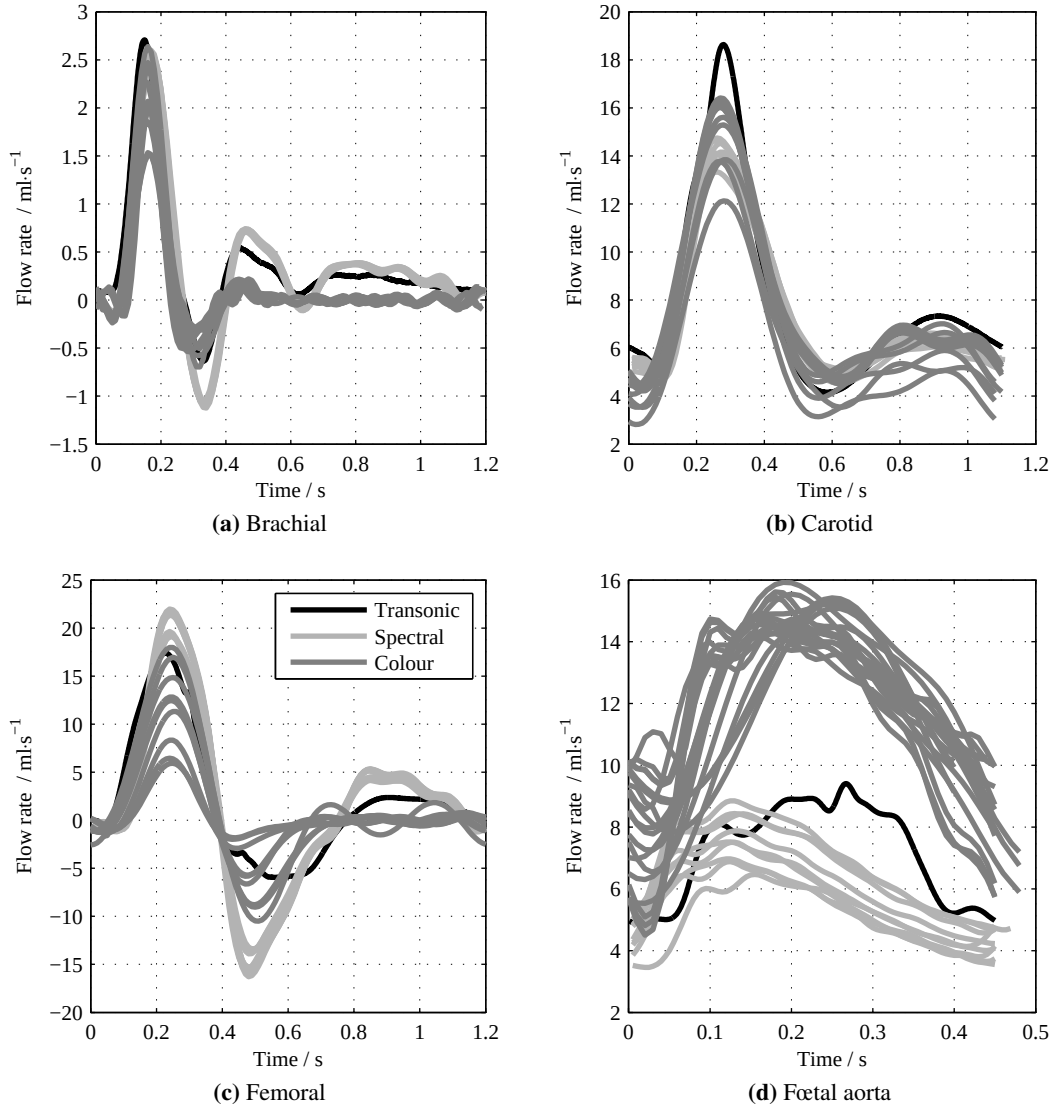

(a) Brachial **(b)** Carotid **(c)** Femoral **(d)** Fœtal aorta

Figure 3.7: *Flow rates in the vascular phantoms measured by the time of flight probe, and reconstructed using the colour and spectral Doppler methods.*

3.3.2 Estimation of wall shear rate in-vitro

The wall shear rate was successfully estimated in all the phantoms studied (Fig. 3.9). The data reveal a variation with depth, similar in magnitude and variability to the reconstructed flow waveforms (Fig. 3.8b and Table 3.9). Again, the bias and variability of the colour data far exceeds that of the spectral Doppler method.

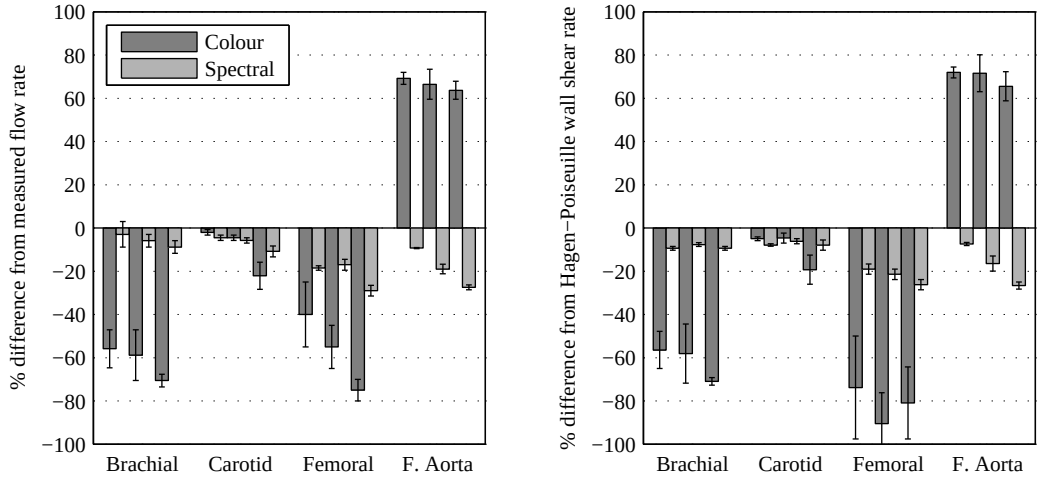

(a) Flow rate differences.

(b) Carotid

Figure 3.8: *Percentage difference from the measured flow rate (via Transonic time of flight probes) of the Womersley reconstructed flow rates using the colour and spectral Doppler methods for all the phantoms studied. Each pair of bars represents one depth studied for the respective phantom; the shallowest is on the left hand side and the deepest on the right.*

3.3.3 Example data from a healthy volunteer

Fig. 3.10 shows the peak velocity and estimated wall shear rate taken from the right superficial femoral, brachial and common carotid arteries in an assumed healthy volunteer. These measurements were taken using the spectral Doppler method only. Table 3.10 shows the development index, the peak, mean and pulse wall shear rate, and the oscillatory shear index from the healthy volunteer.

Artery	Depth / mm	Development index	Wall shear rate / s^{-1}			OSI
			Peak	Mean	Pulse	
Brachial	4–5	1.05 (0.29)	1339 (57)	96 (25)	2313 (53)	0.29 (0.04)
Carotid	12–14	1.10 (0.09)	1191 (29)	137 (7)	1682 (102)	0.14 (0.02)
Femoral	18–19	0.71 (0.08)	830 (53)	40 (6)	1404 (94)	0.40 (0.02)

Table 3.10: *The development index, estimated wall shear rate and* OSI *from a healthy volunteer.*

3.4 Discussion

It is widely believed that the wall shear stress (and consequently shear rate) is important in the initial stages and development of arterial disease. Measurement of the wall shear rate requires high quality velocity measurements next to the arterial wall. This requires two pieces of information; the velocity measurement, and the actual wall position. Both of these are hard to obtain

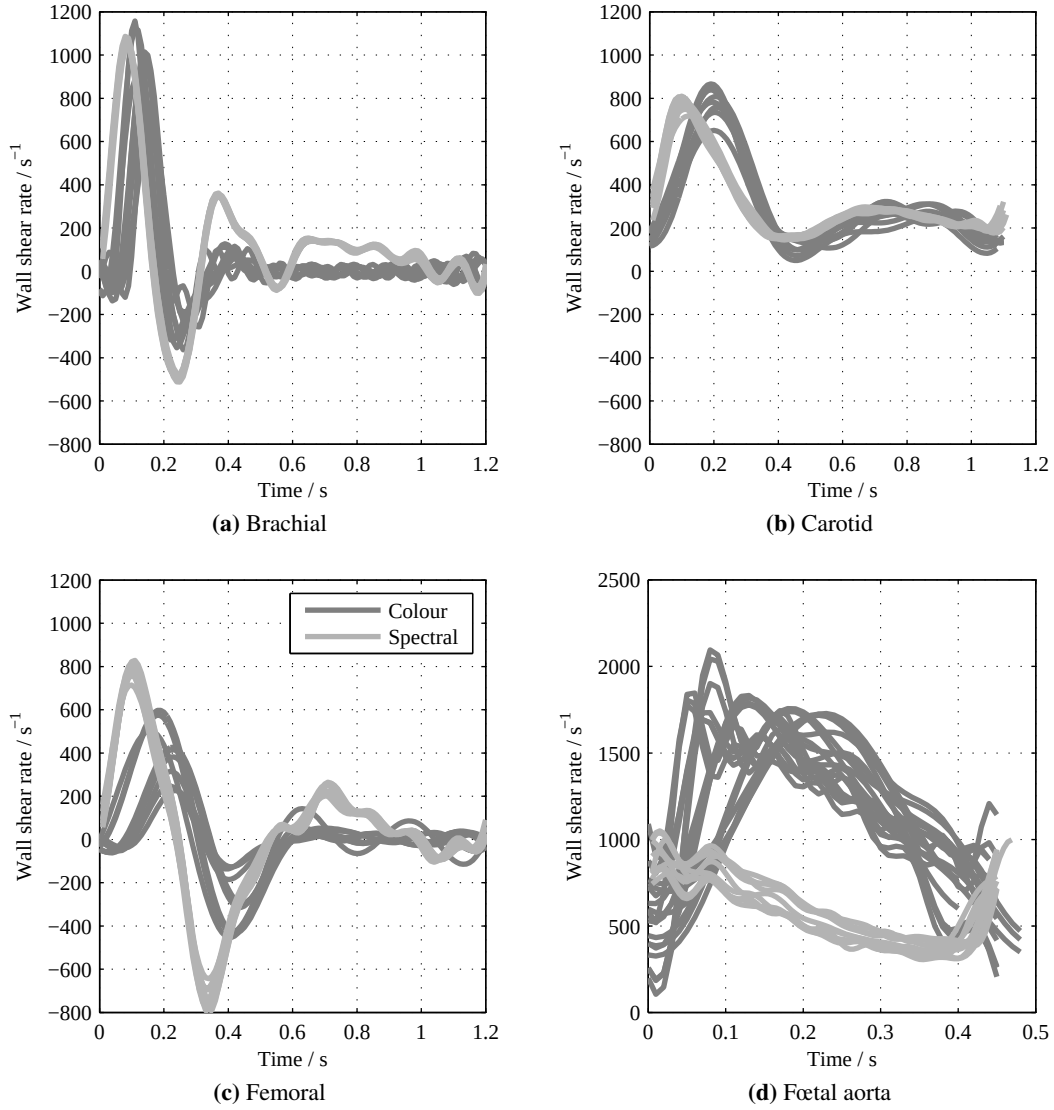

Figure 3.9: *Wall shear rate waveforms in the vascular phantoms reconstructed using the colour and spectral Doppler methods.*

with common, clinical ultrasound machines. Brands et al. (1995) developed a customised, high frequency ultrasound technique to investigate wall shear rate non-invasively, and Samijo et al. (1997, 1998) were able to conduct limited trials across samples of the population. However, follow up work has been limited due to the restricted availability of the equipment.

Struijk et al. (2005) developed a technique for investigating wall shear stress in the fœtal aorta using clinical ultrasound machines. This method avoids the two common problems of wall location and velocity measurement close to the wall by assuming that the blood flow is fully developed (Womersley, 1955). The volume flow is calculated as the sum of all the colour Doppler measurements in each scan-line, integrated around an axis to form a circular velocity

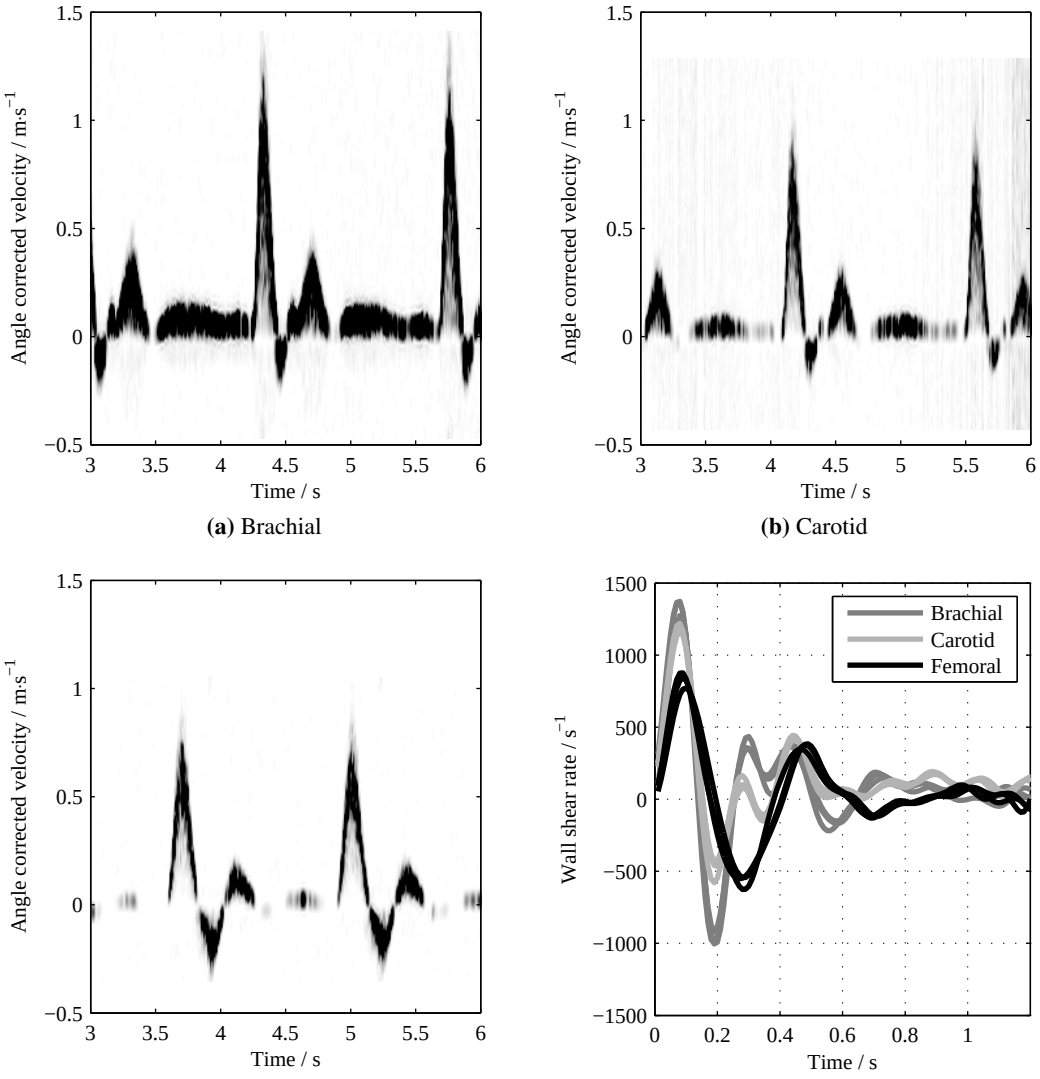

(a) Brachial

(b) Carotid

(c) Femoral

(d) Wall shear rates estimated in a healthy volunteer using spectral Doppler.

Figure 3.10: *Spectral waveforms and the resulting wall shear rate from a healthy volunteer.*

surface; to measure the arterial diameter, Struijk et al. (2005) again used the colour Doppler information with a minor correction to prevent overestimation due to the finite sample size. To calculate the Womersley profiles, the mean diameter and mean velocity surface is obtained for each scan-line (spatial average) in each frame. The final diameter used to calculate the fully developed solutions is the temporal average of the diameter estimates for each frame (i.e. of the spatial averages). Whilst this technique is appropriate to measure arterial diameters in the presence of diastolic flow, it is unsuitable for use in the femoral and brachial arteries where the lack of any significant diastolic flow produces estimated diameters tending to zero for up to half the cardiac cycle. The subsequent temporal averaging distorts the mean arterial diameter,

and consequently produces spurious velocity distributions and wall shear rates when applied to arteries with near zero diastolic flow. The method presented in this paper used B-mode images to estimate arterial diameter, and consequently did not suffer from this source of error.

We have presented a simplification of the method proposed by Struijk et al. (2005). Replacing colour Doppler ultrasound with spectral Doppler greatly improves frame rates, and removes the complications associated with machine settings such as colour box size, line density and angle correction. When using the peak frequency shift in the Doppler spectrum, it is necessary to correct this measurement with a string phantom (Hoskins, 1999), however, as this can be performed after the investigation, it does not add any time to the patient's exam.

3.4.1 Validation of Womersley conditions

Underpinning the entire method is the assumption that suitable arteries are straight pipes with fully developed fluid dynamics (Womersley, 1955). To test this assumption, we have introduced the development index. Fluid behaviour in all the phantoms was consistently close to being fully developed and laminar (Table 3.8). The narrow range for the fœtal aorta phantom is due to the measurements being carried out at the shallowest depth only, with the 5 MHz linear array; all other quoted values for the development index were the averages of repeated measurements at several depths.

Values of the development index in the flow phantoms are all close to unity. This implies that flow in these vessels was fully developed. Although the development index in the brachial and carotid phantoms have values greater than unity, we suggest that this due to the difficulties of accurately measuring velocity with pulsed Doppler ultrasound. Any effects due to non-Newtonian behaviour would be minimal, since the scatterer concentration of the blood mimicking fluid is low. Distension in the phantoms was low, on the order of 1%, implying that the conditions for Womersley flow were satisfied. Consequently, values of the development index greater than unity were likely due to issues with pulsed Doppler velocity estimation, such as non-uniform insonation (Bastos et al., 2000), temporal (Fish, 1991) and spatial velocity gradients in the fluid (Fish, 1986, p 338–376) and broadening due to amplitude modulation (Fish, 1986, p 338–376).

The spectral Doppler method was consistently more accurate than the colour Doppler technique at estimating the mean flow and wall shear rate (Fig. 3.8). The mean differences between the Hagen-Poiseuille flow and wall shear rates, and the corresponding values estimated using the

spectral Doppler method were 14 (8)% and 14 (7)%; comparable figures for the colour Doppler method were 49 (26)% and 56 (32)%. Superficially, it appears that the results for the spectral method agree with those presented by Cezeaux & van Grondelle (1997), who used a modification of Womersley's theory, originally presented by Ling & Atabek (1972), to investigate the effect of non-linear behaviour in oscillatory flow in arteries. Cezeaux & van Grondelle (1997) calculated the oscillatory profiles via Womersley's solution using flow rate and centreline velocity as separate boundary conditions—which are analogous to the colour and spectral Doppler methods—and via the non-linear method, which they considered the reference standard. Treating blood as a Newtonian fluid, the mean wall shear stress and flow rate were underestimated by 22% and 24% respectively in the canine femoral artery using the centreline velocity method. The error in the wall shear stress calculated by Cezeaux & van Grondelle (1997) using the flow rate method was 2%—demonstrably different from the error in mean wall shear rate using the colour Doppler method (56%).

Although the errors obtained by Cezeaux & van Grondelle (1997) agree well with the mean errors for the femoral phantom obtained with the spectral Doppler method (Fig. 3.8a and Fig. 3.8b), it seems unlikely that the errors responsible for the differences are the same. Errors in the numerical model originate from the convective term in the Navier-Stokes equations; this term is due to tapering and distension (which was around 10%) of the arterial vessel. In the phantoms, the vessels had constant area, and distension was much smaller (less than 1%). Secondly, the errors increased with increasing vessel depth, suggesting that the problem lies with the instrumentation, rather than the fluid behaviour.

The colour Doppler method was able to rebuild the systolic peak adequately in the brachial and femoral phantoms, but it performed poorly during diastole, registering close to zero flow for half the cycle or more (Fig. 3.7). This effect is possibly due to the level of clutter filter, which in general will increase with the pulse repetition frequency (PRF). In order to prevent aliasing during systole, the PRF must be set correctly, but this comes at the expense of sensitivity to low velocities during diastole, since the low Doppler frequencies risk falling below the level of the clutter filter. This poor performance during diastole biased the mean colour flow and shear rates towards zero, contributing to the errors shown in Fig. 3.8.

The colour data for the fœtal aorta is markedly different from the comparable data in all the other phantoms (Fig. 3.7 and Fig. 3.8). This finding agrees qualitatively with a recent study (Gerada et al., 2006) of Doppler velocities in the umbical vein, which found that colour Doppler

yielded significantly higher velocities than spectral Doppler. Several mechanisms exist that may be responsible, but the most significant cause lies with the transducer used for the study. For the fœtal aorta phantom, the central Doppler frequency was 2.5 MHz; for all the other phantoms a linear array of central Doppler frequency 5 MHz was used. Using a lower carrier frequency results in longer sample volumes, such that the finite sample volume problem was exaggerated at the edge of the vessel. A second issue was the much greater depth of the vessels, yielding poorer frame rates, hence providing less information from which to rebuild the velocity waveforms. Finally, diastolic velocities in the fœtal phantom remained much larger than zero, such that they were not subject to the effects of the clutter filter seen in the brachial and femoral phantoms, and consequently a source of zero bias was removed from these measurements.

For each phantom studied, a depth dependence is present for both methodologies—it is inferred that this is an artifact of the velocity estimation rather than any changing behaviour of the fluid with increasing depth. Potentially, this effect is due to the thickness of the tissue mimicking material above deeper vessels. The tissue mimic attenuates higher frequencies of ultrasound more than lower frequencies—this increases in an approximately linear manner in the range 1–10 MHz—such that the mean frequency of the travelling pulse is lowered, and that after demodulation the resultant Doppler frequencies are lower also (Evans & McDicken, 2000, p 174–178). This requires that the mean frequency estimator is based on phase domain algorithms (Kasai et al., 1985) rather than time domain methods (Bonnefous & Pesqué, 1986), however, for 'black box' clinical ultrasound machines, it is difficult to discern the exact processing performed on the data, and as such, we are unable to confirm this. The spectral Doppler method is to some extent exempt from the frequency dependent attenuation because the maximum Doppler frequency is dominated by spectral broadening which is much larger than the effect of the attenuation, and also because it uses more pulses to estimate the velocity (Evans & McDicken, 2000, p 185–186).

3.4.2 Example data from a healthy volunteer

Values of the development index taken from the healthy volunteer were close to (or exceeded) unity for the brachial and carotid arteries (Table 3.10). This was not the case in the femoral artery. One can either conclude that flow was not fully established in the femoral artery, or, as an alternative explanation, that this may be an artifact of non-Newtonian behaviour. For shear rates greater than $100\ \mathrm{s}^{-1}$, the viscosity of blood reaches an asymptotic limit (Weaver et al.,

1969), but under low shear conditions, the viscosity increases. This mechanism will produce blunter mean velocity profiles, spuriously suggesting that flow may not be fully developed, when in reality it is affected by thixotropic behaviour. Given that the mean wall shear rate in the femoral artery was less than the asymptotic threshold (40 s^{-1} compared to 100 s^{-1}), and that the shear rate throughout the vessel is usually less than at the wall, it is plausible that flow in this artery would be affected by non-Newtonian behaviour. Consequently, this technique may not be best suited for use in the femoral artery, although a larger population study must be conducted before any firm conclusions can be drawn.

Values of wall shear rate have been estimated in various arteries in the human circulation by several authors. Kamiya & Togawa (1980) proposed that, in accordance with the principle of minimum work (Murray, 1926), wall shear stress should be uniform across all arteries. Evidence to support this argument is scarce, with Dammers et al. (2003) finding significantly different values for mean shear stress in the common carotid and brachial arteries. Values of peak and mean shear rate in the femoral arteries have also been found to be significantly different from those in the brachial and common carotid arteries (Wu et al., 2004). Cheng et al. (2007) reviewed the literature regarding in-vivo wall shear rate and concluded that wall shear stress is neither constant throughout the vascular tree, nor is it constant across species.

Before any rigorous comparison may be made between the technique presented in this paper and other methods that estimate wall shear rate in-vivo, a much larger study must be carried out to establish inter-subject variabilility, rather than intra-subject variation. In the absence of this study, we have compared the single subject values with the literature to confirm the feasibility of the method. Statistical testing has not been carried out with the results, due to the small sample size.

The peak wall shear rate in the common carotid artery of the healthy volunteer, 1191 (29) s^{-1}, agreed well with that measured by Samijo et al. (1997), Tortoli et al. (2006) and Dammers et al. (2003)—1338 (376) s^{-1}, 892 (167) s^{-1} and 1047 (345) s^{-1} respectively. However it is higher than that estimated by Wu et al. (2004), 945 (24) s^{-1}, using MRI. This difference may be due to the rigid wall assumption necessary to satisfy the Womersley solutions; peak WSR occurs at systole, which is also the point of peak distension in arteries, hence any error introduced by the rigid wall method will be maximised at this point.

The mean value of WSR in the common carotid artery, 137 (7) s^{-1}, was consistently lower than values published elsewhere; using ultrasound, Dammers et al. (2003) quote mean wall shear rate to be 359 (111) s^{-1}, while Samijo et al. (1997) found it to be 414 (82) s^{-1} and Tortoli et al. (2006) estimated it as 309 (72) s^{-1}; using MRI, Wu et al. (2004) measured similiar values 333 (61) s^{-1}. The first two ultrasound studies however, use the Shear Rate Estimation System (Brands et al., 1995), which measures shear rate across the arterial diameter and assumes that the *maximum* shear rate is the actual shear rate at the wall. This assumption is maintained by both Tortoli et al. (2006) and Wu et al. (2004). The rigid wall assumption inherent in the Womersley solutions also introduces, to some degree, reverse flow at the walls of the vessel just after peak systole as the vessel diameter is unable to contract, producing negative shear rates. This will reduce the mean WSR, exaggerating the difference between the measured values. These assumptions are likely candidates for the discrepancies between these values. The only other clinical ultrasound system that has been used to estimate mean WSR in the common carotid artery (Forsberg et al., 2000), reports a much larger value than that measured in this study, 414 (155) s^{-1}.

Values of the peak wall shear rate in the brachial artery, 1339 (57) s^{-1}, agreed with those reported by Dammers et al. (2003), 1047 (345) s^{-1}, but were higher than those measured using MRI by Wu et al. (2004), 945 (124) s^{-1}. As in the carotid artery, the difference in peak WSR may arise due to the rigid wall assumption of the Womersley solutions, which will maximise errors at peak arterial distension. The mean WSR in the brachial artery, 96 (25) s^{-1}, was similar to that quoted by both groups, 95 (24) s^{-1} and 194 (101) s^{-1} for the ultrasound and MRI techniques respectively. In the femoral artery, values for the peak, 803 (53) s^{-1}, and mean, 40 (6) s^{-1}, wall shear rate agree well with those reported by Wu et al. (2004)—736 (145) s^{-1} and 130 (58) s^{-1}. That the peak wall shear rate in the femoral artery is not higher than reported by Wu et al. (2004) is interesting—given that the peak WSR in both the carotid and brachial arteries yields a higher value. This is further evidence that non-Newtonian behaviour is more important in the femoral artery as demonstrated by the bluntened value of the development index and the low mean wall shear rate (Table 3.10).

For each artery studied, the pulse wall shear rate and oscillatory shear index were different from that measured by Wu et al. (2004). This is attributable to the rigid wall assumption present in the Womersley equations, and also due to the method used by Wu et al. (2004), which will tend to maximise the wall shear rate, by assuming that peak shear rate is the shear rate at the wall.

For the carotid artery, we have measured a non-zero value for the oscillatory shear index. Flow in the common carotid artery is widely believed to the unidirectional throughout the cardiac cycle (Holdsworth et al., 1999). Although this is not the case in this study, we have already attributed the reduced value for the mean WSR to negative values of WSR that arise due to the rigid walls assumption.

3.5 Conclusion

A simple method to estimate the time-dependent varying wall shear rate in healthy arteries using a clinical ultrasound machine has been developed. In phantoms, the mean wall shear rate was found to be within 14 (8)% of the theoretical value. Mean WSR in the common carotid artery of one healthy volunteer was consistently found to be lower than reported by customised equipment. However, no such differences existed for the mean WSR in the femoral and brachial arteries, and the data required to estimate wall shear rate are readily obtained in a clinical environment, raising the prospect that this technique could be used to study wall shear rate in populations more widely.

Chapter 4
Development of a working fluid for use with particle imaging velocimetry

In the more advanced stages of arterial disease, the peak velocity distal to a stenosis is of clinical interest and estimation of the wall shear rate using the simple method presented in Chapt. 3 is not valid. Doppler ultrasound is used to assess the peak velocity despite errors that are known to affect its accuracy. Measurement of the wall shear rate is difficult, requiring accurate location of the wall position and precise specification of the velocity gradient next to the wall. These issues, that can result in mis-selection of patients for surgery and that are preventing further elucidation of the role of wall shear stress in the progression of atherosclerosis, provide evidence that validation of shear rate and velocity measurements is needed. Chapt. 6 and Chapt. 7 present data obtained using particle image velocimetry (PIV) that is used to validate Doppler ultrasound measurements made in identical flow systems. However, to use PIV in any complex geometry, it is important to minimise refractive errors at the interface between the medium and fluid. Consequently, the aim of this chapter was to develop a fluid for use with PIV. This fluid shall subsequently be used with the flow models presented in Chapt. 6 and Chapt. 7.

4.1 Introduction

Optical techniques such as laser Doppler anemometry (LDA) and particle image velocimetry (PIV) have often been used in the experimental study of blood flow dynamics to accurately measure hæmodynamically significant variables such as the wall shear stress, the size and location of recirculation zones, and the influence of geometry on the prevailing fluid dynamics (Asbury et al., 1995; Bale-Glickman et al., 2003; Friedman et al., 1986; Ku et al., 1985*b*,*a*; Zarins et al., 1983). These variables can be estimated in-vivo using existing non-invasive methods such as magnetic resonance imaging and Doppler ultrasound (Reneman et al., 2006; Struijk et al., 2005; Oshinski et al., 1995; Brands et al., 1995; Cheng et al., 2002), but the measurement process is challenging and is often affected by artifacts and large errors. Optical techniques

benefit from high resolution and accuracy, which can provide gold standard and calibration data to compare with measurements taken using medical systems.

PIV measures the velocity field over the full field of view by correlating the displacement of seeding particles in two successive photographic frames taken by a high speed camera. A fuller description of PIV is given by Westerweel (1997) and Raffel et al. (1998). In order to ensure accuracy with PIV, it is important that the refractive index of the fluid is the same as that of the medium through which it flows. Any mismatch between the indices can produce spurious images via the lensing effects of refraction. This is particularly important when dealing with flow models in which there is curvature—either due to the presence of a stenosis designed to mimic disease in an artery or in physiologically accurate, arterial geometries which are highly irregular and non-planar (Watts et al., 2007). For such models, mathematical correction for any distortion would be extremely difficult.

The primary criteria for the suitability of a particular fluid for use with PIV is its refractive index—it must match that of the vessel. Optical models can readily be engineered from glass and perspex—with a refractive index close to 1.5—but they are largely restricted to geometrical shapes or hand blown pieces. The study of arterial hæmodynamics involves complex, non-planar three dimensional geometries. Fabricating models with appropriate geometries is almost impossible using glass, which would fracture on removal of the core mould. Silicone gel is a suitable replacement which can be poured over a mould as a liquid but which sets to a firm gel, allowing removal of cores; it has a refractive index of 1.41.

The refractive index of a fluid can be adjusted through the use of sodium iodide (NaI) (Budwig, 1994; Narrow et al., 2000), unfortunately, such solutions discolour with exposure to light as crystals of iodide form inside the fluid. This effectively limits the working life of the solution to hours and days, rather than weeks, and can irreprovably damage optical flow phantoms by staining the inside of the flow channel. Sodium iodide is also an expensive commodity; these factors can make the use of such fluids prohibitive.

As an alternative to the use of iodides, Nguyen et al. (2004) developed a method allowing the simultaneous adjustment of kinematic viscosity and refractive index. Controlling temperature allows fine adjustment of the refractive index and viscosity, however, in practice this method requires that the entire fluid loop be submerged in a heat bath. This is impractical, since align-

ment of optical components requires precise adjustment, and lenses must be kept clear from obstruction—so the growth of algæ would present significant problems.

With these problems in mind, this chapter aims to develop a simple solution suitable for use with PIV in moulds cast from silicone. The refractive index must match that of silicone (1.410) and the fluid must not damage the flow phantoms in which it is used. To investigate the effect that a solution with a poorly matched refractive index can have on image quality, a simple analysis of the optical path of the laser light using geometric optics in a typical in-vitro geometry was also performed.

4.2 Materials and methods

4.2.1 Optical path analysis of scattered light from a seeding particle

A schematic diagram of a typical experimental setup, shown in cross section, for a circular lumen, is shown in Fig. 4.1. The laser light enters vertically on the left hand side, and is scattered by a spherical particle. Light is scattered by the particle in all directions, but only light travelling perpendicularly to the camera lens is focussed on the sensor. Considering only the light captured and correctly focussed by the optics, an error is introduced in the apparent position of the particle in the plane of the camera lens, if $n_f \neq n_m$. The error, δy, can be expressed as

$$\delta y = p \tan \alpha_3, \tag{4.1}$$

where δy and p are distances defined in Fig. 4.1. The angle, α_3, is defined as

$$\alpha_3 = \alpha_2 - \alpha_1. \tag{4.2}$$

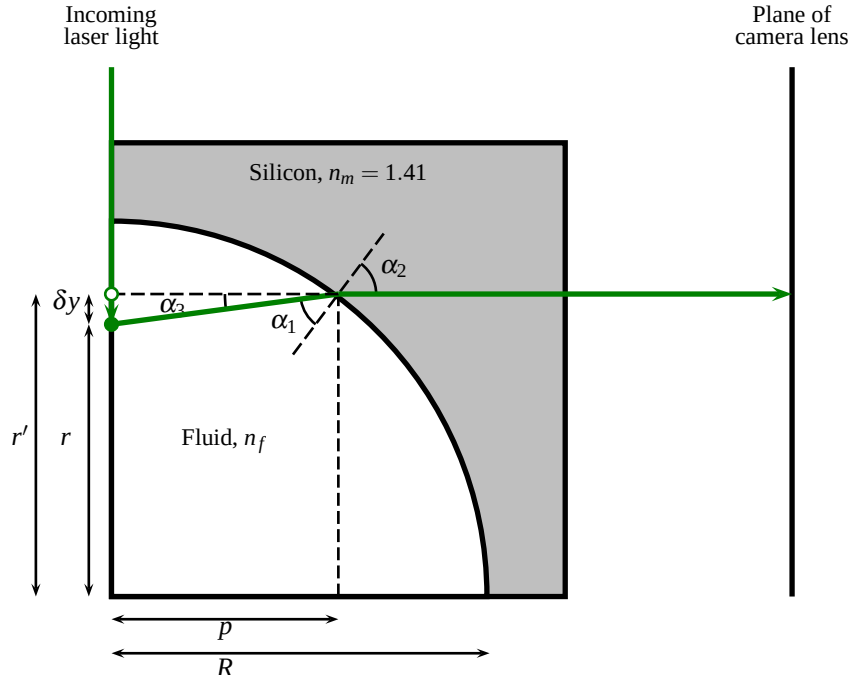

Figure 4.1: *Positional error in* PIV. *If $n_f = n_m$, no deviation will occur at the lumen/model interface and δy will be zero. Otherwise, the particle will spuriously appear at r', rather than at r.*

Simple geometry defines the angle α_2, while Snell's law (Fishbane et al., 1996) yields an expression for α_1:

$$\sin\alpha_2 = \left(1 - \frac{r'}{R}\right); \tag{4.3}$$

$$\sin\alpha_1 = \frac{n_m}{n_f}\sin\alpha_2. \tag{4.4}$$

In Eq. (4.3) and Eq. (4.4), r' and R are distances defined in Fig. 4.1, with n_m and n_f the refractive indices of the model and blood analogue respectively. Finally, some more geometry defines p in Eq. (4.5),

$$p = R\cos\alpha_2. \tag{4.5}$$

Thus, the full expression for δy is given by Eq. (4.6),

$$\delta y = R\cos\alpha_2\tan\alpha_3. \tag{4.6}$$

4.2.2 Design of a fluid suitable for particle image velocimetry

NaCl and glycerol were measured out into single solutions with concentrations ranging from 0%–20% (w/w) for sodium chloride and 0%–30% (w/w) for glycerol. After the NaCl had completely dissolved, the kinematic viscosities of the solutions were measured with a Cannon-Fenske viscometer (Sigma-Aldrich, Missouri, USA) and the refractive indices under white light with an Abbe 60 refractometer (Bellingham and Stanley, London, UK). All measurements were conducted at room temperature (23°C).

Use of the viscometer is described is Sect. 3.2.2 and by British Standard BS188. An Abbe refractometer is used to measure the refractive index of a fluid sample that is constrained between two refracting prisms (Fig. 4.2). The surface of the top prism is roughened, such that light is scattered in all directions. The refractive index of the lower prism is chosen to be large, typically greater than 1.7. This allows measurements of refractive index up to this value. Applying Snell's Law (Eq. (4.4)) and observing that the largest angle of incidence is fixed by the geometry of the refractometer (θ_i) in Fig. 4.2), it is clear that light passing through the prisms and fluid will be refracted, but only to a certain limit. This produces a light region—where light has been refracted at all angles due to a range of incident angles—and a dark region. The boundary between the light and dark regions is used to determine the refractive index of the fluid sample.

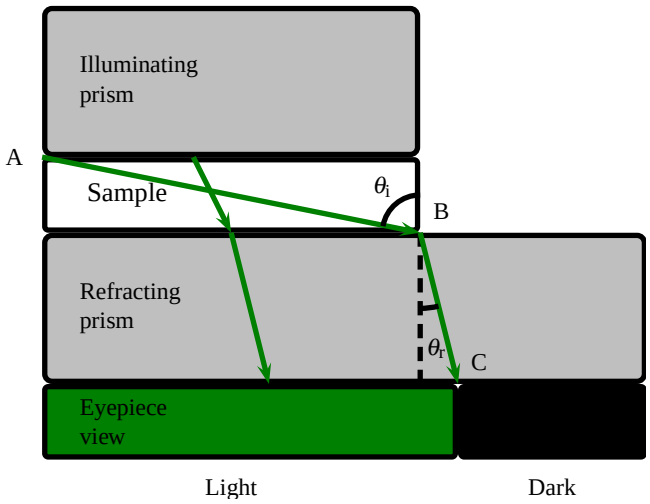

Figure 4.2: *Refracting prisms in an Abbe refractometer.*

In reality, since refractive index is a function of wavelength, this boundary is not a crisp line when Abbe refractometers are used with white light (Fig. 4.3a). Consequently, the Abbe 60 refractometer has a further prism, called a compensating prism, that can be adjusted using a

dial to offset the wavelength dispersion. Correct use of the compensator restores the sharp boundary between the light and dark regions (Fig. 4.3b). Having obtained a sharp interface, the main hand-wheel of the instrument is adjusted to align the boundary with the cross hairs; looking through a second eyepiece allows the refractive index to be read from a scale.

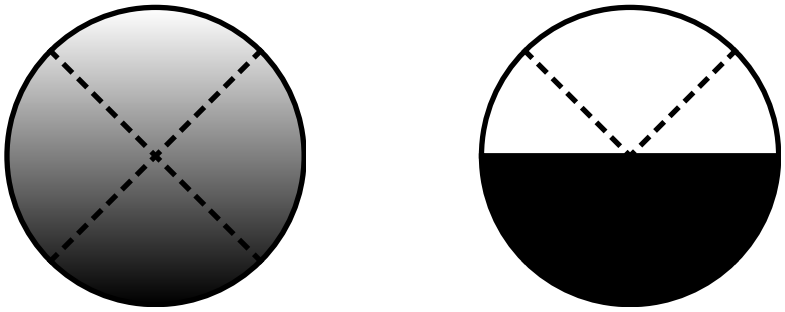

(a) Before compensation. **(b)** After compensation.

Figure 4.3: *Correct use of the compensating prism with an Abbe refractometer.*

To investigate the lifetime of the fluid, the kinematic viscosity and refractive index were measured at three points in time: within two days of fabrication; at one month old; aged three months. Any discolouration of the fluid (as occurs with NaI based solutions) was also noted by inspection.

4.3 Results

4.3.1 Optical path analysis of scattered light from a seeding particle

The fractional error in the apparent scatterer position, $\delta y/r'$, remained constant for around 90% of the vessel lumen (Fig. 4.4). A difference of 1% in the refractive indices gave rise to a positional error of 1%. For particles close to the vessel wall, the error reduced to zero if the fluid refractive index was greater than that of the wall. For fluids with a refractive index inferior to that of the model, the positional error doubled, before eventually becoming undefined as light is internally reflected rather than refracted at the lumen/wall interface.

4.3.2 Design of a fluid suitable for particle image velocimetry

The refractive index of the test fluids varied linearly with glycerol concentration (Fig. 4.5a); the kinematic viscosity varied in an approximately quadratic manner as a function of glycerol

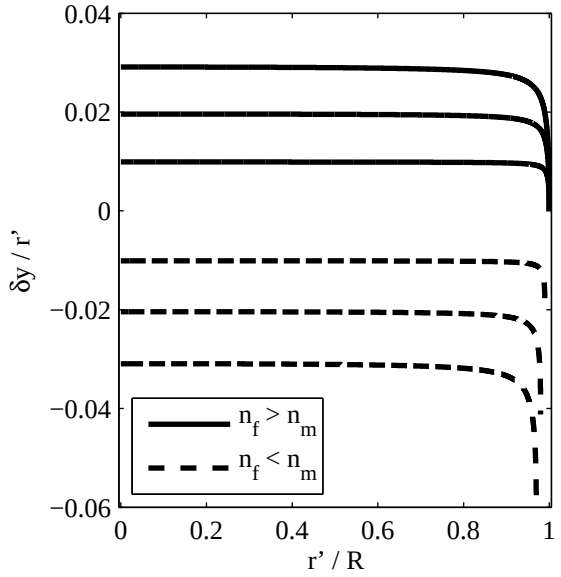

Figure 4.4: *The relative error in δy in Fig. 4.1, for values of $n_f = \{0.97, 0.98, 0.99, 1.01, 1.02, 1.03\}n_m$ versus the apparent position of the scatterer. The data for $n_f < n_m$ are truncated due to total internal reflection. The case $n_f = n_m$ is not shown, as no error occurs when the refractive indices match, hence $\delta y = 0$ for all values of r'.*

concentration (Fig. 4.5b). Increasing the salt concentration increased both the refractive index and the viscosity, although as the concentration approached the saturation point it became difficult to ensure that all the salt had dissolved. The co-efficients for the best fit lines are listed in Table 4.1.

Extrapolation of these data predict several possible concentrations of NaCl and glycerol that match the refractive index of the silicone, 1.410. The practical limit is the saturation point of H_20 (35.7%) and glycerol (around 7%) with NaCl. Using the highest NaCl concentration (15%), the data predict a suitable solution that is 37.1% (w/w) glycerol and 15% (w/w) NaCl. Good agreement was observed between the predicted and measured refractive index of this solution, although the measured viscosity was 16% higher than the approximated quadratic model (Table 4.2). When filling the flow phantoms (which are described in Sect. 5.2.1.2) with the fluid, the fluid/solid interface was not visible, confirming that the refractive indices were well matched (Fig. 4.6).

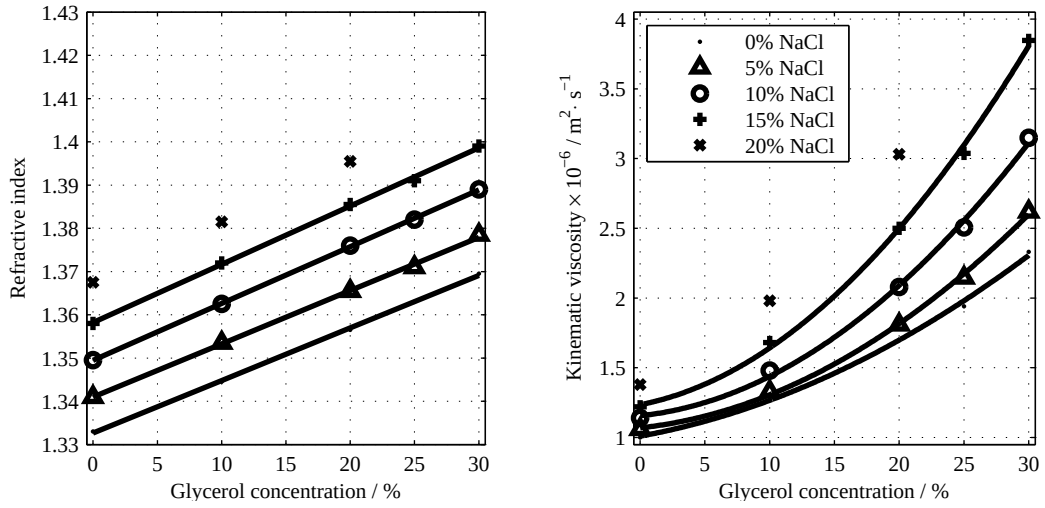

(a) Refractive index. **(b)** Kinematic viscosity.

Figure 4.5: *Variation of refractive index and kinematic viscosity with NaCl and glycerol concentration. The NaCl= 20% data are truncated due to saturation. (The legend applies to both figures.)*

No changes were measured in either the kinematic viscosity or refractive index of the solution with age, nor was any discolouration apparent by inspection. It is concluded that the lifetime of the fluid is greater than three months.

NaCl concentration	Refractive index n $\alpha_0 + \alpha_1 x$		Kinematic viscosity ν $\beta_0 + \beta_1 x + \beta_2 x^2$		
	$\alpha_0 \times 10^{-3}$	$\alpha_1 \times 10^{-3}$	β_0	$\beta_1 \times 10^{-2}$	$\beta_2 \times 10^{-3}$
0	1.21	1.33	1.00	1.69	0.88
5	1.23	1.34	1.07	1.00	1.37
10	1.31	1.35	1.16	0.97	1.85
15	1.35	1.36	1.24	1.81	2.26
20	n/a	n/a	n/a	n/a	n/a

Table 4.1: *The coefficients for the best fit lines shown in Fig. 4.5a and Fig. 4.5b.*

4.4 Discussion

A geometric ray analysis of the optical path traversed by light scattered by seeding particles has been carried out. This analysis showed that failure to accurately match the refractive index of a fluid to that of the surrounding medium (for a circular lumen) produces errors in the apparent position of the particle—the relative error in the particle position can be up to twice the error in

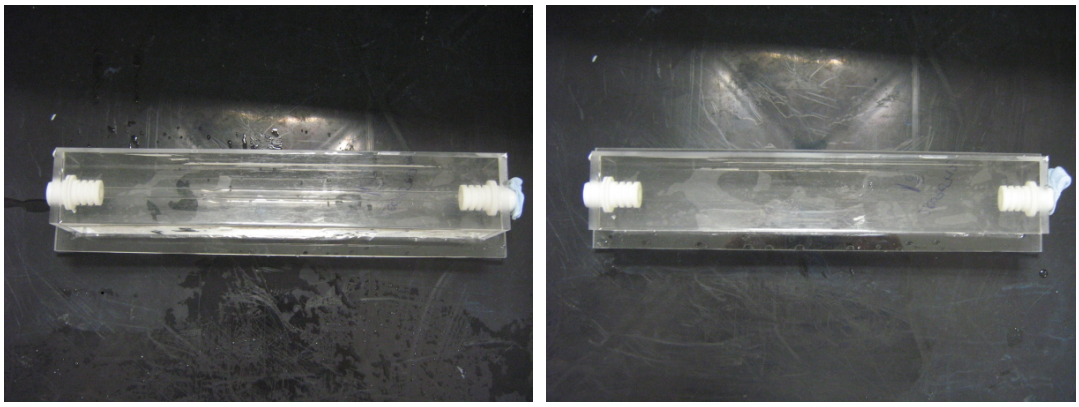

(a) Filled with water. **(b)** Filled with the new PIV fluid.

Figure 4.6: *Photographs of one of the stenosis models described in Chapt. 5 filled with different working fluids. When the model is filled with the new solution, the interface between the fluid and solid becomes invisible.*

	Predicted		Measured	
Fluid	n	$\nu \times 10^{-6}/m^2s^{-1}$	n	$\nu \times 10^{-6}/m^2s^{-1}$
37.1% glycerol, 15% NaCl	$1.410^{\dagger}$	$5.0^{\dagger}$	$1.410 \pm 0.0005^{\ddagger}$	$5.8 \pm 0.1^{\ddagger}$
46% glycerol, 14% NaCl	$1.41^{\star}$	$5.7^{\star}$	$1.423 \pm 0.001^{\ddagger}$	$9.7 \pm 0.2^{\ddagger}$

Table 4.2: *Predicted and measured values for refractive index and kinematic viscosity of two fluids: as extrapolated from data in Table 4.1* †*; as quoted by Sivanesan et al. (1999)***; as measured*‡.

the mismatch of the fluid refractive index. The solution presented in the chapter is able to match the refractive index of the silicone to the resolution of the instrument used, thus reducing the potential positional error to less than 0.1%. Minimising this error is of particular importance in the measurement of velocity gradients, especially in the vicinity of the vessel wall (Bale-Glickman et al., 2003; Reneman et al., 2006).

Whilst this analysis is simplistic, in that it neglects the lobular nature of Mie scattering (van der Hulst, 1981), it demonstrates that correction of the refraction effect is not trivial, given that the error varies with particle position. In anatomic vascular phantoms, any error introduced due to refraction at interfaces will necessarily be much harder to correct, due to the non-planar nature of such vessels.

A simple, empirical and inexpensive method has been developed to control the refractive index of a fluid from 1.333 to 1.473. This solution has a long lifetime, which does not discolour

like iodide based solutions (Narrow et al., 2000) and experiments can be performed at room temperature (23°C), negating the need for a large heat bath (Nguyen et al., 2004).

Common glass ($n = 1.52$) and perspex ($n = 1.488$) are frequently used to make flow phantoms for PIV. However, these materials are not well suited for fabricating models of the complex geometries that occur in the human vasculature, particularly features such as the carotid bulb and bifurcations. Silicone gel is a more suitable material as it can be poured over a low melt core, which can then be removed. Dow-Corning Sylgard 184 is such a silicone gel with refractive index 1.410. The proposed solution matches this value, and as such represents an improvement over that proposed by Sivanesan et al. (1999). If this fluid is used as a blood analogue, it represents a further improvement as the kinematic viscosity is a better match to whole blood than that of Sivanesan et al. (1999), hence minimising the amount of dynamic scaling necessary.

4.5 Conclusion

A solution has been developed that allows particle image velocimetry to be performed with silicone gel with a refractive index of 1.410. The refractive index may be tuned from 1.333–1.473, allowing the solution's use with other materials. The error introduced due to a mismatch between the refractive indices of the fluid and the modelling material has been investigated—the apparent position of scattering particle can be in error by up to 2% for a 1% difference in refractive index.

Chapter 5
Development of a dual phantom flow validation system

In developed stages of arterial disease, Doppler ultrasound is used to categorise patients for surgery based upon the maximum velocity measurement. However, such velocity measurements suffer from large errors and are consequently in need of validation. The role of the wall shear stress in arteries is not fully understood, partly due to the difficulties associated with its measurement. In Chapt. 3, a simple technique was developed to estimate the wall shear rate in healthy arteries. Although this method may be useful to allow the estimation of normal values of shear in populations, it is unsuited for use in diseased arteries in patients.

In this chapter, paired validation flow systems are developed and the performance of the systems is characterised. One system uses particle image velocimetry and is considered to be a gold standard, the other uses a dual beam Doppler system. These systems are used in subsequent chapters to quantify the accuracy of velocity and shear rate measurements made with Doppler ultrasound in situations where the direction of flow cannot be assumed.

5.1 Introduction

The selection of patients for endarterectomy relies on the accurate assessment of arterial diameter (ECST collaborators, 1998; Barnett et al., 1998). Angiography is the clinical gold standard for quantification of carotid stenosis, but estimation of maximum blood velocity by Doppler ultrasound is the preferred approach, being both non-invasive and more economic (Bluth et al., 1988; Robinson et al., 1988; Spencer & Reid, 1979). However, in patients with significant stenosis, such velocity estimates are subject to large errors since it is typically only possible to measure one component of velocity and it is difficult to predict the true direction of blood motion. This difficulty in specifying velocity direction is compounded by asymmetric broadening of the received Doppler signal (Fish, 1986, 1991; Hoskins, 1996).

Near-zero wall shear stress, in the presence of atherosclerotic risk factors, promotes endothelial dysfunction and plaque development (Slager et al., 2005*a*). Vascular remodelling is able to maintain the low shear stress conditions as plaques develop, but ultimately, as the lumen area reduces, the wall shear stresses around plaques change dramatically, sometimes with long-term destablising effects (Slager et al., 2005*b*). Non-invasive measurement of the wall shear stress is extremely difficult, and current techniques are generally only applicable in broadly straight, disease-free arteries (see Chapt. 3).

Using an in-vitro flow phantom approach, attempts to validate clinical Doppler ultrasound measurements in stenotic vessels have been precluded by two main issues. The choice of materials is restricted to those with acoustic properties similar to soft tissue. Acceptable acoustic tissue mimics are often so weak that they rupture even at low stresses (Poepping et al., 2002) or an increase in the tensile strength is offset by a reduced tackiness, resulting in leaking at the interface between the TMM and external plumbing (Meagher et al., 2007). Consequently, the accuracy of Doppler ultrasound measurements made in complex geometries which can generate large velocity gradients is unknown.

Doppler ultrasound velocity measurements are used to pre-screen patients for angiography. However, in complex geometries, the accuracy of these measurements is unknown, which has implications for the value of the clinical measurements. The wall shear stress is hypothesised to play a large role in the development and destabilisation of atherosclerotic plaques, but its non-invasive measurement remains difficult. In this chapter, parallel flow systems are developed with a series of idealised cosine stenosis geometries. One system allows the collection of assumed gold standard data using particle image velocimetry. The other system is constructed using materials that are acoustically equivalent to soft tissue and blood, enabling a clinical Doppler ultrasound scanner to obtain velocity measurements. The accuracy of velocity and wall shear rate measurements in the inlet region are compared to assess the performance of each system.

5.2 Materials and methods

5.2.1 Stenosis models

5.2.1.1 Stenosis rods

Brass rods of 8 mm diameter were machined on a computer controlled lathe to a series of progressively tighter cosine shaped stenosis geometries (Fig. 5.1a). The rods were constructed in two sections, with the throat of the stenosis forming the join between the halves. The rods were manufactured by Pentland Precision Engineering Ltd (Edinburgh, UK) out of a copper and zinc alloy with a steel pin in the stenosis throat to reinforce the junction between each half (Fig. 5.1b). To enable comparison of measurements with other values taken from the literature, the models had a cosine based geometry, such that in normalised co-ordinates they were equivalent to models used by Ahmed & Giddens (1983*a*). The geometry was defined by Eq. (5.1),

$$r(x) = \frac{D}{2}\left\{1 - \frac{1}{2}\kappa\left[1 - \cos\left(\frac{x\pi}{D}\right)\right]\right\}. \tag{5.1}$$

In Eq. (5.1), $r(x)$ is the radius as a function of axial distance x, D is the inlet diameter—which was 8 mm—and κ was the degree of stenosis, expressed in the range 0–1, for example, for a 60% stenosis by diameter, κ took a value of 0.6. For convenience, It is useful to normalise the axial co-ordinate by the inlet diameter, such that

$$Z = \frac{x}{D}, \tag{5.2}$$

where x is the axial distance from the centre of the stenosis. This allows comparison with measurements taken in scale models of the same geometry.

5.2.1.2 Stenosis models for use with particle image velocimetry

The stenosis models used for PIV were made using a simple lost core technique. The models consisted of a case made from perspex, with connectors fitted to holes cut in either end, through which the stenosis rods extended both into and out of the models. (The extension of the rods out of the case through the connectors allowed the removal of the rods after casting.) With the rods in place, silicone rubber was prepared and poured in liquid form into the case. After the

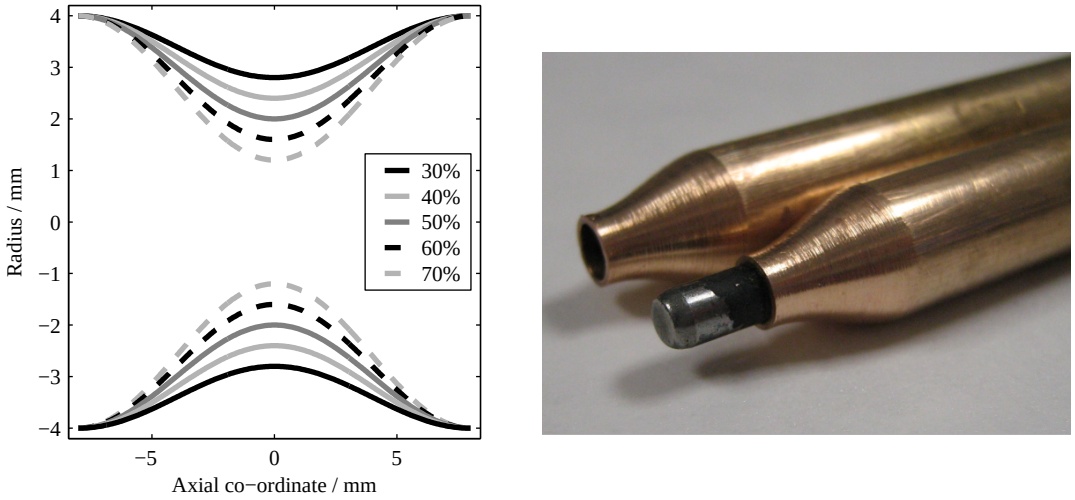

(a) The geometries of the stenosis rods used in this study; the degree of stenosis is based on the diameter reduction from the inlet.

(b) Photograph of the two halves that together formed the 50% stenosis core.

Figure 5.1: *The stenosis geometries used in this study.*

silicone had cured, the rods were withdrawn, leaving a continuous lumen inside the transparent model. Fig. 5.2 shows a completed model, prior to the removal of the core rods.

The models used in this study were fabricated using optically clear silicone rubber (Sylgard 184, Dow Corning, Barry, UK) in the Department of Clinical Engineering at the University of Liverpool. The models were constructed from perspex sheets that were assembled into boxes and stuck together using super glue for the end walls and silicone sealant for the side panes. The side panes were designed to be removable to ensure minimal distortion of the laser light sheet on entering the silicone. The narrow end walls had circular holes cut in them, allowing the connectors to be fixed in place. The connectors were made from Delrin, with the inner lumen machined to the same diameter as the brass rods. To prevent the connectors from leaking under high pressures, a series of ridges was cut in the delrin, which helped it bond with the silicone and produce a more robust seal.

With the rods in place, the silicone rubber was prepared according to the instructions, degassed to remove air bubbles, and poured into the case. The rubber was left to set in a cool oven (around 40°C) for four hours. After the silicone had set, the rods were withdrawn.

Unfortunately, production of the stenosis models does not produce identical replicas of the core rods (or even linearly scaled models). The casting process resulted in imperfections at the throat

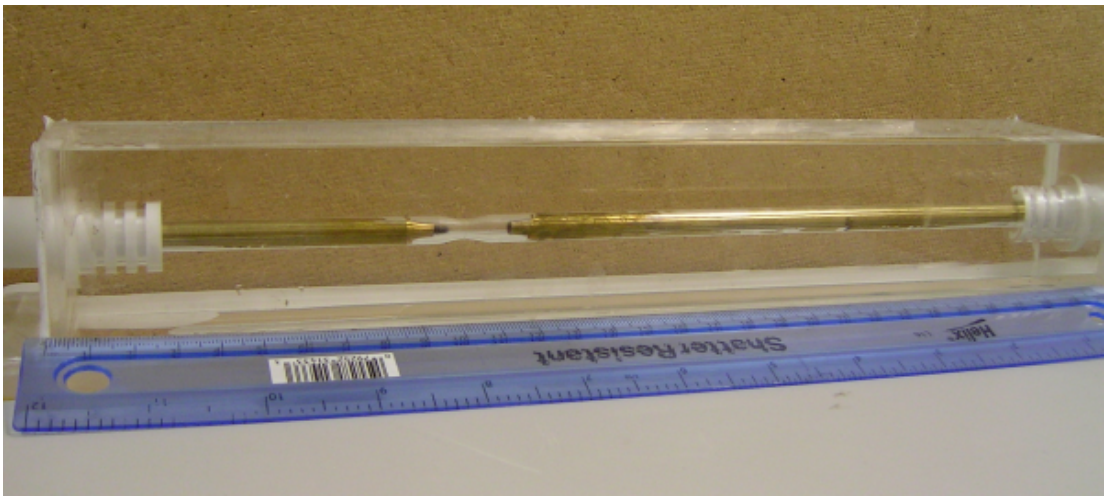

Figure 5.2: *A completed stenosis model for use with* PIV*, before removal of the core rods.*

of the stenosis, where the core rods joined one another (Fig. 5.3). On withdrawing the rods, a small lip remained in some of the models. Removal of this lip was difficult. The problem was exaggerated by the high tensile strength of the silicone rubber, requiring the use of stiff brushes. Some lips proved impossible to remove (Fig. 5.3b), while removal of the lip produced other effects, such as minor bulges at the stenosis throat (Fig. 5.3e).

The final size of the flow channel for each model was assessed from photographs. Images were captured from the PIV system (described in Sect. 5.2.2) at the desired flow rate. The wall positions were marked by hand on the mean (time-averaged) image from several data sets, ignoring imperfections at the stenosis throat (Fig. 5.13). To calculate the degree of stenosis of each model, κ, Eq. (5.3) was used,

$$\kappa = 1 - \frac{D_0}{D_{-1}}, \tag{5.3}$$

where D is the lumen diameter, and the subscript refers to the normalised co-ordinate, Z, defined in Eq. (5.2) and Fig. 6.1. Thus, D_{-1} is the lumen diameter at $Z = -1$.

5.2.1.3 Stenosis models for use with Doppler ultrasound

The stenosis models used with Doppler ultrasound were fabricated using a lost core technique. The brass stenosis rods were placed inside the perspex boxes previously described in Sect. 3.2.2. Acoustic equivalent tissue mimicking material (Teirlinck et al., 1998) was subsequently poured

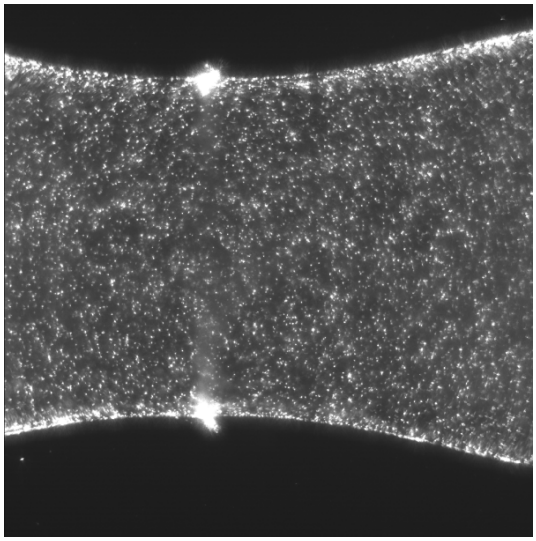

(a) 30%

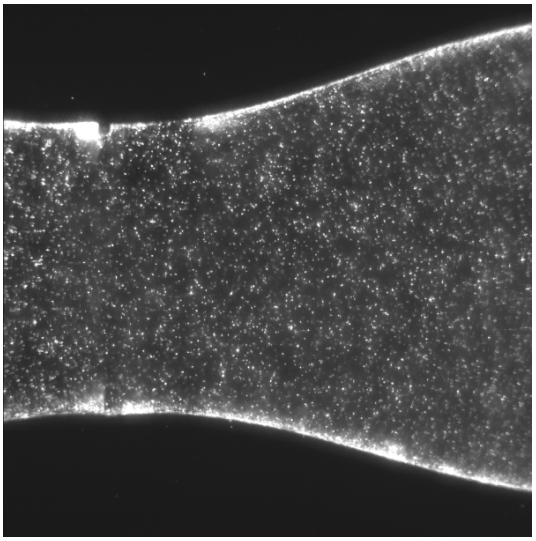

(b) 40%

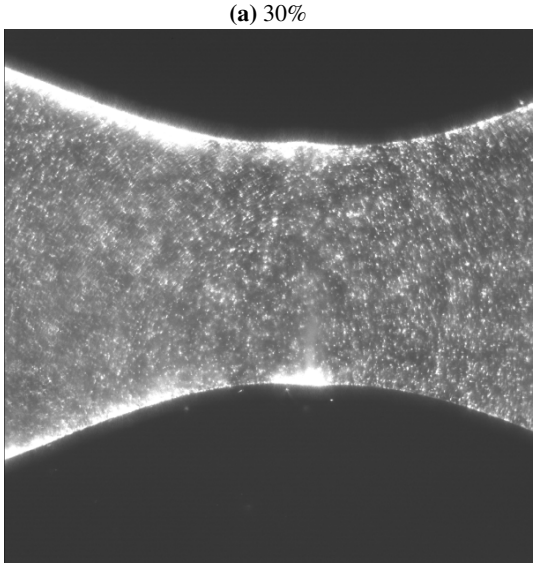

(c) 50%

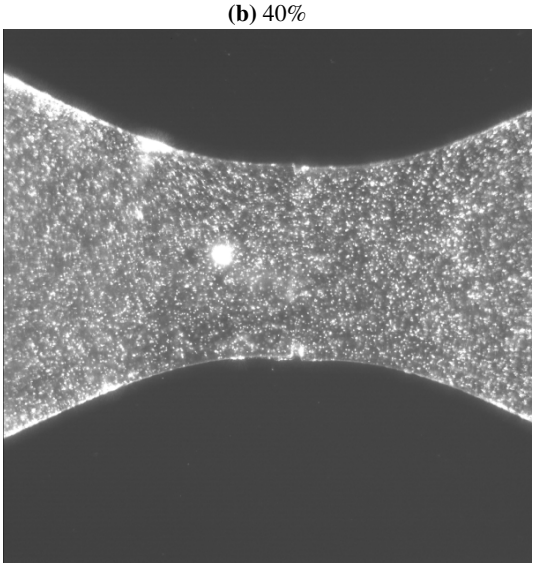

(d) 60%

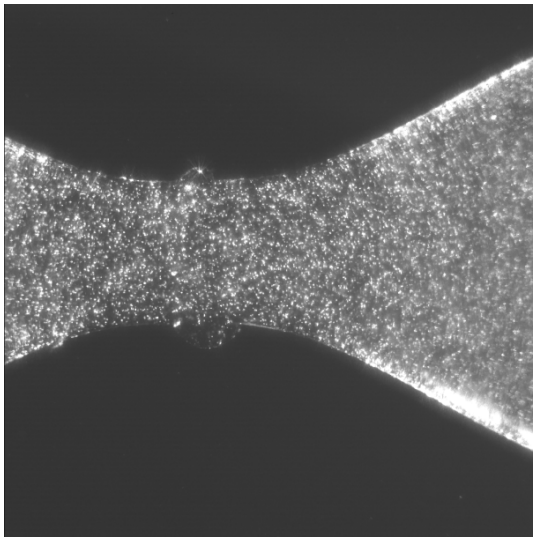

(e) 70%

Figure 5.3: *Imperfections in the* PIV *models at the stenosis throat. (Each photograph has a slightly different scale.)*

over the joined rods until the level of the liquid agar covered the stenosis rods to a depth of 10–15 mm. After the TMM set, the rods were withdrawn from either end of the phantom boxes, leaving a flow channel inside. To preserve the acoustic properties of the phantoms when not in use, they were covered with a glycerol/water solution (9% w/w) and cling film, to prevent evaporation.

The casting process produced lip effects at the stenosis throat in the ultrasound models. However, removal of the lip was much easier, since the tissue mimicking material is rather brittle. Simply replacing the casting rod after withdrawing it and rotating was usually enough to remove the imperfection. The integrity of the stenosis was maintained by guiding the process using the ultrasound scanner. For cases where this did not work adequately (diagnosed by recirculation and flow separation in the stenosis throat) the model was discarded and refabricated.

B-mode images were used to assess the geometry of the ultrasound stenosis models. Images were acquired proximal to, distal to, and at the site of the stenosis in each model under steady flow conditions. A video was stored by the ultrasound machine and transferred offline for analysis. The edge of the lumen was marked by hand (Fig. 5.13). To quantify the degree of stenosis of the model, lines of interest were marked across the lumen by hand at $Z = -1, 0, 1$. For each location, the transducer was laterally centred upon the line of interest to optimise the resolution (Murray, 2004). The final diameter was calculated by marking profiles and fitting Gaussian curves at the wall/lumen interface as described in Sect. 3.2.4.3.

5.2.2 Particle image velocimetry

5.2.2.1 Fluid circuit and flow conditions

The working fluid used in the fluid loop is described in Chapt. 4. To ensure that it remained at a constant temperature and hence prevent changes to the viscosity, an air-conditioning unit and a water bath containing ice was used. The temperature of the fluid was constantly monitored using a mercury thermometer; measurements were only taken if the temperature of the reservior was in the range 21–23°C.

The completed models were connected into a flow circuit driven by a magnetically coupled gear pump (Micropump model 132, Michael Smith Engineers Ltd, Surrey, UK) powered by an electric motor (M586TE, McLennan Servo Supplies Ltd, Surrey, UK) connected to a bench top power supply. The flow rate through the circuit was measured with a graduated cylinder

and a stopwatch. The driving voltage through the pump was monitored with a multimeter; this enabled previous flow rates to be recovered without having to repeat flow rate measurements. The flow rate in the fluid loop was set such that the nominal Reynolds number ranged from 200–1000 for the 50% model. For the remaining models the nominal Reynolds number was set to 500.

To ensure that flow entering the models was fully developed, rigid perspex pipes one metre in length, with the same internal diameter as the lumen of the silicone models (8 mm), fitted directly into the delrin connectors at the model inlet and outlet. To minimise leakage at the model, the outer diameter of the perspex tubes was machined to fit snugly into the connectors. The perspex pipes were connected to the gear pump using nalgene tubing (Nalge (Europe) Ltd, Hereford, UK)—this tubing also formed the return loop for the fluid to a reservoir. Cable ties fastened the tubing at all fixings to minimise leakage.

5.2.2.2 Imaging optics

Fifty image pairs were collected upstream of the stenosis in each model. For the 50% model, data for each flow rate were also collected. The measurement process was repeated three times. Each set of 50 image pairs required around 100 Mb of hard disk storage.

In order to observe the motion of the fluid, polyamide seeding particles (Dantec Dynamics Ltd, Bristol, UK) were added to the circulating fluid at a concentration of approximately one and a half level teaspoons of particles (7.5 mL) for 3 kg of fluid. These particles have a density of 1140 kg·m^3 and the quoted size distribution ranging from 20–22 μm. However, under inspection with a microscope, the mean particle size was determined to be around 10 μm, with only the largest particles having diameters greater than 20 μm. The settling velocity, u_∞, was less than 0.1 mm·s^{-1}, based on Eq. (2.37).

To improve the homogeneity of the scatterer size distribution, the fluid/particle solution was passed through a 300 μm sieve. Large clumps of particles scatter more light and can saturate the CCD—which can even burn out pixels—as well as scattering light with a non-Gaussian intensity profile, which would increase the effect of peak locking.

The light sheet was produced using a dual cavity pulsed neodymium-doped yttrium aluminium garnet (Nd:YAG) laser (New Wave Solo 200XT, Dantec Dynamics, Bristol, UK) operating at a wavelength of 1064 nm. The laser beams from both cavities share an optical path, and pass

through a frequency doubling unit such that the output from the laser aperture has a wavelength of 532 nm. The use of a dual cavity laser allowed delays between both images that are not tied to the natural frequency of the laser cavity. For example, typical repetition rates for copper vapour lasers are around 50 kHz, tying the minimum pulse separation to 20 μs. The magnitude of the jitter present in the trigger signals was measured with a digital oscilloscope over a logarithmic range of Δt and was on the order of tens of nanoseconds. The laser beam passed through two lens modules (80X62 cylindrical lens and 80X63 light sheet thickness module, Dantec Dynamics Limited, Bristol, UK) that allowed control of the divergence and thickness of the light sheet. The light sheet in the vicinity of the stenosis models was around 400 mm wide and around 0.5 mm thick.

Pairs of photographs were captured using a high speed digital camera (Kodak Megaplus ES1.0, Dantec Dynamics, Bristol, UK) with a CCD sensor with 1008×1016 pixels. A standard Nikor 50 mm lens was used to form an image of the light scattered by the tracer particles. Photographic bellows (Cameratiks, Edinburgh, UK) were used to increase the magnification of the system. The camera was fitted to a 3D traverse (LG Motion Limited, Basingstoke, UK), which allowed control of the camera position to 0.2 mm (Fig. 5.4). A magnetic spirit level ensured that the camera was aligned vertically, minimising any distortion of the flow field due to refraction at the interface of the phantom.

The camera and laser were controlled using a hardware processing unit (Flowmap 2100, Dantec Dynamics, Bristol, UK) designed for PIV. The Flowmap processor communicates with a personal computer (PC) running Windows XP (Microsoft Corp, Seattle, WA, USA) on a private network, using Flowmanager 4.71 (Dantec Dynamics, Bristol, UK). The processing unit controls the Q-switching and flashlight charging of both cavities of the laser using TTL signals. The camera is connected to the processing unit with a high speed serial connector.

5.2.2.3 Image analysis

In order to convert pixels into real world measurements, a photograph of a rule was taken at the same focus setting as for the captured images of the tube (Fig. 5.5a). To do this, the rule was placed on top of the silicone models and the camera was moved away from the phantom using the traverse system. This typically required 35–38 turns, depending on the focus settings. This was repeated for every data acquisition.

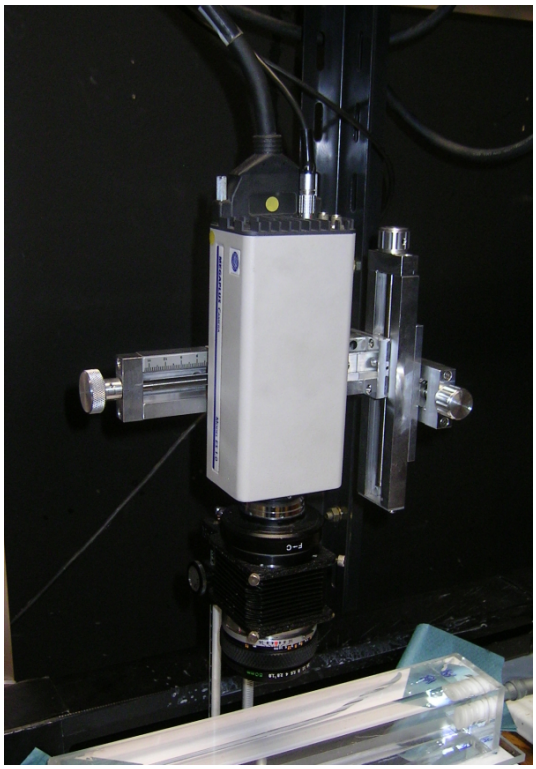

Figure 5.4: *The imaging optics for* PIV.

To obtain a conversion factor from pixels to metres, the captured photograph was analysed using Matlab 2006a (The Mathworks, MA, USA). First, the region of the image containing the graduations was marked by the user (Fig. 5.5a). This region was analysed on a row by row basis: high frequency noise in each row was removed with a one dimensional median filter, and a threshold was applied to the gradient of the filtered signal. The locations of the samples which exceeded the threshold were stored, and their separation corresponded to the distance between the leading edges of the graduating marks on the rule. A further threshold was applied to these separation data to remove outliers, and the remaining data points were plotted on a histogram. A Gaussian curve was fitted to the histogram (Fig. 5.5b), with the mean corresponding to the mean separation between the rising edges of successive graduations of the rule.

The image pairs were analysed using the open source MatPIV toolbox (version 1.6.1, Sveen (2004)). MatPIV is a cross-platform, open-source toolbox for analysing PIV images that runs in the Matlab environment. Although Dantec's Flowmanager is capable of using a variety of methods for analysing the images acquired, the exact nature of the analysis is hidden from the user and methods such as the median filter are missing from the software. To suppress spurious

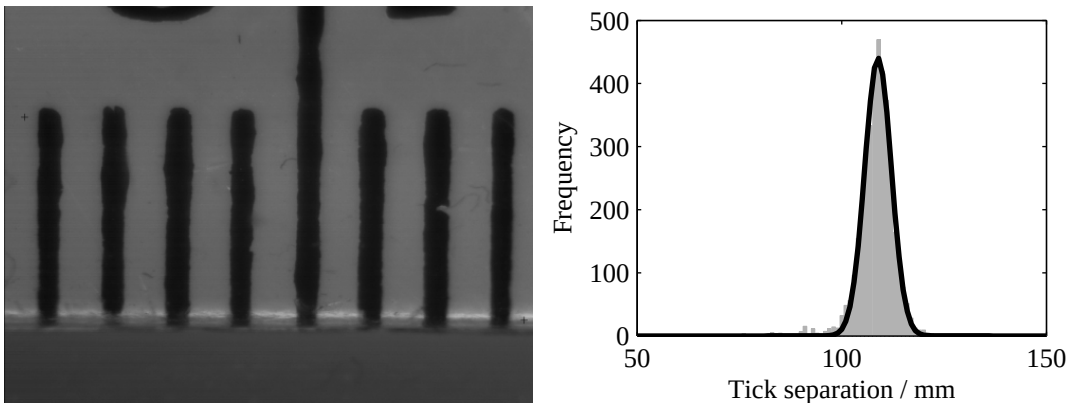

(a) An example image of a rule, used to convert pixels into real world measurements for PIV.

(b) A histogram of the number of pixels separating each tick for the image shown in Fig. 5.5a.

Figure 5.5: *Calculation of the scaling factor for* PIV.

vectors outside of the flow area, the lumen was marked by hand. Pixels outside the lumen were set to the mean pixel value for each image (which was subtracted from all IAs before cross-correlation analysis due to the assumption of homogeneity Eq. (2.45)).

As an independent means of assessing the accuracy of the algorithm used by MatPIV—which is just an implementation of Sect. 2.3.2.4—a series of test PIV images were generated in Matlab. The test images consisted of a number of Gaussian shaped particles (with a normal distribution of sizes; mean diameter 2.5 pixels, standard deviation 0.3 pixels) at random locations in the image map. Particle brightness was approximated as a linear function of the particle diameter, reflecting the increased scattering cross-section of larger particles in PIV. The original image map was four times larger than the desired output to reduce interpolation artifacts. To simulate particle motion, two output images were obtained by interpolating new images with a reduced image size (that matched the resolution of the Kodak camera) with a shift in the x-axis ranging from 0.1 to 12 pixels in 0.1 pixel steps. Gaussian distributed noise was added to the output image pairs separately. New image pairs were generated for all simulated displacements. Fifty pairs of images were generated for each set of image displacements. This process is shown schematically in Fig. 5.6.

All images—simulated and experimental—were processed with interrogation areas equal to 32×32 pixels. Each IA overlapped its neighbour by 50%. A variety of window functions were tested to try to minimise aliasing artifacts due to use of the fast Fourier transform. As discussed in Sect. 2.3.2.4, the use of windowing functions is not necessary if the criteria for optimised

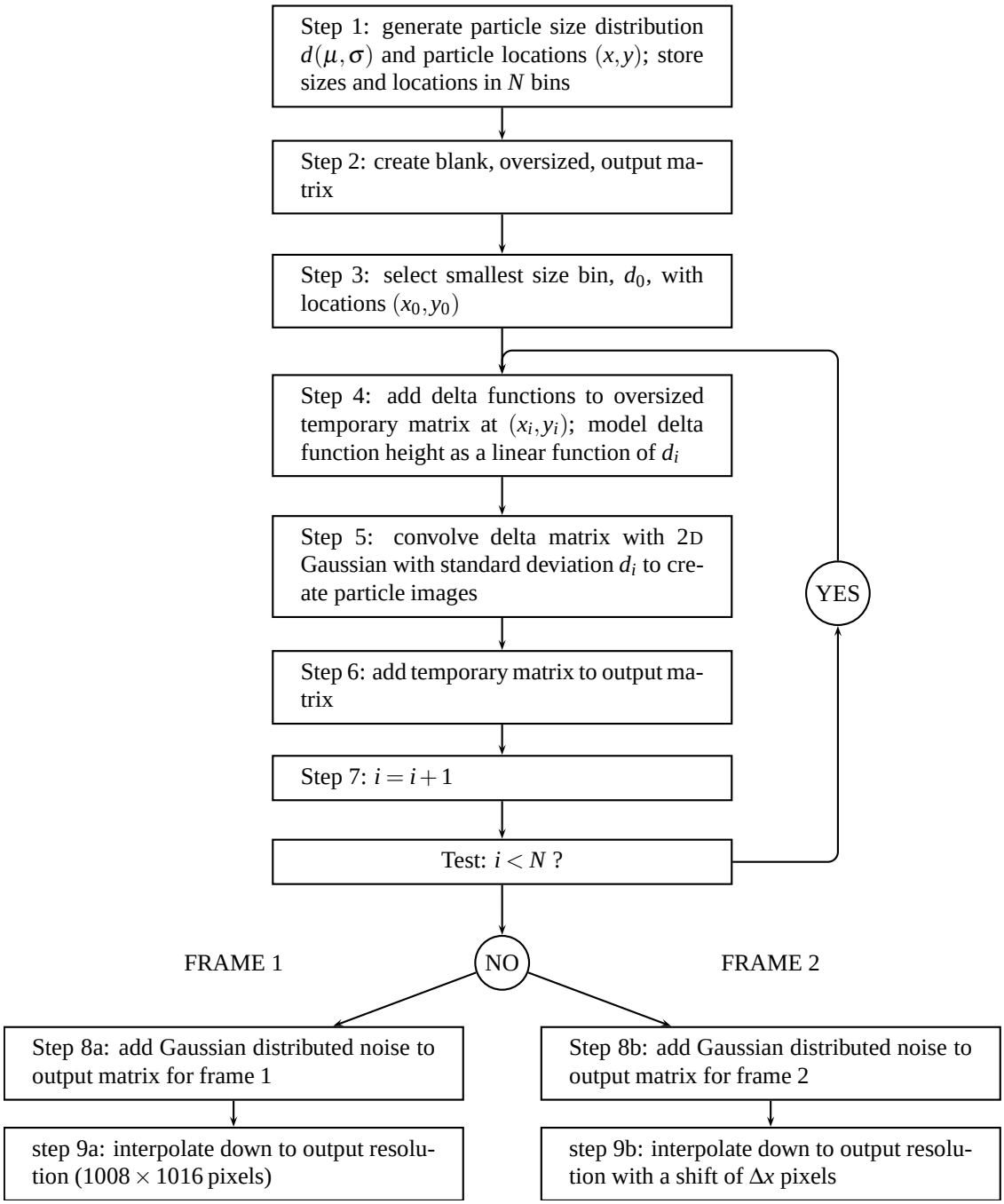

Figure 5.6: *Block diagram showing the process used to generate test* PIV *images to assess the accuracy of the algorithm used by Mat*PIV.

PIV is followed. This is borne out in the results for the simulated test PIV images that are shown in Fig. 5.7.

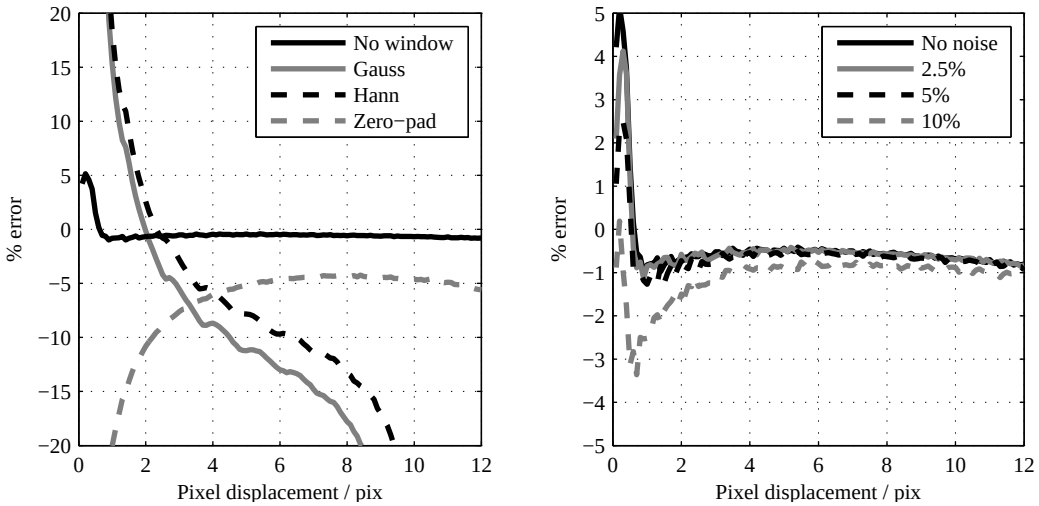

(a) The effect of different windowing functions on the PIV algorithm.

(b) Percentage error in the PIV algorithm at different noise levels.

Figure 5.7: *The mean displacement for each set of image pairs calculated using the cross-correlation method described in Sect. 2.3.2.4 compared to the actual displacement.*

5.2.2.4 Validation of vector maps

Having obtained vector maps from the image pairs, it is necessary to validate the data to remove outliers that arise from random correlations in the interrogation areas (Westerweel, 1997). The median filter is particularly effective at removing high frequency noise (ie, one-off outlying data points). To validate the PIV velocity maps, a two-dimensional median filter was applied to the x and y components of velocity of every image map. The filtered velocity map was compared with the raw data; any points that differed by more than 10% in either component of velocity from the filtered data were replaced by the median value. Data validated in this manner show a high degree of consistency, with no distortion of the underlying trends (Fig. 5.8).

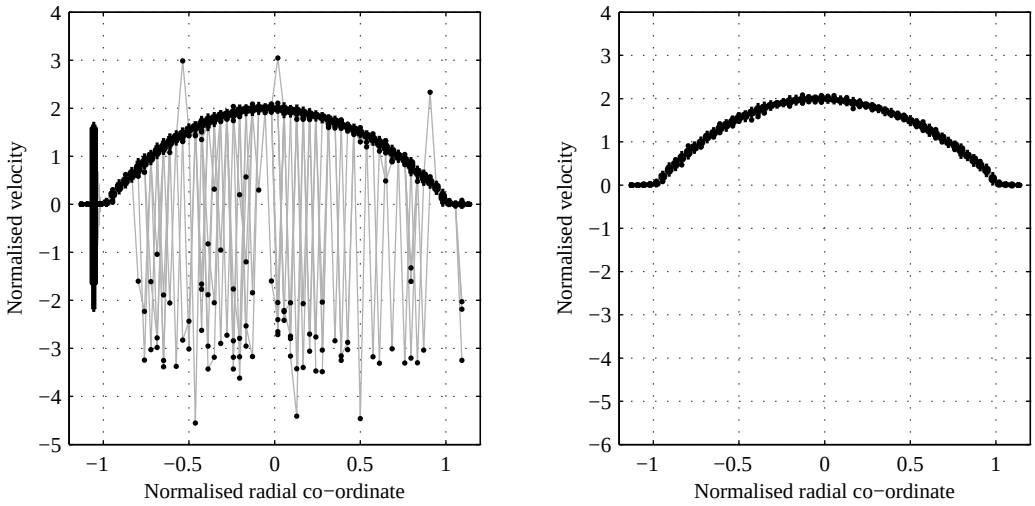

(a) Unvalidated velocity profiles obtained using PIV.

(b) The same velocity profiles after validation with a 10% local median filter.

Figure 5.8: *The effect of validation on* PIV *velocity data. Fifty separate velocity profiles are shown on each axis. The velocities have been normalised by the mean velocity in the pipe.*

5.2.3 Doppler ultrasound

5.2.3.1 Fluid circuit and flow conditions

The working fluid and flow circuit was the same as used in Chapt. 3, with the exception of replacing the straight tube phantoms with the stenosis models. The same gear pump and amplifier were also used. Flow rates were measured with a graduating cylinder and stopwatch, and calibrated so that the Reynolds number matched that in the PIV models.

5.2.3.2 Ultrasound acquisition

All of the ultrasound data presented in this chapter were collected with the same ATL HDI5000 clinical scanner (ATL Ultrasound, Bothell, WA, USA) that was used in Chapt. 3 and transferred with the Researchlink option to a PC for off-line analysis. Machine settings were optimised for peripheral vascular applications with linear array transducers. The data were collected using an L12–5 38 transducer (central B-mode frequency 12 MHz, central Doppler frequency 5 MHz).

Accurate relative positioning of the transducer was accomplished with a micro-manipulator (Fig. 5.9). The transducer was mounted on a traverse system. Positioning along the manipulator axis was accurate to 0.1 mm and controlled with a vernier scale. Two laboratory scissor jacks

supported the traverse system, allowing control of the vertical positioning; a spirit level was used to ensure that the traverse was horizontal.

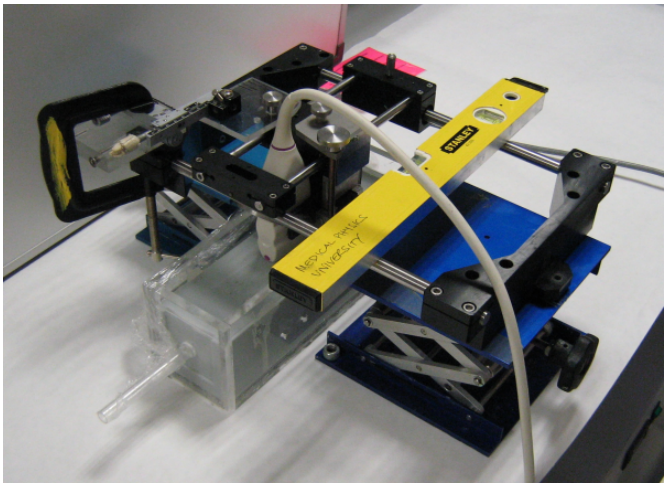

Figure 5.9: *Aligning the transducer with the traverse system.*

Measurement sets were collected three times. The transducer was used longitudinally and centred on the stenosis throat ($Z = 0$) with the micrometer set to the middle of its range. This allowed fine control over axial positioning for positive (distal) and negative (proximal) displacements. To optimise image quality, the alignment was adjusted until the near and far intima-media layers were clearly visible. The transducer was then moved to the desired position with the micro-manipulator to prepare for data collection.

To collect angle independent velocity data, ultrasound measurements were collected at each location and for each flow rate with the beam steered in two different directions. As the ultrasound machine does not support data collection with alternating beam directions, this produced two separate data files, one with the beam steered to the left, and another with it steered right. This restricted data analysis to time averaged means.

Data were collected using colour flow imaging with the machine settings listed in Table 5.1. Each recording was long enough to fill up the machine buffer (about 310 frames for the L12–5).

5.2.3.3 Ultrasound processing

All ultrasound analysis was implemented in Matlab R2006a (The Mathworks, Natick, MA, USA), using the XIFtoolbox v0.4.2 to load data files. To obtain angle independent velocity estimates, the vector approach described by Hoskins et al. (1994) was implemented. Each steered

Setting	Value
Persistence	Off
Smoothing	Off
Sensitivity	Medium
Wall-filter	Low
DMD	Off

Table 5.1: *Colour machine settings used on the* HDI5000 *in this chapter.*

beam estimated the true velocity projected along the direction of propagation (Fig. 5.10a), where V_L and V_R are given by

$$V_L = V\cos(\psi-\theta), \tag{5.4}$$

$$V_R = V\cos(\pi-\psi-\theta); \tag{5.5}$$

with V, V_L, V_R and the angles ψ and θ are defined in Fig. 5.10a. Rearranging and solving these equations for V and θ yields:

$$\theta = \psi-\tan^{-1}\left(\frac{\cos(\pi-2\psi)-{}^{V_R}/_{V_L}}{\sin(\pi-2\psi)}\right); \tag{5.6}$$

$$V = \sqrt{\left(\frac{V_L-V_R}{2\sin({}^{\pi}/_{2}-\psi)}\right)^2+\left(\frac{V_L+V_R}{2\cos({}^{\pi}/_{2}-\psi)}\right)^2}. \tag{5.7}$$

Having implemented the vector Doppler equations, taking care to ensure that θ lies in the correct sector due to the periodicity of trigonometric functions, angle independent velocity measurements were obtained (Fig. 5.10b).

5.2.4 Calculation of velocity profiles and derived quantities

Having obtained the velocity 2D vector fields, velocity profiles and derived quantities such as the wall shear rate were extracted by interpolating the velocity field at the desired co-ordinates. To allow comparison between the ultrasound and PIV data, all velocities were normalised using Eq. (2.9).

Measurement of the wall shear rate requires two pieces of information: location of the wall and the velocity gradient at the wall location. To convert measurements of WSR into shear

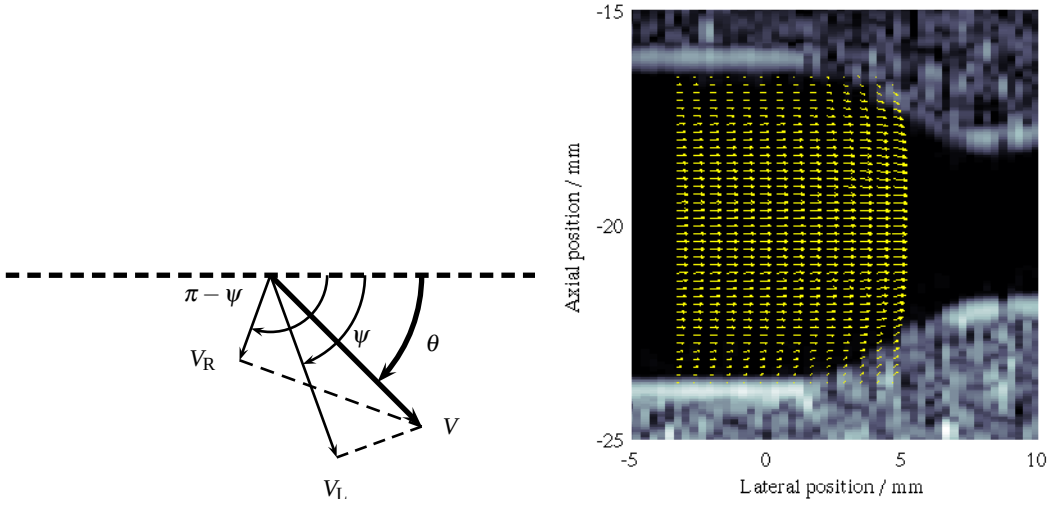

(a) The geometry of vector Doppler utlrasound. (Adapted from Hoskins et al. (1994)).

(b) An implementation of the vector Doppler approach, proximal to a 50% stenosis.

Figure 5.10: *Vector Doppler ultrasound.*

stress requires one further piece of information, the local fluid viscosity. Both experimental systems used low concentrations of scatterers, and can be considered Newtonian fluids, under this approximation, the shear rate is linearly related to the shear stress, so the wall shear stress shall be considered from here on. Measurements of WSS made with Doppler ultrasound and PIV were normalised using Eq. (2.10).

For both systems, the wall locations were marked by hand from the average image acquired from each data set (Fig. 5.13). This was time consuming, but relatively straight forward in the ultrasound models. For the PIV models, specifying the wall was less simple, since the tracer particles tended to attach themselves to the vessel wall; this causes large amounts of glare at the fluid/wall interface. Very bright spots can cause the pixels at the CCD of the digital camera to saturate; the accumulated charge subsequently bleeds into adjacent pixels (Fig. 5.11a). This made accurate identification of the maximum in the peak corresponding to the wall very imprecise, since the peak had a flat top due to saturation. Consequently, the wall position marked on the images was the outermost radial location of the bright region (Fig. 5.11b).

Having marked the position of the vessel walls on both models, the local angle of each segment of wall was calculated. This angle is needed to resolve the component of velocity parallel to each wall segment. The wall shear rate at each point along the wall was estimated using a linear fit consisting of the resolved parallel component of velocity measured at three sites. The first position was the marked wall point. Viscous fluid theory requires that the fluid velocity at this location should be equal to the wall velocity (effectively zero for a stationary wall). To examine

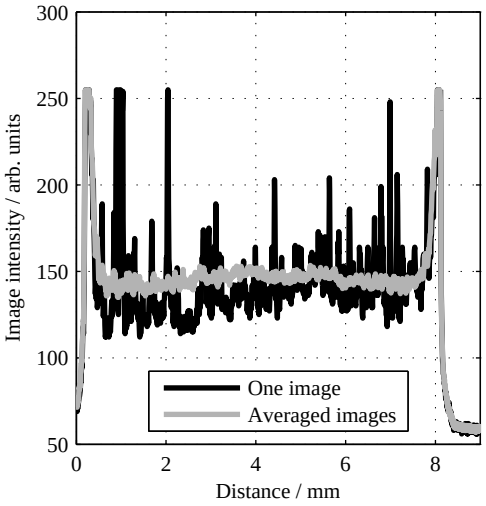

(a) Saturation of the CCD at the wall in PIV.

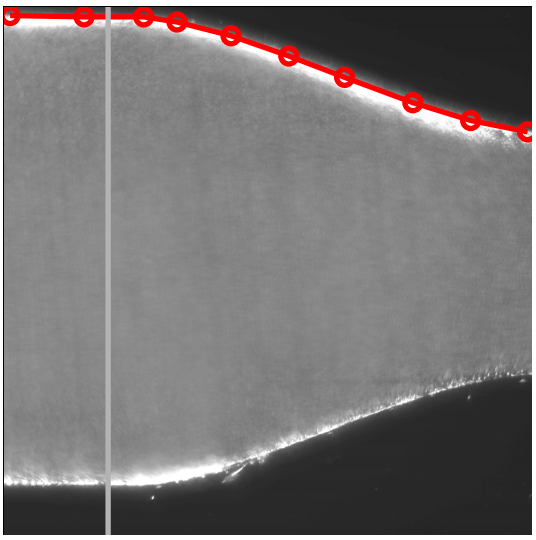

(b) The wall position marked by hand with the PIV models. The corresponding velocity profile has also been shown.

Figure 5.11: *Marking the wall position in* PIV.

Method	Ultrasound			PIV	
	Wall	δx	Force zero	δx	Force zero
A	B-mode	$1/2\lambda$	No	$1/2$IA	No
B	Colour threshold	$1/2\lambda$	No	—	—
C	B-mode	$1/2\lambda$	Yes	$1/2$IA	Yes
D	B-mode	λ	Yes	IA	Yes
E	B-mode	2λ	Yes	2IA	Yes

Table 5.2: *Fitting methods used to estimate the* WSR. *For* PIV*, the wall location was always assessed from the images.*

the effect of the no-slip condition, the WSR was estimated by both modalities with and without forcing zero velocity at the wall (Table 5.2). To examine the effect of the imaging resolution, the location of subsequent data points was varied. For the ultrasound data, the next two sites were located at multiples of the wavelength from the vessel wall ($n/2$ and $n\lambda$ with n equal to $1/2$ and 1; 1 and 2; and finally 2 and 4). For the PIV data, the inner two points were located at the same multiples of the interrogation area size from the vessel wall.

Choosing these values for the δx reduced the amount of shared information in each sample volume, yielding more independent velocity estimates. Velocities at the marked wall were not forced to zero with methods A and B; although this violates viscous theory—the no-slip condition—this approach has been implemented before (Ahmed & Giddens, 1983*a*,*b*) and does still demonstrate the limitations of the instrumentation. The velocities used to calculate the

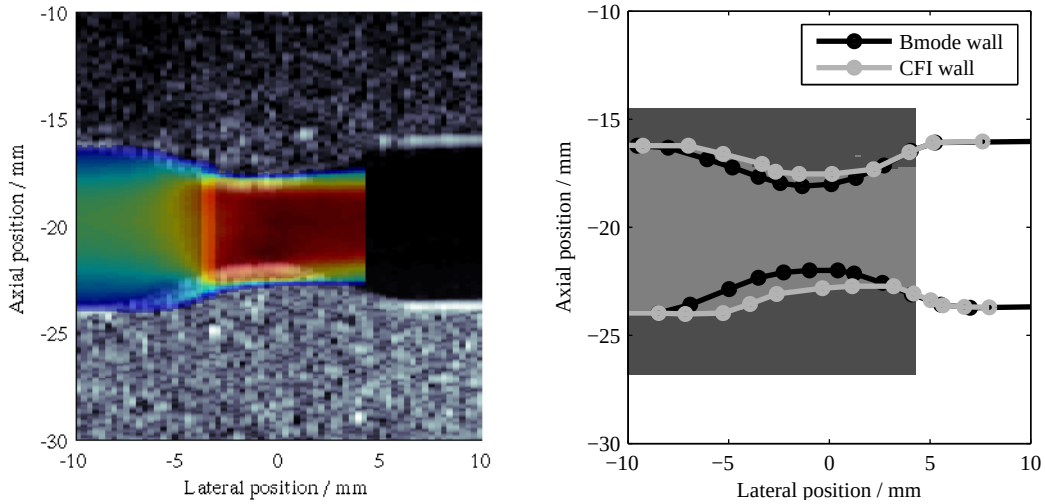

(a) Bleeding of the colour flow data in the 50% stenosis. **(b)** The B-mode and modified wall positions. The light grey shows where the velocity exceeded 1 cm·s^{-1}.

Figure 5.12: *The modified wall position used with colour flow imaging.*

shear rate were obtained by interpolation the velocity field; occasionally this resulted in undefined values (referred to as an `NaN`), in these circumstances, the exception was replaced by zero to allow calculation of the shear rate. This is acceptable, since the `NaN` indicates that the point location is clearly outside of the lumen, so the velocity is zero.

Under laminar flow conditions, this B-mode wall and the edge of the velocity field coincided. However, for complex flow fields, the colour flow map bled into the tissue (Fig. 5.12a), resulting in artificially reduced shear rates with method A. As an alternative, a modified wall position combined the B-mode geometry with a velocity threshold based method (Fig. 5.12b). The B-mode wall position was displayed on top of a 1 cm·s^{-1} velocity threshold image. Where the velocity field extended beyond the real wall, the wall location was moved to include the local velocity field. Where the thresholded velocity field was contained within the B-mode wall, the WSR at the real wall was calculated.

5.3 Results

5.3.1 Stenosis models

The degree of stenosis in the ultrasound models compared well with the PIV (Fig. 5.13f). The mean difference between the degree of stenosis, κ, in the optical and acoustic models was 1 (3)%. Despite this good agreement, the differences were significant in the 30% models ($p < 10^{-3}$), 40% models ($p < 0.05$) and 60% models ($p < 0.05$). Distension in the models was minimal. In both 50% models, changing the flow rate from Re = 200 to Re = 1000 resulted in a changes to the diameter of less than 1%.

5.3.2 Velocity measurement

Developed velocity profiles were measured in both systems, (Fig. 5.14 and Figs. B.6a–B.10a), although deviations from Poiseuille-like conditions were observed with both modalities. In all the stenosis models, the differences between the centreline velocities measured by DUS and PIV were significant. ($\kappa = 0.6$, $p < 0.05$. All other differences were to the $p < 0.01$ level.) Maximum velocities were consistently underestimated by Doppler ultrasound at Re=500 (mean underestimate 14 (1)%), and some velocity profiles were faintly skewed (Fig. 5.14a). No relationship existed between the stenosis model and the maximum normalised inlet velocity (Fig. 5.14c).

Changing the flow rate produced deviations from Poiseuille flow in both the PIV and ultrasound systems. The velocity profiles remained parabolic for all Reynolds numbers with the PIV system, but the magnitude of the normalised maximum velocity decreased linearly although not significantly ($r^2 = 0.97$, Fig. 5.14d). For the DUS system, velocity profiles obtained at Reynolds numbers of 800 and 1000 were skewed to one side, and blunter at the centre. This suggests that the flow was not entirely developed, despite adequate inlet length (Eq. (3.7)). Values of the development index (Eq. (3.10)) confirmed this hypothesis (0.80 and 0.64 at Reynolds numbers of 800 and 1000, respectively). The normalised centre line velocity was inversely and quadratically proportional to the Reynolds number ($r^2 > 0.99$), producing significant differences in $\hat{V}$ compared at Re=200, 600 and 1000 ($p < 10^{-3}$ and $p < 10^{-5}$). The proportionality suggests dependency upon area and hence distension, however, the difference in diameter between the minimum and maximum Reynolds number was less than 1% in both systems. The differences between the normalised inlet centreline velocity measured by PIV and DUS were significant for

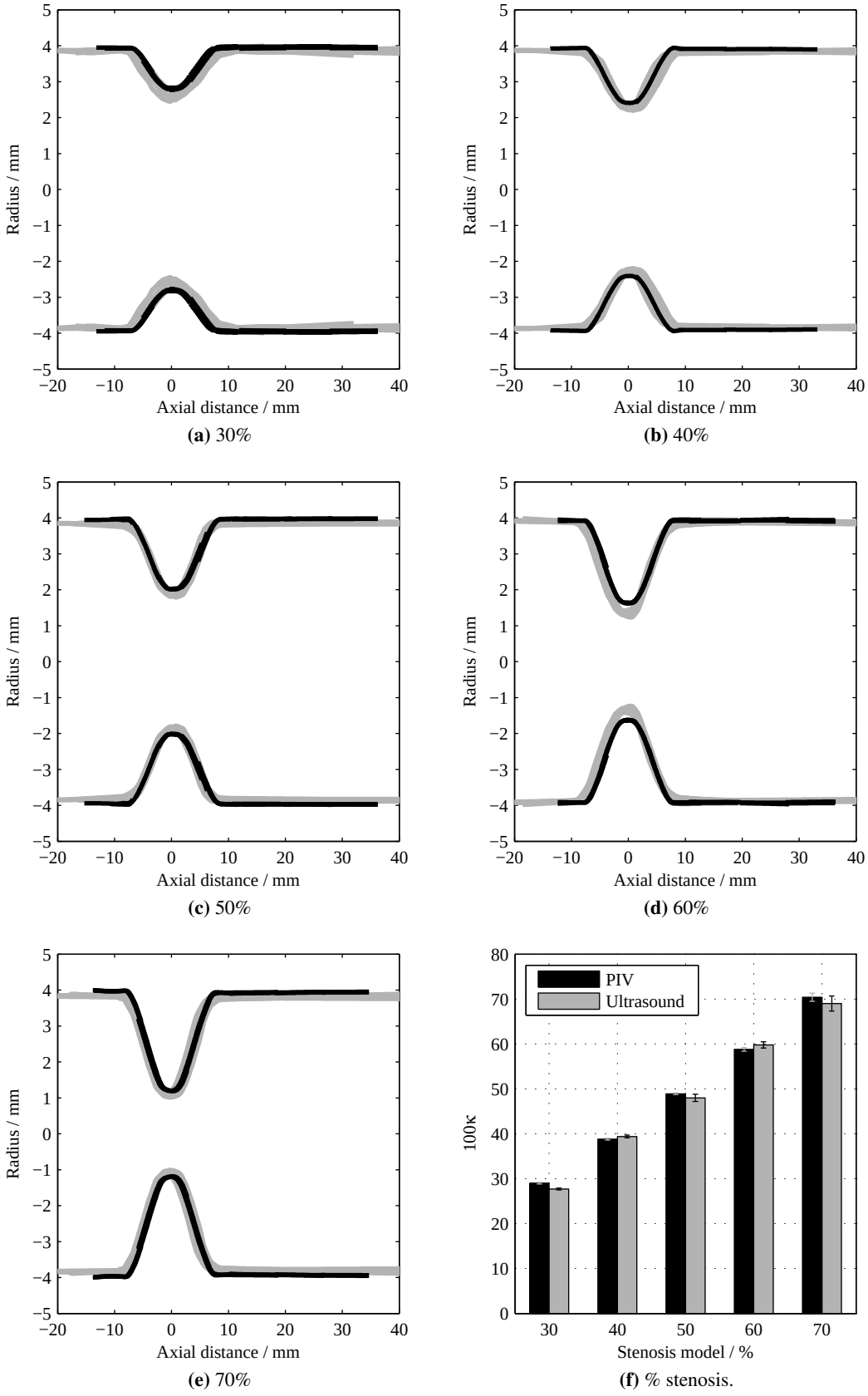

(a) 30% **(b)** 40% **(c)** 50% **(d)** 60% **(e)** 70% **(f)** % stenosis.

Figure 5.13: *Stenosis geometries measured by ultrasound and with the* PIV *system at* $\mathrm{Re} = 500$.

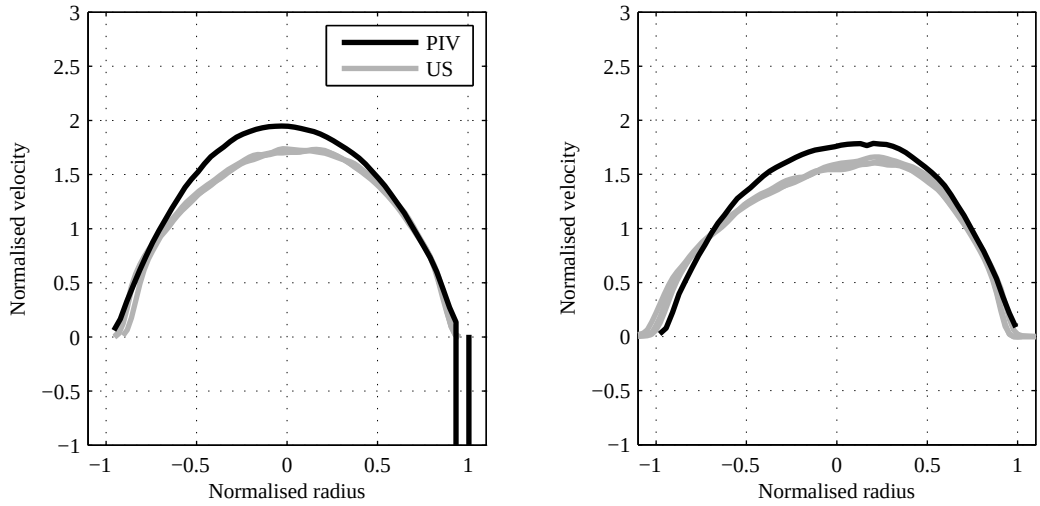

(a) Mean inlet velocity profiles in the 30% stenosis model at Re = 500.

(b) Mean inlet velocity profiles in the 50% stenosis model at Re = 1000.

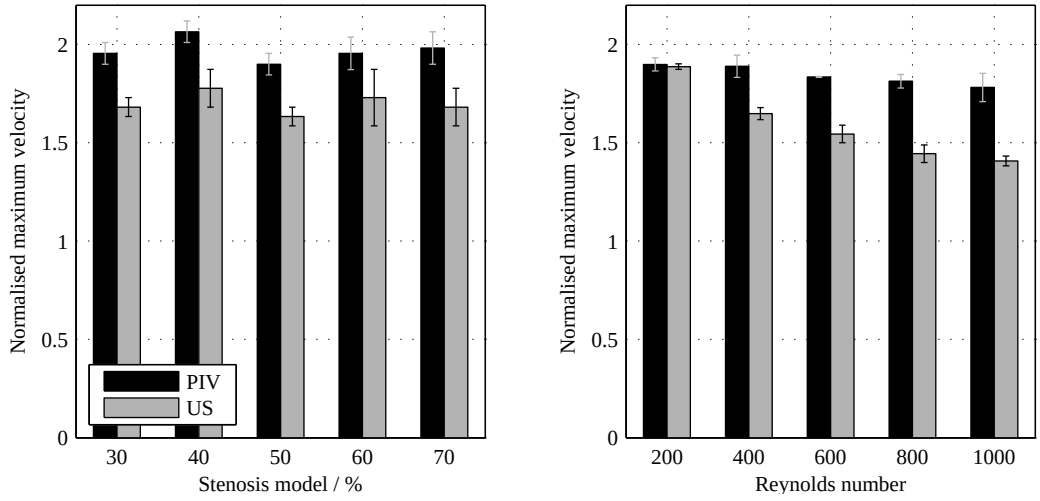

(c) Maximum inlet velocity at Re = 500.

(d) Maximum inlet velocity in the 50% stenosis model.

Figure 5.14: *Inlet velocity conditions in the stenosis models.*

Re = 400 ($p < 0.01$) and Re $\geq$ 600 ($p < 10^{-3}$). The mean difference between the centreline velocity measured by both modalities was –14 (8)%, (range –21 to –1%).

5.3.3 Wall shear stress measurement

Estimating wall shear stress at the inlet was difficult with ultrasound and PIV. As expected, no systematic variation was present in the WSS estimates when using different models (Fig. 5.15a), although the performance of the different WSS methods was highly variable.

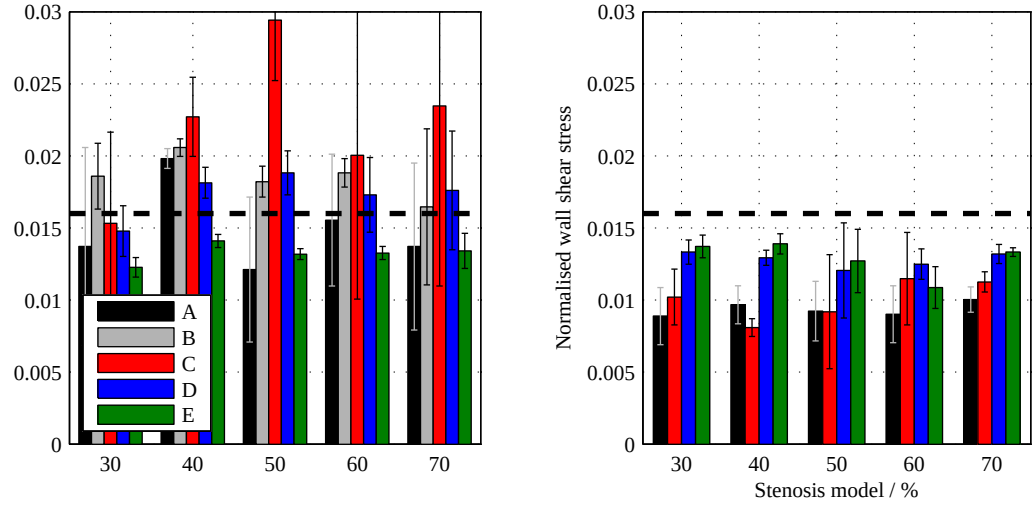

(a) Inlet WSS measured with Doppler ultrasound.

(b) Inlet WSS measured with PIV.

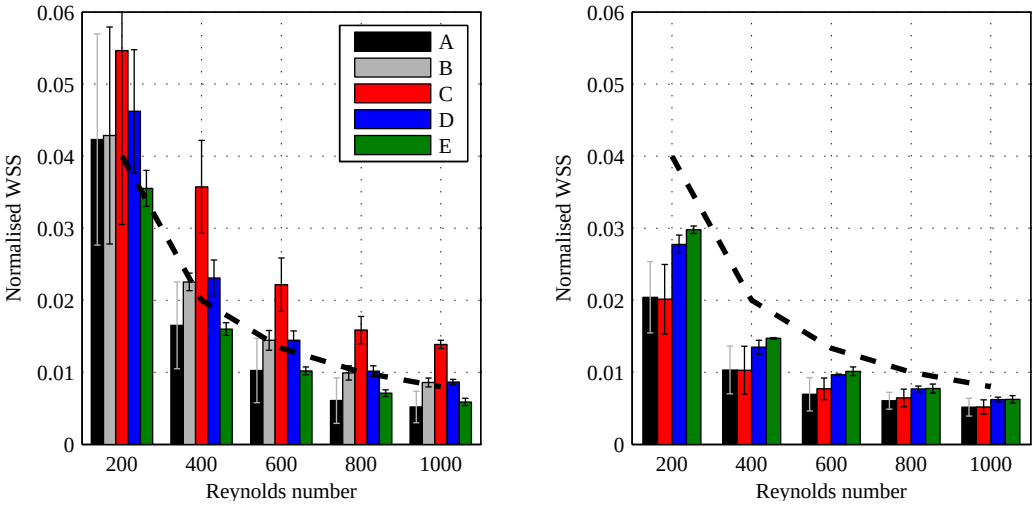

(c) Inlet WSS measured with Doppler ultrasound.

(d) Inlet WSS measured with PIV.

Figure 5.15: *Mean inlet* WSS *in the different stenosis models. The Poiseuille value of* WSS *is the dashed black line.*

Doppler ultrasound estimates of the wall shear stress were reasonable (Fig. 5.15a). Methods A and D were able to measure the theoretic WSS to within 10%, although the standard deviation of the values was extremely large (Fig. 5.16a). Method B, which marked the wall position at the edge of the colour flow data without assuming zero velocity at the "wall" overestimated the idealised inlet WSS, as did C. Despite the substantial differences, the variability of the data points was such that the theoretic value lay within or close to one standard deviation of the mean. Comparing the values of WSS produced with methods C, D and E, which forced zero velocity at the B-mode wall produced consistent results. For steady flow—even flow that is not completely developed—the boundary layer develops a parabolic form. Approximating the

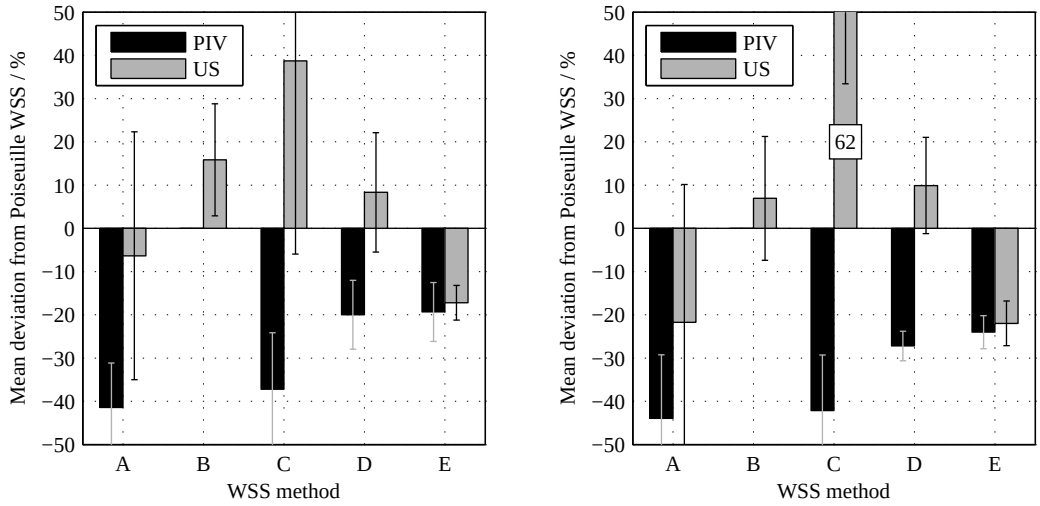

(a) Deviation from Poiseuille WSS in all the stenosis models at Re=500.

(b) Deviations from Poiseuille WSS in the 50% model at all flow rates studied.

Figure 5.16: *Mean deviation from Poiseuille* WSS *using different estimation strategies.*

velocity profile with a linear fit at the wall (and zero velocity at the wall) introduces a bias to the WSS measurement that is directly proportional to the distance from the wall of the first velocity point (assuming a no-slip condition and only one velocity point) (Lou et al., 1993). Since δx was greater for method D than for strategy C, and greatest for method E, the estimated wall shear stress is expected to be lower.

WSS was underestimated in all the PIV models, using all methods (except B, which was applied to ultrasound data only). Methods D and E performed best, with the least bias and smallest variability, –20 (8)% and –19 (7)%, respectively, compared to the theoretic optimum performances of –6 and –11% (Lou et al., 1993). Methods A and C both exhibited biases exceeding 30% and produced generally comparable velocity estimates (Fig. 5.15b). This is not surprising; the only difference between these methods is that the velocity point at the wall was forced to zero—if velocities are already close to zero, little difference will occur. In principle, one would expect method E to measure lower shear rates than method D, which in turn would yield lower shear rates than C. This is not the case, providing evidence that the velocity points close to the wall were dominated by error.

Varying the flow rate did not substantially affect the accuracy of WSS estimation (Fig. 5.16b). The mean bias and variability of methods A–E at high and low flow rates were comparable to values taken at Re=500 upstream of the stenosis in the other stenosis models.

5.4 Discussion

5.4.1 Similarity of the stenosis geometries

The stenosis geometries were similar in the ultrasound and PIV models, with mean differences in κ of 1%. Although the differences were significant in some of the stenosis models, this was an artifact of the large reproducibility of the methods used to mark the lumen. Typically, measuring the lumen diameter using the Gaussian fitting method resulted in standard deviations of the order of tens of microns—an order of magnitude smaller than the wavelength of ultrasound. Performing the statistical tests using the wavelength rather than the standard deviation resulted in the apparent significance vanishing.

Distension in both series of models was minimal (less than 1%). This implies that the geometries will not change under pulsatile flow at Reynolds numbers in the range 200-1000, and as such that the flow dynamics inside each model will remain similar.

5.4.2 Agreement of inlet velocity profiles

One would expect the greatest agreement between both imaging modalities to occur upstream of the stenoses, where flow was undisturbed and laminar, with enough inlet length to ensure Poiseuille-like velocity profiles. Under such conditions, it is possible to assess the performance of each system by comparing measured velocities and wall shear stresses with the theoretic solution.

In all the models, parabolic velocity profiles were observed at Reynolds numbers of 500, although some velocity profiles were faintly skewed to one side. Ignoring errors arising from instrumentation, sources of this systematic error arise from the geometry of the stenosis models, and the manner in which they are connected into the fluid loop. Deviations from long straight pipes, such as corners, introduce helical secondary flow structures that are extremely stable and can skew velocity profiles. Alternatively, discontinuities in pipe size, which typically occur at junctions, effectively introduce upstream stenoses, which would affect flow conditions downstream. For the ultrasound stenosis models, the casting process inevitably produces some minor discontinuity. To build the models, the liquid agar is poured around the brass stenosis rods, which meet in the middle of the box, and are held in place by short sections of perspex pipe (Fig. 3.1a). The diameter of the perspex tubes is slightly larger than the brass rods, so

some discontinuity occurs at the pipe/TMM interface. Similarly, connecting the flow phantom into the fluid loop introduces minor stenoses at the outer edges of the perspex tubes—this also applies to the optical models.

Maximum inlet velocities in the PIV system did not vary across different stenosis models and agreed well with the Poiseuille value. No variation was present in the corresponding ultrasound models, but the centreline velocity was underestimated by 15%, on average. Determining the source of this error is impractical, since the ultrasound machine is effectively a black box device. To specify with any degree of certainty why the bias occurs, requires complete characterisation of the system for all machine settings. This task involves measurement of the size of the Doppler sample volume and the impulse response of the transducer and the processing electronics, knowledge of the number of pulses used to estimate the velocity, knowledge of the algorithm used to estimate the phase shift (for example, the auto-correlator (Kasai et al., 1985) or the cross-correlator (Bonnefous & Pesqué, 1986)), knowledge of the level of the clutter filter, among many other parameters. Sources of error unrelated to the ultrasound machine include frequency dependent attenuation by the tissue mimic. In Chapt. 3 apparent reductions in the flow rate estimated using CFI with increasing depth, were partly attributed to the increasing amount of TMM between the transducer and the lumen (Fig. 3.8a). The same mechanism may apply in this case, as the top of the lumen in the stenosis models was around 20 mm below the surface of the phantom.

Varying the flow rate produced surprising results in both the ultrasound and PIV models. The normalised peak inlet velocity fell linearly in the optical models (although not significantly), and in a quadratic manner when measured with DUS (and significantly). Flow that is not fully developed or skewed to one side would reduce the measured centreline velocity, and this effect would increase as flow rate (and hence the necessary inlet length) increases. For Reynolds numbers of 600 and below, no deviations (other than mild skewness) were evident in the profiles measured with DUS, and all the inlet profiles in the optical models appeared fully developed (ie, no blunt core profile). At higher Reynolds numbers, the velocity profiles in both models were blunter in the centre, which would contribute to the reduced centreline velocity. The flatter velocity profile suggests that some degree of disturbance was introduced at the connections to the perspex boxes as discussed previously. However, deviations from fully developed flow cannot solely account for the reduction in the centreline velocity, since the value varied even when the velocity profiles were parabolic.

Identifying sources of systematic error in the PIV system responsible for the decrease in centreline velocity is difficult. The obvious sources of systematic error lie in calculation of the scale factor of the camera in the fluid viscosity and flow rate. However, the low flow rate data were collected at the same time as the high flow rates. Any error introduced as a consequence would manifest itself as a constant offset, rather than an increasing offset. Errors in the fluid viscosity and flow rate would present themselves in a similar manner, as a constant, rather than increasing offset, with an extra component due to random error. During data acqusition, the temperature of the working fluid was kept within 21–23°C using ice to minimise changes of viscosity, and the flow rates were calibrated using a graduated cylinder. Given the care with which these data were acquired, and the fact that some deviations from parabolic inlet profiles occurred, it is a reasonable explanation that the decrease in the normalised inlet velocity was as a result of disturbed inlet flow due to small changes in diameter at the model connectors.

5.4.3 Estimation of wall shear stress

Estimating the wall shear stress was difficult with both methods. Even at the inlet, for Reynolds numbers of 500 and below (for flows which had good parabolic inlet velocity profiles), the variance and bias of the normalised shear stresses was high, and the measured values were highly dependent on the strategy applied. As discussed in Chapt. 3, previous efforts to quantify wall shear rate have assumed velocity profiles (typically parabolic) close to the wall or that the maximum wall shear rate near to the wall is equivalent to the WSR, without much justification (Brands et al., 1995; Köhler et al., 2001; Oyre et al., 1997; Samijo et al., 1997; Wu et al., 2004). To avoid this assumption, the strategies tested all relied on a linear approximation to the velocity gradient.

To justify the selection of method C as the best performing strategy, one must examine the strengths and weaknesses of each method, particularly from a practical aspect. At first glance, C performed poorest at the inlet, with biases (of opposite magnitudes) around 40%. In principle, C should measure higher shear rates than D and E for a parabola. The ultrasound data clearly demonstrate this, but the opposite occurs in the PIV data. This effect is an artifact of particle accumulation next to the vessel wall. As the scattering particles became attached to the wall, bright images of stationary particles biased the measured velocities (via the cross-correlation algorithm) for each IA near to the wall towards zero. For IAs further away from the wall, the

signals were no longer affected by stationary particles, with the result that larger velocities and hence gradients can be measured.

Method C produced artificially large wall shear stresses in the ultrasound phantoms. This effect is an artifact of CFI. Sample volumes have a finite size, thus velocities are measured outside the vessel lumen. Method B was proposed to examine the effect of this phenomenon on the estimated WSS, and, despite not forcing the "wall" point to zero, it produced reasonable (within 10–20%) estimates for the Poiseuille WSS. As one would expect, since the measured edge velocities were close to zero, this method also produced shear rates that were larger than those produced by A, which measured the velocity gradient at the location of the B-mode wall. Recalling that CFI typically measures velocities beyond the lumen (since colour flow uses longer pulse sequences and lower frequencies than B-mode imaging), the velocity gradient at the correct (ie, B-mode) wall position will usually be smaller than at the edge of the velocity field. (An example of this, in a stenosis, rather than at the inlet, is shown in Fig. 5.12. The effect on the WSS is seen in Fig. 6.7a and 6.7b.) However, measuring the velocity gradient at the location of the B-mode wall, but setting the wall velocity to zero—the no-slip condition—will produce larger shear rates, as the velocity points used to calculate the gradient are taken from points further inside the lumen (than for method B) but the gradient is constrained to pass through zero.

5.5 Conclusion

Two independent systems have been developed to study flow through a series of idealised stenoses. Each system used a different imaging technology, but the fluid mechanics inside each system were similar as the relevant dimensionless numbers were conserved. The PIV system is considered a gold standard and will be used in the following chapters to validate measurements made with Doppler ultrasound distal to the stenosis.

At the inlet to the models, flow was Poiseuille-like for Reynolds numbers equal to and below 600. Above this value, the discontinuity at the connectors mildly disrupted the development of the velocity profiles, resulted in a blunter core profile. This reduced the magnitude of the centreline velocity. Assuming Poiseuille conditions (for undisturbed velocity profiles), CFI-based Doppler ultrasound underestimated the centreline velocity by 14 (1)%. Using the PIV system, no systematic error was present. Measurement of the wall shear stress was difficult with both

techniques. The performance of several methods was examined. In the PIV system, all of the methods underestimated the Poiseuille value by at least 20%. Three of the proposed methods were able to correctly measured the Poiseuille value using Doppler ultrasound, although this is an artifact of the extreme variability of the measurements.

Chapter 6
Steady flow through stenosed tubes: a validation study

Doppler ultrasound is used to pre-screen patients based on the maximum velocity measurement despite sources of error that can distort the measurement by more than 30%. The wall shear stress in arteries is hypothesised to be responsible for the development and progression of atherosclerosis. However, measurement of this force in the presence of disturbed flow is technically challenging, not least because the direction of flow is unknown. In Chapt. 5, a dual flow system was developed and the performance of the imaging systems in simple flow conditions was assessed. In this chapter, the same system is used to study flow through a series of idealised stenoses to validate velocity and shear stress measurements made with Doppler ultrasound in situations where the direction of flow cannot be assumed.

6.1 Introduction

As described in Sect. 5.1, Doppler ultrasound is the preferred method for assessing carotid stenosis as it is non-invasive and more economic (Bluth et al., 1988; Robinson et al., 1988; Spencer & Reid, 1979). However, the errors in Doppler derived maximum velocity can be large, especially for significant stenosis, since only one component of velocity is measured. Asymmetric broadening of the Doppler spectrum compounds this problem (Fish, 1986, 1991; Hoskins, 1996).

The wall shear stress is believed to be responsible for the initiation of atherosclerosis and the destabilising of plaques (Slager et al., 2005*a*,*b*). However, non-invasive quantification of the wall shear stresses acting on plaques is extremely difficult. Current techniques for estimating WSS are applicable only in relatively straight arteries (Brands et al., 1995; Samijo et al., 1997; Oyre et al., 1997; Tortoli et al., 2006); identification of the vessel wall, particularly with ultrasound, is somewhat intractable; while complex flow patterns and turbulence render velocity estimation a time consuming process (Reneman et al., 2006).

To alleviate some of the problems with measuring the WSS in-vivo, many groups have studied flow through stenoses either numerically or with in-vitro flow systems. Geometries have ranged from idealised stenoses (Ahmed & Giddens, 1983*a*,*b*; Bluestein et al., 1999; Köhler et al., 2001; Reese & Thompson, 1998), to physiologic models of excised arteries post-mortem (Bale-Glickman et al., 2003; Friedman et al., 1986; Ku & Giddens, 1987). The use of image guided modelling, which combines non-invasive imaging of arteries with computational fluid dynamics (CFD) is becoming popular, since it allows calculation of the hæmodynamics along the entire length of bifurcations and stenoses (Ryval et al., 2004; Stroud et al., 2000; Sherwin & Blackburn, 2005; Varghese et al., 2007*a*). Despite these advantages, CFD is extremely time consuming, remains largely unvalidated, and highly dependent on boundary conditions and geometries that are obtained from modalities such as ultrasound and MRI.

Ahmed & Giddens (1983*a*,*b*) studied flow through symmetric stenoses in a series of experiments using laser Doppler anemometry. Even today, these experiments represent the forefront of understanding of flow through stenoses at Reynolds numbers characteristic of arteries. That is not to say that the data are without flaws. The data are widely used to validate turbulence models for CFD (Ryval et al., 2004; Sherwin & Blackburn, 2005; Varghese et al., 2007*a*). Difficulties reproducing some of the data—at locations where flow should be laminar—have led to suggestions that some of the Reynolds numbers are subject to rounding errors (Ryval et al., 2004). Downstream of the stenosis, computational models predict much longer regions of recirculation than observed in these experiments (Sherwin & Blackburn, 2005; Varghese et al., 2007*a*). Consequently, further experimental validation of the post-stenotic flow field will help improve CFD modelling of stenoses.

In the presence of complex flow, the error in Doppler ultrasound velocity measurements is largely unknown. Similarly, the error in Doppler derived estimates of the wall shear stress are also unknown. In this chapter, the dual flow system developed in Chapt. 5 is used to study steady flow through the idealised stenosis geometries. This chapter aims to quantify the errors in Doppler ultrasound measurements of maximum velocity and wall shear stress.

6.2 Materials and methods

6.2.1 Locations of velocity measurement

Velocity measurements were acquired at a series of axial locations proximal and distal to the stenosis throat (Fig. 6.1). Time averaged velocity profiles measured using PIV and Doppler ultrasound were compared at integer values of the normalised co-ordinate Z, defined in Eq. (5.2). The images were aligned so that the location of each velocity profile corresponded roughly to the centre of the field of view.

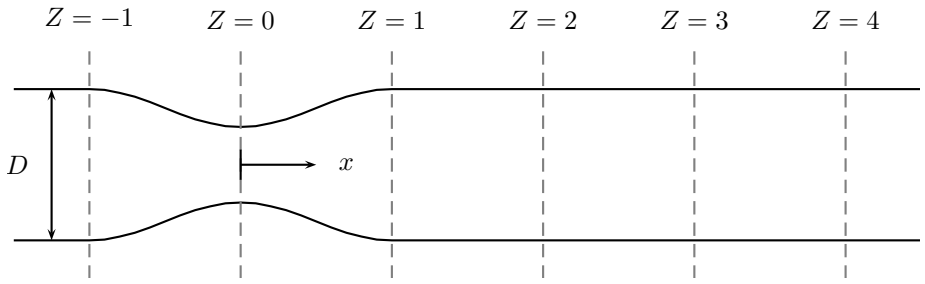

Figure 6.1: *Velocity profile locations in the stenosis models. Z is defined in Eq.* (5.2)*.*

The flow rate was set so that the nominal Reynolds number ranged from 200–1000 for the 50% model. For the remaining models the nominal Reynolds number was set to 500. To quantify the effective flow rate between different stenosis models at different flow rates, the stenotic Reynolds number, Re_0, was defined based on the degree of stenosis, κ, and the upstream Reynolds number Re_{-1} using continuity, such that

$$A_{-1}\overline{v_{-1}} = A_0\overline{v_0}, \tag{6.1}$$

where A indicates lumen area, $\bar{v}$ is mean velocity and the subscripts refer to values of the normalised axial co-ordinate, Z, defined in Eq. (5.2) and Fig. 6.1. Given that κ can be expressed as

$$1-\kappa = \frac{D_0}{D_{-1}}, \tag{6.2}$$

with D_0 the diameter at the stenosis throat, one can consider the area in terms of diameter, which yields an expression for the stenotic Reynolds number

$$\begin{aligned}
\mathrm{Re}_{-1} &= \frac{D_{-1}\overline{v_{-1}}}{\nu}, \\
&= \frac{1}{\nu}\frac{D_0}{1-\kappa}\frac{\overline{v_0}A_0}{A_{-1}}, \\
&= \frac{\mathrm{Re}_0}{1-\kappa}\frac{D_0^2}{D_{-1}^2}, \\
&= \frac{\mathrm{Re}_0}{1-\kappa}\frac{(1-\kappa)^2 D_{-1}^2}{D_{-1}^2}, \\
&= (1-\kappa)\,\mathrm{Re}_0. \qquad (6.3)
\end{aligned}$$

6.2.2 Particle image velocimetry

Pairs of images were acquired at the locations defined in Fig. 6.1, comprising one location before the stenosis (as described in Chapt. 5), one image roughly centred on the stenosis throat, and several images distal to the stenosis. After one complete pass from $Z = -1$ to $Z = 4$, the acquisition process was repeated two further times, producing three complete sets of measurements.

For each location studied, the timing separation between the image frames was set to optimise the image quality according to the criteria described in Sect. 2.3.2.5. Specifically, Δt was varied such that the maximum displacement of particles between the two frames in the region of highest velocity was approximately eight pixels, allowing optimised PIV analysis with interrogation areas of 32×32 pixels. In this study, the range of Δt was 15–100μs.

6.2.3 Doppler ultrasound

The working fluid and flow circuit was the same as used in Chapt. 5. Flow rates were measured with a graduated cylinder and stopwatch, and calibrated so that the Reynolds number at the stenosis throat (Re_0 in Eq. (6.3)) matched that in the PIV models.

The ultrasound data presented in this chapter were collected with the same equipment, using the same machine settings, data acquisition protocols and analysis tools as previously described in Chapt. 5. However, since velocities measured with Doppler ultrasound are proportional to the

frequency shift induced in the carrier signal (Eq. (2.34)); the maximum frequency shift measurable is limited by the Nyquist theorem to the range $\pm 1/2\text{PRF}$. At higher Reynolds numbers and more severe stenoses, the maximum PRF of the scanner was not high enough to prevent aliasing of the velocity data, so a lower frequency transducer was used, the L7–4 linear array (central Doppler frequency 4 MHz). When using the L7–4, the buffer size on the ultrasound machine was smaller than with L12–5, allowing the collection of around 230 frames, rather than around 310.

Measurement sets were collected three times. The transducer was aligned as described in Sect. 5.2.3. It was subsequently moved using the micro-manipulator to the desired location and vector data were recorded. On completion, the transducer was moved axially to the next position. After complete collection of one measurement set (vector data acquired at all the Z values given in Fig. 6.1) the transducer was removed, replaced at the stenosis throat and realigned. The measurement protocol was then repeated.

6.2.4 Calculation of velocity profiles and derived quantities

Distal to all the stenoses studied, a high velocity jet developed with maximum velocity $\hat{V}_0$. The length of the post-stenotic jet, L_J, was defined as the axial distance (Z) where the centreline velocity fell below $1/2\hat{V}_0$. Turbulence intensity was measured using the two-dimensional version of Eq. (2.14). Transition from the laminar fluid regime to turbulence was defined to have occurred if the turbulence intensity increased distally, compared to its uptream value.

Estimates of the recirculation length, L_R, distal to the stenoses were derived from the wall shear stress. L_R was defined as the normalised axial co-ordinate (Z) where the normalised shear stress magnitude exceeded 0.001—which was the approximate noise level—and was oriented in the direction of the bulk flow.

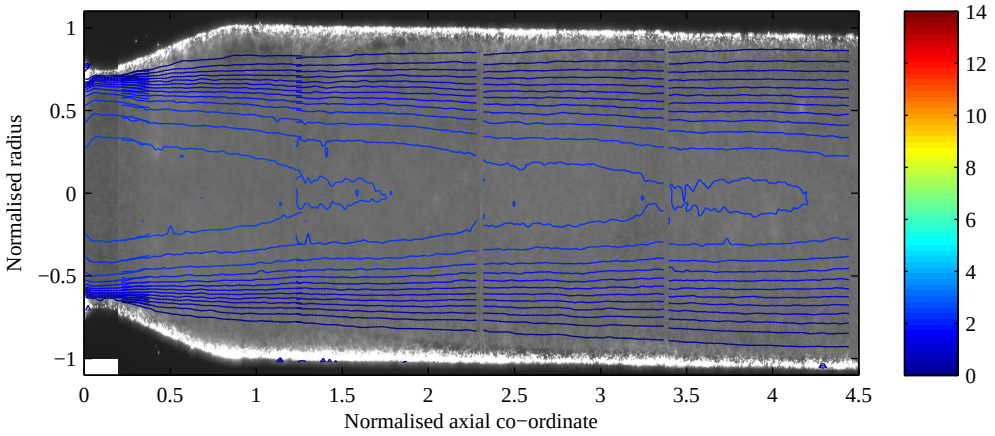

(a) Normalised velocity magnitude contours distal to the 30% stenosis by PIV.

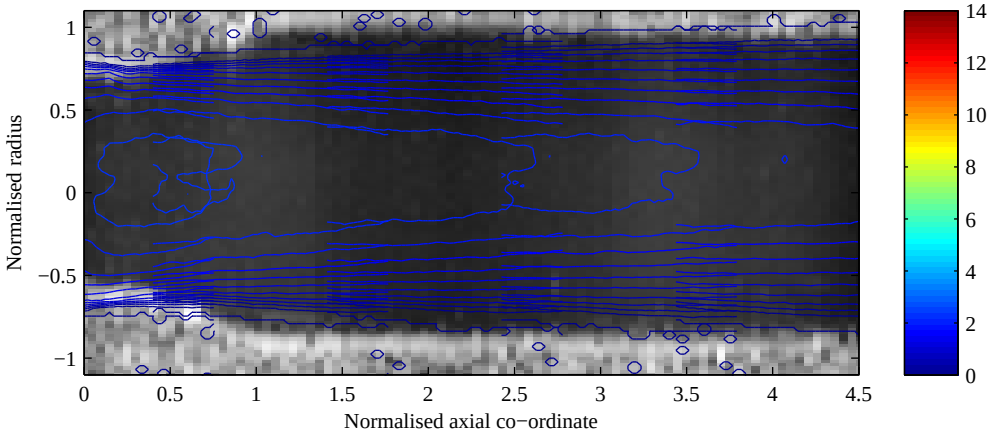

(b) Normalised velocity magnitude contours distal to the 30% stenosis by Doppler ultrasound.

Figure 6.2: *Normalised velocity magnitude contours distal to the 30% stenosis model.*

6.3 Results

6.3.1 Effect of the degree of stenosis

6.3.1.1 Comparison between velocities

Flow distal to the 30% stenosis remained symmetric and laminar over the entire region studied (Fig. 6.2). For the more severe stenoses, asymmetric laminar jets and recirculation regions developed, followed by regions with rapidly fluctuating velocities and transitional/turbulent fluid behaviour (Figs. 6.3–6.4 and Figs. B.1–B.5). Flow in the 40% model was transitional for $Z > 2$ (Fig. 6.5b), while flow in the 30% model remained laminar over the entire region studied. This suggests that the critical stenotic Reynolds number, Re_0, lies somewhere in the range 714–833 (Eq. (6.3)). In the 50% model at $Z = 1$ large velocity fluctuations occurred in the shear layer next to the asymmetric recirculation region (Fig. B.3c). The recirculation region

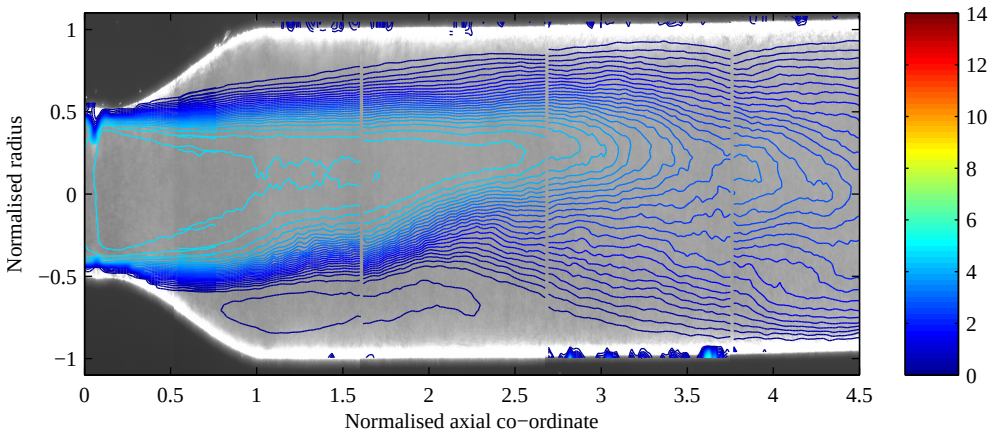

(a) PIV model.

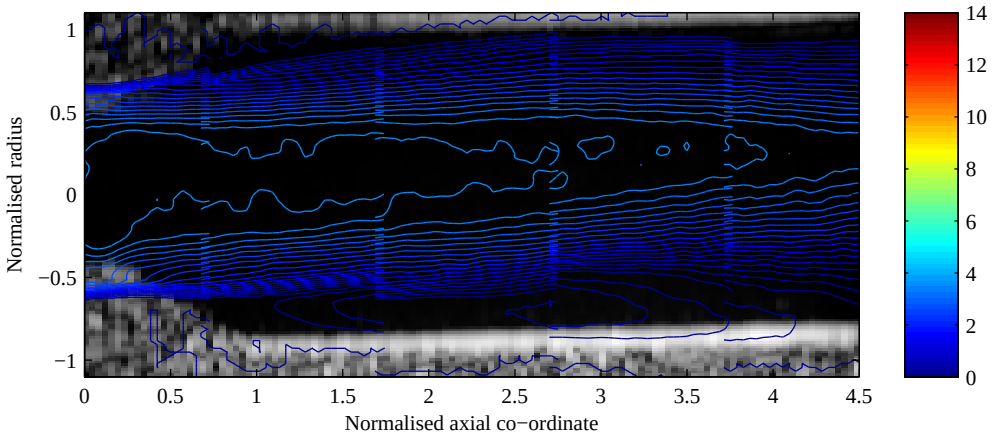

(b) DUS model.

Figure 6.3: *Normalised velocity magnitude contours distal to the 50% stenosis.*

disappeared by $Z = 3$, corresponding to an increase in the turbulent energy (Fig. 6.5c) and the efficient momentum exchange associated with turbulence. In the 60% model, the recirculation regions were again asymmetric and showed signs of shear layer instabilities next to the largest recirculation region (Fig. B.4c). In contrast to the 50% model, the recirculation persisted until around $Z = 3$ despite the more proximal transition to turbulence (Fig. B.4e and Fig. 6.5d). In the 70% model, flow was intensely turbulent by $Z = 1$ (Fig. 6.5e) where it was characterised by highly asymmetric recirculation regions and an equally asymmetric jet.

In the mildest stenosis, the ultrasound data agreed well with the PIV data, remaining laminar and mostly symmetric over the region studied although the maximum velocities were underestimated marginally (Fig. B.6 and Fig. 6.5a). In the 40% model, the DUS data showed qualitative agreement with the PIV velocity profiles, although in the stenosis throat, spurious velocities were measured outside of the vessel lumen (Fig. B.7b). Recirculation regions developed and

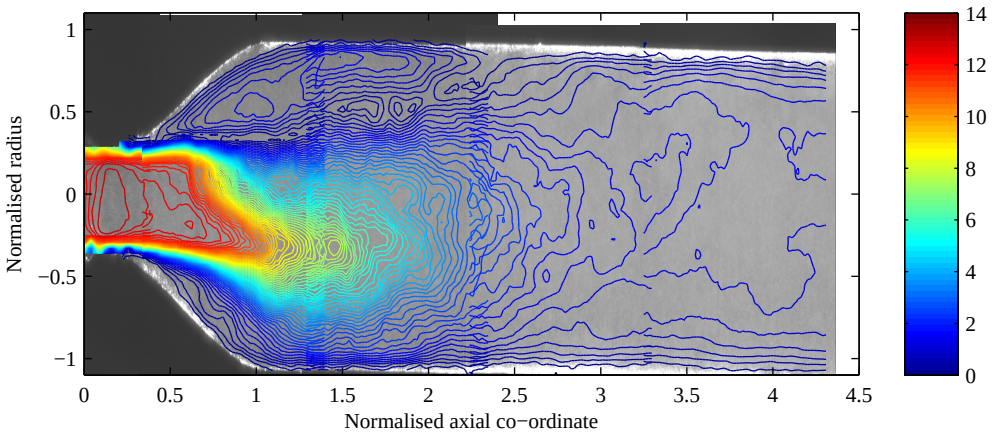

(a) PIV model.

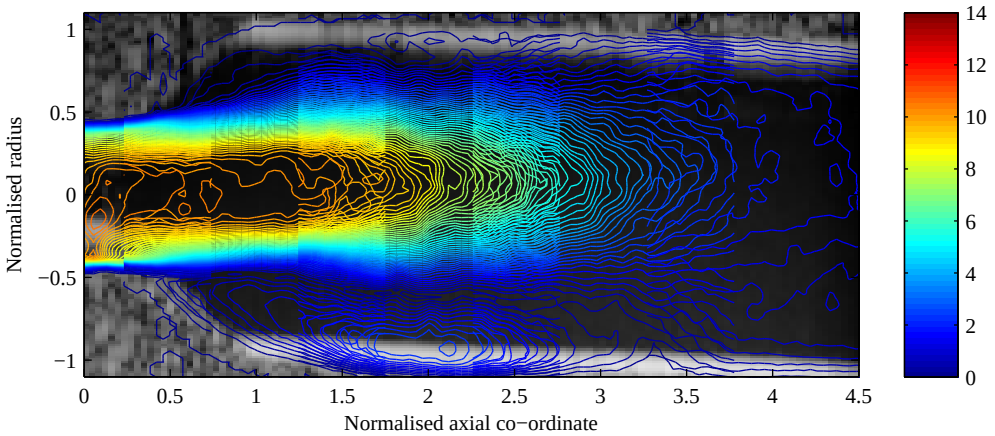

(b) DUS model.

Figure 6.4: *Normalised velocity magnitude contours distal to the 70% stenosis.*

dissipated more proximally in the ultrasound models (Fig. B.7d) despite the transition to turbulence occurring in both models at around $Z = 3$ (Fig. 6.5b). In the 50% model, the maximum velocity was again underestimated by DUS and was accompanied by the detection of spurious velocities outside of the vessel lumen (Fig. B.8b). Qualititative agreement with the PIV data was present until around $Z = 1$, beyond which recirculation ceased in the PIV data but persisted when measured with DUS (Fig. B.8). In general, the agreement between the PIV and DUS velocity profiles was remarkably good for the 60% model (Fig. B.9). Relatively little bleeding of the CFI data occurred at the stenosis throat, and the recirculation regions were similar both in radial and axial size to the PIV data. The transition to turbulence occurred in both models just distal to $Z = 1$, although the jet velocity in the PIV model decreased more abruptly along its length (Fig. 6.5d and Fig. B.9d). In both systems, the velocity profiles had no recirculation at $Z = 4$, indicative of efficient turbulent mixing. In the 70% model, CFI velocities were measured well outside the vessel walls and the peak velocity underestimated the maximum PIV value

(Fig. B.10b). Ignoring the substantial asymmetry of the PIV jet, qualitative agreement (including in maximum velocity) was present at $Z = 1$. By $Z = 2$, the PIV jet had become turbulent and slowed sharply, but in the ultrasound system, the jet extended much further (Fig. 6.5e), leading to poor agreement between the velocity profiles until $Z = 4$, by which point the velocity profiles in each system were largely flat and turbulent.

The best qualitative agreement between the velocity fields measured by PIV and ultrasound was observed in the 30% model; this may be due to the symmetry present in the velocity maps measured by both modalities. The degree of asymmetry in the velocity fields measured by ultrasound, distal to the stenoses, increased with the severity of the stenosis (Figs. 6.2b–6.4b). This is in agreement with the velocity profiles in the PIV models. The variation of the Doppler velocity measurements cannot be displayed in the same manner as the PIV data, since the vector data were not acquired in the same instant and so only time-averaged data can be presented.

For all the stenosis models, a high velocity jet developed downstream of the stenosis (Fig. 6.5). The jet was characterised by a stable region in which the velocity remained largely unchanged, beyond which the velocity decreased. The length of the stable zone reduced with increasing stenosis severity. In the narrowest stenoses (60 and 70%), the stable region was followed by an initially sharp spatial deceleration which became more gradual. For milder stenoses, the end of the stable region was not clearly defined, as the velocity slowly reduced along its length. The length of the stable region was consistently longer when measured in the ultrasound models than in the optical system. Measurements of the stenosis jet length, L_J, agree with this qualitative observation (Fig. 6.6 and Table 6.1): for stenoses where the jet stopped within the observed region ($\kappa \geq 0.6$) the jet length was significantly longer when measured by with DUS. Peak velocity in the jet was significantly higher when measured with PIV than with ultrasound; the mean difference between the measured maximum velocities was 15%. This difference agrees with the observed underestimation upstream. In all the models, the maximum velocity was inversely proportional to $(1-\kappa)^2$, as expected.

The deceleration of the stenotic jet was accompanied by a sharp rise in turbulence intensity (Fig. 6.5). The increase usually occurred more proximally in the PIV models than in the ultrasound models. In the 60 and 70% models, the peak turbulence intensity measured by ultrasound was over 70% higher than when measured with PIV, for comparison, velocity fluctuations under laminar conditions were on the order of 3% and 16% for PIV and DUS, respectively (Fig. 6.5a).

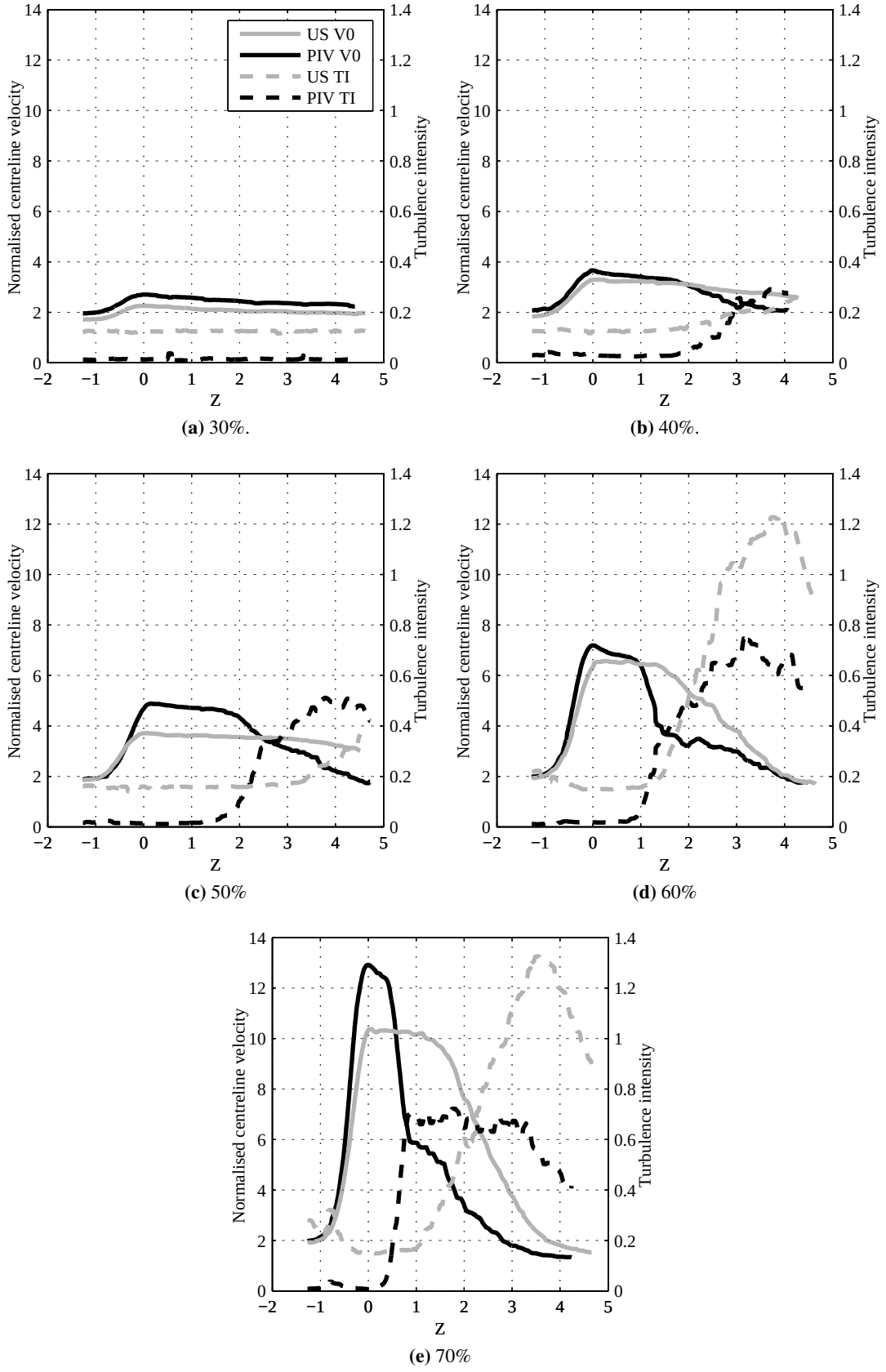

(a) 30%.

(b) 40%.

(c) 50%

(d) 60%

(e) 70%

Figure 6.5: *Centre line velocity and turbulence intensity in the stenosis models.*

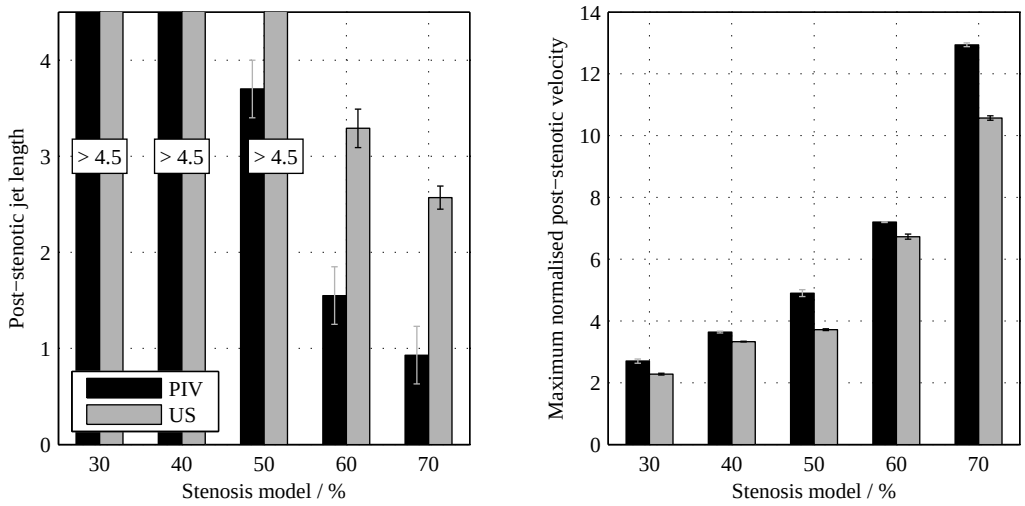

(a) Jet length in the stenosis models.

(b) Peak jet velocity in the stenosis models.

Figure 6.6: *Properties of the stenotic jet in the stenosis models.*

Stenosis	L_J		$\hat{V}_{max}$	
model	PIV	DUS	PIV	DUS
30	> 4	> 4	2.70 (0.07)	2.28 (0.03)†
40	>4	> 4	3.64 (0.03)	3.33 (0.01)‡
50	3.7 (0.3)	> 4	4.90 (0.11)	3.72 (0.03)‡
60	1.6 (0.3)	3.3 (0.3)†	7.20 (0.01)	6.73 (0.08)†
70	0.9 (0.3)	2.6 (0.1)†	12.94 (0.06)	10.57 (0.07)*

Table 6.1: *Stenosis jet properties as a function of* κ. $^{\dagger}p < 10^{-3}$; $^{\ddagger}p < 10^{-4}$; $^{*}p < 10^{-6}$.

6.3.1.2 Comparison of wall shear stress

Wall shear stresses estimated with PIV using methods A and B (see Sect. 5.2.4, page 116), which did not assume the zero slip condition, were extremely sensitive to noise in the velocity point at the wall (Figs. 6.7a–6.7b). Method A produced unrealistic shear stresses at the stenosis throat with Doppler ultrasound (Fig. 6.7a). Inspection of velocity profiles at the stenosis throat ($Z = 0$) reveals that this was due to the measurement of apparent velocities outwith the limits of the lumen (Figs. B.6b–B.10b). All other methods produced values that qualitatively agreed with those estimated using PIV (Figs. 6.7b–6.7e). As seen at the inlet, method E estimated lower WSS than method D, which in turn measured lowered values than method C. Distal to the stenosis, all methods for estimating shear stress except method E measured recirculation.

Comparing the estimated shear stresses with values from the literature suggests which strategy is most appropriate (Fig. 6.7). Considering Poiseuille-like flow throughout the narrowing provides a lower limit for the shear stress, implying that methods D and E, at least over the acceleration phase, are not capable of reliably measuring the WSS. Considering the ultrasound data, it appears that assuming the no slip condition leads to improved WSS estimation, so methods A and B should be rejected.

Other than the experimental results provided by Ahmed & Giddens (1983*a*), shear stress data from similar stenosis geometries is sparse in the literature. Reese & Thompson (1998) developed a simple, analytic model of flow upstream of a stenosis, which can be adjusted for any geometric stenosis. All the WSS methods—by both modalities—estimate lower values of maximum shear stress than predicted by Reese & Thompson (1998) and measured by Ahmed & Giddens (1983*a*). Method C returned the maximum WSS values, but still underestimated the Reese/Ahmed value by 23/41% with PIV, and 42/56% with Doppler ultrasound. It is of value to note that the figure, –41%, is the difference between the value measured by the PIV system and the Poiseuille inlet WSS, suggesting that the Ahmed value is correct. Despite the poor performance of method C at the stenosis inlet, all further WSS calculations and derived parameters in this chapter (such as recirculation length) are based on estimates produced using method C.

Dominant recirculation regions occurred in the 50–70% stenosis models when measured both with PIV and DUS (Fig. 6.9). The approximate sizes of the recirculation regions, L_R, did not vary with the degree of stenosis, although this may be distorted by the lack of information for the less severe models (Fig. 6.8c). For the two cases where the size of the dominant recirculation region was successfully measured by both techniques, significant differences in estimated size were present. (In the 60% model, L_R=4.1 [0.1] by PIV vs. 2.8 [0.1] for ultrasound, $p < 10^{-4}$; for the 70% model, L_R=2.6 [0.1] by PIV vs. 3.0 [0.1] for ultrasound, $p < 0.01$.) The maximum normalised WSS was inversely proportional to $(1-\kappa)$ when measured by both PIV and DUS ($r^2 = 0.98$ and $r^2 = 0.97$, respectively). Significant differences were present in the estimates of maximum WSS at the stenosis throat and in the minimum WSS in the dominant recirculation region (Table 6.2 and Fig. 6.8).

The magnitude of the mean percentage differences between $\hat{\tau}_{w,max}$ when measured by PIV and ultrasound was 41 (26)% (mean [SD]) (range –33 to +75%); the equivalent figure for $\hat{\tau}_{w,min}$ was 32 (130)% (range –73 to +247%). The large variation in the mean differences shows that WSS estimation was difficult with both techniques. In particular, measurement of extremely

Stenosis model	$\hat{\tau}_{w,max}$		$\hat{\tau}_{w,min}$	
	PIV	DUS	PIV	DUS
30	0.057 (0.013)	0.100 (0.008)‡	–0.001 (0.000)	0.000 (0.000)†
40	0.100 (0.010)	0.162 (0.007)‡	–0.005 (0.001)	–0.002 (0.002)†
50	0.200 (0.008)	0.164 (0.010)‡	–0.007 (0.005)	–0.023 (0.007)†
60	0.367 (0.007)	0.307 (0.017)‡	–0.059 (0.003)	–0.075 (0.003)‡
70	0.743 (0.019)	0.497 (0.030)*	–0.086 (0.006)	–0.111 (0.003)‡

Table 6.2: *Maximum and minimum* WSS *in the stenosis models.* $^{\dagger}p < 0.05$*;* $^{\ddagger}p < 0.01$*;* $*p < 10^{-3}$.

low values of shear stress distal to the 30% stenosis was not possible with ultrasound, while for PIV, tracer particles accumulated next to the wall in the recirculation zones, producing large amounts of glare which introduced large localised errors into the WSS measurements (Fig. 6.9).

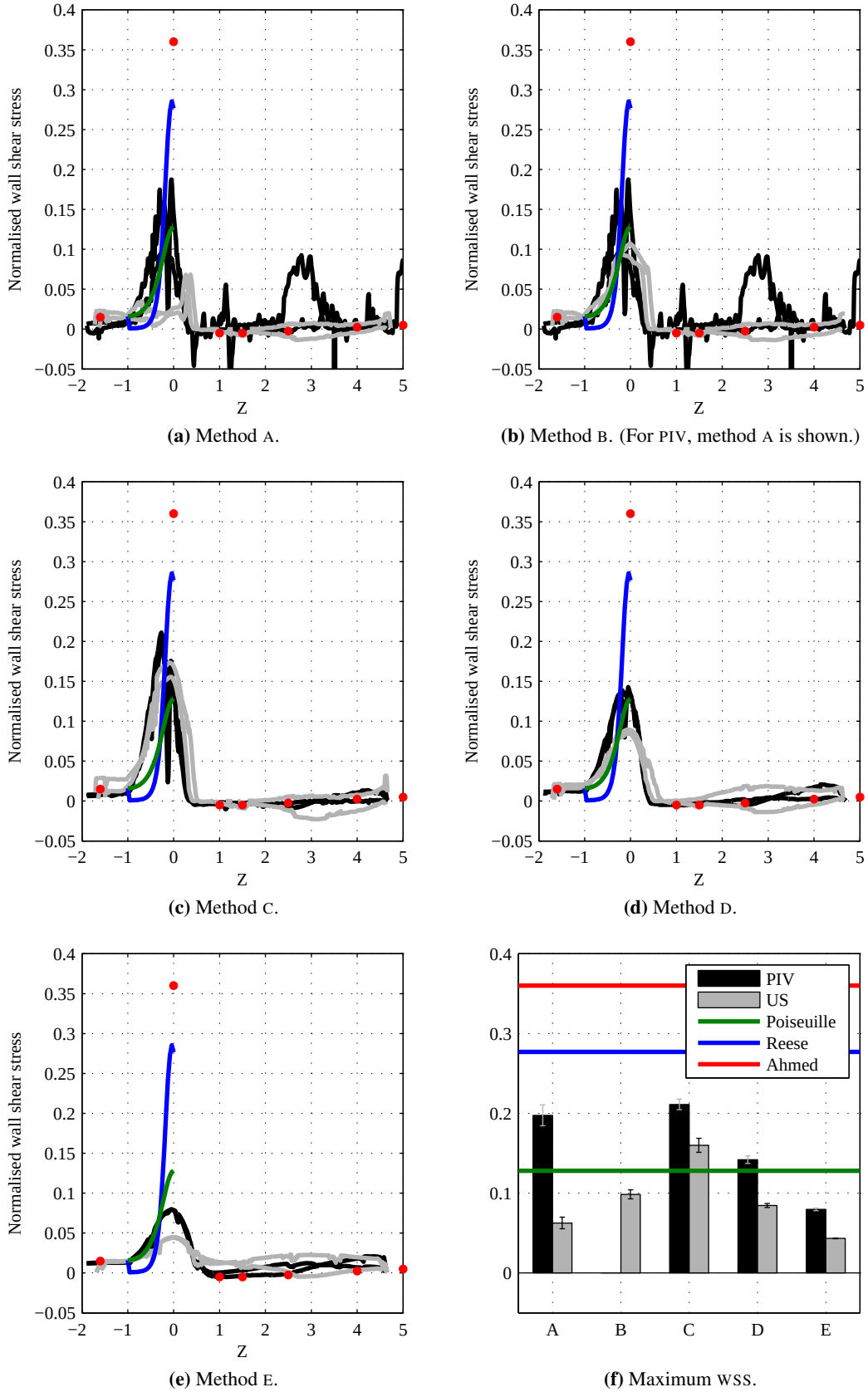

(a) Method A.

(b) Method B. (For PIV, method A is shown.)

(c) Method C.

(d) Method D.

(e) Method E.

(f) Maximum WSS.

Figure 6.7: *Wall shear stress estimated by methods* A–E *in the 50% stenosis model.*

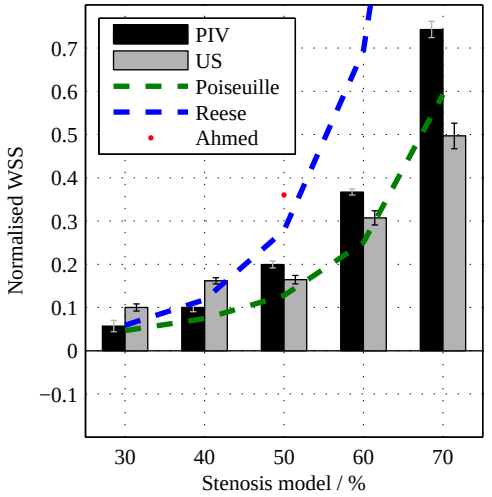

(a) Maximum WSS at the stenosis throat.

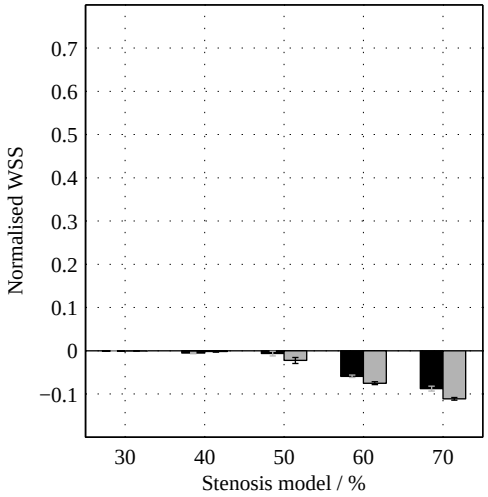

(b) Minimum WSS in the dominant recirculation region.

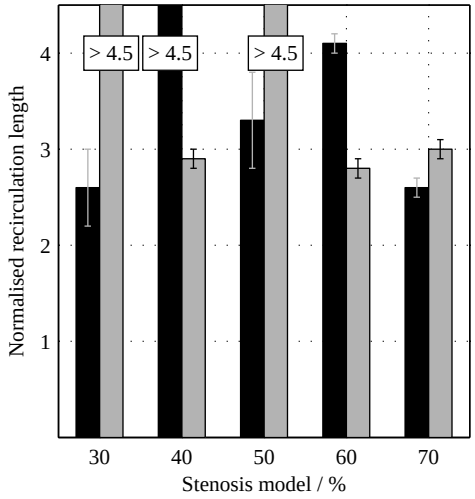

(c) Recirculation length in the stenosis models.

Figure 6.8: *Maximum and minimum* WSS *in the stenosis models.*

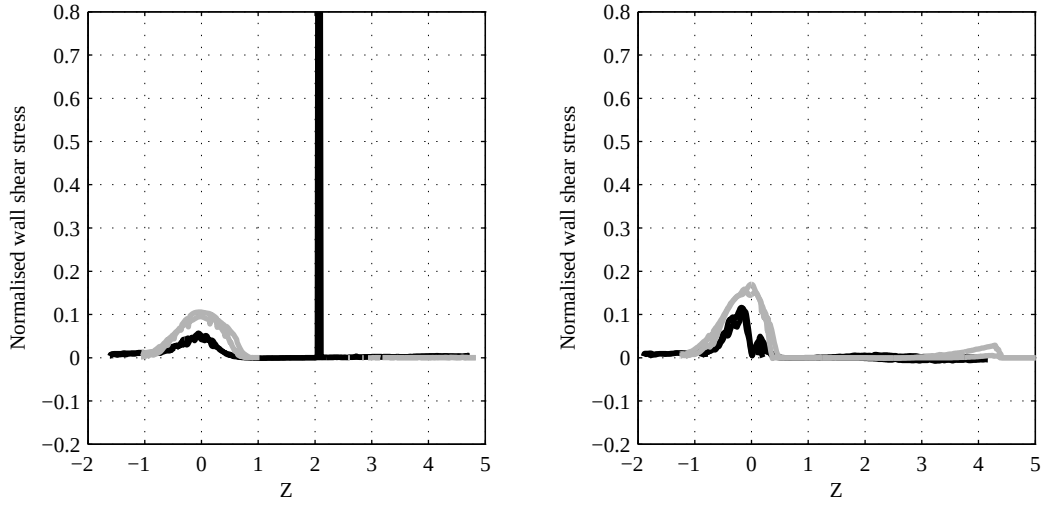

(a) 30%

(b) 40%.

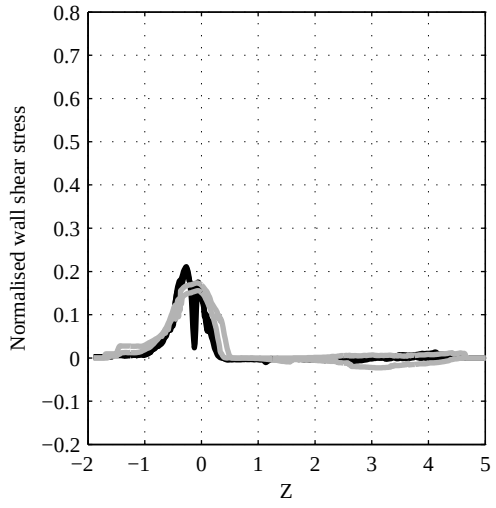

(c) 50%

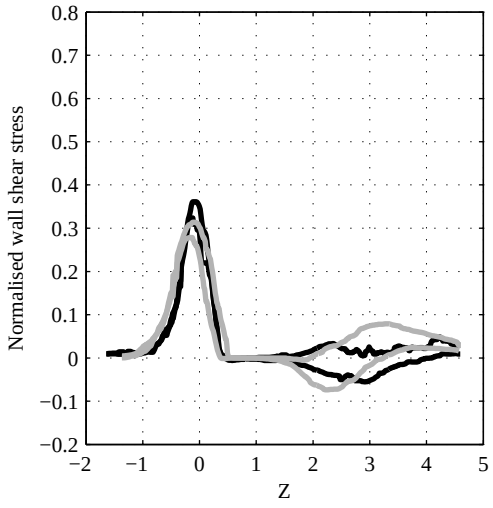

(d) 60%

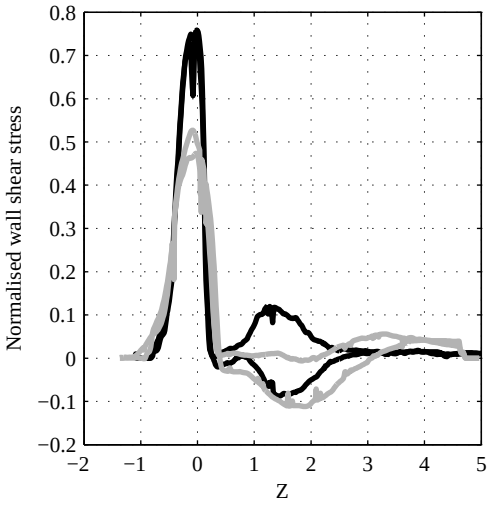

(e) 70%

Figure 6.9: *Normalised wall shear stress in the stenosis models.*

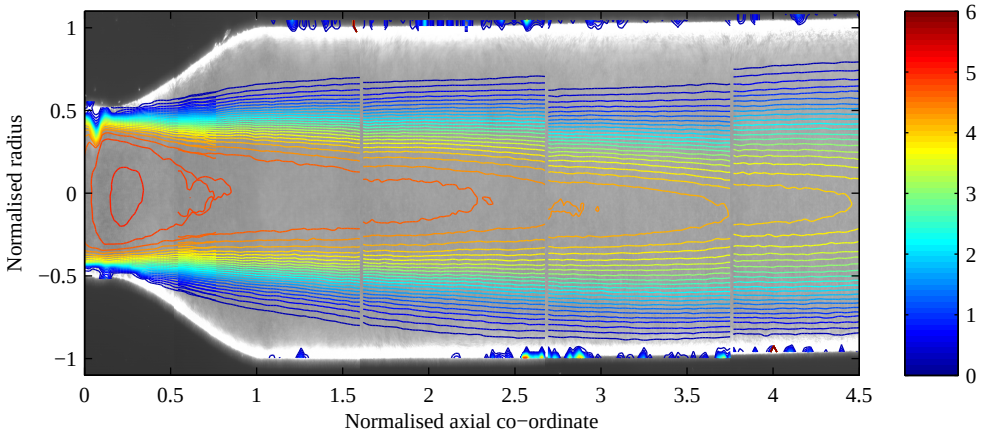

(a) PIV model

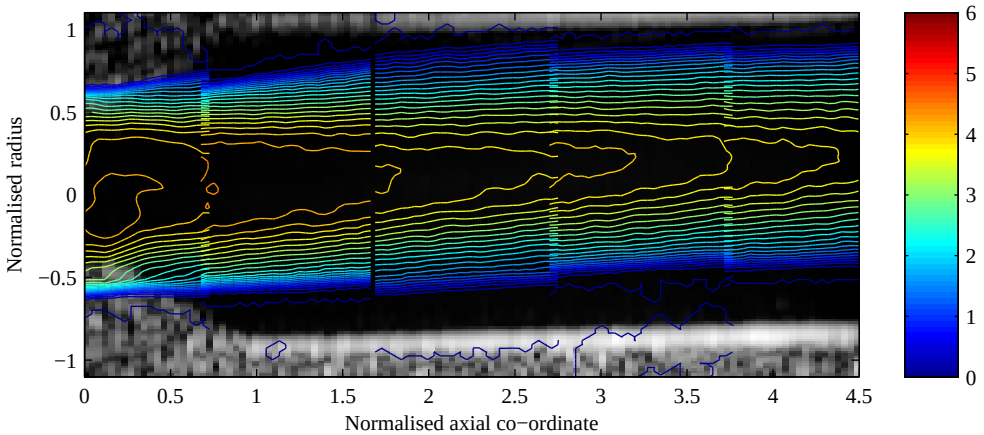

(b) DUS model.

Figure 6.10: *Normalised velocity magnitude contours distal to the 50% stenosis at Re=200.*

6.3.2 Effect of flow rate

6.3.2.1 Comparison between velocities estimated with PIV and Doppler ultrasound

Flow remained laminar and largely symmetric over the region studied at the lowest Reynolds number (Fig. 6.10a and Fig. 6.13a). Downstream of the stenosis throat, the magnitude of the velocity fluctuations increased in the PIV models for Reynolds numbers greater than 200 (from stenotic Reynolds number, $\mathrm{Re}_0 \geq 800$), and at Reynolds numbers greater than 500 for the DUS models ($\mathrm{Re}_0 \geq 1000$), resulting in discontinuities in the reassembled contour plots (Figs. 6.11a–6.12b).

At higher Reynolds numbers, asymmetric recirculation regions developed which were typically next to unstable shear layers (Sherwin & Blackburn, 2005). At $\mathrm{Re} = 400$, the velocity profiles were broadly symmetric at $Z = 1$. The transition to turbulence occurred between $Z = 1$ and

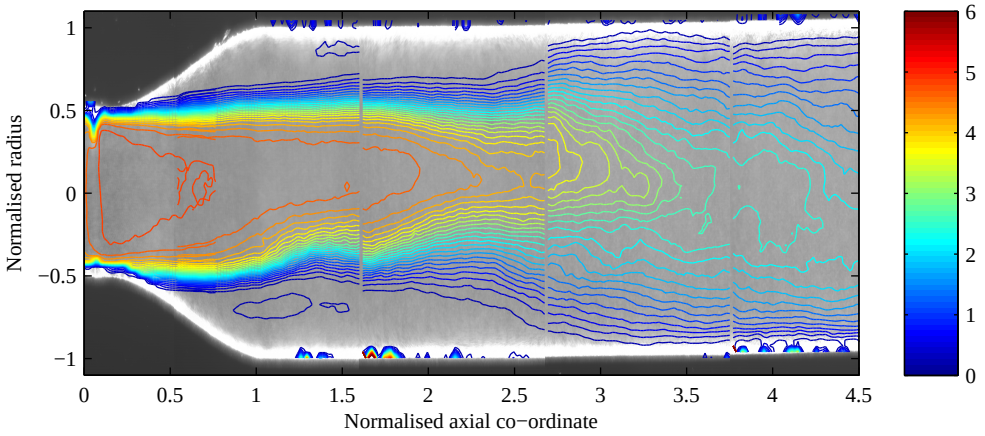

(a) PIV model.

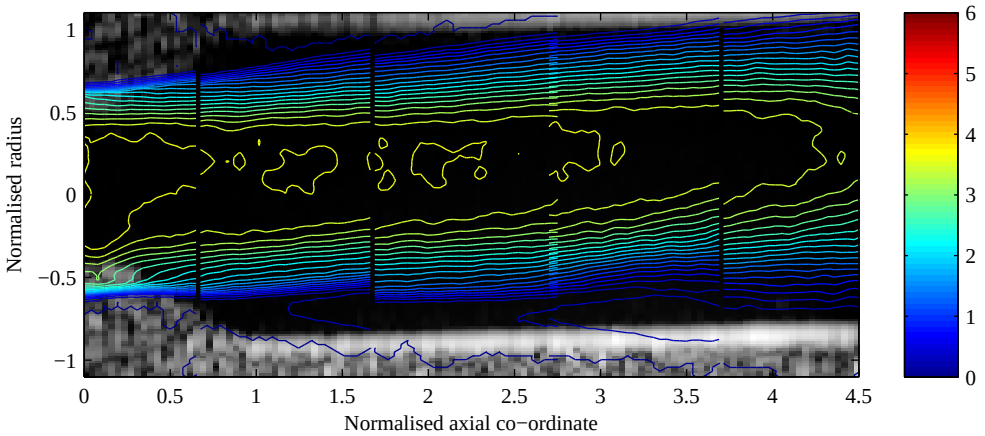

(b) DUS model.

Figure 6.11: *Normalised velocity magnitude contours distal to the 50% stenosis at Re=600.*

$Z = 2$, which is consistent with the end of the recirculation region due to efficient turbulent mixing (Fig. 6.13b and Fig. B.12d). At Re $= 600$, the symmetry at $Z = 1$ remained, but just beyond it the transition to turbulence began (Fig. 6.13b). By $Z = 4$, the velocity profiles were almost symmetric, representative of efficient turbulent mixing (Fig. B.13f). At the highest Reynolds numbers (Re $= 800, 1000$), the velocity profiles at $Z = 1$ were very unstable, with very large velocity fluctuations present in the layer (Fig. B.14c and Fig. B.15c). By $Z = 2$, the velocity profiles were more symmetric, suggestive of momentum exchange between the fluid layers, and by $Z = 4$, the velocity profiles at each flow rate were quite flat (Fig. B.14f and Fig. B.15f). Examining the centreline turbulent velocity fluctuations implies that the transition to turbulence, at both flow rates, began before $Z = 1$ (Fig. 6.13).

The ultrasound data agreed qualitatively with the PIV data at the lowest flow rate except at the vessel wall (Fig. B.16). At the stenosis throat, velocities were measured beyond the ex-

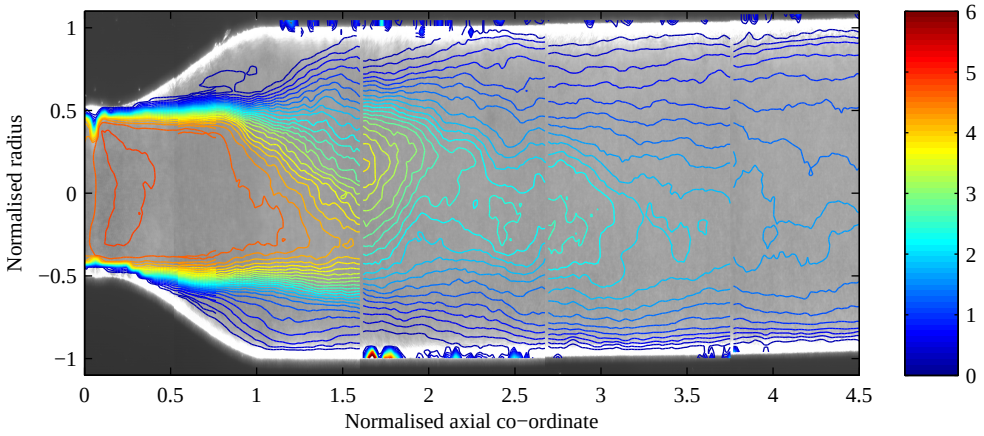

(a) PIV model.

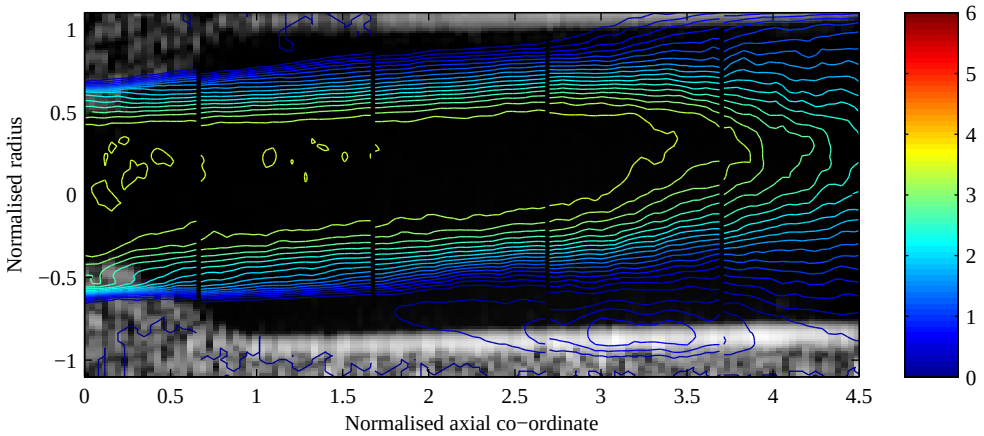

(b) DUS model.

Figure 6.12: *Normalised velocity magnitude contours distal the 50% stenosis model at Re=1000.*

tent of the lumen. Distal to the stenosis, some of the very low velocity profiles were truncated before reaching the wall (Fig. B.16f). At Re = 400, the data were broadly similar at the stenosis throat at as Re = 200. An asymmetric recirculation region developed between $Z = 1$ and $Z = 2$, and persisted beyond the region studied, in contrast to the PIV data (Fig. B.17). Measured with Doppler ultrasound, the flow at Re = 400 remained laminar over the entire region studied (Fig. 6.13b). For Reynolds numbers greater than 400, the flow regime became turbulent around $Z = 3$ (Fig. 6.13) but the general evolution of the velocity profiles did not change, showing bleeding of the colour data in the vessel walls at the stenosis and the persistence of flow separation up to $Z = 4$ (Figs. B.18–B.20).

Distal to the stenosis, the stenotic jet was again characterised by a high velocity region that was relatively free from velocity fluctuations. As the fluid decelerated, these fluctuations increased in magnitude (Fig. 6.13). The length of the jet was consistently greater when estimated with

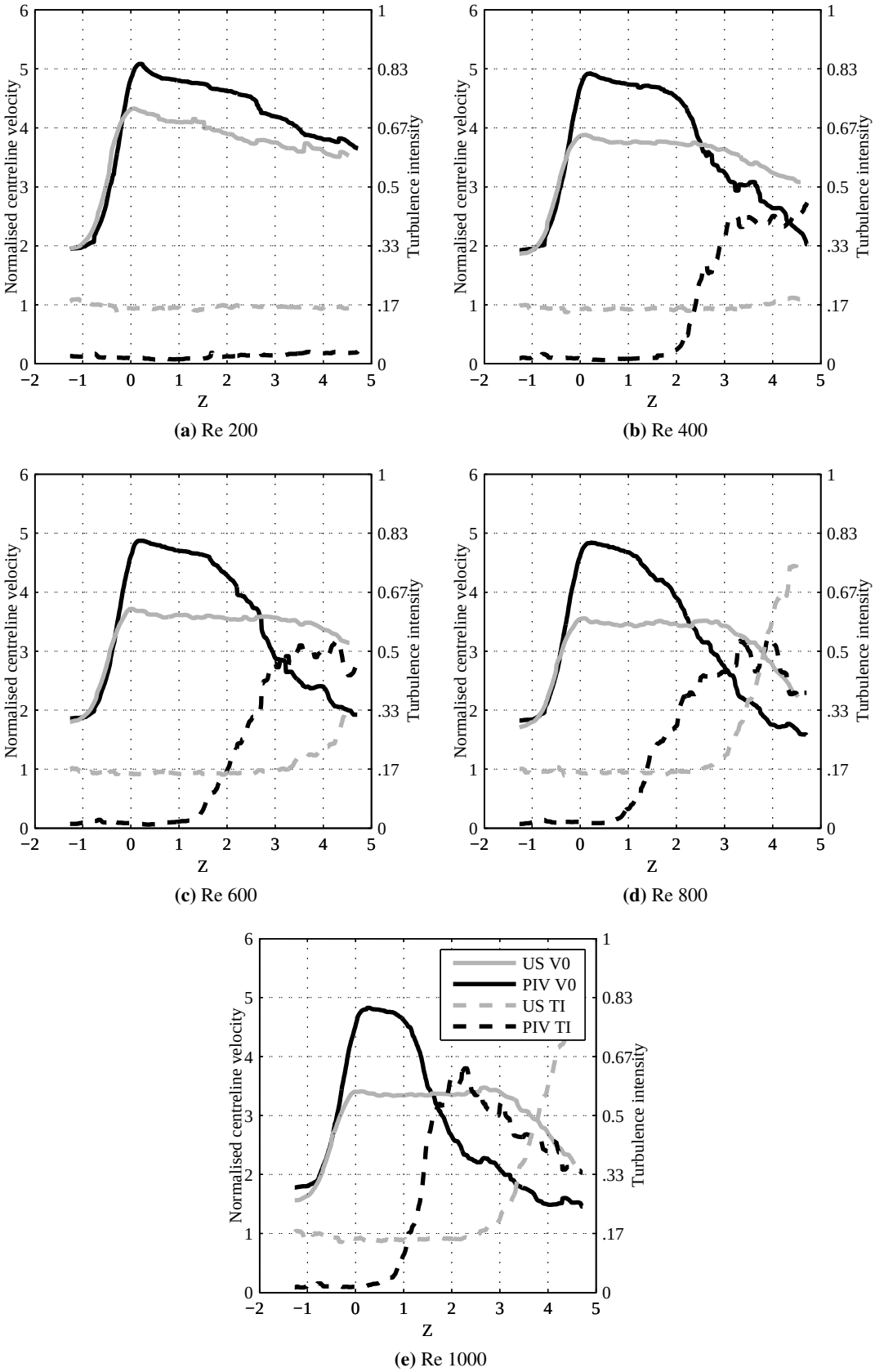

(a) Re 200

(b) Re 400

(c) Re 600

(d) Re 800

(e) Re 1000

Figure 6.13: *Centre line velocity and turbulence intensity as a function of flow rate.*

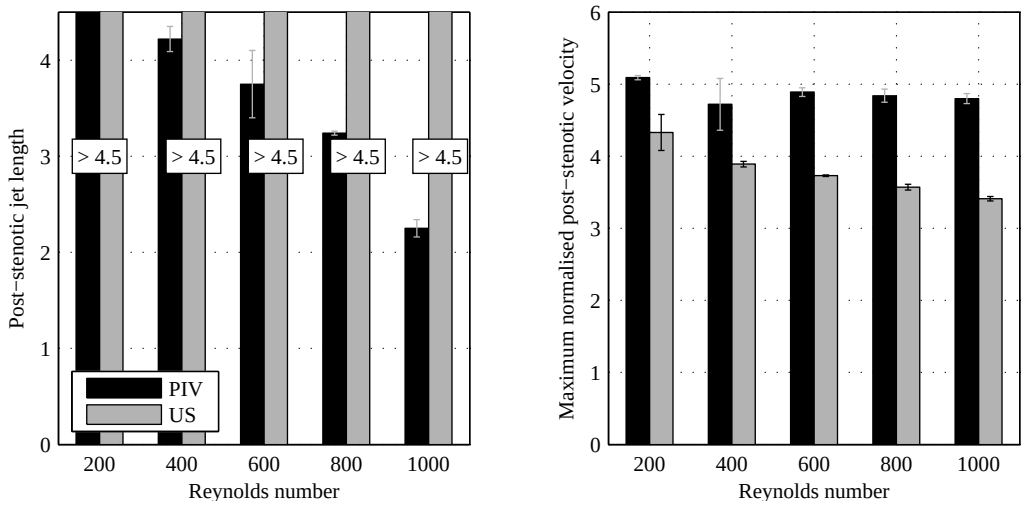

(a) Stenosis jet length in the 50% model. **(b)** Peak stenotic jet velocity in the 50% models.

Figure 6.14: *Stenosis jet properties as a function of the flow rate.*

Doppler ultrasound than with PIV, this corresponded with the peak in the velocity fluctuations, which occurred more proximally in the optical models. In the PIV models, the jet length, L_J, was negatively related with the Reynolds number ($r^2 = 0.96$, Fig. 6.14a), confirming that the jet length reduces as the flow rate increases. This is expected, as momentum is transferred more efficiently between fluid layers at higher Reynolds numbers. In the ultrasound model, the jet length extended beyond the region studied for all flow rates, preventing the detection of any relationship between L_J and the flow rate. The peak velocity did not change with flow rate when measured with PIV (Fig. 6.14b). When studied with DUS, however, $\hat{V}_{max}$ was linearly and negatively related to the normalised flow rate ($r^2 = 0.94$). The maximum velocities measured by both modalities were all significantly different (Table 6.3). The differences increased linearly, and became more significant, as the flow rate increased; this is consistent with the decrease in the measured maximum velocity by DUS. The mean difference between the measured peak velocities was –22 (6)% (range –15% at Re = 200 to –30% at Re = 1000).

6.3.2.2 Wall shear stress comparison

All wall shear stresses presented here were calculated using method C (Sect. 5.2.4 and Fig. 6.7). With both modalities, the normalised wall shear stress decreased with increasing flow rate (Figs. 6.15–6.16). This is a consequence of the normalisation criteria, which divides the measured WSS by the square of the mean velocity (Eq. (2.10)). The maximum WSS, $\hat{\tau}_{w,max}$, at the

Re_{-1}	L_J		$\hat{V}_{max}$	
	PIV	DUS	PIV	DUS
200	> 4	> 4	5.09 (0.03)	4.33 (0.25)‡
400	4.22 (0.13)	> 4	4.72 (0.36)	3.89 (0.04)†
600	3.75 (0.35)	> 4	4.89 (0.06)	3.73 (0.01)§
800	3.24 (0.02)	> 4	4.84 (0.09)	3.57 (0.04)*
1000	2.25 (0.09)	> 4	4.84 (0.07)	3.41 (0.03)§

Table 6.3: *Properties of the post-stenotic jet in the 50% model.* $^{\dagger}p < 10^{-2}$; $^{\ddagger}p < 10^{-3}$; $^{*}p < 10^{-4}$; $^{\S}p < 10^{-5}$.

stenosis throat was inversely proportional to the Reynolds number when measured with PIV ($r^2 > 0.99$) and with DUS ($r^2 > 0.99$) (Fig. 6.15a). Considering the normalisation criteria, this implies that, in each model, the maximum WSS increased linearly with flow rate. Significant differences were present between the PIV and DUS measurements of maximum wall shear stress for all except the lowest flow rate (Table 6.4). The magnitude of the percentage difference between the DUS and PIV measurements increased with flow rate (mean 19 (12)%, range –29 to +3%). Considering only the mean of the percentage differences yields a mean difference of –18 (14)%, confirming that the ultrasound system measured lower values. At Re = 1000, the PIV value of maximum WSS is some 45% less than when measured with LDA (Ahmed & Giddens, 1983*a*). This value is again very close to the difference observed using method C and the Poiseuille WSS (–41%).

All measured maximum wall shear stresses were greater than the equivalent Poiseuille case (Fig. 6.15a). The percentage difference between the Poiseuille value and the measured value increased as the flow rate increased for the optical models—this implies that the flow became less Poiseuille-like. Conversely, differences between the Poiseuille value and the ultrasonically estimated maximum WSS decreased with increasing flow rate. Drawing conclusions, it would appear that flow became *more* parabolic when passing through a stenosis at higher Reynolds numbers. This is an unlikely conclusion, implying some source of error in the instrumentation arising from the finite sample volume size (see Sect. 6.4.1.2, p. 163).

Significant differences were present in the estimated values of the minimum WSS, $\tau_{w,min}$, measured with PIV and DUS (Table 6.4 and Fig. 6.15c). In percentage terms, the range of differences between the ultrasonically and optically estimated minimum values runs from 10 to 1500%. This extreme range spans three orders of magnitude, which is an artifact of measuring values in the vicinity of zero. The difficulty of dealing with such small numbers was evident in the PIV

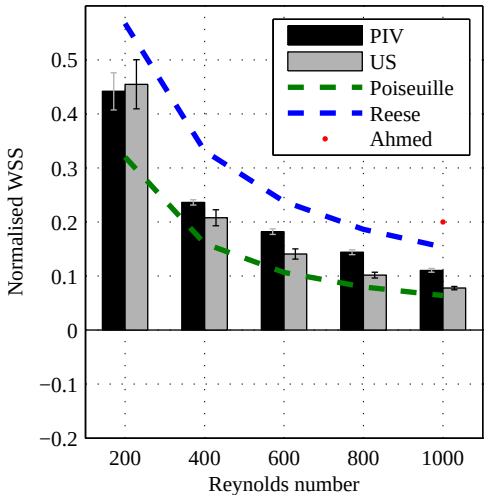

(a) Maximum WSS at the stenosis throat.

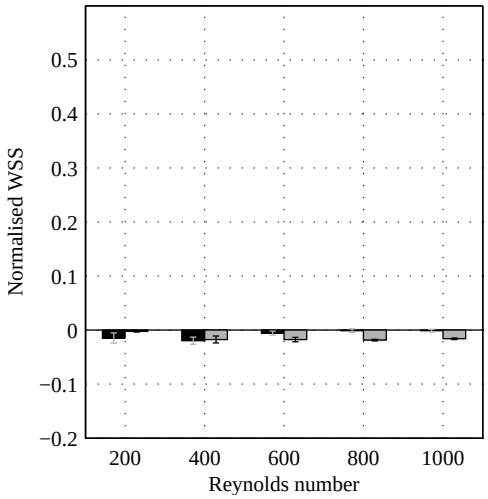

(b) Minimum WSS in the dominant recirculation region.

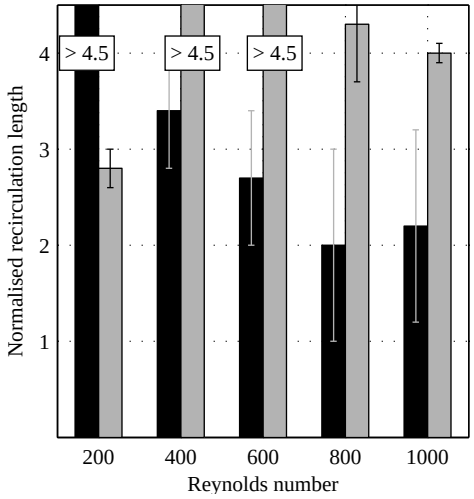

(c) Length of the recirculation regions.

Figure 6.15: *Maximum and minimum* WSS *in the stenosis models.*

models for Reynolds numbers greater than 400. In these cases it was not possible to distinguish which recirculation region was dominant, since the magnitude of the minimum (negative) shear stress was on the order of the noise level, so the minimum WSS represents the average minimum value from both walls.

The length of the dominant recirculation region reduced as the flow rate increased when measured with PIV, although due to the large standard deviations, the significance of this is in question (Fig. 6.15c). Drawing conclusions from the ultrasound measurements of L_R would be tentative, since the dominant recirculation regions extended beyond the region studied for

Re_{-1}	$\hat{\tau}_{w,max}$		$\hat{\tau}_{w,min}$	
	PIV	DUS	PIV	DUS
200	0.442 (0.034)	0.455 (0.045)	–0.015 (0.010)	–0.002 (0.001)†
400	0.236 (0.005)	0.208 (0.015)†	–0.020 (0.007)	–0.018 (0.006)
600	0.182 (0.005)	0.141 (0.009)‡	–0.006 (0.004)	–0.018 (0.004)‡
800	0.144 (0.005)	0.102 (0.005)*	–0.001 (0.003)	–0.019 (0.002)*
1000	0.110 (0.004)	0.078 (0.003)*	–0.001 (0.003)	–0.016 (0.001)*

Table 6.4: *Maximum and minimum* WSS *in the 50% stenosis model.* $^{\dagger}p < 0.05$*;* $^{\ddagger}p < 0.01$*;* $^{*}p < 10^{-3}$

intermediate flow rates, although, if one ignores the lowest flow rate, the length does appear to be reducing.

6.3.3 Comparison with the literature

The asymmetry present in the PIV system contrasts with previous data obtained using plexiglass models (Ahmed & Giddens, 1983*a*) and with computational studies (Ryval et al., 2004). The asymmetric data may be compared with previous studies by reflecting these velocity data about the vessel axis and taking the mean (Fig. 6.17).

At the stenosis throat, the maximum difference between the previously published data and the PIV data is 15%. By continuity, one would expect the normalised velocity in a 50% stenosis (by diameter) to be four, thus it initially appears that some uncertainty is present in the PIV data. However, Ryval et al. (2004) also noticed a deviation between the Ahmed & Giddens' data and their computational model. After rescaling their flow rate, they obtained the same normalised results and concluded that the Reynolds number quoted by Ahmed & Giddens had been rounded up. Prudence dictates that all results reported by these authors should be treated with caution.

Comparison of the measured velocity profiles with (Ahmed & Giddens, 1983*b*) at Re = 1000 reveals a qualitative agreement until $Z = 2.5$ (Fig. 6.18). At the stenosis throat, the maximum velocity measured with PIV is 10% higher than by Ahmed & Giddens. The DUS velocities are around 17% lower than the LDA data. As at Re = 500, maximum velocities measured with LDA scarcely exceed $\hat{V} = 4$, the value one would expect by continuity. Distally, the DUS data agree well (excepting the maximum velocity) with the LDA data until $Z = 4$. At $Z = 1$, the PIV data agree well with the LDA data except at the walls, although this appears to be an artifact of symmetrisation. Beyond $Z = 1$, the PIV and LDA data are in poor agreement. The PIV data

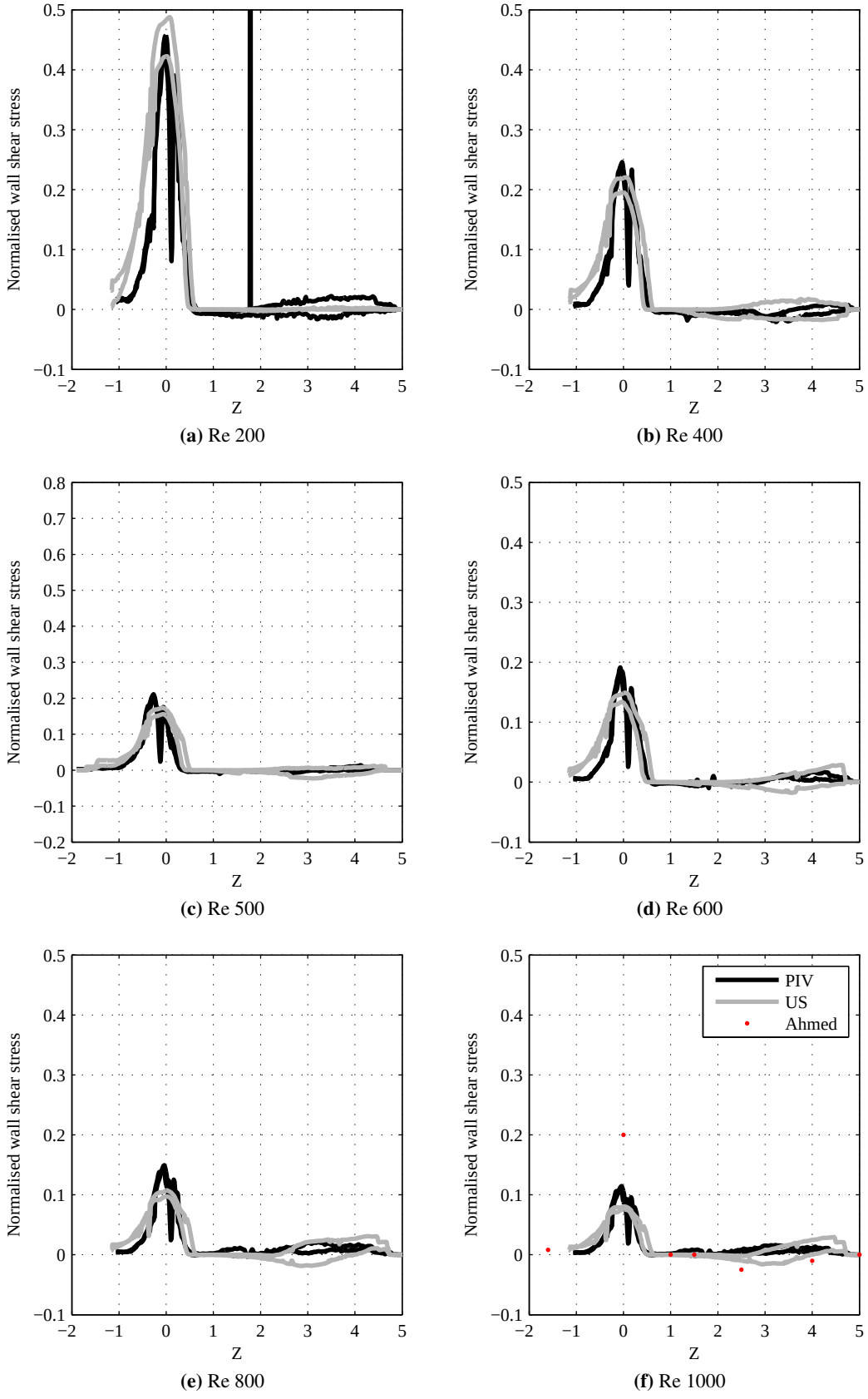

(a) Re 200 **(b)** Re 400 **(c)** Re 500 **(d)** Re 600 **(e)** Re 800 **(f)** Re 1000

Figure 6.16: *Wall shear stress as a function of flow rate.*

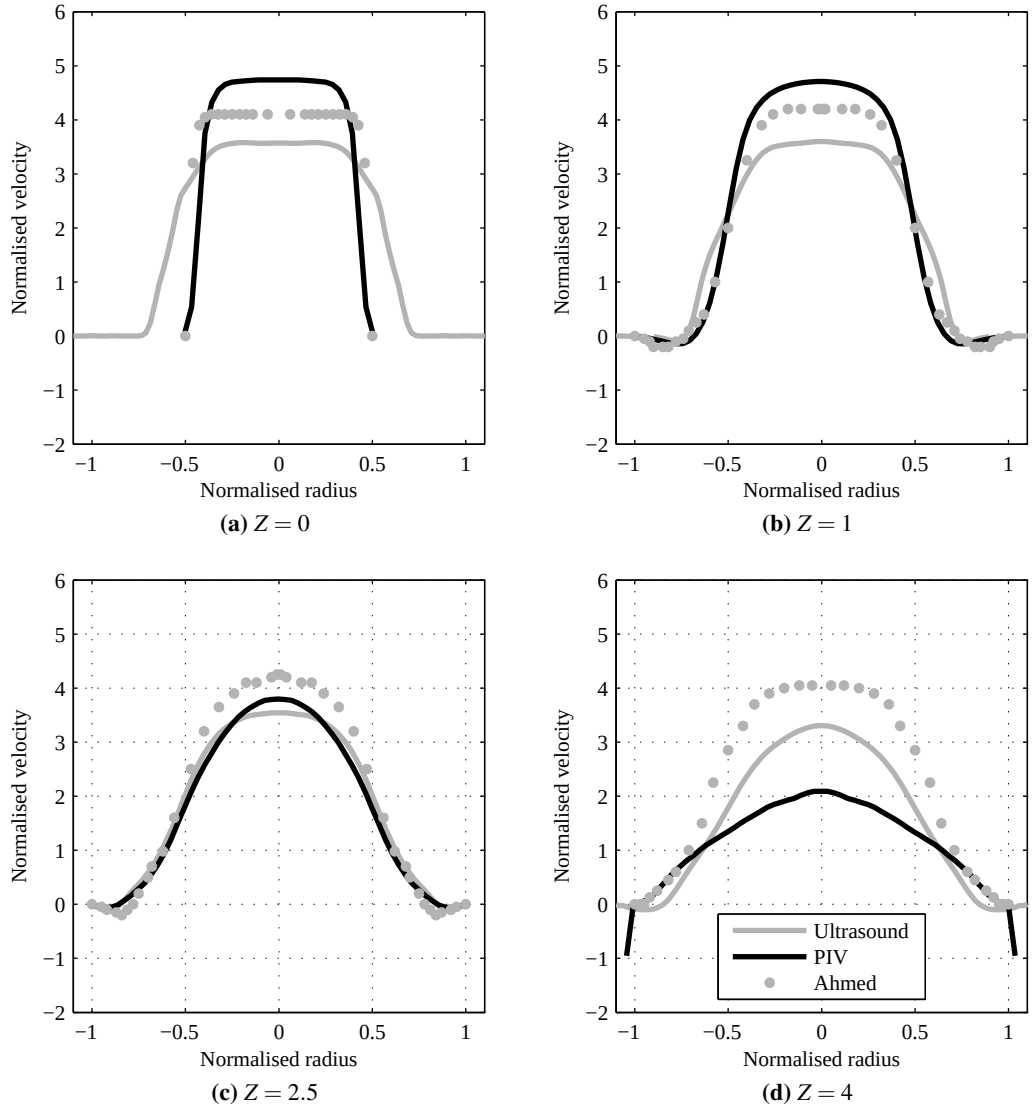

(a) $Z = 0$ **(b)** $Z = 1$ **(c)** $Z = 2.5$ **(d)** $Z = 4$

Figure 6.17: *Velocity profiles in the 50% stenosis model at* $\mathrm{Re} = 500$ *after symmetrisation, compared with data published by Ahmed & Giddens (1983*a*).*

implies that the has already become transitional, resulting in the breakdown of the high velocity jet and efficient mixing of momentum.

The asymmetry present in the more severe stenoses is evident in the velocity profiles calculated from the same data. Box-whisker plots of the velocity profiles measured by PIV show the increasing variability of the velocity measurements with axial distance and the degree of stenosis (Figs. B.1–B.5). In the 40, 50 and 60% stenoses, the velocity fluctuations are greater on the side of the jet next to the larger region of flow separation (Figs. B.2–B.4). (The presence of turbulence in the 70% model made quantifying regions of increased fluctuations very difficult.) This increased variation is unlikely to be due to turbulence, rather it is probably due to oscilla-

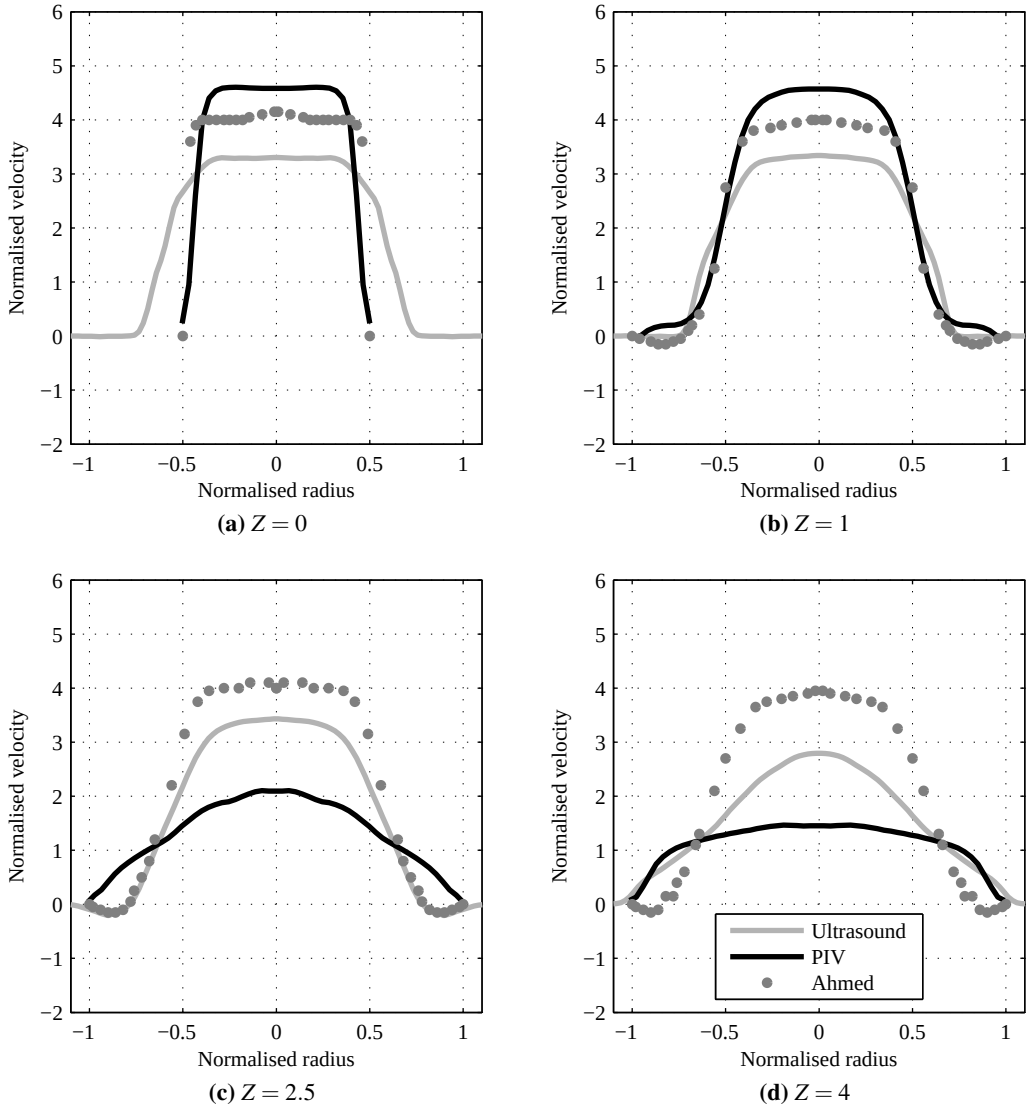

(a) $Z = 0$ **(b)** $Z = 1$ **(c)** $Z = 2.5$ **(d)** $Z = 4$

Figure 6.18: *Velocity profiles in the 50% stenosis model at* $\mathrm{Re} = 1000$ *after symmetrisation compared with data published by Ahmed & Giddens (1983*b*).*

tions in the shear layer that are introduced by upstream instabilities and fluctuations (Sherwin & Blackburn, 2005). Examining sequences of images of the velocity maps reveals that the jet direction varies, even under steady flow. Data collected with PW Doppler ultrasound distal to the stenosis also show this characteristic, periodic behaviour for low stenotic Reynolds numbers (Fig. 6.19).

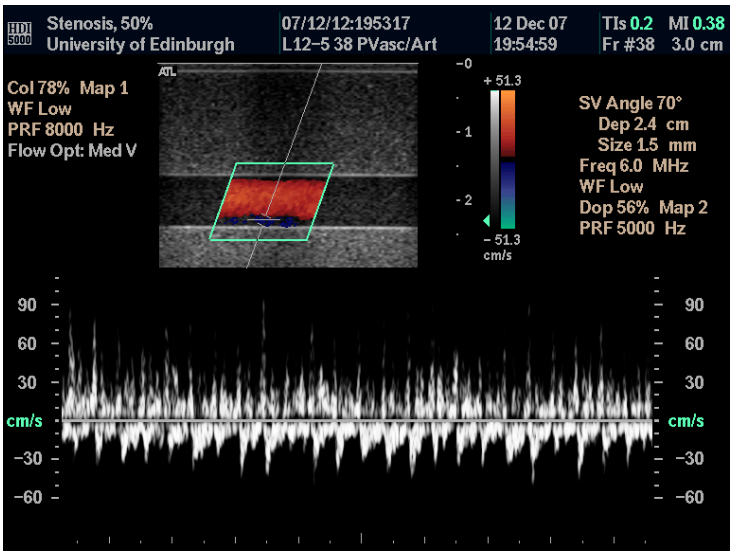

Figure 6.19: *Velocity fluctuations measured with* PW *Doppler ultrasound distal to the 40% stenosis model.*

6.4 Discussion

Accurate estimation of peak velocity through stenoses is essential to minimise patient risk. Doppler ultrasound is typically used to pre-screen patients for angiography, but its ability to accurately measure the peak velocity is questionable and highly dependent on operator experience. This chapter has examined the performance of a dual-beam Doppler system in idealised stenoses by comparing measurements made in the paired flow systems developed in Chapt. 5.

The wall shear stress is hypothesised to play a substantial role in the initiation and progression of atherosclerosis. Measuring the WSS in-vivo is hard, particularly in arteries that cannot be considered as straight tubes. This chapter has compared WSS measurements using the dual flow system to estimate the error in the Doppler ultrasound measurements.

6.4.1 Effect of the degree of stenosis

6.4.1.1 Velocity comparison

In the sense that flow through each stenosis was characterised by a high velocity jet, recirculation accompanied by regions of low and reversed shear stress, and that the size of these features broadly decreased as the stenosis severity increased, measurements made with Doppler ultra-

sound agreed with the gold standard, PIV. However, a more meaningful comparison between the systems requires quantitative analysis.

Considering the maximum velocity in each stenosis, significant differences were present between the PIV and ultrasound data. However, significant differences were also present upstream of the stenosis (Chapt. 5), although not to the same level, and the mean underestimate, 15%, was the same. This implies that the differences arose not because of any change to the fluid behaviour, but because of a combination of the frequency dependent attenuation of the tissue mimicking material and the ultrasound instrumentation. As discussed in Sect. 3.4.1 (p. 85) theTMM attenuates higher frequencies of ultrasound more than lower frequencies. This increases in an approximately linear manner in the range 1–10 MHz, such that the mean frequency of the travelling pulse is lowered. When the received signal is demodulated, the resultant Doppler frequencies are lower also (Evans & McDicken, 2000, p 174–178). No relationship existed between the degree of underestimation and the degree of stenosis.

Progressing downstream of the stenosis, large differences occurred: the lengths of the jets were shorter when measured with PIV; the recirculation regions were different sizes in the ultrasound/optical models; and the asymmetries were qualitatively more pronounced in the PIV models. Two hypotheses can be considered to explain this situation; either the PIV system was a direct analogue for the ultrasound system and the differences were artifacts of the experimental procedure used with the ultrasound system, or something unforeseen resulted in different behaviour in each system.

To validate the first argument, potential sources of different behaviour must be analysed. The most likely source for the differences between the two flow systems was the Reynolds number. However, this was carefully controlled by regularly testing the fluid viscosity, ensuring the temperature was within narrow limits during data acquisition, and by measuring the flow rates with a graduated cylinder and stopwatch. Consequently, a high degree of confidence—albeit qualitative—exists that the normalised flow rates were similar in the stenosis models. That the data for the mildest stenoses agree provides support to this argument. Examining the geometry of each stenosis model, even after distension (which was minimal), suggests that the degree of stenosis, κ, was very well matched between each model, so any differences in the gross amount of narrowing were unlikely to because of the observed differences.

Another geometric problem may have played a more important role. When the PIV models were constructed, the "lip" that formed at the meeting point of the core rods was difficult to remove, due to the high tensile strength of the silicone. Although it was possible to clear the majority of it with stiff pipe cleaners, complete removal—and verification of its removal—was difficult (Fig. 5.3). Consequently, any residual lip may have caused some disturbance at the stenosis throat, which would introduce minor instabilities to the flow, decreasing its stability. This could lead to transitional fluid behaviour occurring proximally; examining the turbulent velocity fluctuations, the sharp increase in the TI always occurs more proximally in the PIV models than in the ultrasound models (Fig. 6.5). Alternatively, any residual lip may introduce asymmetry to the stenosis throat, which may affect the formation of the jet, causing increased distal asymmetry.

In the ultrasound models, a similar effect occasionally occurred. When flow was first pumped through the phantoms, sometimes the post-stenotic jet was extremely skewed to one side. In these cases, careful examination of the stenosis throat often revealed a flap of TMM attached to the lumen. Typically, the flow phantom required reconstruction, but sometimes acceptable flow conditions could be restored by pushing a core rod back towards the throat (guided by the B-mode image) and dislodging the flap.

An alternative explanation for different fluid behaviour lies in the different fluids used. The PIV fluid contained scattering particles at a very low concentration (<0.1%). The ultrasonic BMF contained orgasol particles at a concentration close to 2%. Although the concentration of orgasol particles was low, compared to blood, for example, any effects due to non-Newtonian behaviour could be expected to be an order of magnitude larger than similar effects in the PIV fluid. If the BMF is a shear thickening fluid, then at the outlet of the stenosis, the high shear regions at the edges of the jet would effectively have higher viscosities, and hence lower Reynolds numbers, locally reducing the Reynolds number and rendering the flow more stable. Practically, it is likely that the magnitude of any hypothetical viscosity change would be less than 1%, even for the acoustic BMF, since the concentrations are low and the particle sizes are very much smaller than the vessel diameter.

If one disregards the geometric differences, non-Newtonian effects, and accepts that the Reynolds numbers were the same in both models, then the error must lie with the instrumentation. Assuming temporarily that the ultrasound system is a gold standard, then the most likely reason why the PIV system measures a much shorter jet length may be due to the presence of through-

plane velocities. If the flow is turbulent, fluid particles will be exchanged between the layers. This will reduce the signal-to-noise ratio for each interrogation area, as particles passing through the light sheet may be imaged in one frame, but not the other. Such particles bias the displacement of the IA towards zero (Westerweel, 1997), and would consequently reduce the apparent jet velocity in regions of turbulence. To reduce the effect of through plane velocity, the SNR in each IA may be increased by increasing the size of the interrogation areas, at the expense of velocity resolution. Velocity maps calculated with larger IAs (64×64 pixels^2) still demonstrated the abrupt end to the stenotic jets, suggesting that the PIV measurements were an accurate representation of the particle (and hence fluid) motions.

The optical data consisted of three repeated collections, each consisting of fifty pairs of images. Each set was collected at the optimum speed of the system, of around 15 Hz. Ultrasonic measurements allowed the buffer on the machine to fill up with the beam steered in one direction, before steering the beam in the other direction and recollecting the data. The buffer on the ATL5000 is large enough to store between 230 and 310 images, depending on the current transducer. As a consequence, each vector map measured with Doppler ultrasound is a combination of around 500 separate image frames, over ten times the number of velocity measurements as the PIV data. The expected outcome is that random noise should be more symmetric in the ultrasound system, reducing any biasing effects due to small sample sizes. Although this is a genuine effect, any major random error affecting one measurement set would not be present in another, by definition. However, the mean velocity profiles acquired with PIV at each location are usually quite representative (for the 70% model, one acquisition at $Z = 1$ is noticeably different to the other two sets), implying that, despite the smaller sampling set, the PIV data was representative of experimental conditions.

Considering the alternative hypothesis, that the fluid dynamics in both systems were equivalent and that the PIV system was a gold standard, the large size of the ultrasonic sample volume may have increased the smoothing of the velocity field. In Chapt. 3, the full width, half-maxima of the beam width was measured with a hydrophone, a micro-manipulator and an oscilloscope; it ranged from 2.4–3.9 mm. This beam width was for the 5 MHz transducer, so one might expect a comparable or larger width for lower frequencies. Recall that the vector data were acquired from two directions. It is reasonable to assume that the effective sample volume would be larger than the single beam approach, since the combined vector velocity estimate is derived from the mean of the mean frequency estimated in each sample volume. Consequently, the degree of

spatial smoothing (over the combined sample volume sizes) at any one site may be substantial. The effect of this larger sample volume on a high velocity post-stenotic jet that abruptly slows down (since we are testing the hypothesis that the PIV data are accurate) would be to reduce the peak velocity, to extend the jet length, and to make it more symmetric. All three of these effects would occur because the increased spatial averaging would reduce the magnitude of large spatial gradients. The symmetrisation effect would be aided by the existence of a torus of recirculation regions distal to the stenosis. This torus would not be perfectly symmetric, but any asymmetries may be exaggerated by the PIV data, as it measures only one plane through the stenosis models. (The plane thickness is equal to the light sheet thickness, which was less than 1 mm.) The large width of the ultrasound beam would measure an increased volume fraction of the torus of recirculation regions, with the effect that the apparent size of small recirculation regions would be increased, with the opposite applying to larger ones.

Quantifying the magnitude of the sample volume effect is difficult. A system is either symmetric, or it is not. Under a rigorous regime, none of the velocity profiles measured in any of the stenosis models were symmetric. Arbitrary figures of merit designed to assess the degree of symmetry are subjective, so qualitative descriptions are as valid. Examining Figs. 6.2–6.4b, one can imagine that the 30 and 50% ultrasound velocity maps are broadly the same as the PIV data. However, the 70% PIV and DUS data are extremely different from one another, both in terms of jet length and asymmetry. The ultrasound jet persists beyond $Z = 2.5$, but entire length, L_J, in the PIV model is less than one. Although L_J is defined by the centreline velocity, and the PIV jet appears to persist away from the centreline to $Z \approx 1.5$, this still corresponds to an axial displacement of 8 mm—twice the size of the beam width and hence larger than one might imagine the effective sample volume size of the dual beam ultrasound system.

Having discussed possible reasons for the observed differences, it seems clear that neither hypothesis is entirely true. Hypothesis one proposed that the PIV system adequately described the fluid dynamics in both systems, and that any differences were due to flaws in the ultrasonic measurement, arising from procedure or instrumentation. An increased amount of symmetry is expected under this regime, along with lower shear rates and hence lower maximum velocities. However, the increased effective sample volume size is unable to reconcile the large differences in the stenotic jet length, suggesting hypothesis two—that some unexpected flaw in the PIV system produced deviations from the idealised fluid dynamics—is at least partly valid. The

most likely source of error lies in imperfections in the PIV stenosis models at the throat, which introduce instabilities in the flow that cause the transition to turbulence more proximally.

6.4.1.2 Wall shear stress comparison

The decision to settle on method C as the preferred strategy for estimating WSS was not taken only on the basis of the inlet wall shear stresses. Having obtained estimates of WSS by all the methods through the stenosis constrictions and downstream, it was clear that some methods were unsuitable. Using Doppler ultrasound with method A fails in the narrowest part of the stenosis as the colour Doppler measurements extend into the vessel wall, lowering the shear stresses. Although B produces broadly similar values to method C (and agrees much better with Poiseuille values in the inlet region), the measurements contain a lot of experimental noise, since they include the lowest velocity point (which was set to zero in methods C–E). Methods D and E produced curves with similar shapes to C along the length of the stenosis, but with smaller magnitudes, since the shear rates were estimated using a larger δx. The final piece of evidence that recommended method C instead of the other strategies was considering the Poiseuille condition in the stenosis throats. At the narrowest part of the stenosis, the velocity profile is expected to be mostly flat, with a thin boundary layer. Consequently, the expected shear rate would be be higher than the undisturbed, parabolic case. Only method C measured shear stresses greater than the undisturbed value using both techniques (Fig. 6.7f).

The maximum wall shear stresses (measured using method C) were significantly higher in the PIV models than in the ultrasound models. Shear stresses estimated in the tightest stenosis with DUS were actually lower than the equivalent Poiseuille WSS, suggesting that a large source of error was present. The underestimation stems from a combination of the large sample volume, the effect of the wall filter on relatively slow moving fluid, and the reduced peak velocities measured in the ultrasound models. SVs close to the wall contained some region out of the vessel lumen, so the mean frequency and hence velocity measured is lower. (This happens to some extent with PIV, too, but the large size of the Doppler SV increases the magnitude of this effect.) This effect is compounded by the clutter filter, a necessity of signal processing which removes the large amplitude wall signal, but one that comes at the expense of removing some of the signal from slow moving fluid close to the wall. Finally, the reduced maximum velocities that were observed in the stenosis also reduce the measured maximum WSS. At the stenosis

throat, the velocity profiles are mostly flat, so most of the fluid will be going at the maximum velocity. If the maximum velocities are reduced, then so will the maxium shear rates.

The effect of the SV and wall filter is clear if one examines the stenotic velocity profiles (Figs. B.6b–B.10b). All of the velocity profiles measured with PIV have a flat top with relatively square shoulders marking the approximate edge of the boundary layer. This change is smoother in the ultrasound data. Between the high velocity region and the boundary layer (defined by the steepest gradient), a third region exists (on either side of the velocity profiles and in all of the models) where the gradient is approximately half that of the boundary layer. This third schema usually occurs at the vessel walls and intersects with the boundary layer present in the PIV data, suggesting that it is at least partly due to the clutter filter. The existence of flow beyond the vessel walls is as a result of the finite SV size.

Given the variety of sources of error, the differences between the maximum measured wall shear stresses are not too severe (41% mean difference). In the 30 and 40% models, the maximum WSS was higher in the ultrasound models than in the PIV models. The situation reversed for the more severe stenoses, as the maximum WSS was higher when measured optically. In the tightest stenoses, the higher jet velocities prevented the use of the 5 MHz transducer, since the frequency shifts aliased in the stenosis throat. The lower frequency transducer would certainly have a longer axial pulse length, and could generally be expected to have a larger SV. To accommodate the increased pulse length, all of the proposed WSS measurement strategies considered velocity measurements located at separations that scaled with the wavelength (Table 5.2). Consequently, at lower frequencies, the increased size of the SV would reduce the maximum measured shear stresses further, as seen in Fig. 6.8a.

Comparison between the minimum wall shear stresses is difficult, particularly in the cases where no recirculation region was dominant. For $\kappa \geq 0.5$, it was possible to assign dominant status to a particular recirculation region with both modalities, since it is quite clear from the axial traces of WSS (Fig. 6.9). However, for the milder stenoses, the magnitude of the shear stresses was comparable to the magnitude of the experimental noise (Table 6.2). With both experimental techniques, measurements of the whole field of view were of interest, requiring that parameters were set to measure the high jet velocities at the centre of the lumen. Simultaneously measuring very fast and very slow moving things requires a large dynamic range, but for any particular instrument the dynamic range tends to be approximately constant. With ultrasound, measurement of high velocities requires a high PRF. As the time between successive

pulses falls, the resulting phase shift from slow moving scatterers close to the vessel wall will also fall. Ultimately, the shift will become so small that it will fall below the noise level or filtered by the clutter filter. The same effect occurs with PIV. To measure fast moving fluid, the time between the images must be reduced. This reduces the distance that the slow moving fluid moves between each image until eventually, the displacement is indistinguishable from noise. In the PIV models, this problem was compounded by particles attaching to the vessel wall, in much the same manner as at the inlet, although the use of strategy C helped, since the velocity point at the wall, and hence most affected by the glare, was set to zero.

The size of the recirculation regions did not follow any defined trend. This is at least partly due to the fact the measurements were taken only up to $Z \leq 4$, preventing measurement of recirculation regions that were longer than this. Estimates of L_R were inevitably linked to measurements of WSS. As previously discussed, the very small shear stresses were difficult to measure, since their magnitudes were often comparable to the amount of noise in the system.

6.4.2 Effect of the flow rate

6.4.2.1 Velocity comparison

At low flow rates, the downstream velocity maps measured by PIV and Doppler ultrasound agreed well. The agreement became poorer with increasing flow rate. This behaviour was broadly the same as changing the degree of stenosis, indicating that the fluid behaviour was defined by the stenotic Reynolds number. The transition from laminar behaviour occurred when the upstream Reynolds number was changed from 200 to 400 corresponding to stenotic Reynolds numbers of 400 and 800. This figure is consistent with the range for the critical Reynolds number obtained by varying κ (714 and 833). This suggests that, for stenoses with smooth cosine geometries, the critical stenotic Reynolds number lies in the range 714–800. Close inspection of the turbulent velocity fluctuations at $\mathrm{Re}_{-1} = 400$ reveals that although the PIV velocity fluctuations increased substantially, the increase in the ultrasound fluctuations was far less marked. This suggests that 800 is very close to the critical Reynolds number.

The maximum velocity in the post-stenotic jet did not change when measured with PIV, but decreased in a linear manner when measured with ultrasound. This contrasts with the situation at the inlet where the centreline velocity fell in a linear manner when measured with PIV, and quadratically when using DUS. The apparent change in behaviour may be an artifact of the small

number of data points, which made distinguishing between linear and quadratic relationships difficult. This is contradicted by the mean difference between the two systems measured at the model inlets and even at the site of maximum stenotic velocity—velocities estimated using Doppler ultrasound were, on average, 15% lower than those measured with PIV. Varying the flow rate, resulted in mean differences of –22% and the differences increased and became more significant with increasing flow rate.

The length of the jet, L_J, extended beyond the region studied at all flow rates when measured using DUS. In the optical models, the jet length reduced as the flow rate increased. This is effectively the same result obtained in a different manner to varying κ. Increasing the flow rate increases the stenotic Reynolds number; upon expansion, the layers of high shear are unstable, and vortices are generated, which ultimately leads to the turbulent breakdown of the jet. At higher flow rates, the magnitude of the velocity gradient is greater in the shear layer, generating more vortices so that the transition to turbulence occurs more proximally.

6.4.2.2 Wall shear stress comparison

The maximum WSS was inversely proportional to the flow rate. Considering the normalisation criteria, this is equivalent to a linear increase, as expected. Ultrasonic measurements were lower than the PIV values for all except the lowest flow rate. This effect is similar to that described previously—DUS measured higher shear stresses than PIV in the 30 and 40% models (equivalent to low flow rates) but tighter stenoses (for higher flow rates) the PIV values were greater. All measured values of maximum wall shear stress were larger than the equivalent Poiseuille values. However, the percentage difference between the ultrasonic and Poiseuille value fell as flow rate increased, which could draw one to the spurious conclusion that the velocity profile became more parabolic. In reality, increasing the flow rate results in the stenotic velocity profile becoming flatter (Figs. B.16b–B.20b). As described previously, the major sources of error in the ultrasonic measurements were from the size of the sample volume, the wall filter level and the underestimation of the maximum velocity. The effects of the wall filter and SV size are again visible in the stenotic velocity profiles. The third region in the ultrasonic profiles contrasts with the square shoulders of the PIV data, and the velocities extend well beyond the confines of the lumen.

The minimum WSS measured by PIV did not change with flow rate. For flow rates with $\mathrm{Re}_{-1} \geq 600$ the minimum shear stress was comparable to the noise in the images, so estimates of $\tau_{w,min}$

were presented as the mean of data from both walls. This implies that denoting the dominant recirculation region was difficult and that the velocity profiles were quite symmetric. Inspection of the mean velocity profiles show that this was not the case (Figs. B.16–B.20). However, when one considers the magnitude of the velocity fluctuations, it is apparent that measuring the WSS with sufficient precision to discriminate one wall from the other is moot (Figs. B.11–B.15).

The minimum wall shear stress measured with DUS did not change when it was possible to define a dominant recirculation region ($\mathrm{Re}_{-1} \geq 400$). For the lowest flow rate, the magnitude of $\tau_{\mathrm{w,min}}$ was similar to the noise level, as was the equivalent PIV measurement. Despite this, a significant difference was present between these two measurements, albeit at a low level, due to the small magnitude both of the measurement and its uncertainty. To some extent, this suggests that a higher level of p should be considered significant. Evidence from the 30% stenosis model supports this. The difference between $\tau_{\mathrm{w,min}}$ was significant, but the combined magnitude of the measurements and uncertainties were equal and very small (0.001 and 0.001, Table 6.9). Considering a significance level of $p < 10^{-3}$ at a stroke declassifies the significance of the differences between the WSS measurements made by PIV and DUS—including the maximum and minimum values—for all flow rates with $\mathrm{Re} \leq 600$ and for all the stenosis models except the 70% model at Re=500.

The similarities in the magnitudes of the $\tau_{\mathrm{w,min}}$ measurements and their uncertainties are represented in the measurements of the size of the recirculation regions. Specifying where the minimum WSS exceeded the threshold was difficult due to the noise, resulting in large uncertainties (Fig. 6.15c). Excepting the lowest flow rate, the ultrasound data may show that L_{R} is reducing, although a more thorough study encompassing more outlet lengths and more flow rates would be necessary to confirm this.

6.4.3 Comparison with the literature

6.4.3.1 Velocity comparison

Comprehensive experimental data are scarce in the literature. Ahmed & Giddens (1983*a*) studied flow through identical scale models with laser Doppler anemometry but the data presented are difficult to extract from the paper. Their velocity profiles are a reasonable match with the symmetrised profiles, with maximum velocities falling in between the PIV and DUS data, except at $Z = 4$. Somewhat suspiciously, however, the maximum velocity quoted by Ahmed &

Giddens does not change from the value predicted by continuity. This has been observed before (Ryval et al., 2004), suggesting that the Reynolds number was, in reality, lower than quoted in the paper. Further questions about the quality of their results are reaised on examination of Fig. 2 from Ahmed & Giddens (1983*a*). All of the velocity profiles quoted in the paper are restricted to one half of the velocity profile, while the visualisation data appear slightly skewed to one side of the vessel. No mention of this is made in the paper. At $Z = 4$, only the ultrasound data are in agreement at the centreline (with 20%) with the Ahmed data. Although not explicitly quoted in this paper, this implies that Ahmed's stenotic jet length exceeds that of the PIV data.

At Re = 1000, the measured velocity profiles agree well with published velocity profiles in the stenosis throat (Ahmed & Giddens, 1983*b*). However, progressing distally beyond the stenosis, the agreement rapidly deteriorates (Fig. 6.18). The overall agreement between the PIV data and the LDA data is poorer than at Re = 500. This is consistent with the reduced stenotic jet length at higher flow rates (Fig. 6.14a) and the increased level of turbulence (Fig. 6.13).

Some of the differences between the previously published data and the measured DUS and PIV arise from experimental procedure. An advantage of laser Doppler anemometers is that they can acquire velocity samples at high frequencies and over long time scales. In contrast, CFI acquisitions are limited in length by the buffer of the ultrasound machine and typically have upper sampling frequencies of 15–20 Hz. Similarly, PIV acquires enormous volumes of image data which requires lengthy processing to extract velocity maps, effectively limiting the length of data acquisitions. The sampling frequency of the camera used in this study is typical of digital cameras designed for PIV, which was capable of acquiring fifteen image pairs per second. Since LDAs can run for extended periods while sampling at high frequencies, Ahmed & Giddens were able to observe oscillations in their data due to vortex shedding. The frequencies of vortex shedding varied by model and flow rate with a range from 1–15 Hz. On top of the shedding frequencies, they observed lower frequency oscillations, which they were unable to explain. To eliminate their influence from the final mean frequencies, they used long sampling times (150 s).

The relatively low sampling rate of the PIV system and the use of time averaged vector Doppler ultrasound precluded any investigation of the frequency of the velocity fluctuations. However, PW Doppler data were acquired at some locations distal to some of the stenoses. These data reveal periodic (as opposed to random and hence turbulent) velocity fluctuations were present in

the flow at low flow rates and mild stenoses (Fig. 6.19). At higher stenotic Reynolds numbers, the oscillations were not observed, although since collection of spectral Doppler was not the primary aim of the experiments, the data are unsystematic and sparse.

Sherwin & Blackburn (2005) numerically studied flow in a 50% cosine stenosis, without employing turbulence models, instead they directly simulated the smallest eddies, which are estimated by the Kolmogorov scale (Schlichting, 1987). To examine the stability of the flow (which is analogous to experimental noise) they introduced perturbations to the solutions. The effect of small perturbations caused the previously symmetric jet to become skewed to one side, and subsequently demonstrating Coanda attachment. After the transition of turbulence, the authors observe that the jet direction oscillates from one side of the vessel to the other, with a normalised time scale that corresponding to >600 s in the ultrasound models and >1700 s for the PIV models. Since typical experimental acquisitions using PIV and Doppler ultrasound lasted less than 10 seconds, no movement of the stenotic jet would be observed, with the effect that the asymmetry appeared constant, rather than quasi-stationary. This observation potentially solves the discrepancy between the asymmetry of the visualisation data and the symmetry of the velocity profiles reported by Ahmed & Giddens (1983*a*). The exposure times of the photographs will be much shorter than the acquisition of the LDA data; if the flapping frequency of the jet was high enough, then the measured velocity profiles would appear symmetric.

Varghese et al. (2007*a*) also used direct numeric simulation to study flow through cosine stenoses, investigating the effect of eccentricity on the fluid dynamics. The authors conclude that geometric perturbations as small as 5% are capable of breaking downstream symmetry (at $\mathrm{Re}_{-1} = 500$) and introducing turbulence (at $\mathrm{Re}_{-1} = 1000$). Their results predict the transition to turbulence at $Z = 6$, more distally than observed by Ahmed & Giddens (1983*a*). To account for this, they suggest that the more proximal transition arose due to upstream experimental noise which was absent from their simulations. If valid, this explanation would also apply to the DUS and PIV data. Flow was driven with a pump in these experiments, while Ahmed used a head tank. Using a pump introduces a greater source of variability than gravity, and may explain why the length of the velocity profiles are in poor agreement when measured with PIV (Fig. 6.17). This observation may also explain why the PIV data and DUS are often in poor agreement. Identical gear pumps were used in each fluid circuit. However, to maintain dynamic similarity, the flow rate was higher in the PIV loop. Although the pump's maximum quoted flow rate was approximately

twice that used in this study (83 ml $\cdot s^{-1}$ vs. 36 ml $\cdot s^{-1}$), the flow stability in the PIV system may have been affected by the pump operating closer to capacity.

Focussing on the similarities between the dual flow systems, both observed asymmetric jets distal to the stenosis. The asymmetry contradicts previously published experimental data (Ahmed & Giddens, 1983*a*,*b*), although flow visualisation photographs in these papers suggest that the data may have been less symmetric than the velocity profiles suggest. Although numeric studies contain no experimental noise, the introduction of minor perturbations was able to break the downstream symmetry and result in the transition to turbulence more proximally (Sherwin & Blackburn, 2005; Varghese et al., 2007*a*). Consequently, the asymmetries are likely to be more representative of arterial blood flow than perfectly symmetry jets.

The asymmetry of the jet and the differences between the distal velocity field measured by PIV and DUS have clinical relevance. Estimation of the maximum velocity with PW Doppler ultrasound requires knowledge of the direction of blood flow. In undisturbed conditions, it is conventional to align the angle correction with the vessel wall. Clearly, this approach is invalid if the stenotic jet is angled with respect to the vessel, as these data suggest. The differences observed in the measured velocity fields placed in context with the literature suggest that upstream velocity fluctuations are an issue. Larger velocity fluctuations give rise to shorter post-stenotic jets and the transition to turbulence more proximally. Effectively, this implies that the region distal to the stenosis that is subject to atherogenic low and oscillating shear stresses is reduced if the inlet flow is less stable. It does however, raise another question; how stable is less stable, and are velocity fluctuations of these magnitude commonly seen in arterial disease?

Gach & Lowe (1998, 2000) studied flow emerging from an abrupt stenosis (50% by diameter) with MRI. Despite the difficulties MRI suffers in the presence of turbulence, they established that the transition from laminar to turbulent flow occurred at stenotic Reynolds numbers (Re_0) ranging from 250–350. (The equivalent Re_{-1} were 125–175.) In the PIV models, the transition from laminar flow occurred in the 40% model, but not in the 30% model, the implied critical stenotic Reynolds number is in the range 720–833. For a streamlined stenosis, the flow is less disturbed, so the critical Reynolds number will be higher than for the abrupt case. Both values are substantially lower than the critical Reynolds number in a straight pipe, which is around 2300 (Schlichting, 1987).

Estimates of the critical stenotic Reynolds number were also produced by Yongchareon & Young (1979). Using LDA, they studied flow through tight stenoses (67% by diameter) with three geometries: an abrupt step shaped stenosis (comparable to Gach & Lowe (2000)); a streamlined cosine stenosis as used in this study; and an orifice, which was an abrupt stenosis with minimal axial length. The authors recognised the difficulty of defining exactly when the transition from laminar flow began, but ultimately they settled on values of turbulence intensity exceeding 0.3. With this definition, they obtained critical upstream Reynolds numbers of 295 (16), 328 (18) and 250 (15), for the step stenosis, streamlined stenosis and orifice, respectively. Converting these into Re_0 yields values of 894 (48), 994 (55) and 758 (45). These values agree well with the range for the critical stenotic Reynolds number (720–833) obtained in this chapter.

6.4.3.2 Wall shear stress comparison

The maximum wall shear stresses at the stenosis throat are all lower than other published values in the literature (Fig. 6.8a). As expected, for the mildest stenoses, values of wall shear stress converged towards the Poiseuille value. For the tightest stenosis, however, the WSS value measured with DUS was actually *lower* than the undisturbed case, clearly suggesting a problem. Maximum WSS in the 50% stenosis model compares poorly with the value reported by Ahmed & Giddens (1983*b*): 0.36 versus 0.18 by PIV, and 0.10 using Doppler ultrasound. However, for other axial locations, the normalised shear stresses agreed with these published data (Fig. 6.9c). Comparing the maximum WSS for Re = 1000 with Ahmed & Giddens (1983*b*) yields poor agreement: 0.20 compared with 0.11 and 0.08 using PIV and DUS, respectively (Fig. 6.15). As recognised in Sect. 6.3.1.2 and Sect. 6.3.2.2, the difference between the Ahmed values and the PIV values (relative to the Ahmed data) correspond to approximately –41%. This is the same difference measured between the Poiseuille and the PIV (with method C) values of WSS in the straight part of the models (Chapt. 5). In principle, this information could be used to correct all of the PIV values of WSS. This results in excellent agreement between the values of $\tau_{w,max}$ measured with DUS and (the corrected) PIV at the throat of the 30 and 40% stenosis models (0.10/0.10 and 0.16/0.17 for DUS/[corrected] PIV in the 30 and 40% models, respectively). However, for the tighter stenoses, when the Doppler method already under-read the PIV, the agreement becomes much poorer.

Maximum WSS at the stenosis throat also disagrees with the momentum based model (Reese & Thompson, 1998). For all κ, values of maximum WSS in the stenosis throat predicted by

the model were greater than the values measured with PIV (mean difference 31%, range –3 to –60%); the model's agreement with values measured with Doppler ultrasound was even poorer (mean difference 55%, range +69% to –74%). The largest differences between predicted and measured values occur in the tightest stenoses, where the validity of the model may be called into question. However, values of the model compare quite favourably with values measured with LDA, 0.28 vs. 0.36 at Re = 500 (Ahmed & Giddens, 1983*b*). Altering the flow rate did not generally affect the agreement between the model's predictions and the maximum measured WSS. Measured optically, the mean difference between the maximum WSS values was on average, –25 (3)% (range –22 to –28%); comparable figures obtained with Doppler ultrasound were –39 (11)% (range –20 to –50%).

The maximum WSS reported by Varghese et al. (2007*a*) for the axisymmetric model agrees well with the values reported by Ahmed & Giddens. At the throat of the stenosis, the shear stress was 22 times larger than the inlet Poiseuille value, corresponding to a value of 0.36. Once again, these values are substantially larger than the peak values measured by DUS and PIV.

Comparing the minimum WSS values with the sparse literature, the magnitude of the negative shear stresses in the (limited) Ahmed & Giddens (1984) data were greater than both the PIV and DUS values ($Z = 2.5, 4$). The greatest percentage differences at the respective locations were 130/90% ($Z = 2.5$) and 200/350% ($Z = 4$) for PIV/DUS. The scarcity of other values in the literature is consistent with the difficulties observed in this study, although perhaps it indicates an unjustified concentration on maximum shear stress, especially if one considers that large shear stresses can be vasoprotective, while small values are likely to stimulate atherogenesis.

The recirculation lengths measured distal to the stenoses showed no discernable relationship, in part because of the limited number of downstream locations studied. However, for the PIV data, only two models and flow rates resulted in the recirculation region extending beyond the region studied ($\kappa = 0.4$; $\kappa = 0.5$ at Re = 200) allowing limited comparison with other results. Comparing with Ahmed & Giddens, recirculation regions disappear from the velocity profiles in the 50% model between $Z = 4$ and $Z = 5$ for both Re = 500 and Re = 1000. The comparable figures measured with PIV were $Z = 3.3(0.5)$ (Re = 500) and $Z = 2.2(1.0)$ (Re = 1000). By DUS, the recirculation length at Re = 500 extended beyond the region studied, but at Re = 1000 $L_J \approx 4.0(0.2)$.

The numeric studies of Sherwin & Blackburn (2005) and Varghese et al. (2007*b*) both observed recirculation lengths in excess of $Z = 10$ for Reynolds numbers in the range 500–1000. The minor geometric pertubation brought the transition to turbulence closer to the stenosis, but did not reduce the time averaged recirculation length $Z \approx 10$ (Varghese et al., 2007*b*). In the turbulent region, instantaneous normalised shear stresses ranged from –8 to 16, resulting in extremely large gradients of shear stress, suggesting that considering only the time averaged value of $\tau_{\mathrm{w,min}}$ and L_{R} may be misleading.

Gach & Lowe (1998, 2000) studied the recirculation lengths of flow through axisymmetric sudden and smooth stenoses (both 50% by diameter) with MRI. Despite significant subjectivity in their definition of recirculation length—derived not from the direction of the wall shear stress, but from the (approximate) location of impact of the post-stenotic jet on the vessel wall—their data agree well with previously published values. Examining the collected data from other works published in their paper, the recirculation length grows linearly up to a maximum of approximately $Z = 5$ at $\mathrm{Re}_0 = 200$. The recirculation length reaches a plateau with Z between 2 and 5 for stenotic Reynolds numbers below about 2000. In this context, the measurements for the PIV recirculation length are an general agreement with the literature. Considering that the magnitude of velocity fluctuations rose sharply in all of the ultrasound models close to the end of the regions studied (Fig. 6.5 and Fig. 6.13) it is reasonable to assume that the transition to turbulence was imminent. This implies that the recirculation lengths in the ultrasound models would not greatly exceed $Z = 5$ and would therefore be in reasonable agreement with the literature also.

6.5 Conclusions

This chapter has examined steady flow in similar geometries representative of arterial stenoses with a dual system approach under an original hypothesis that the results would, in a qualitative manner, be similar. However, flow in the validation system became transitional at lower Reynolds numbers and more proximally than the ultrasound system, resulting in poor agreement. Comparison of the data with the literature suggests that the differences originate from upstream noise.

Doppler ultrasound was able to measure wall shear stress under Poiseuille conditions to within 10% of the theoretic value, although it was highly dependent on the methodology used. In

regions of disturbed flow, ultrasonic estimates of WSS consistently underestimated values measured by PIV, which were themselves lower than values published in the literature for similar geometries. However, in qualitative terms, DUS is capable of detecting areas of elevated WSS and regions where it is close to zero, at least in idealised geometries.

Maximum velocity estimates made by the dual beam Doppler system were, on average, 15% lower than the equivalent velocities measured by PIV. This figure did not change with the degree of stenosis, but the error increased with flow rate. Increasing the flow rate by a factor of five (while remaining within physiologic values) increased the magnitude of the underestimation from 15% to 30%.

Chapter 7
Pulsatile flow through stenosed tubes: a validation in-vitro study

In Chapt. 6, the dual flow phantom system developed in Chapt. 5 was used to validate Doppler ultrasound velocity and wall shear stress measurements in idealised stenoses under steady flow. Clearly, in-vivo blood flow is unsteady, so the performance of the Doppler system is expected to differ from the steady case. In this chapter, a physiologic waveform is supplied to the dual systems and the Doppler measurements are validated.

7.1 Introduction

As discussed in Sect. 5.1, Doppler ultrasound is used to pre-screen patients before angiography. Typically, patient selection is based on the peak systolic velocity (PSV) or on the ratio of the PSV to the peak end diastolic velocity (PEDV) (Bluth et al., 1988; Robinson et al., 1988; Hunink et al., 1993; Alexandrov et al., 1997). However, the maximum velocity measurement is subject to large errors, since most Doppler systems only estimate one component of the velocity. Estimation of the true velocity from this measurement introduces large errors, as the direction of flow is not known. This problem is compounded, since the direction may change throughout the cardiac cycle.

The wall shear stress (WSS) is hypothesised to be responsible for the initiation and progression of atherosclerosis (Slager et al., 2005*a*,*b*). Low and oscillating values of WSS are correlated with lesion development (Ku et al., 1985*a*,*b*; Zarins et al., 1983), but at present, the non-invasive measurement of WSS is limited to relatively straight, disease free vessels (Brands et al., 1995; Samijo et al., 1997; Oyre et al., 1997; Tortoli et al., 2006), which prevents further study exactly where it is needed.

Previous studies of pulsatile flow through stenoses have demonstrated that oscillatory flow is less stable than steady flow (Cassanova & Giddens, 1978) and that distal recirculation is transient rather than constant (Ahmed & Giddens, 1984; Varghese et al., 2007*b*). These results

imply that the transition to turbulence occurs at lower flow rates, and that downstream of even mild stenoses, the direction of the WSS vector oscillates throughout the cardiac cycle. In the context of Slager's hypothesis, this body of work suggests that distal flow conditions are conducive to further development of atherosclerosis.

The existing literature is limited, however, since previous studies have only considered sinusoidal flow about a mean value. These waveforms are not physiologic, and do not allow the pseudo-steady flow conditions of diastole to develop. Consequently, in this chapter the dual flow system developed in Chapt. 5 is used to study flow through idealised stenoses with a physiologic flow waveform. The aims of this chapter are: to quantify the magnitude of the errors present in estimates of PSV and PEDV; and to estimate the errors present in measurements of the wall shear stress at peak systole and end diastole.

7.2 Materials and methods

7.2.1 Stenosis models and flow similarity

The stenosis models used in this chapter were described previously in Sect. 5.2.1. Velocity data were measured at the same locations as for steady flow in the 30%, 50% and 70% models (Fig. 6.1). An idealised flow waveform (Fig. 7.1a) representative of pulsatile flow in arteries (Thompson et al., 1985) was scaled such that peak inlet velocities in the ultrasound models were in the physiologic range (Fig. 7.1b). Driving the ultrasound flow system with an appropriately scaled version of this waveform produced realistic velocities in the flow phantom (Fig. 7.1).

To maintain parity between the separate flow systems, the dimensionless numbers for each system must be equal (Sect. 2.1.2.) The fluid developed for use with PIV in Chapt. 4 has a greater kinematic viscosity (5.8 $mm^2 \cdot s^{-1}$) than that of the ultrasonic BMF (3.3 $mm^2 \cdot s^{-1}$). Consequently, the flow rate and frequencies in PIV model must be scaled by the ratio ν_{PIV}/ν_{US} to maintain Reynolds number and normalised frequencies. In practice, this process is non-trivial, since the the frequency response of a particular flow system is a function of the pump, the amount of the fluid in the system (inertial effects) and the stiffness of the tubing and the material that comprises the phantom (compliance effects, which are analogous to capacitance in electrical circuits). In general, this behaviour is non-linear (Frayne et al., 1992). The behaviour of the system is further complicated by the presence of reflected pressure waves that propagate along the tubing wall and ultimately are reflected from the fluid reservoir (Hoskins, 2007).

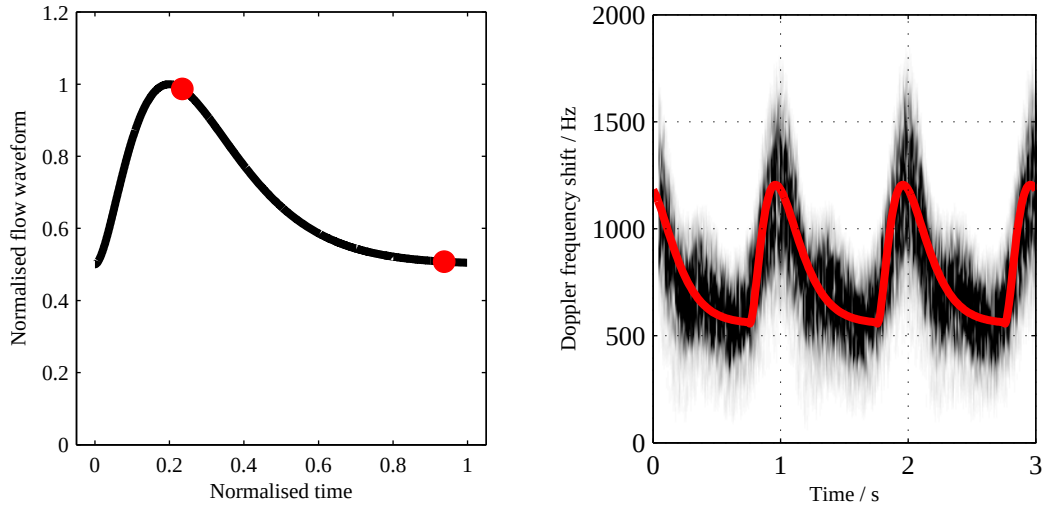

(a) The normalised waveform used to drive the gear pump in this study. Measurements were taken at systole and diastole, denoted in red.

(b) A spectral Doppler trace obtained from the inlet to the 30% stenosis model. The drive waveform has been rescaled and superimposed on top.

Figure 7.1: *Inlet flow conditions in the pulsatile phantoms.*

Driving the PIV system with a scaled version of the waveform depicted in Fig. 7.1a yielded similar results to those obtained by Frayne et al. (1992) (Fig. 7.2a). The inertial effect from the body of fluid and the compliance of the tubing reduced the high frequency content of the measured flow waveform relative to that of the desired flow waveform (Fig. 7.2b).

To improve the shape of the waveform such that it represented a scaled version of the desired waveform, the long—around 3 m—pipe from the outlet of the flow phantom to the fluid reservoir was replaced by a second, temporary reservoir, connected using less than 50 cm of tubing. Fluid was returned to the primary reservoir using a gravity feed mechanism. The frequency response of the modified system was improved, with a corresponding augmentation in the waveform shape (Fig. 7.2). After modifying the PIV fluid loop, the inlet flow waveforms to the PIV and DUS models agreed well (Fig. 7.3).

Flow similarity between the PIV and ultrasound systems was assessed by comparing the inlet flow waveforms to the phantoms, after normalisation (equivalent to using the Reynolds number) and correction of any phase difference between the two waveforms. The flow waveforms were considered equal from the purposes of this study if the differences between equivalent waveforms were always less than 5%.

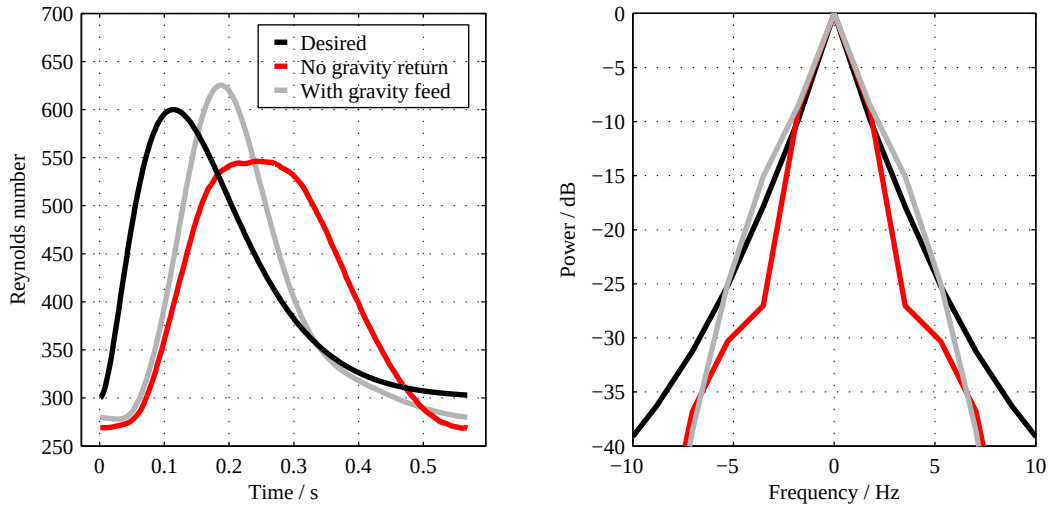

(a) The measured and the desired original flow waveforms obtained from the PIV system in the same configuration as for steady flow.

(b) The power spectra of the measured and desired flow waveforms from the PIV system in steady state configuration.

Figure 7.2: *High frequency attenuation of flow waves in the* PIV *flow system.*

7.2.2 Particle image velocimetry

All of the data were acquired in the same fluid circuit as described in Chapt. 6. Two changes were necessary to the fluid loop: the gravity feed mechanism was added to minimise the smearing of the high frequencies in the flow waveform, and the gear pump was controlled by the Labview interface program described in Chapt. 3. The interface program is capable of generating two analogue output signals at sampling rates up 1 kS·s^{-1}. The second output channel produced a square TTL-like signal at the desired point of the waveform to trigger the PIV processor unit to start acquisition. The time delay between the rising edge of the triggering TTL signal and the rising edge of the first Q-switch trigger was quite variable. Measuring the delay was difficult since the triggering events only repeated every 568 ms, below the optimum range of digital oscilloscopes. The average delay was estimated from around 100 triggering events to be 40 ms, with a range from about 10–60 ms.

The Transonic flow meter described in Chapt. 3 measured the volume flow rate at the stenosis model inlet. The measured flow waveform was slightly delayed with respect to the signal generated by the Labview interface program. To avoid introducing further timing errors, the rising edge of the TTL trigger signal was set based on the measured flow signal, rather than relative to the signal generated by the interface program.

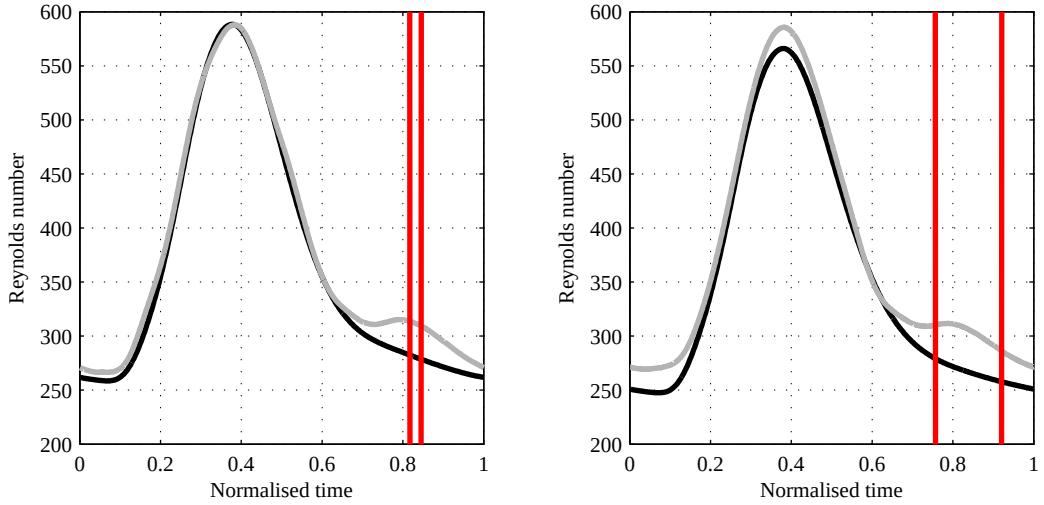

(a) 30% model.

(b) 50% model.

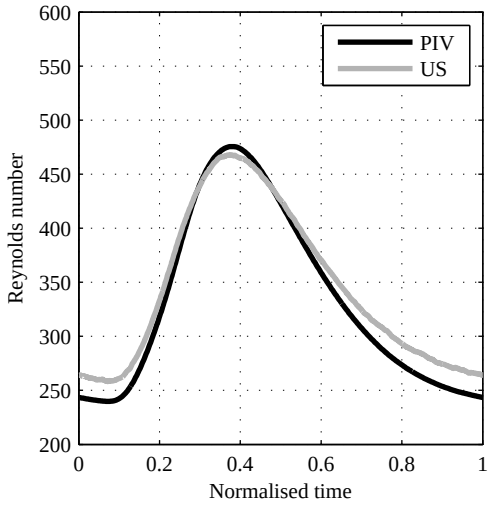

(c) 70% model.

Figure 7.3: *Inlet Reynolds numbers to the stenosis models. The regions between the red lines indicate where the differences between the flow rates exceeded 10%.*

The PIV processor acquired data in burst mode. In this mode, the system listens for an external triggering signal (provided by the interface program); on reception, it acquires a preset number of image pairs at the specified frequency, before reverting to listening for the external trigger. Using burst mode is preferable, as all image pairs are in phase with each other, since they run off the hardware clock of the processing unit. To prevent the trigger points and the flow waveform from drifting out of phase, however, resynchronisation every pulsatile cycle was essential. To study relevant clinical flow conditions, the PIV processor acquired two image pairs per burst, corresponding to peak systole and end diastole. These data points are shown in Fig. 7.1a.

The imaging system was the same as described in Chapt. 6. The time separation, Δt, of the image pairs ranged from 100 μs at the phantom inlets to 15 μs in the stenosis throat of the 70% model. Since systolic and diastolic data were acquired in one acquisition cycle, they shared the same value of Δt, which reduced the dynamic range of the diastolic velocity measurements.

The image pairs were analysed with MatPIV as described in Chapt. 6. Minimal distension occurred in the phantoms, despite the pulsatile nature of the flow (<1%).

7.2.3 Doppler ultrasound

The fluid circuit was described previously in Chapt. 6. Unlike the PIV system, no modification (ie, gravity feed) was necessary to obtain the desired flow waveform. To trigger the ultrasound scanner, the second output channel of the Labview interface program generated a TTL-like signal at the desired point of the synthesised cardiac cycle. This signal acted as an ECG wave, which caused the scanner to trigger data acquisitions from the rising edge. Once again, the time of the triggering signals was relative to the measured flow waveform, rather than relative to the signal generated by the PC.

To estimate the delay between the ultrasound machine receiving the TTL pulse via the ECG and actually acquiring each frame, an ultrasound pulse from a single element transducer was transmitted into the L12-5 transducer using coupling gel. The single element system produced a simple four pulse burst of ultrasound at 6 MHz using a signal generator. To detect when the ultrasound machine received the signal, a photo-resistor connected in a potential divider circuit monitored the screen of the ultrasound machine. The photo-resistor was able to detect changes in the screen intensity due to the vertical refresh rate at 50 Hz, implying that the effective sampling frequency was much greater than 100 Hz. To assess the triggering delay, a second signal generator simultaneously supplied a TTL pulse to the ECG port of the utlrasound machine and to the simple ultrasound system. The delay between the photo-resistor detecting the change in intensity on the ultrasound screen and the rising edge of the TTL pulse was measured using a digital oscilloscope. This delay was estimated to be 100 ms. In reality, the delay was probably less than this; the header details of the data files suggest that the each frame acquisition time was on the order of 36 ms.

The ultrasound machine is able to trigger via the ECG signal up to three times per second. This allowed data collection at systole and diastole from the same synthesised cardiac cycle.

Occasionally the ultrasound scanner dropped frames, producing ambiguities in the time variable of each frame. However, the differences between systole and diastole were large enough to distinguish between frames. As a double check, each triggering pulse produced by the interface program was set to a different level, allowing discrimination between frames even when the CFI data in each frame was similar.

Ultrasound data were acquired using the HDI5000 ultrasound machine described previously. For the 30% stenosis model, the L12–5 38 linear array was used. In the more severe stenosis models, aliasing again prevented use of the 5 MHz probe, so the L7–4 transducer was used instead. For each data acquisition, two separate data files were recorded with the ultrasound beam steered in both directions to obtain angle independent vector data. Machine settings were the same as used in Chapt. 6.

7.3 Results

7.3.1 Upstream flow conditions

7.3.1.1 Velocity comparison

The measured velocity profiles upstream of the stenosis agreed with the fully developed oscillatory velocity profiles profiles predicted by Womersley's theory (Fig. 7.4). The only qualitative differences were minor and occurred only in the 30% model: at peak systole, the PIV velocity profile was skewed slightly, and the diastolic velocity profile in the 30% ultrasonic stenosis model differed substantially from the PIV and Womersley values close to the wall.

The centreline velocities measured with PIV and DUS agreed well with each other both at peak systole (Fig. 7.5a) and end diastole (Fig. 7.5b). The mean difference between the centreline velocities was greater at diastole than at systole (DUS relative to PIV: –1 [2]% vs.–10 [4]%, ranges –5 to 1% and –16 to –5%). The centreline velocities predicted by Womersley's solution were within 1% of the measured values except at diastole using DUS (mean difference –13 [1]%). This difference is in agreement with the PIV/DUS diastolic difference, and is despite the fact that the flow rate in the ultrasound phantoms actually exceeded the flow rate in the optical phantoms in late diastole (Fig. 7.3a). The Womersley derived centreline velocities in both flow systems (generated from the measured flow rate) were within 2% of each other at systole and diastole. Despite the generally good agreement between these data, statistically

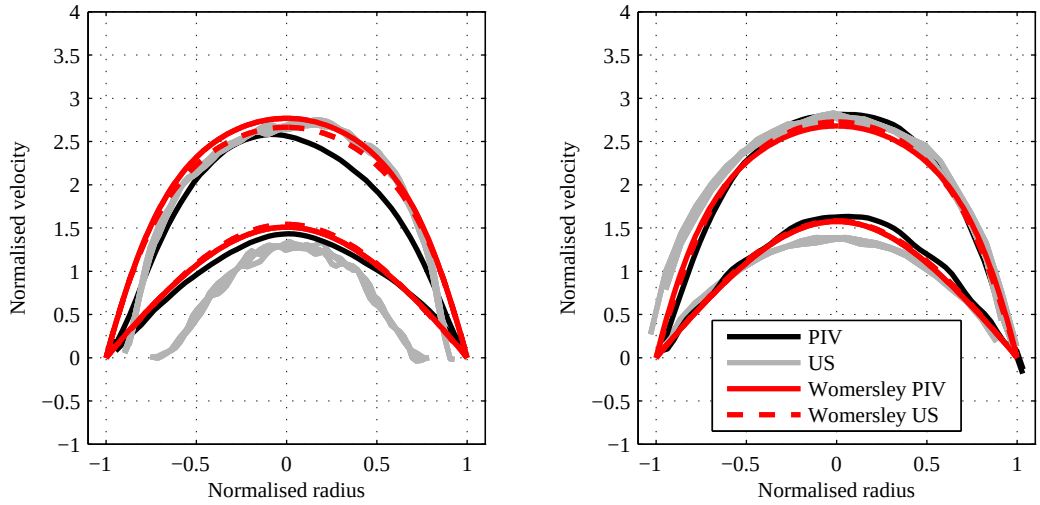

(a) 30% model.

(b) 50% model.

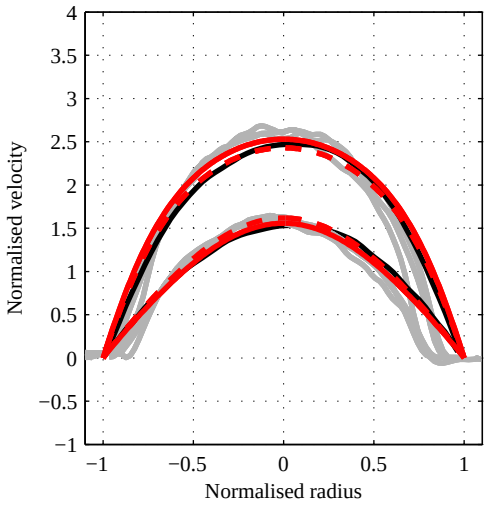

(c) 70% model.

Figure 7.4: *Inlet velocity profiles measured by* DUS *and* PIV*, compared with the Womersley solutions, at peak systole and end diastole.*

significant differences were present. The DUS/PIV data were significantly different at diastole ($p < 10^{-3}$) and at systole in the 50% model ($p < 0.05$); the Womersley/DUS values were also significantly different at diastole ($p < 10^{-2}$); and the Womersley/PIV data were significantly different at systole and diastole ($p < 0.05$).

7.3.1.2 Wall shear stress comparison

The wall shear stress remained difficult to measure. Close to the vessel wall, low velocities were hard to detect due to glare from the vessel wall in the PIV models and the effect of the clutter

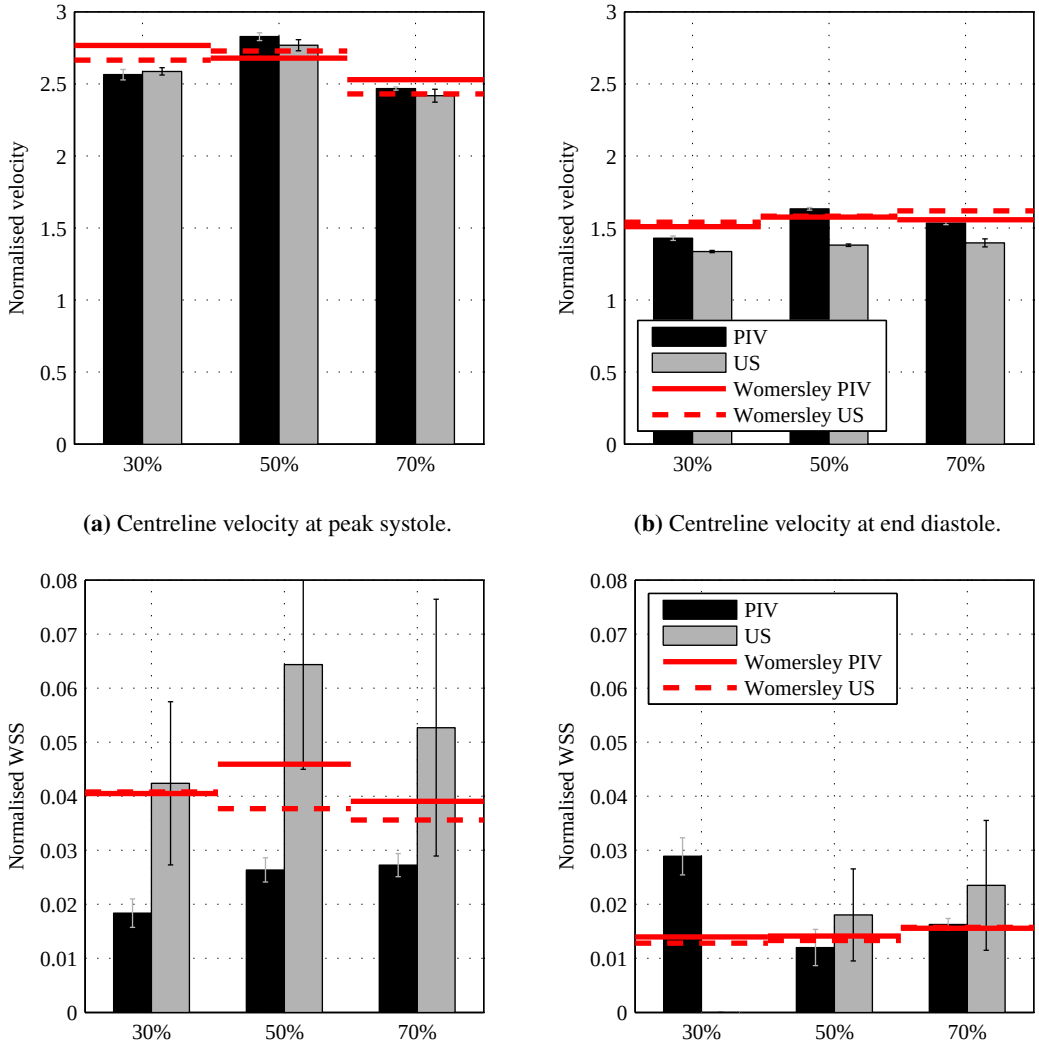

(a) Centreline velocity at peak systole.

(b) Centreline velocity at end diastole.

(c) WSS at peak systole.

(d) WSS at end diastole.

Figure 7.5: *Centreline velocity and* WSS *at the inlet of the stenosis models compared with their equivalent Womersley values.*

filter in the ultrasonic models. At diastole in the 30% model, no velocities at all were measured in the vicinity of the wall (Fig. B.28a), which prevented the estimation of WSS (Fig. 7.5d). The mean difference between the DUS and PIV estimated wall shear stresses was extremely large. At systole, the magnitude of the mean difference (standard deviation) was 261 (135)%; at diastole, this reduced to 141 (100)%. The estimated WSS by DUS agreed with the Womersley values, although this was mostly due to its high variability (mean systolic difference 41 (58)%, range –41 to 123%; mean diastolic difference, ignoring the 30% data, 42 (68)%, range –59 to 139%). At peak systole, the mean difference between the PIV and Womersley values of WSS was –42 (12)%; during diastole the difference reduced to 32 (58)%, mostly due to differences

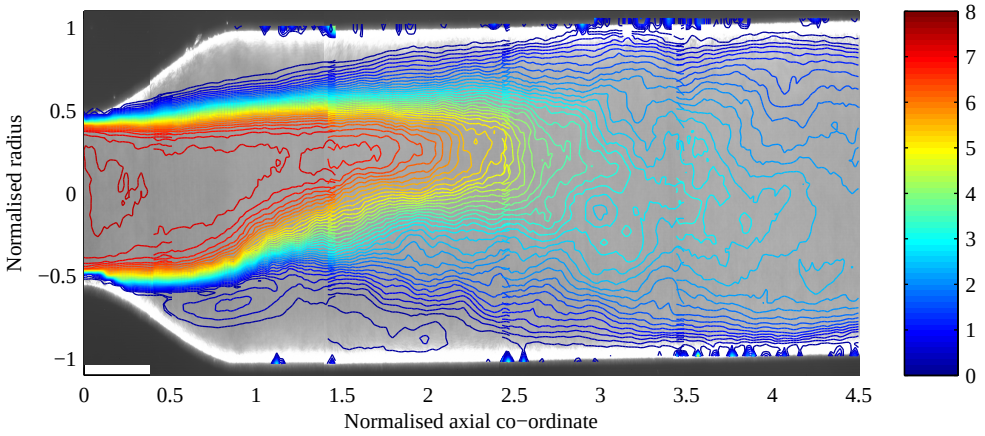

(a) Normalised velocity contours measured with PIV.

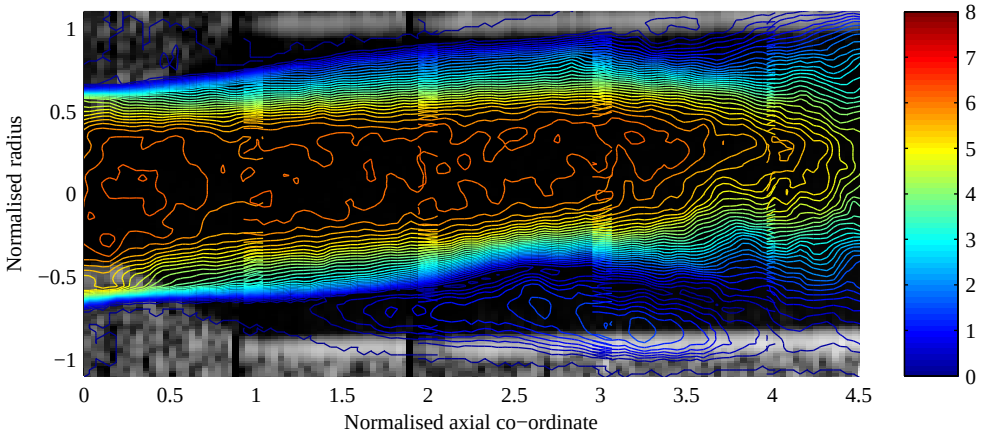

(b) Normalised velocity contours measured with Doppler ultrasound.

Figure 7.6: *Normalised velocity magnitude contours at peak systole distal to the 50% stenosis.*

in the 30% model. It is worth noticing that the mean difference at systole is the same difference observed under Poiseuille flow using method C (Sect. 5.3.2 and Fig. 5.16). Differences between the Womersley values of WSS were always less than 18% (mean difference 6 (7)%). Significant differences were present between the PIV/DUS values of WSS in the 50% model and at systole in the 30% model ($p < 10^{-2}$). No such differences were present between the ultrasound-derived Womersley values and the DUS data. Significant differences were present between the PIV and corresponding Womersley values of WSS. In the 30% and 50% models, the differences were significant both at systole and diastole ($p < 10^{-4}$); in the 70% model, the differences were only significant at systole ($p < 10^{-2}$).

7.3.2 Post-stenotic flow conditions

7.3.2.1 Velocity comparison

Flow remained laminar and was predominantly symmetric in the 30% stenosis model. The post-stenotic jet was stable, persisting over the entire region studied during systole and diastole (Figs. 7.8a–7.8b and Figs. B.21–B.22). Rather than recirculation, the regions next to the wall were characterised more as stagnation regions. In the 50% stenosis model, during systole flow an asymmetric, high velocity jet developed which showed signs of shear layer fluctuations on the side next to the largest recirculation region (Fig. 7.6). The jet became turbulent around $Z = 2$ and decelerated sharply (Fig. 7.8c), resulting in the turbulent transfer of momentum throughout the vessel, characterised by blunt velocity profiles (Figs. B.23e–B.23f). During diastole, although evidence of shear layer oscillations was present in the velocity fluctuations (Figs. B.24d–B.24e), the reduced velocity gradient increased the flow stability, with the effect that it remained laminar over most of the region studied (Fig. 7.8d and Fig. B.24). In the 70% model, the post-stenotic jet was highly asymmetric leading to flow separation accounting for around half of the vessel lumen (Fig. B.25d). Flow became intensely turbulent at around $Z = 1$ (Fig. 7.8e). During diastole, flow remained turbulent (Fig. 7.8f) although the transition occurred more distally at around $Z = 2$. The stenotic jet was more symmetric and surrounded by very large stagnation regions (Fig. B.26c).

During systole, velocity profiles measured in the 30% stenosis model with Doppler ultrasound were in excellent agreement with the equivalent measurements made with the optical system (Fig. B.27). In late diastole, although the velocity profiles remained symmetric, the agreement was poorer, as the ultrasound system failed to measure the low velocities close to the wall (Fig. B.28).

In the 50% model, spurious Doppler velocities were measured outside of the stenosis throat lumen during systole and diastole, and the peak velocity underestimated that measured by PIV (Fig. B.29b and Fig. B.30b). Beyond the stenosis throat, the agreement between the PIV and DUS was adequate during systole and good during diastole. During systole, and measured with ultrasound, the post-stenotic jet appeared to be more stable, extending well beyond $Z = 3$ (Fig. B.29e and Fig. 7.8c). Development of recirculation regions appeared to occur more distally with the ultrasound system. During systole, a large region developed at around $Z = 2$

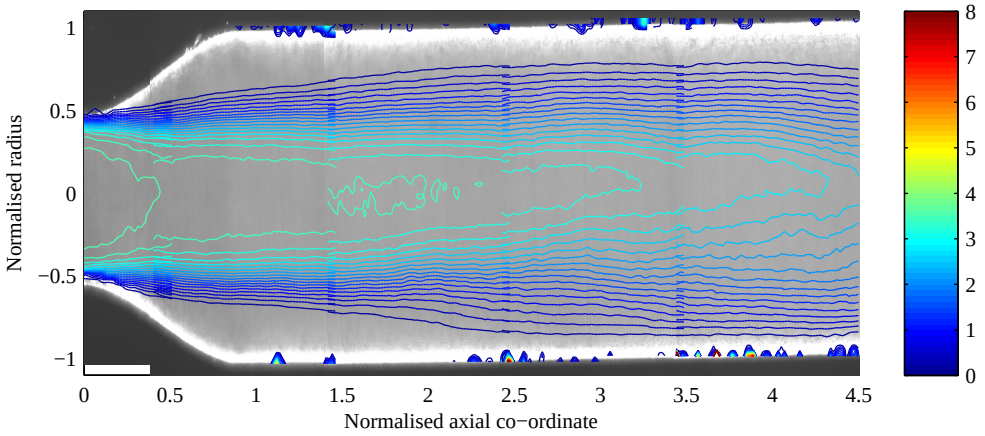

(a) Normalised velocity contours measured with PIV.

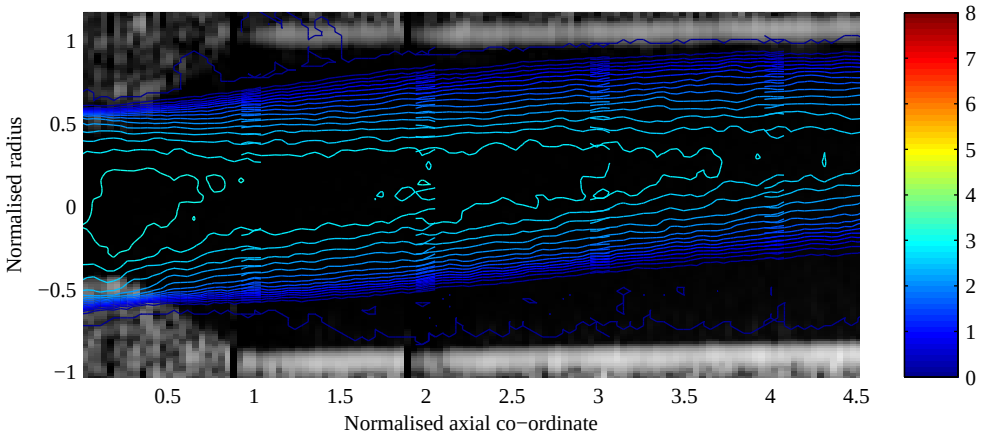

(b) Normalised velocity contours measured with Doppler ultrasound.

Figure 7.7: *Normalised velocity magnitude contours at end diastole distal to the 50% stenosis.*

extending to around $Z = 4$ (Figs. B.29d–B.29f). In diastole, the ultrasound machine failed to measured low velocities close to the wall (Fig. B.30).

In the 70% model, velocities at the stenosis throat agreed qualitatively with the PIV data during systole and diastole, although non-zero velocities extended beyond the vessel lumen (Fig. B.31b and Fig. B.32b). Distal to the stenosis, the velocity profiles were asymmetric, although the post-stenotic jet was aligned along the vessel axis and persisted until around $Z = 2$ (Fig. 7.8e and Fig. B.25). Asymmetric flow separation was present, with much larger effects at one side of the vessel (Fig. B.31d) . The recirculation regions persisted until $Z = 3$, which was about where the transition to intense turbulence occurred. During diastole, the jet persisted over the entire region studied (Fig. B.32) and the magnitude of velocity fluctuations increased only at the very end of the region studied ($Z = 4$). The velocity profiles were broadly symmetric and

showed signs of stagnation rather than recirculation up to $Z = 2$ (Figs. B.32c–B.32d). Beyond this point, a large asymmetric recirculation region was present.

In the 30% stenosis model, the post-stenotic jet length, L_J, extended over the entire region studied (Fig. 7.9a and Fig. 7.9b). In the 50% model, the ultrasound jet was stable enough at systole and diastole to extend over the entire region studied. In the optical models, this also happened at diastole, but at systole the length fell to $Z = 2.8$. Even in the most severe stenosis, the high velocity jet was stable enough to extend beyond $Z = 4.5$ in the ultrasound model at diastole, although its length fell to $Z = 2.5$ at systole. In the PIV model, L_J was 0.7 (0.1) and 2.5 (1.4) during systole and diastole, respectively. The difference between the systolic values was significant ($p < 0.05$).

The maximum velocities measured in this 30% model showed excellent agreement at systole (Fig. 7.9c). Significant differences were present between the maximum systolic velocity measurements in the 50% and 70% models (Table 7.1). During diastole, the differences were greater than at systole and significant in all of the stenosis models (Fig. 7.9d). The mean difference between the centreline velocities was –12 (8)%. Treating these figures as systolic and diastolic values shows that better agreement occurred at peak systole (–8 [8]% vs.–16 [4]%).

Stenosis	Systole		Diastole	
model	PIV	DUS	PIV	DUS
30	3.66 (0.01)	3.66 (0.01)	2.04 (0.03)	1.81 (0.01)‡
50	7.88 (0.12)	6.35 (0.02)†	4.00 (0.05)	3.19 (0.01)‡
70	16.33 (0.11)	15.38 (0.03)†	9.52 (0.13)	7.90 (0.04)†

Table 7.1: *Maximum normalised velocity, $\hat{V}_{\max}$, in the stenosis jet.* $^{\dagger}p < 10^{-4}$*;* $^{\ddagger}p < 10^{-5}$.

7.3.2.2 Wall shear stress comparison

Measurement of WSS was difficult, and showed substantially more noise than under steady flow (Fig. 7.10). In the ultrasound models, the maximum normalised WSS was broadly independent of the degree of stenosis (Figs. 7.11a–7.11b), despite a clear trend in the PIV models. WSS measurements at the stenosis throat made with DUS were higher than those obtained with PIV in the 30% models and significantly different (Table 7.2). In the 50% stenosis, these values were generally comparable. For the most severe stenosis, the PIV-derived WSS values were significantly higher than their DUS equivalents. The mean difference between the DUS and

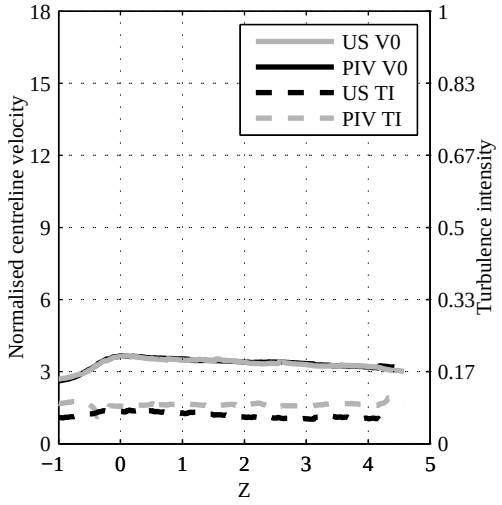

(a) Peak systole in the 30% model.

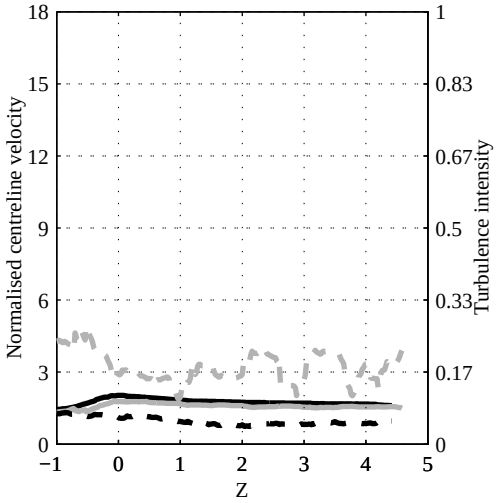

(b) End diastole in the 30% model.

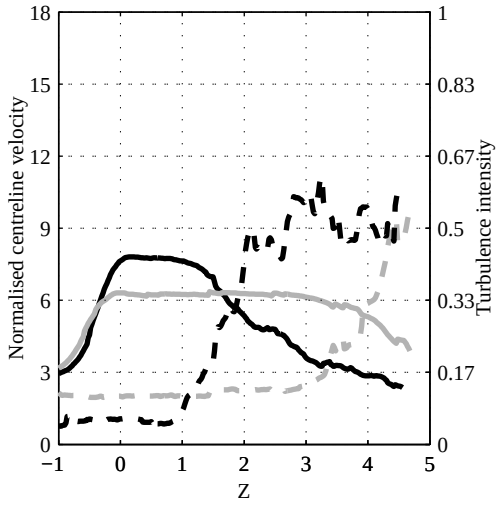

(c) Peak systole in the 50% model.

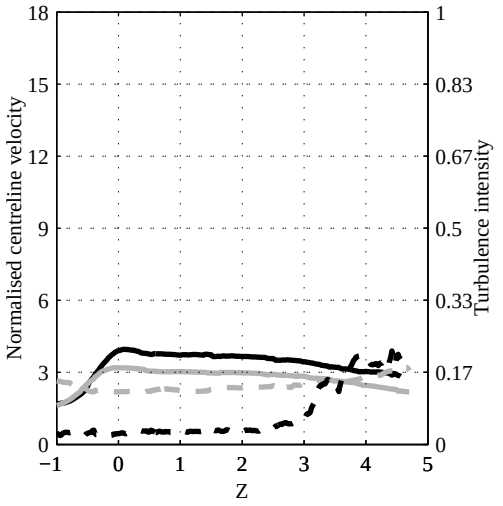

(d) End diastole in the 50% model.

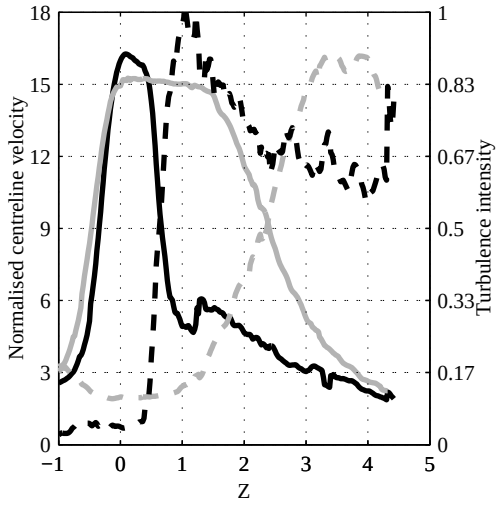

(e) Peak systole in the 70% model.

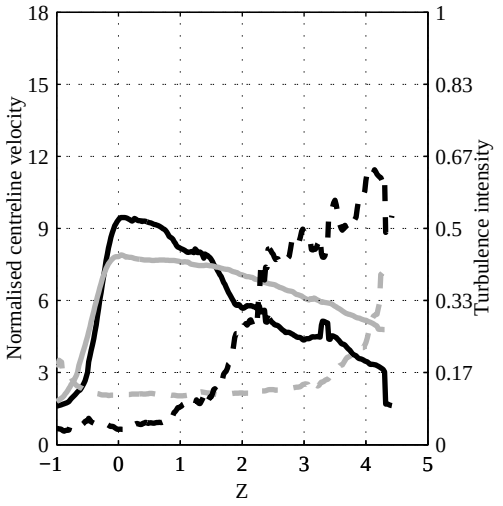

(f) End diastole in the 70% model.

Figure 7.8: *Centreline velocity and turbulence intensity in the stenosis models at peak systole and end diastole.*

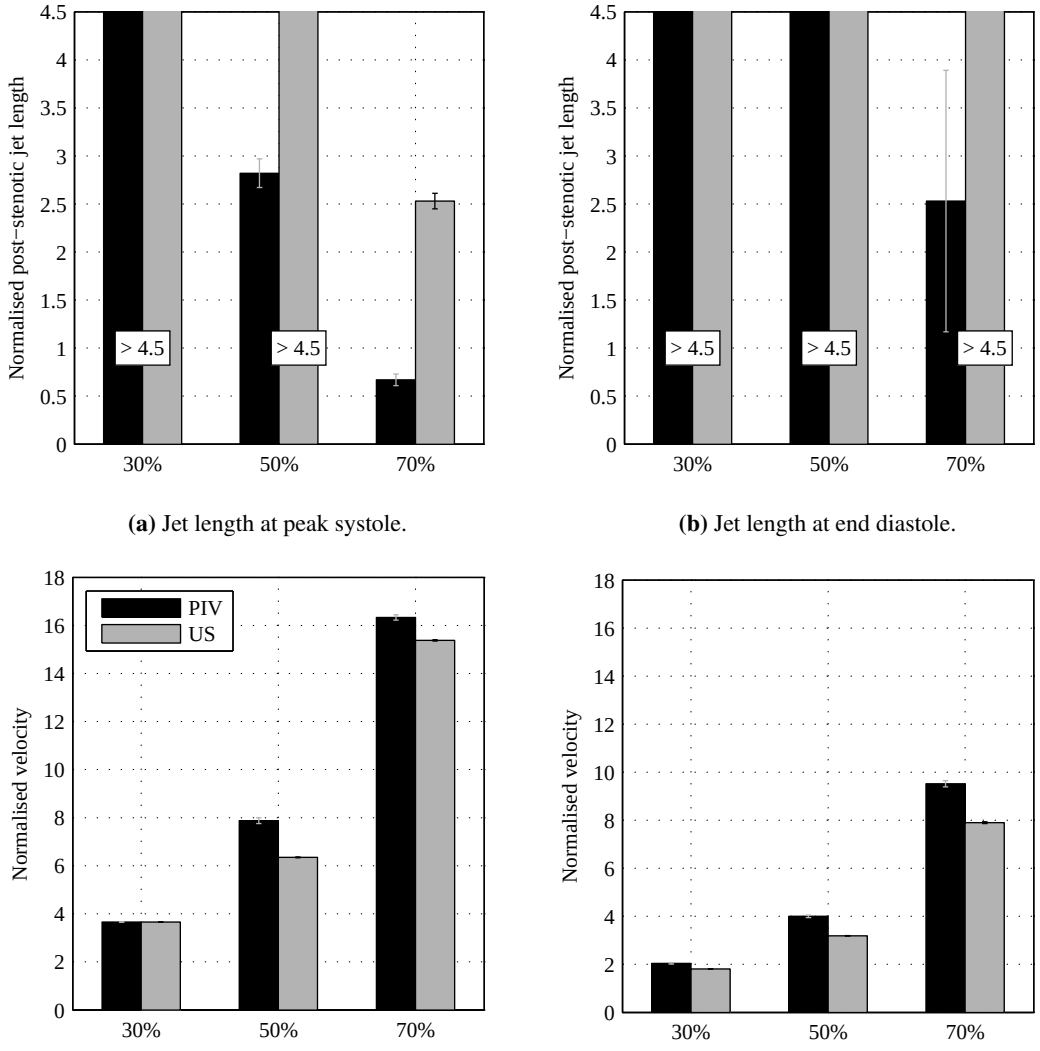

(a) Jet length at peak systole.

(b) Jet length at end diastole.

(c) Maximum post-stenotic velocity at peak systole.

(d) Maximum post-stenotic velocity at end diastole.

Figure 7.9: *Properties of the post-stenotic jet in the stenosis models.*

PIV maximum WSS values was 41 (108)% (range –54% to 263%). Separating the systolic and diastolic mean values gives 69 (138)% and 13 (53)%, respectively.

Measurement of the minimum wall shear stress was dominated by experimental noise, which was typically of the same magnitude as the measurement (Fig. 7.11d and Table 7.3). No diastolic values can be reported for the 30 and 50% ultrasonic models, as the velocity data was truncated before the edge of the vessel. The only significant difference between the PIV and DUS measurements occurred in the 70% model at peak systole ($p < 0.05$).

Measurements of the recirculation were subject to large errors due to the difficulty of establishing where the WSS exceeded the threshold. In the ultrasound 30% stenosis model, L_R extended

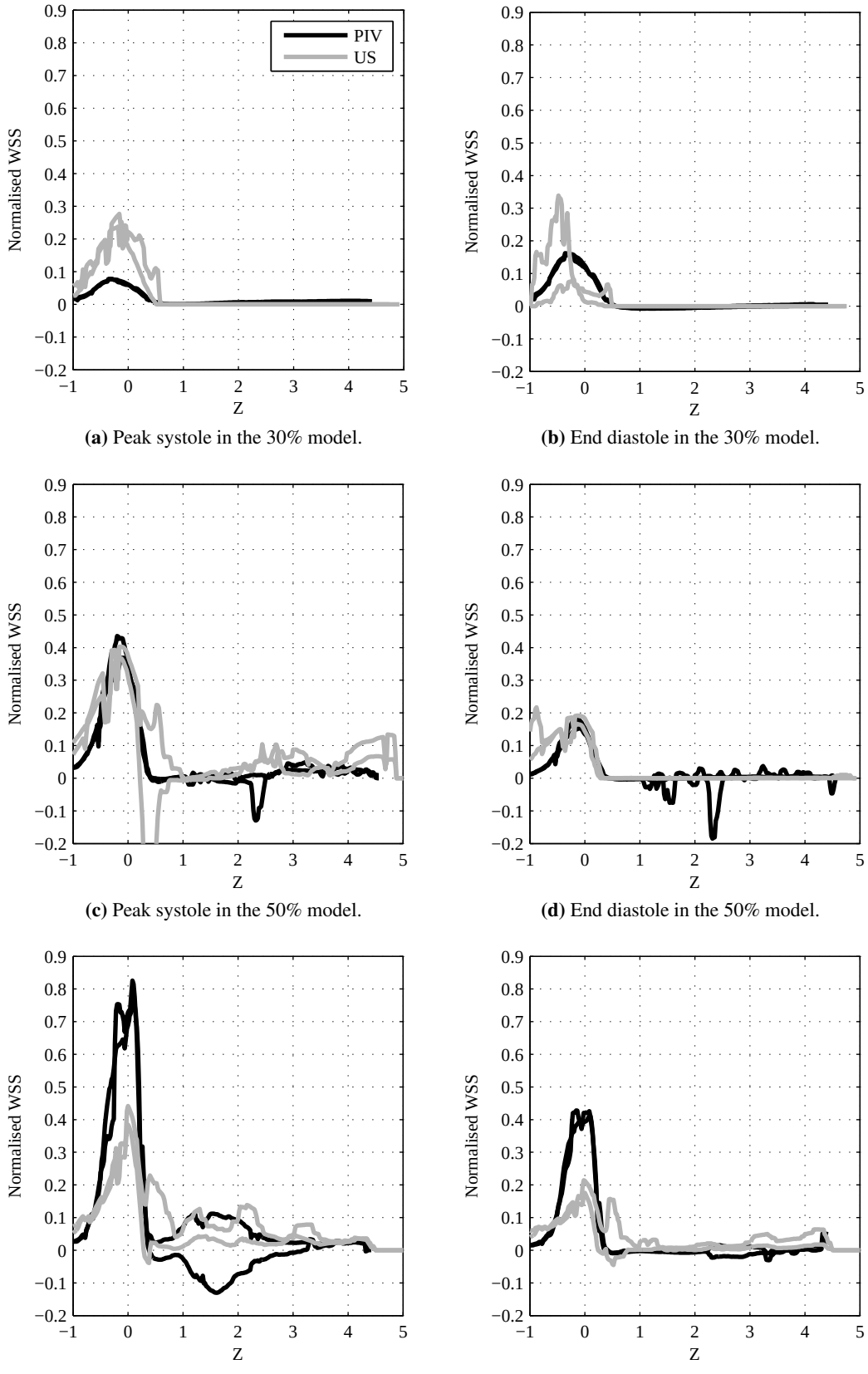

(a) Peak systole in the 30% model.

(b) End diastole in the 30% model.

(c) Peak systole in the 50% model.

(d) End diastole in the 50% model.

(e) Peak systole in the 70% model.

(f) End diastole in the 70% model.

Figure 7.10: *Normalised* WSS *in the stenosis models at peak systole and end diastole.*

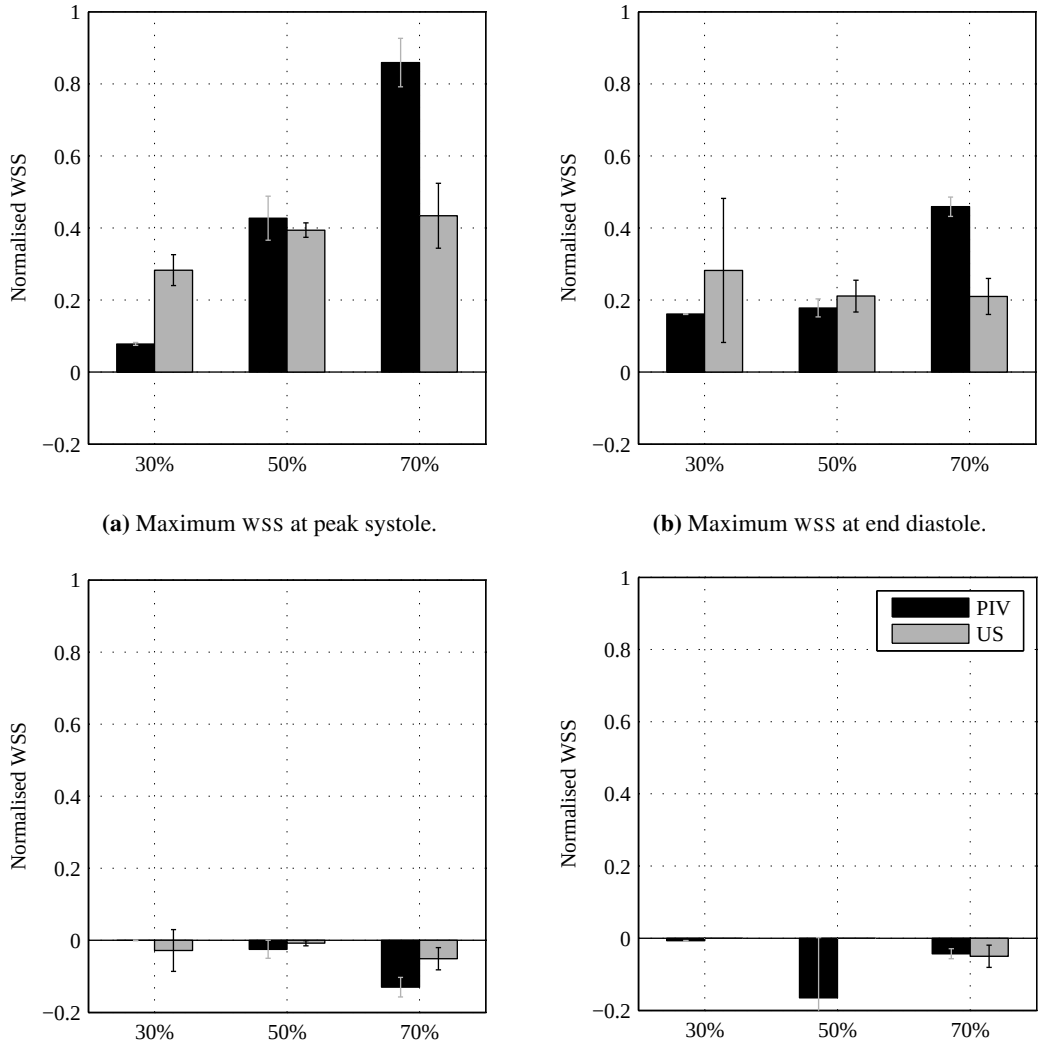

(a) Maximum WSS at peak systole.

(b) Maximum WSS at end diastole.

(c) Minimum WSS at peak systole.

(d) Minimum WSS at end diastole.

Figure 7.11: *Maximum and minimum values of* WSS *in the stenosis models.*

beyond the region studied, both at systole and diastole (Fig. 7.12). Recirculation lengths were similar in the 50% stenosis model. In the 70% model, the PIV and DUS values for L_R were similar at diastole, but significantly different at systole ($p < 10^{-3}$).

Stenosis	Systole		Diastole	
model	PIV	DUS	PIV	DUS
30	0.078 (0.004)	0.283 (0.043)‡	0.161 (0.001)	0.282 (0.200)†
50	0.427 (0.061)	0.394 (0.020)	0.178 (0.025)	0.211 (0.044)
70	0.859 (0.067)	0.434 (0.090)†	0.459 (0.027)	0.210 (0.050)‡

Table 7.2: *Maximum normalised* WSS, $\hat{\tau}_{w,max}$, *in the stenosis throat.* $^{\dagger}p < 10^{-2}$; $^{\ddagger}p < 10^{-3}$.

Stenosis	Systole		Diastole	
model	PIV	DUS	PIV	DUS
30	0.000 (0.001)	–0.028 (0.058)	–0.007 (0.001)	—
50	–0.025 (0.025)	–0.008 (0.007)	–0.165 (0.167)	—
70	–0.130 (0.027)†	–0.051 (0.031)	–0.043 (0.014)	–0.050 (0.031)

Table 7.3: *Minimum normalised* WSS, $\hat{\tau}_{w,min}$, *distal to the stenosis throat.* $^{\dagger}p < 0.05$.

7.4 Discussion

7.4.1 Upstream flow conditions

7.4.1.1 Velocity comparison

Somewhat in contrast to the results acquired in Chapt. 5, excellent agreement between theoretic and experimental velocity profiles was present at the inlet of the flow phantoms. The only deviations of note were mild skewness in the 30% PIV systolic velocity profile, and close to the wall using CFI. The excellent agreement of the Womersley values for the dual systems confirms that they were indeed dynamically similar.

Under pulsatile flow, one expects the non-deterministic nature of the various systems—such as the interface program (which runs on a PC), the PIV processor (which is just a PC with an extra hardware card) and the ultrasound machine—to introduce timing errors which are not present under steady flow. These errors will change the point in the cardiac cycle when the velocity profile is measured. Considering only random (Gaussian) jitter, the mean time delay may be subtracted to leave a random distribution of delays centred on zero. (If the mean triggering delay varies systematically, further errors may be introduced. This is beyond the scope of this argument.) The actual effect of jitter is dependent on the flow rate through the vessel. If the flow rate is not changing (ie,, it is steady), then the jitter will have no effect on the measured velocity profiles. If the flow rate is increasing in a linear manner, then the symmetric nature of the jitter implies that no bias will be introduced to the velocity measurements, but that the variance of the measurements will increase. If the rate of change of the flow rate is non-linear,

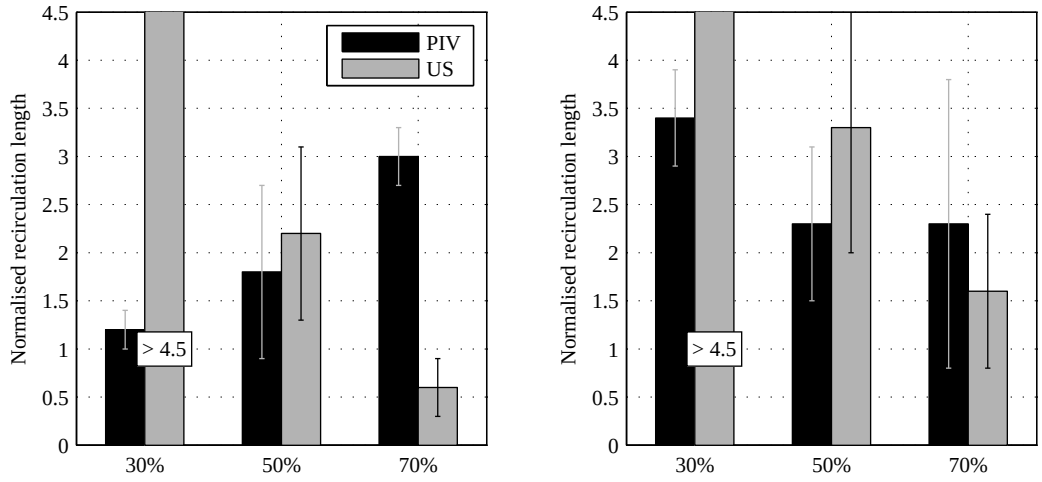

(a) Recirculation length at peak systole.

(b) Recirculation length at end diastole.

Figure 7.12: *Recirculation region sizes at peak systole and end diastole in the stenosis models.*

then the velocity noise distribution is not symmetric, so a bias is introduced into the velocity measurements. This bias is related to the second derivative of the flow. (The flow rate is the first derivative of flow.)

The effect of this bias would be most pronounced at periods when the flow rate is changing most rapidly. Peak systole is a turning point in the flow rate waveform, so the second derivative will be large and negative (as it represents the maximum of the flow wave). Thus, if the jitter is large, the mean flow rate in the systolic frame would be biased towards zero, which would, in general, reduce the measured velocities. Examining the systolic velocity profiles, the centreline velocities measured by PIV and DUS were both within 1% of the Womersley values. This implies that any bias introduced by jitter in the triggering system was very small, and hence that the jitter in the triggering system was small. At end diastole, since the rate of change of the flow rate (with respect to time) is close to zero, any resulting bias would be even smaller.

The diastolic deviations from the theoretic velocity profiles are artifacts of the limited dynamic range and of the clutter filter of the ultrasound scanner. To prevent aliasing during systole, the pulse repetition frequency was increased. Typically, adjusting the PRF also increases the threshold level of the wall filter; resulting in data loss close to the vessel wall.

7.4.1.2 Wall shear stress comparison

As observed in previous chapters, measurement of the wall shear stress was more difficult than velocity measurement. As an example of the problems associated with measuring velocity gradients, as opposed to velocities, one only needs to study Fig. 7.5c, and compare it with Fig. 7.5a. Despite the excellent agreement between the Womersley predicted centreline velocities in both systems (within 2%), the difference between values of the theoretic velocity gradient at the wall in the 50% model was 18%.

Glare from the fluid/solid interface affected the PIV measurements close to the wall, while ultrasound velocities were affected by the clutter filter and the size of the Doppler sample volume. The differences between shear stresses measured by DUS/PIV were extremely large (261% at systole and 141% at diastole). This figure is distorted by the systematic trend that the Doppler data tended to over-estimate the Womersley value, while PIV measured lower values. Despite the tendency to overestimate WSS, due to the high variability of the ultrasound data, the differences between the Womersley value and the estimated value were not significant. The mean difference between the ultrasound data and the Womersley values was 41 (58)% and systole and 42 (68)% at diastole (ignoring the 30% model). These differences are comparable to the difference between the value of measured under Poiseuille flow in Chapt. 5.

Values of WSS estimated from the PIV data were significantly different to the theoretic values. During systole, the mean underestimate was 42%, the same figure obtained in Chapt. 5. However, at diastole the mean difference between the figures was +32%, suggesting that PIV actually produced higher values. This figure was distorted by the surprising result obtained from the 30% model, which suggested that the WSS was higher during diastole than at systole. If this result is disregarded, the differences are no longer significant. This result is somewhat surprising. Given that Δt (ie, the time separation between the paired images) was the same at systole and diastole, and that the WSS was underestimated at systole, at diastole, the mean displacement in each IA should be lower, producing lower estimated values of WSS. (Strictly, retrograde flow may occur next to the wall. However, with this waveform, minimal reversal occurs.) A possible explanation lies in the triggering of the PIV processor from the interface program. Although the triggering delay was measured and approximately compensated for, it did fluctuate. Any increase in the delay could result in triggering just after maximum systole, which would produce lower velocity gradients. Similarly, delaying the trigger beyond end dias-

tole would cause the system to trigger in (very) early systole, which would increase the diastolic values.

7.4.2 Post-stenotic flow conditions

7.4.2.1 Velocity comparison

Distal to the stenosis, the agreement between the velocities was generally similar to the agreement observed under steady flow. In mild stenoses and at low flow rates (ie, for low stenotic Reynolds numbers, Re_0), the velocity profiles were broadly symmetric, and laminar, resulting in good agreement between the DUS/PIV velocity profiles. At higher stenotic Reynolds numbers, the increased degree of asymmetry broadly resulted in poorer agreement between the PIV and ultrasound data. Turbulence was present in the 70% model during systole and diastole, corresponding to stenotic Reynolds numbers of approximately 1580 and 830, both greater than the value determined for the critical stenotic Reynolds number in Chapt. 6. Flow remained laminar during diastole in the 50% model ($Re_0 \approx 520$) but was turbulent during systole ($Re_0 \approx 1160$). Flow remained laminar in the 30% model during systole even though the stenotic Reynolds number was slightly greater than the critical value ($Re_0 \approx 830$).

Doppler ultrasound estimates of maximum velocity were always lower than velocities estimated with PIV. Surprisingly, the differences were smaller during systole than at diastole (mean difference –8 [8]% vs.–16 [4]%). The diastolic value agrees with the underestimation measured in Sect. 6.3.1, but the systolic value contradicts the findings of Sect. 6.3.2.1, which established that differences between the centreline velocity increased with with flow rate. This finding may be a result of jitter in the triggering of the PIV system. If the jitter was sufficiently large, the mean systolic velocities would be subject to a bias towards zero as described previously. This would reduce the difference between the measured maximum systolic velocities. However, the good agreement between the measured and theoretic maximum velocities during systole suggests that the jitter was too small to have a significant effect.

An alternate explanation is that changes to the flow waveform as it passed through the stenosis may increase the magnitude of any bias introduced by the trigger jitter. The outlet flow waveform contained higher frequencies than the inlet waveform, so the peak corresponding to systole was sharper distal to the stenosis. Thus, for the same amount of jitter in the triggering

system, the biasing effect could be increased, which would appear to reduce the differences between the measured maximum velocities.

During systole in the PIV models, the stenotic jet length, L_J, reduced as the degree of stenosis increased. This agrees with Sect. 6.3.1, and is again a result of the unstable shear layers causing the transition to turbulence more proximally. During diastole, the lower velocities increased the stability of the jet, so it persisted to greater Z values. The ultrasound data agree qualitatively with the PIV observations. However, in all cases except systole in the 70% model, the jet was sufficiently stable that it persisted for the entire region studied.

7.4.2.2 Wall shear stress comparison

Measurement of the wall shear stress was affected much more by experimental noise than under steady flow (Fig. 7.10). This is unsurprising, since there are many more variables to control under oscillatory flow. Even at the inlet, despite the good agreement in the measured centreline velocities (within 1%), the differences between the wall shear stresses much larger.

In the PIV models, the maximum WSS at systole increased as the degree of stenosis increased. This is in agreement with Sect. 6.3.1, which found that the maximum WSS was inversely proportional to $(1-\kappa)$. Due to the limited number of stenosis models studied in this chapter, establishing relationships between variables was not possible. Similarly, during diastole, the maximum WSS increased with increasing κ. When measured with DUS, maximum WSS increased as the degree of stenosis increased at systole, although the rate of increase was much smaller. During diastole, the maximum WSS was broadly independent of κ. This contrasts with the steady flow case which established a strong inverse relationship between the Doppler-estimated $\tau_{w,max}$ and $(1-\kappa)$.

The lack of a relationship between the maximum Doppler WSS at diastole was probably an artifact of the increased PRF necessary to measure flow without aliasing during systole. In most CFI systems, the level of the clutter filter and the system PRF are related, so that increasing the PRF raises the frequency threshold. Consequently, the velocities close to the wall during diastole are affected more by the clutter filter than if the ultrasound machine settings were optimised solely for diastole (in which case, the PRF and hence level of the wall filter would be lower).

Measurement of the minimum WSS was largely dominated by noise (Fig. 7.10 and Fig. 7.11). Only in the 70% stenosis models were the negative wall shear stresses measured with uncertainties less than the magnitude of the measurement. In the 30% and 50% PIV models all that can be concluded is that, distal to the stenosis, the wall shear stress was very close to zero. Its direction cannot be specified, but the recirculation—or stagnation—regions persisted both at systole and diastole. In the 70% model, the WSS was negative both at systole and diastole. Using Doppler ultrasound, measurement of the minimum WSS was not possible in the 30% and 50% models during diastole, as the Doppler data were truncated by the clutter filter. During systole, the minimum values of the WSS again failed to exceed the uncertainty in the measurement, forcing the conclusion that they were very close to zero. In the most severe stenosis, the minimum wall shear stress was the small and negative during systole and diastole, implying that the recirculation region was persistent throughout the cardiac cycle.

In the optical models, the size of the recirculation regions increased with increasing stenosis severity at systole, but showed no general relationship during diastole. This is at odds with the results of Sect. 6.3.1 which found no relationship between L_J and κ. However, extrapolation based on these limited data would be tenuous, considering the amount of noise present in the minimum WSS measurements. The size of the recirculation region in the ultrasound models reduced as the degree of stenosis increased. This relationship was present during systole and diastole. These results are at odds with Sect. 6.3.1, which found no relationship between L_J and κ in the ultrasound models. Once again, the limited scope of this study precludes the wide extrapolation of the results.

7.4.2.3 Comparison with the literature

Previous studies of pulsatile flow through stenosis models have typically used sinusoidal flow waveforms, which are not physiologic, and precludes quantitative comparison with the data presented in this chapter. However, the general structures and qualitative observations may be discussed.

Cassanova & Giddens (1978) studied flow through streamlined and abrupt stenoses. They established that the flow was less stable under pulsatile conditions. The 30% stenosis model showed no signs of turbulence at peak systole, corresponding to a stenotic Reynolds number of around 830. During diastole in the 70% model, flow did develop turbulence, and the stenotic Reynolds number was around 830. These values are very close to the value of around 800

estimated in Chapt. 6, which suggests that, at least from these limited pulsatile data, the flow was not substantially less or more stable than under steady conditions.

Several authors have observed that the distal recirculation regions are transient when flow waveform is sinusoidal (Ahmed & Giddens, 1984; Varghese et al., 2007*b*). During the early acceleration phase of the sine wave, the distal flow field was entirely orientated in the positive Z direction but by the peak flow phase the recirculation regions reformed (Varghese et al., 2007*b*). The results appear to disagree with the data in this chapter. However, since data were collected only at systole and end diastole, it is not possible to state whether the flow separation did not dissipate and reform between the times studied.

7.5 Conclusion

In this chapter, the fluid mechanics distal to a range of simplified stenoses has been studied using the paired flow system developed in Chapt. 5. Maximum Doppler velocity measurements at peak systole and end diastole were compared with gold standard PIV data. In the inlet region to the stenosis models, the error in the Doppler maximum velocity measurement was less than 1% when compared to the PIV measurements and to the theoretic value. During diastole, the DUS underestimated the theoretic value by 13%. In the stenosis throat, the mean difference between the centreline velocities measured by PIV and Doppler ultrasound was –12%, which broadly agrees with the underestimation observed in Chapt. 6. During systole, the mean difference was –8%, at end diastole, the differences increased to –16%.

Estimates of the wall shear stress made with the dual flow systems broadly agreed, in the sense that elevated WSS was measured in the stenosis throat, and regions of near zero WSS were detected distally. However, quantitative assessment of the WSS remained a formidable challenge, with more noise present in the measurements than in the steady flow situation.

Chapter 8
Conclusions and further work

In Chapt. 3, a simple method to estimate the time varying wall shear rate in healthy arteries using clinical Doppler ultrasound techniques was developed and validated. This method is accurate to within 14% of the theoretic value of WSR. Test measurements from one healthy volunteer demonstrated the applicability of this method in-vivo.

Chapt. 4 and Chapt. 5 described the development of a dual flow validation system that allowed the validation of velocity measurements made with Doppler ultrasound against a gold standard technique. In steady flow conditions, Doppler maximum velocity measurements underestimated the theoretic values by 14%. The equivalent error in the gold standard measurement was less than 1%. Under the Newtonian fluid approximation, wall shear stresses estimated with Doppler ultrasound were within 10% of the theoretic value, although this figure disguised the extreme variability of the measurements.

Chapt. 6 used the dual flow validation system to study flow through a series of idealised stenosis models to validate Doppler ultrasound maximum velocity measurements. On average, the maximum velocities measured using Doppler ultrasound distal to the stenosis throat underestimated the gold standard data by 15%. This error did not change as the degree of stenosis was changed, but the underestimation increased at the flow rate increased. Over a range of physiologic flow rates (Re = 200 to Re = 1000) that underestimation of the maximum velocities ranged from –15% to –30%. Measurements of wall shear stress using Doppler ultrasound were able to distinguish regions of high shear stress from regions of low WSS, but quantitative measurement remained difficult.

Chapt. 7 studied physiologic pulsatile flow through the simplified stenosis models using the dual flow validation system to validate maximum velocity measurements during systole and diastole. The mean difference between the Doppler measurements and the gold standard was –12%. Estimation of the wall shear stress with Doppler ultrasound subject to much more experimental noise than under steady flow, but distinguishing between regions of near-zero and high WSS remained possible.

The work in this thesis can be extended in several ways. Among the most obvious is to perform a population study in healthy adults to establish normal values of WSR, using the technique developed in Chapt. 3. The dual flow validation system represents a powerful tool for studying hæmodynamics and validating Doppler velocity measurements. The existing study into pulsatile flow concentrated on the clinically relevant systolic and diastolic phases of the cardiac cycle. Future studies could examine the intermediate flow dynamics, to establish whether the recirculation regions are transient with a physiologic flow waveform or not. Other studies could be performed using aneurysm models to validate Doppler ultrasound measurements in different diseases.

Appendix A
Publications

A.1 Journal papers

- J. R. Blake, S. Meagher, K. H. Fraser, W. J. Easson and P. R. Hoskins, 'A method to estimate wall shear rate with a clinical scanner', *Ultrasound in Medicine and Biology*, **34**: 760–774, (2008).

- K. H. Fraser, S. Meagher, J. R. Blake, W. J. Easson and P. R. Hoskins, 'Characterization of an abdominal aortic velocity waveform in patients with abdominal aortic aneursym', *Ultrasound in Medicine and Biology*, **34**: 73–80, (2008).

A.2 Conference proceedings

- S. Meagher, J. R. Blake, W. J. Easson and P. R. Hoskins, 'Validation of ultrasound velocity measurements against particle image velocimetry', *Proceedings of the second* IASTED *international conference*, (2005).

Appendix B
Supplementary data

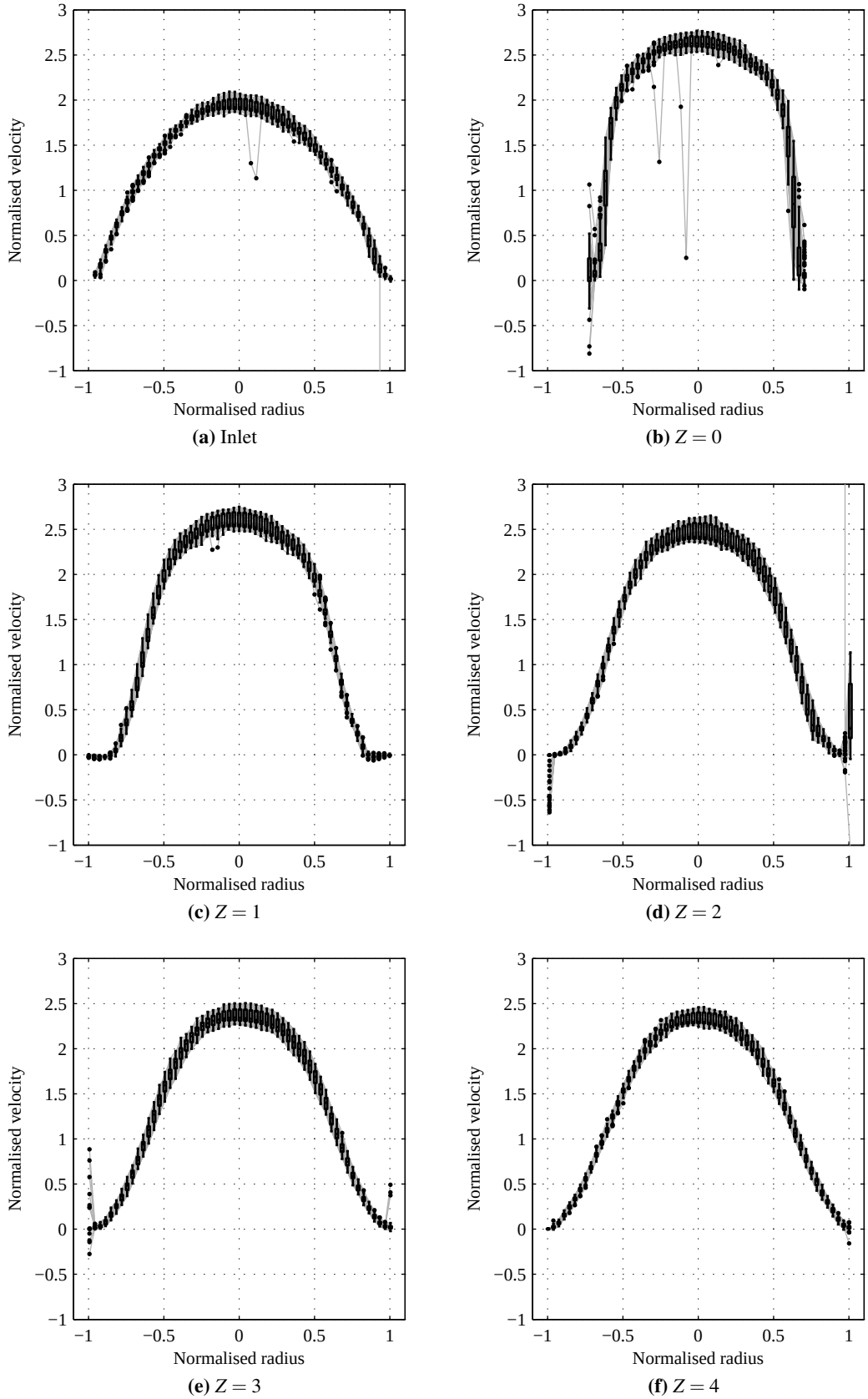

(a) Inlet **(b)** $Z = 0$

(c) $Z = 1$ **(d)** $Z = 2$

(e) $Z = 3$ **(f)** $Z = 4$

Figure B.1: *Velocity profiles in the 30% stenosis model measured with* PIV *(*$\mathrm{Re}_{-1} = 500$*)*

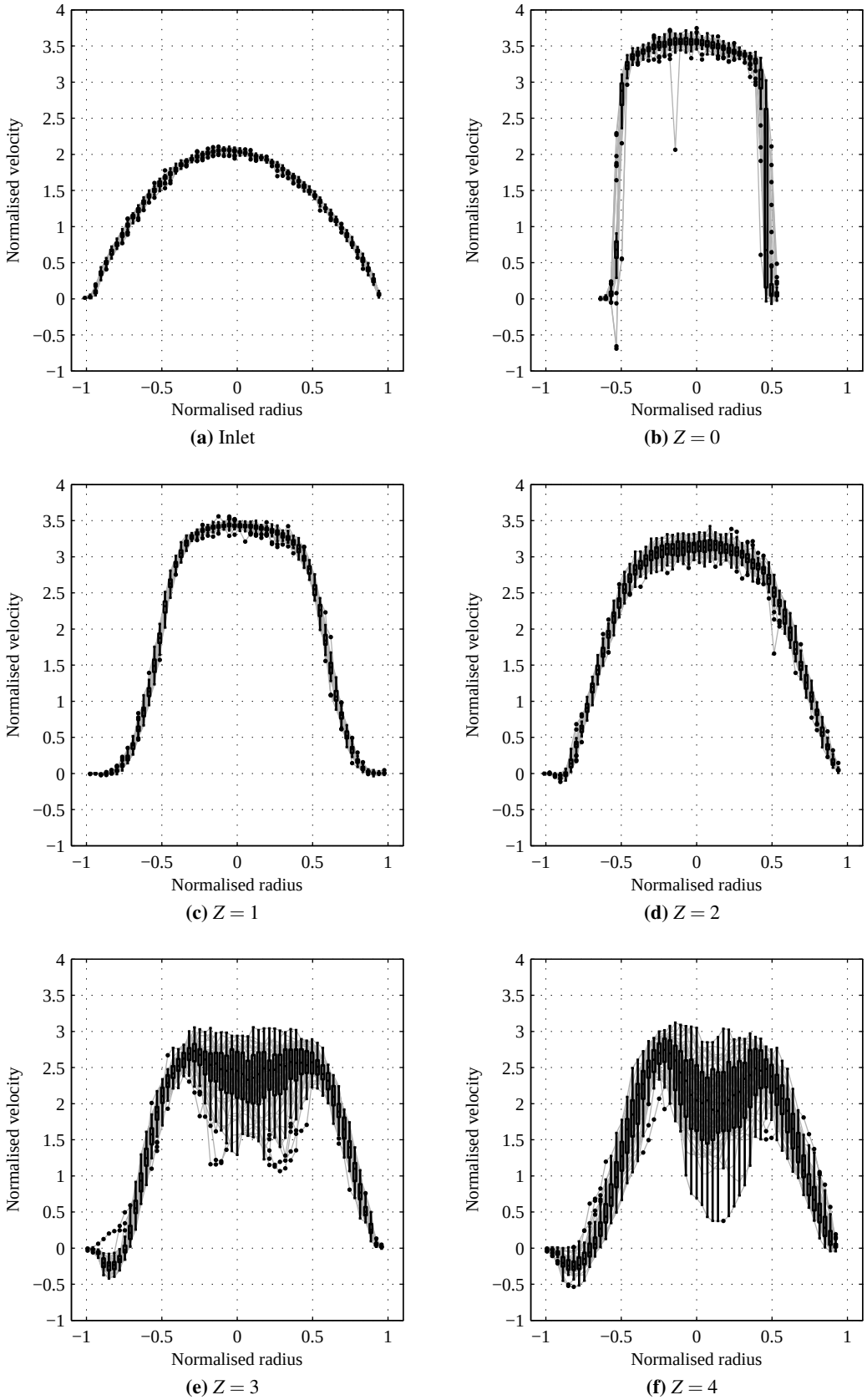

(a) Inlet **(b)** $Z = 0$

(c) $Z = 1$ **(d)** $Z = 2$

(e) $Z = 3$ **(f)** $Z = 4$

Figure B.2: *Velocity profiles in the 40% stenosis model measured with* PIV *(*$\mathrm{Re}_{-1} = 500$*)*

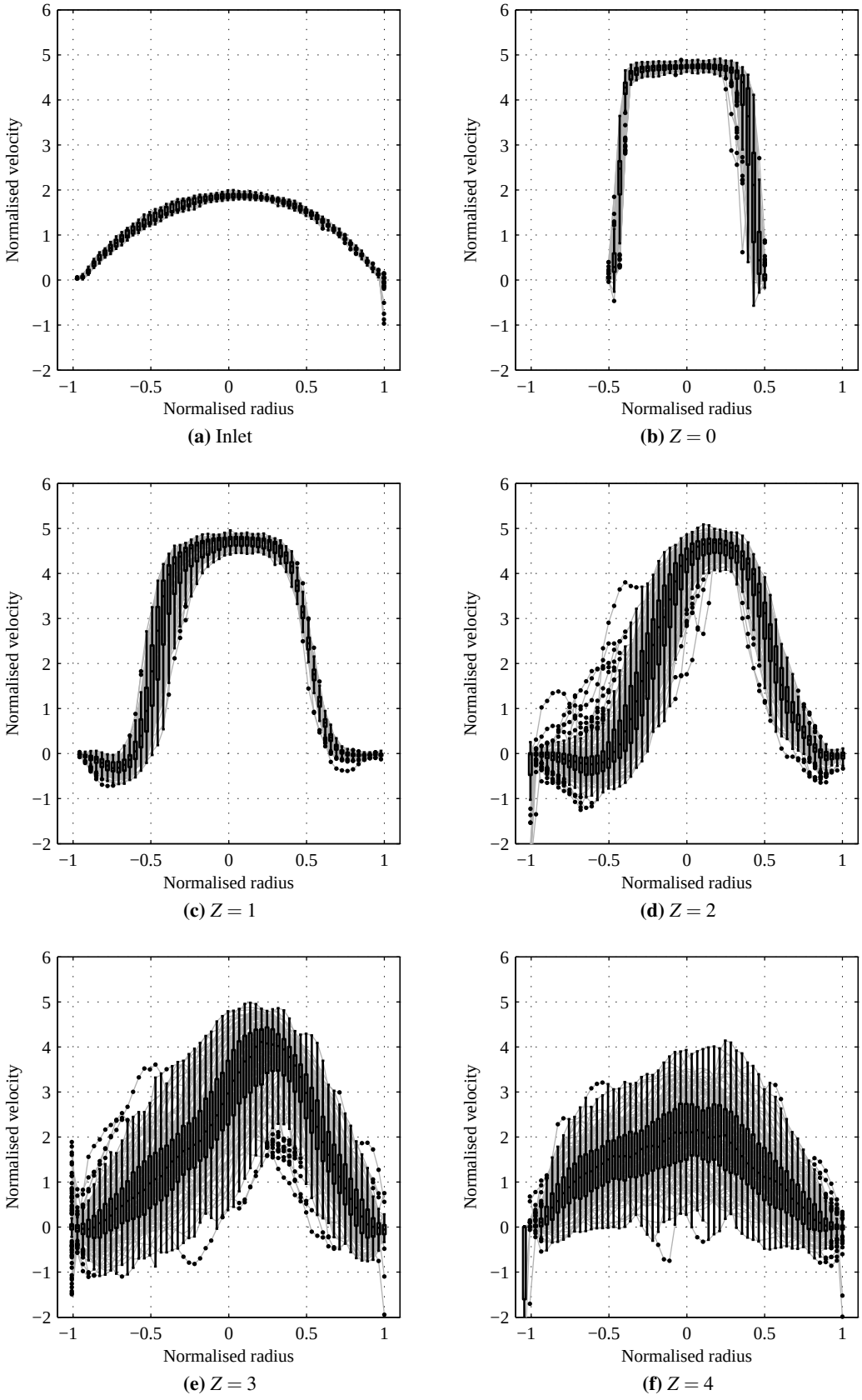

(a) Inlet **(b)** $Z = 0$ **(c)** $Z = 1$ **(d)** $Z = 2$ **(e)** $Z = 3$ **(f)** $Z = 4$

Figure B.3: *Velocity profiles in the 50% stenosis model measured with* PIV *(*$\mathrm{Re}_{-1} = 500$*)*

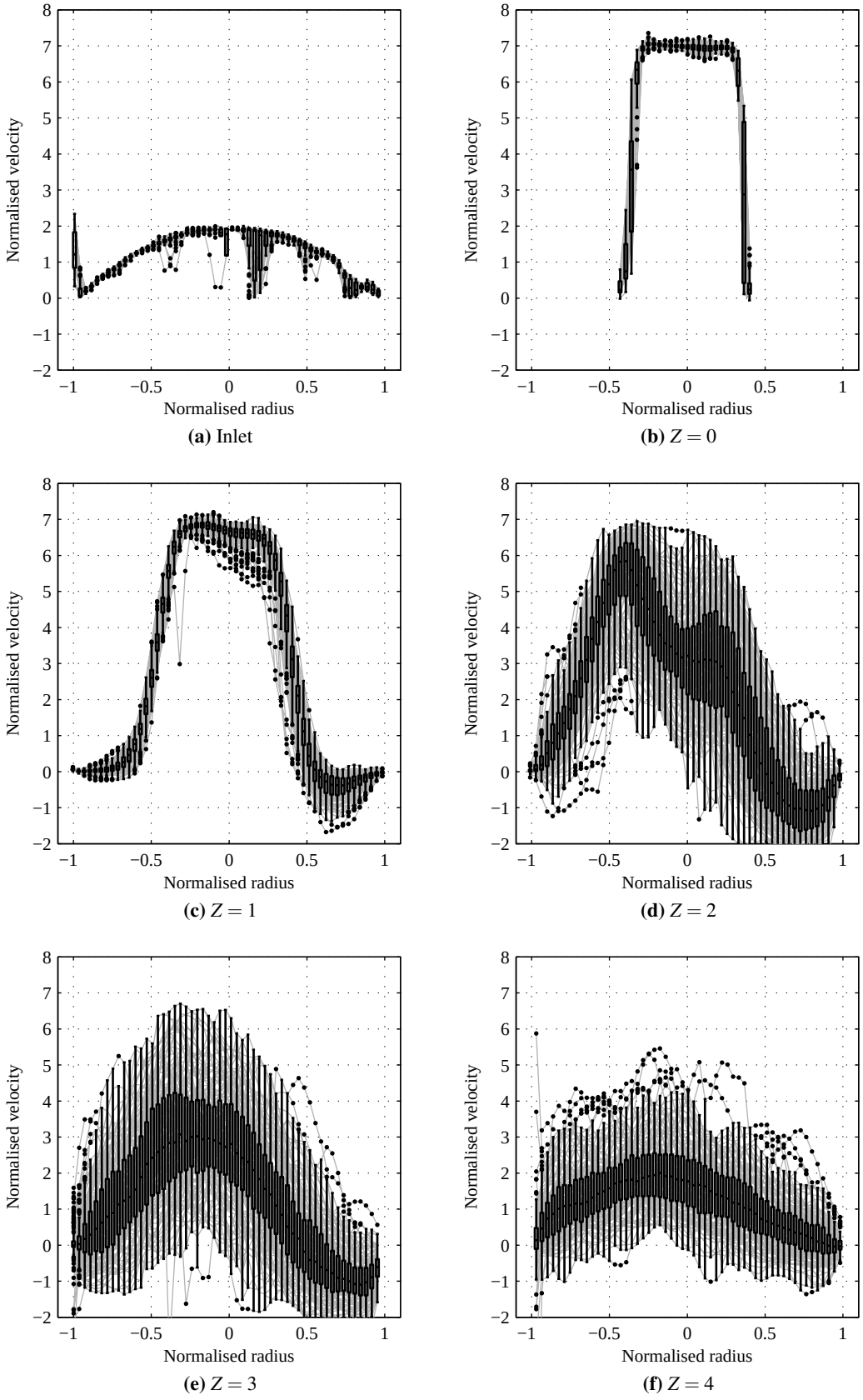

(a) Inlet **(b)** $Z = 0$

(c) $Z = 1$ **(d)** $Z = 2$

(e) $Z = 3$ **(f)** $Z = 4$

Figure B.4: *Velocity profiles in the 60% stenosis model measured with* PIV *(*$\mathrm{Re}_{-1} = 500$*)*

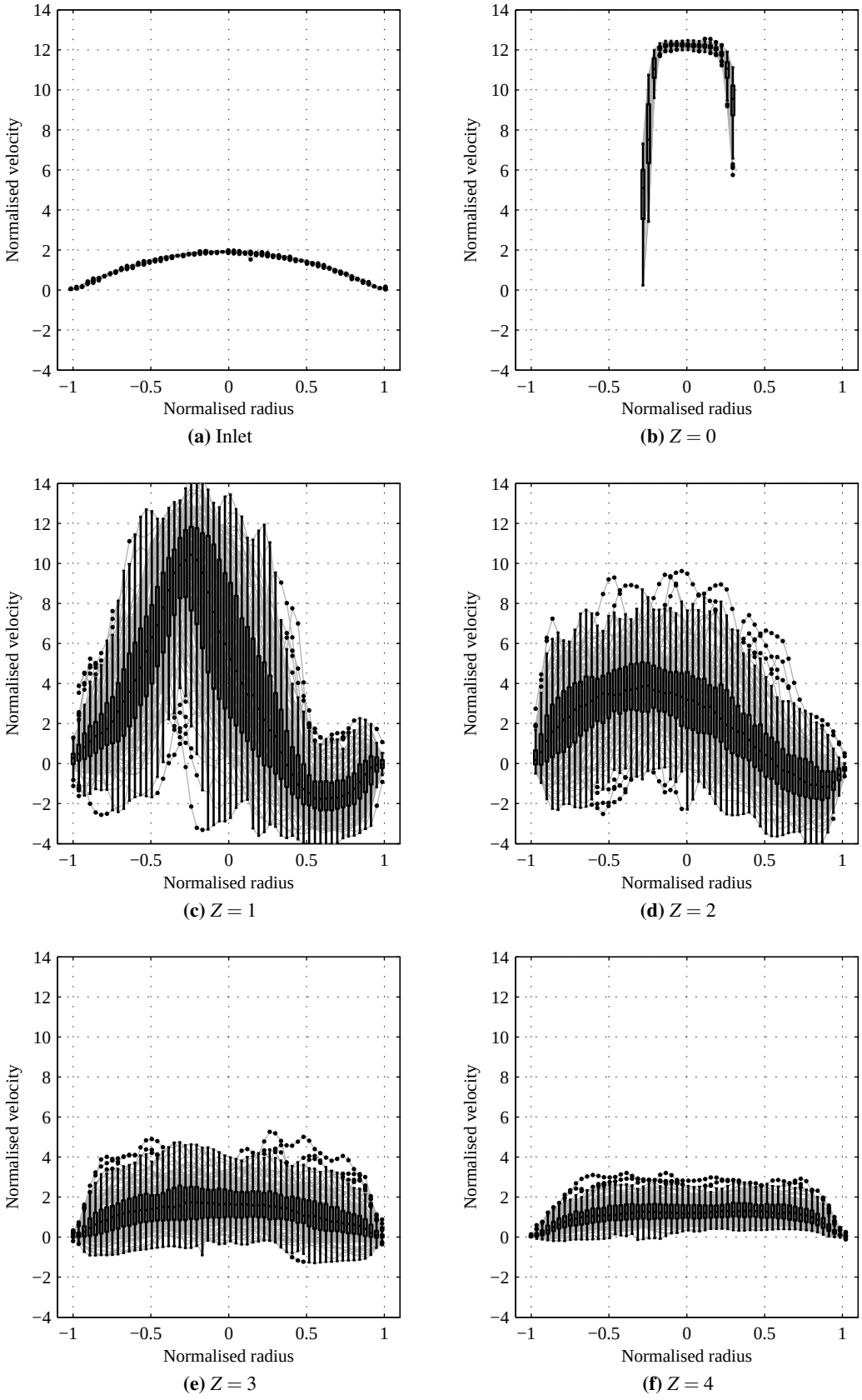

(a) Inlet **(b)** $Z = 0$

(c) $Z = 1$ **(d)** $Z = 2$

(e) $Z = 3$ **(f)** $Z = 4$

Figure B.5: *Velocity profiles in the 70% stenosis model measured with* PIV *(*$\mathrm{Re}_{-1} = 500$*)*

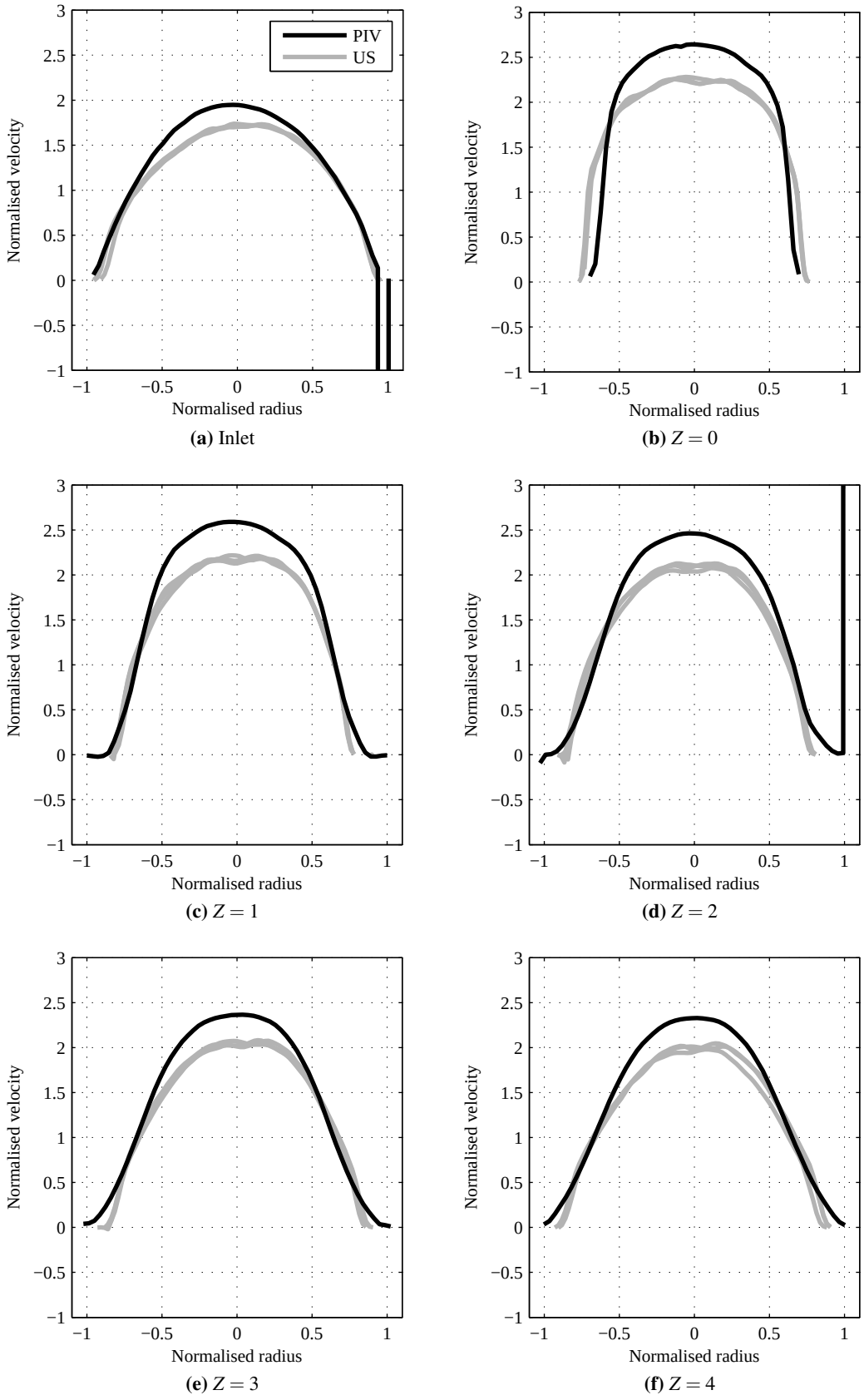

(a) Inlet **(b)** $Z = 0$

(c) $Z = 1$ **(d)** $Z = 2$

(e) $Z = 3$ **(f)** $Z = 4$

Figure B.6: *Velocity profiles in the 30% stenosis model measured with* PIV *and* DUS *(*$\mathrm{Re}_{-1} = 500$*)*

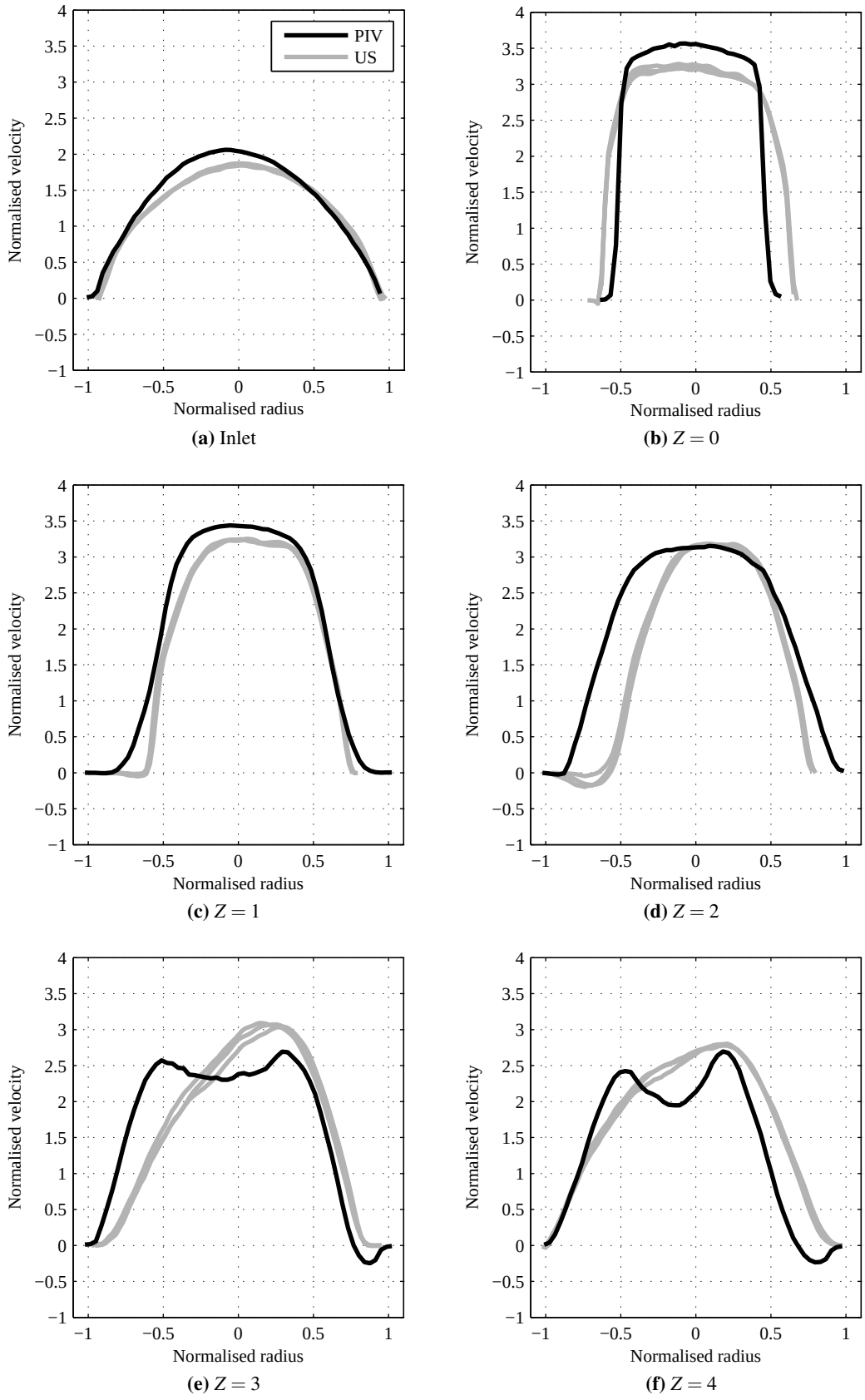

(a) Inlet **(b)** $Z = 0$

(c) $Z = 1$ **(d)** $Z = 2$

(e) $Z = 3$ **(f)** $Z = 4$

Figure B.7: *Velocity profiles in the 40% stenosis model measured with* PIV *and* DUS *(*$\mathrm{Re}_{-1} = 500$*)*

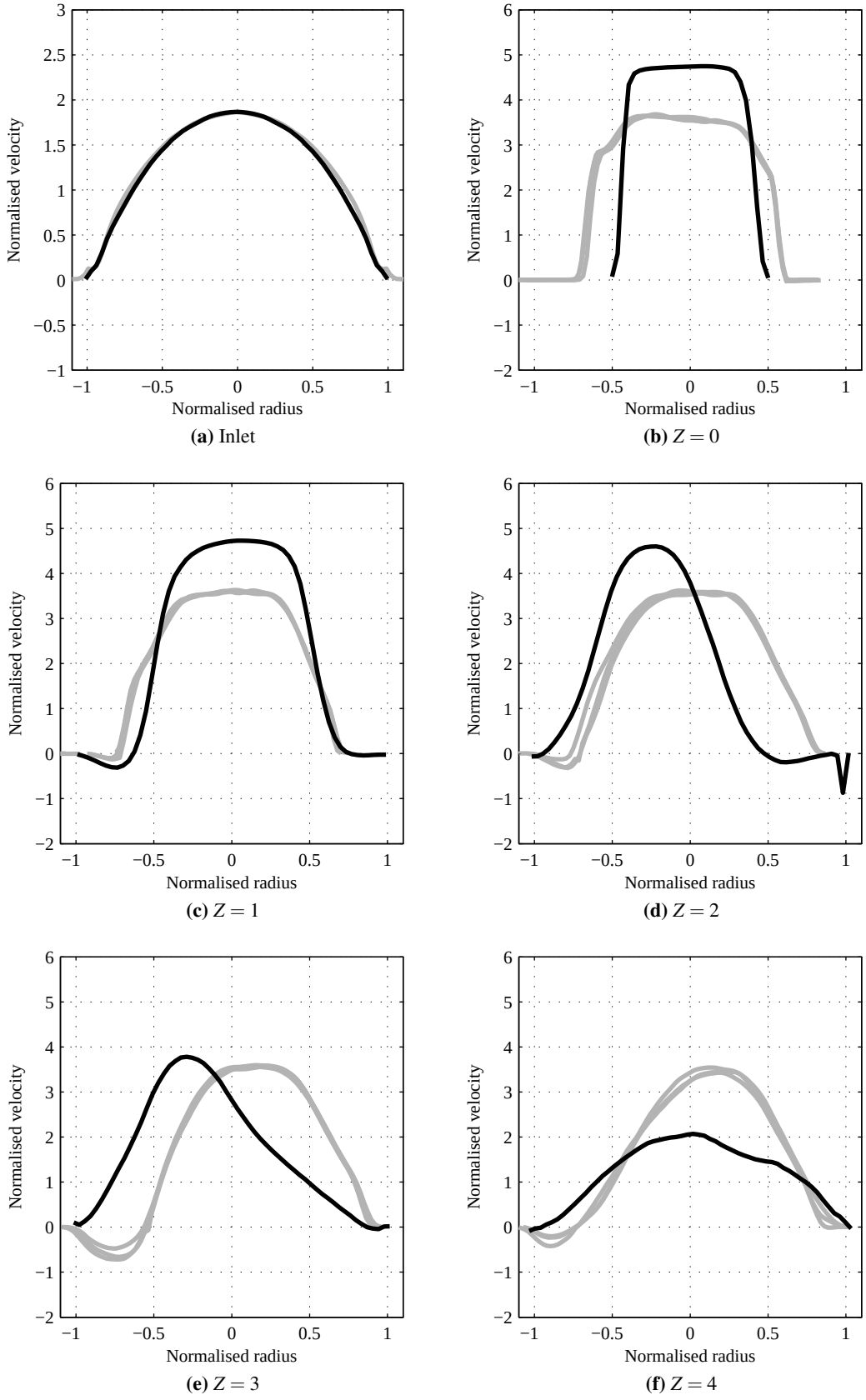

(a) Inlet **(b)** $Z = 0$ **(c)** $Z = 1$ **(d)** $Z = 2$ **(e)** $Z = 3$ **(f)** $Z = 4$

Figure B.8: *Velocity profiles in the 50% stenosis model measured with* PIV *and* DUS *(*$\mathrm{Re}_{-1} = 500$*)*

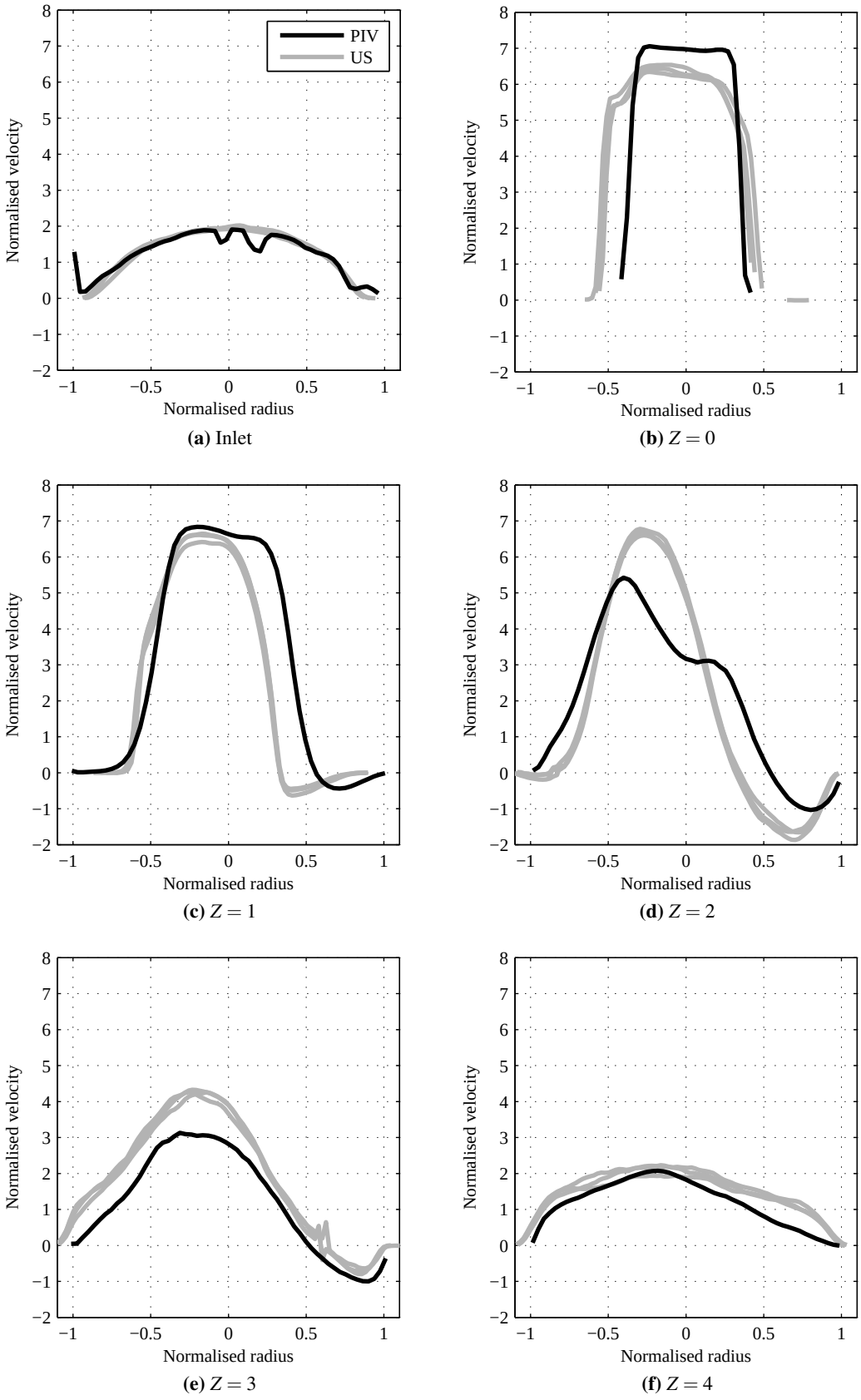

(a) Inlet **(b)** $Z = 0$ **(c)** $Z = 1$ **(d)** $Z = 2$ **(e)** $Z = 3$ **(f)** $Z = 4$

Figure B.9: *Velocity profiles in the 60% stenosis model measured with* PIV *and* DUS *(*$\mathrm{Re}_{-1} = 500$*)*

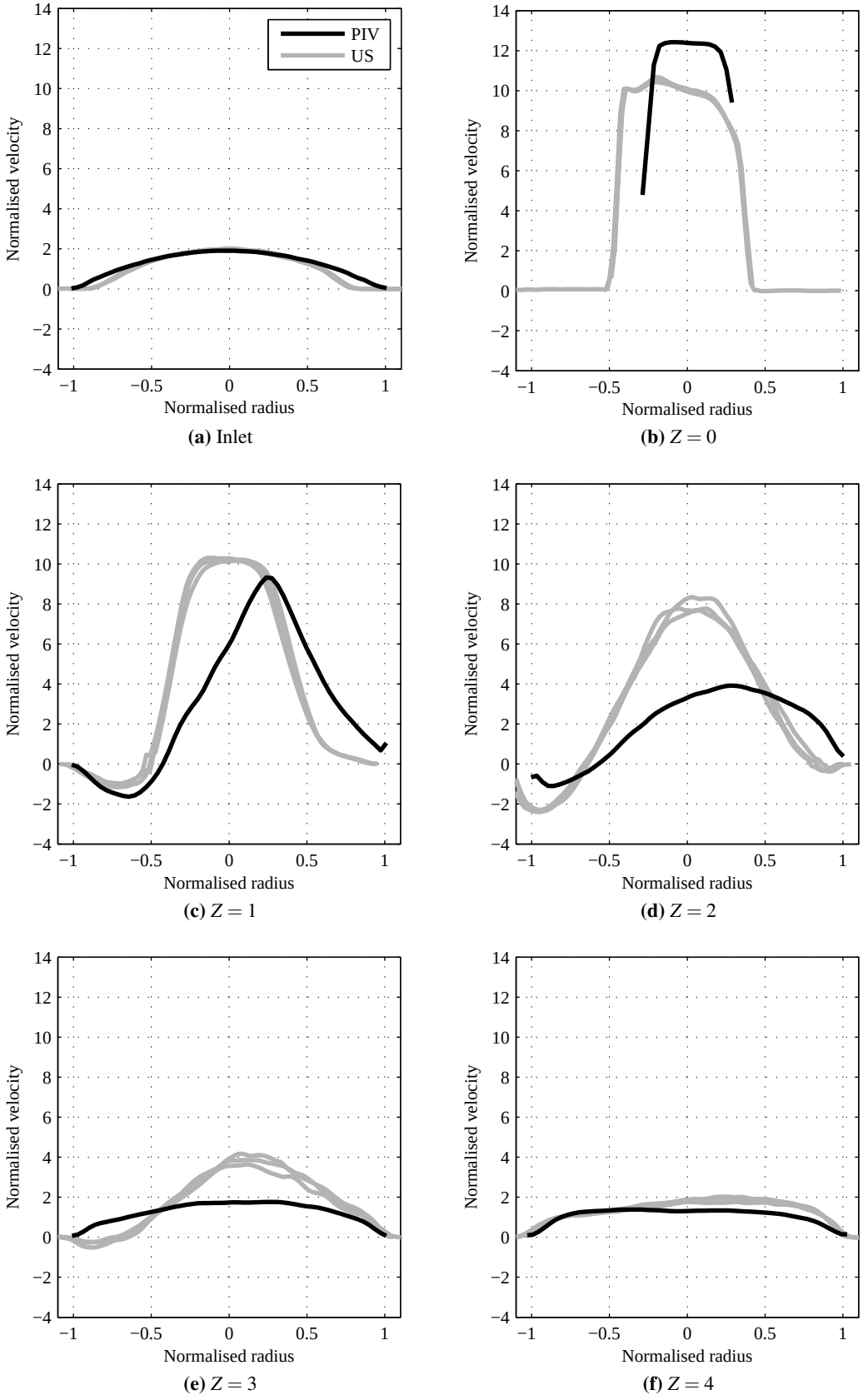

(a) Inlet **(b)** $Z = 0$

(c) $Z = 1$ **(d)** $Z = 2$

(e) $Z = 3$ **(f)** $Z = 4$

Figure B.10: *Velocity profiles in the 70% stenosis model measured with* PIV *and* DUS *(*$\mathrm{Re}_{-1} = 500$*)*

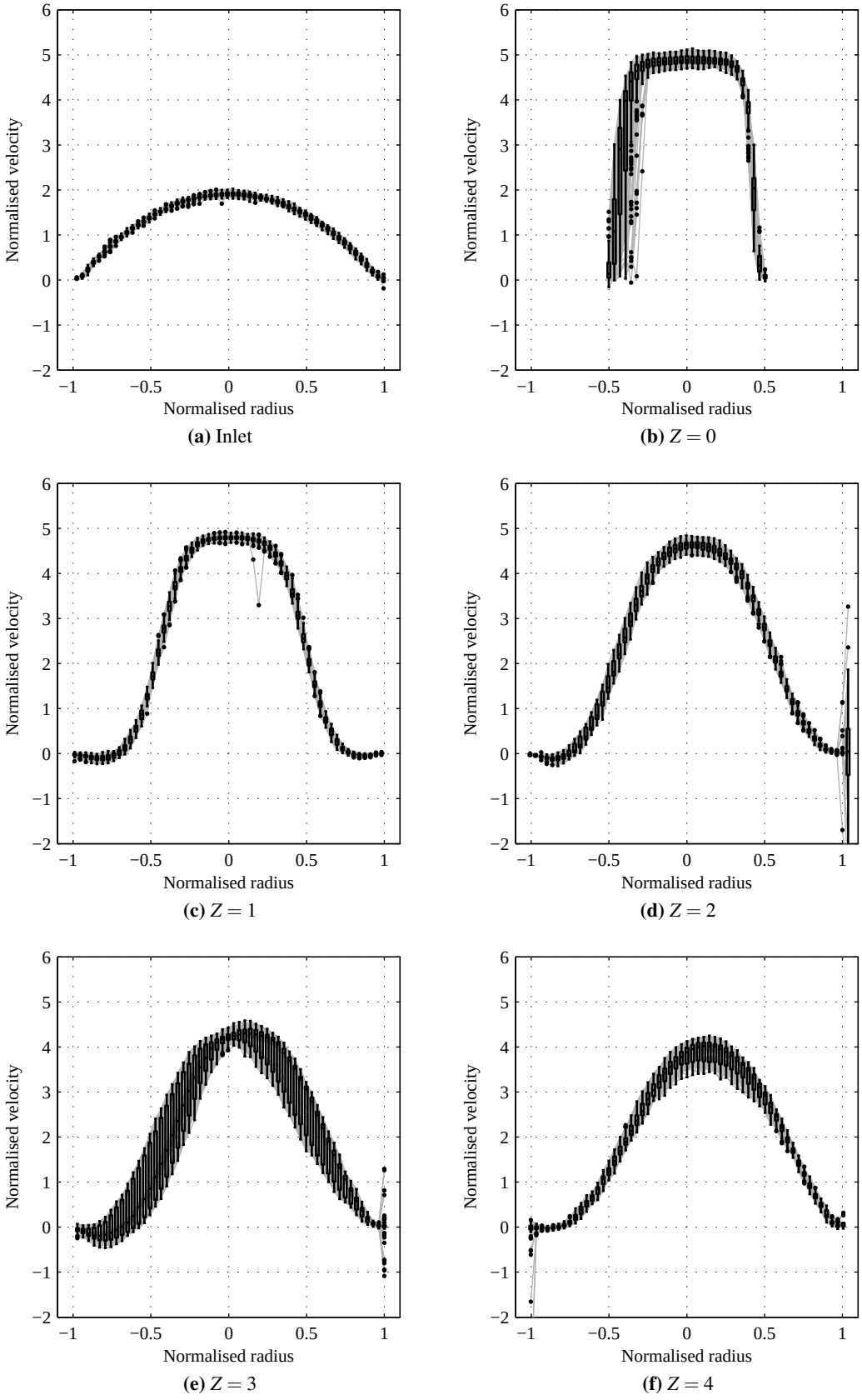

(a) Inlet **(b)** $Z = 0$

(c) $Z = 1$ **(d)** $Z = 2$

(e) $Z = 3$ **(f)** $Z = 4$

Figure B.11: *Velocity profiles at* Re_{-1} *=200 in the 50% stenosis model measured by* PIV

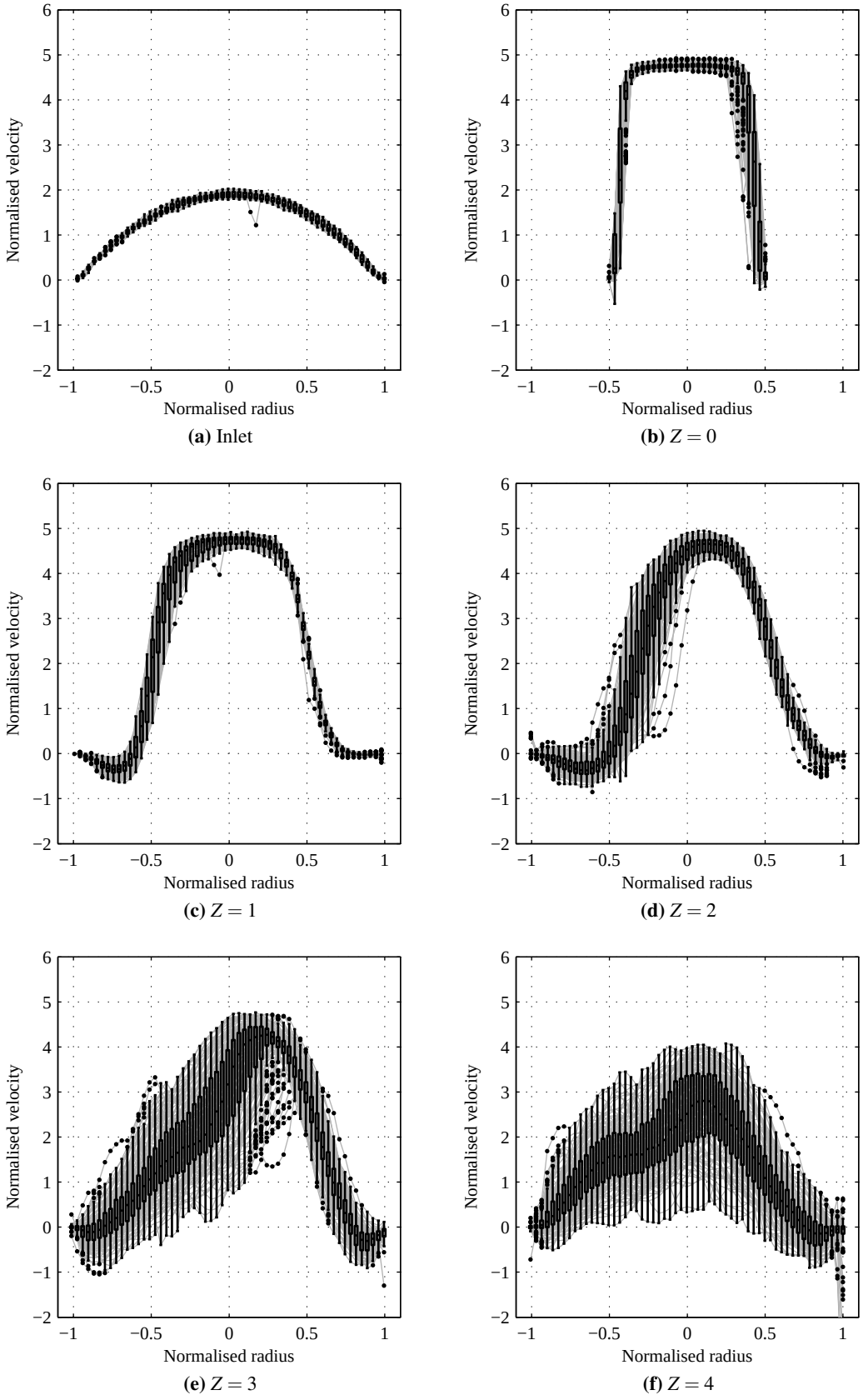

(a) Inlet **(b)** $Z = 0$

(c) $Z = 1$ **(d)** $Z = 2$

(e) $Z = 3$ **(f)** $Z = 4$

Figure B.12: *Velocity profiles at* Re_{-1} *=400 in the 50% stenosis model measured by* PIV

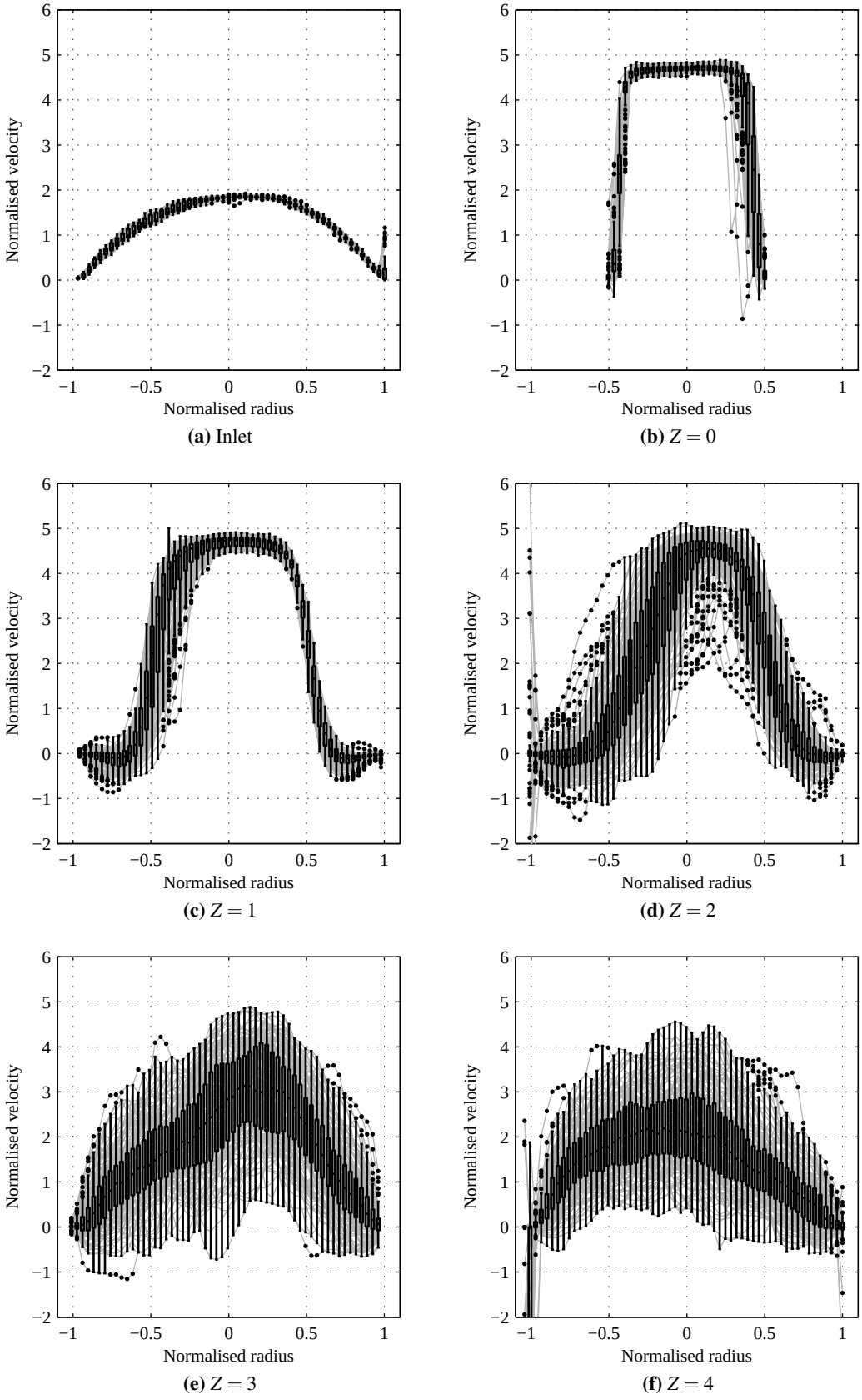

(a) Inlet **(b)** $Z = 0$ **(c)** $Z = 1$ **(d)** $Z = 2$ **(e)** $Z = 3$ **(f)** $Z = 4$

Figure B.13: *Velocity profiles at* Re_{-1} *=600 in the 50% stenosis model measured by* PIV

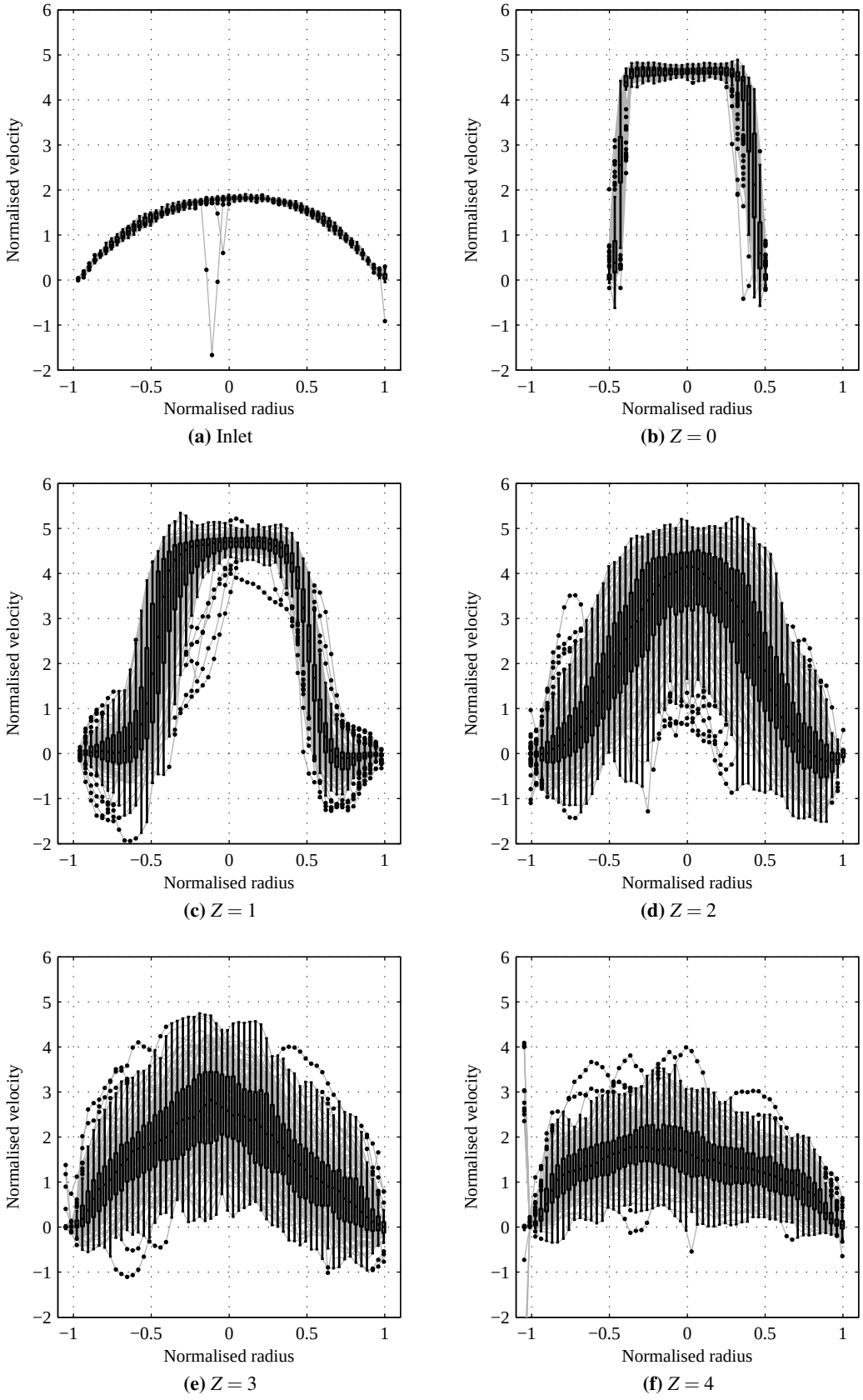

(a) Inlet **(b)** $Z = 0$

(c) $Z = 1$ **(d)** $Z = 2$

(e) $Z = 3$ **(f)** $Z = 4$

Figure B.14: *Velocity profiles at* Re_{-1} *=800 in the 50% stenosis model measured by* PIV

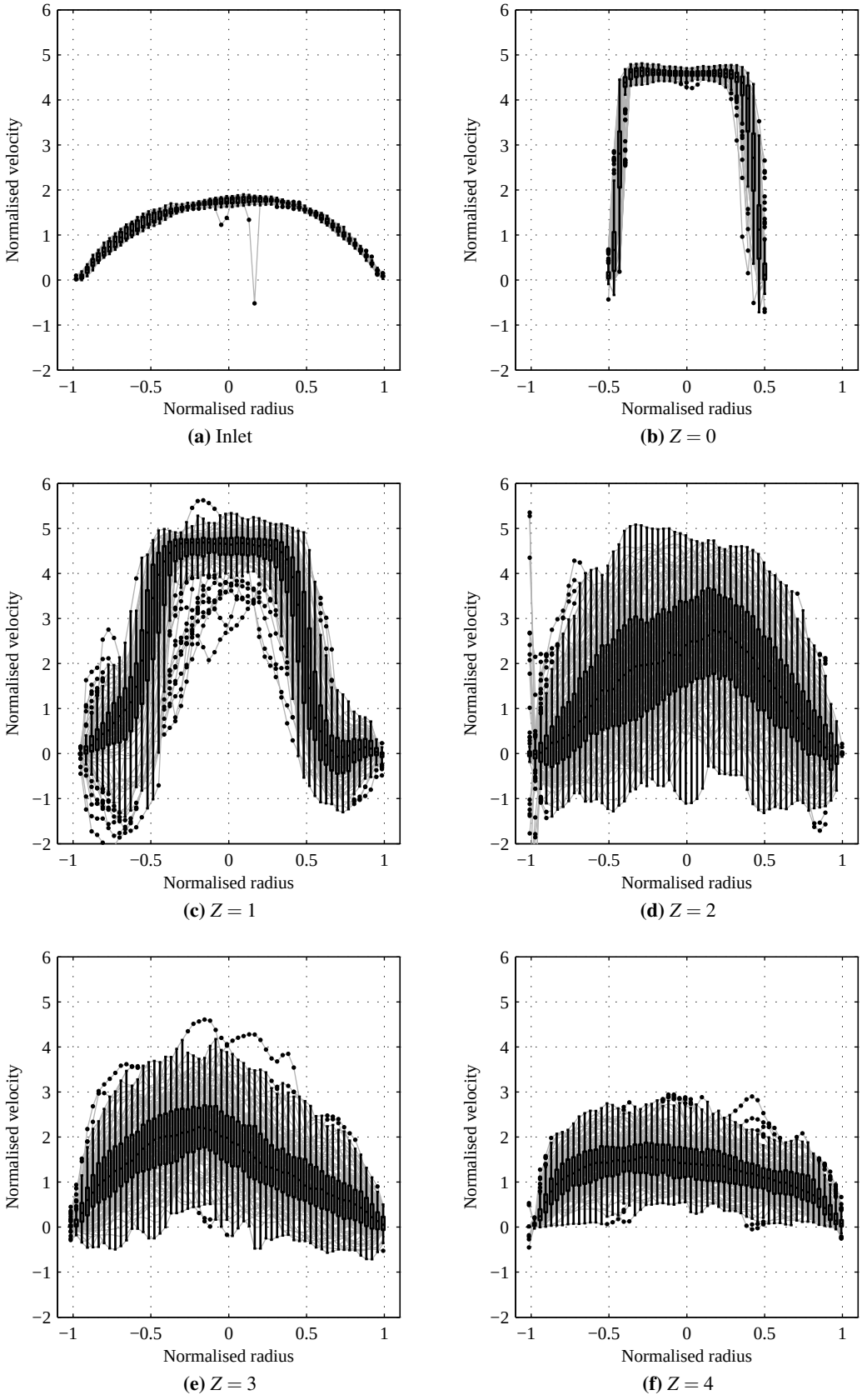

(a) Inlet **(b)** $Z = 0$ **(c)** $Z = 1$ **(d)** $Z = 2$ **(e)** $Z = 3$ **(f)** $Z = 4$

Figure B.15: *Velocity profiles at* Re_{-1} *=1000 in the 50% stenosis model measured by* PIV

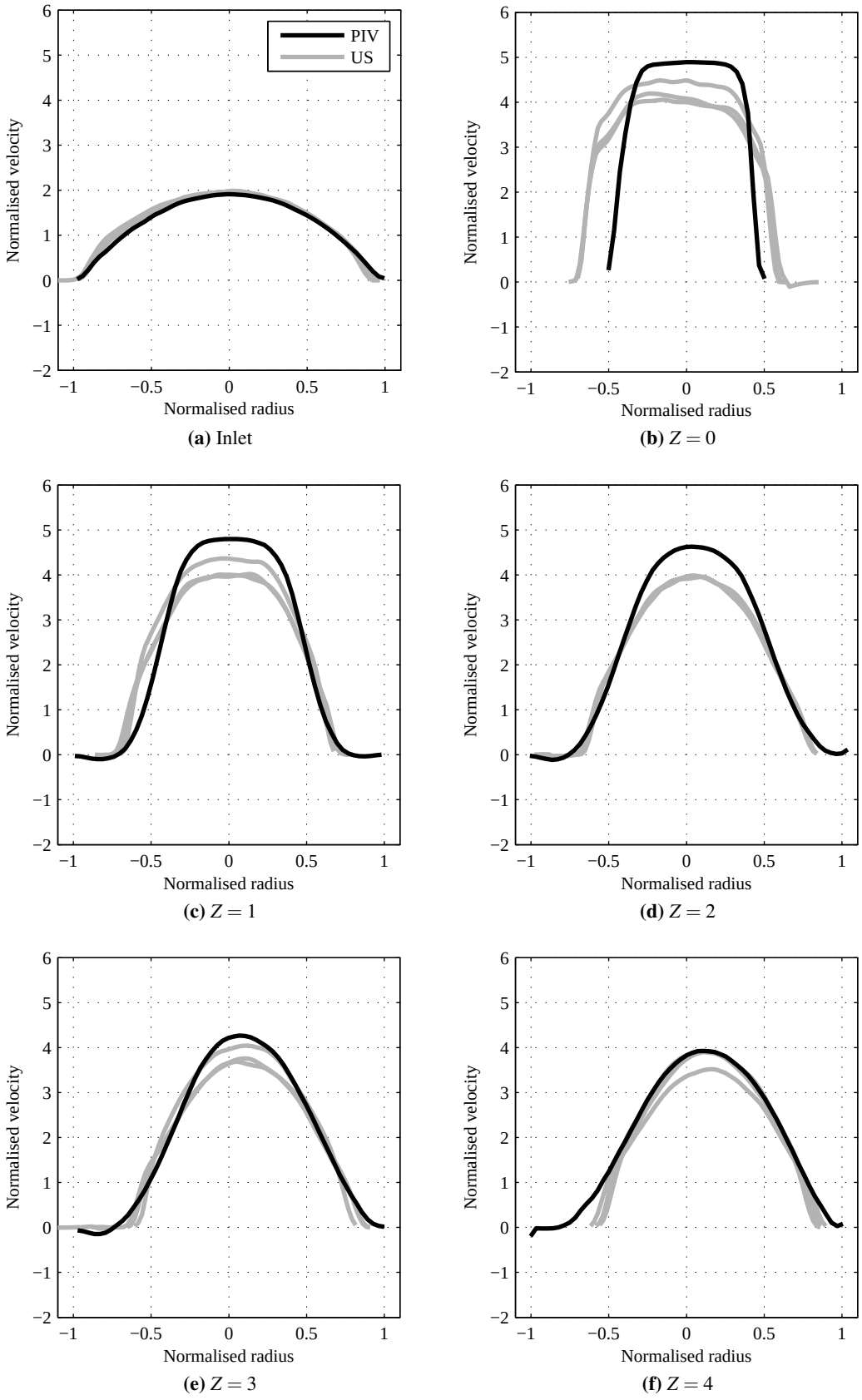

(a) Inlet **(b)** $Z = 0$

(c) $Z = 1$ **(d)** $Z = 2$

(e) $Z = 3$ **(f)** $Z = 4$

Figure B.16: *Velocity profiles at* Re_{-1} *=200 in the 50% stenosis model measured by* PIV *and* DUS

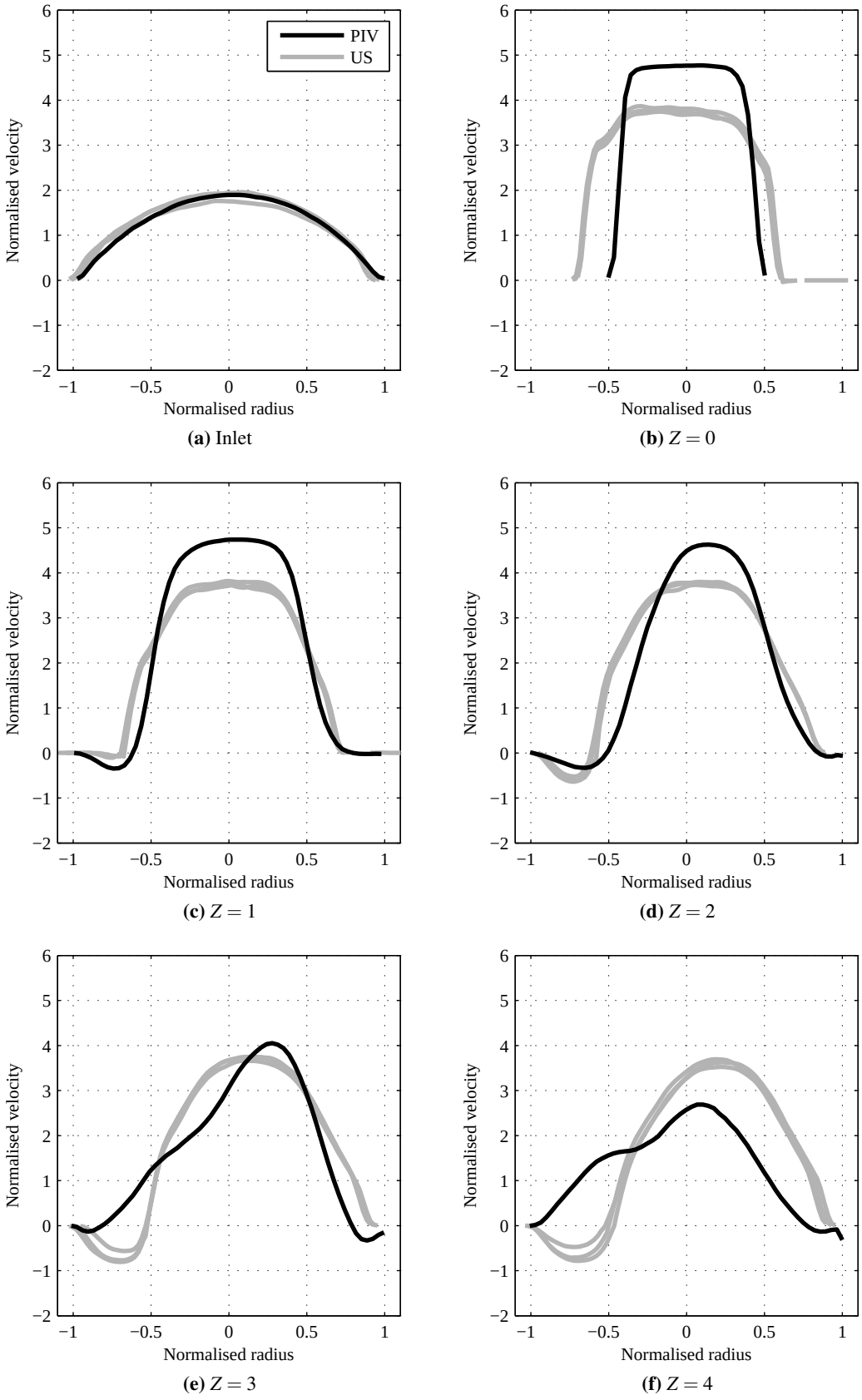

(a) Inlet **(b)** $Z = 0$

(c) $Z = 1$ **(d)** $Z = 2$

(e) $Z = 3$ **(f)** $Z = 4$

Figure B.17: *Velocity profiles at* Re_{-1} *=400 the 50% stenosis model measured by* PIV *and* DUS

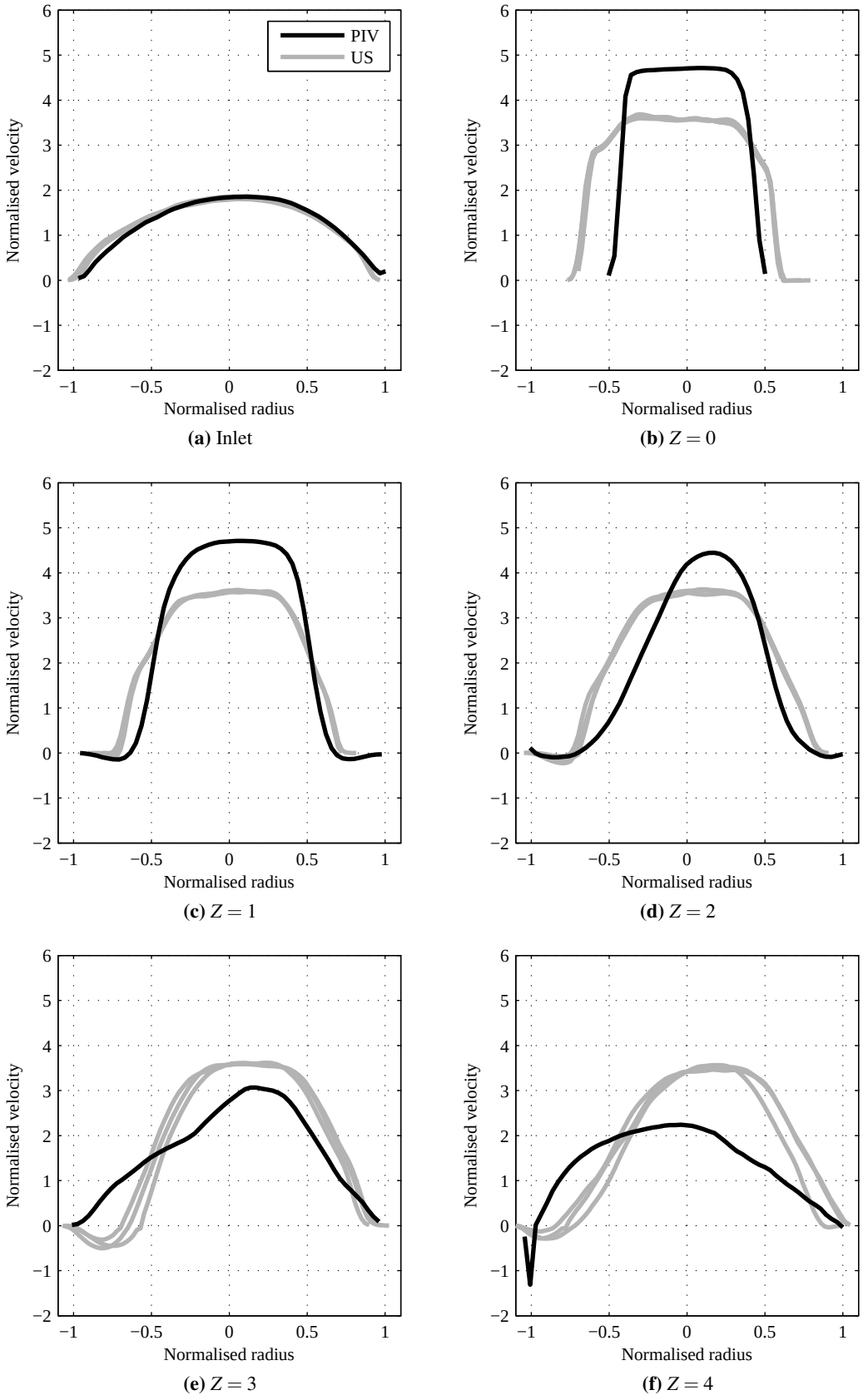

(a) Inlet **(b)** $Z = 0$

(c) $Z = 1$ **(d)** $Z = 2$

(e) $Z = 3$ **(f)** $Z = 4$

Figure B.18: *Velocity profiles at* Re_{-1} *=600 in the 50% stenosis model measured by* PIV *and* DUS

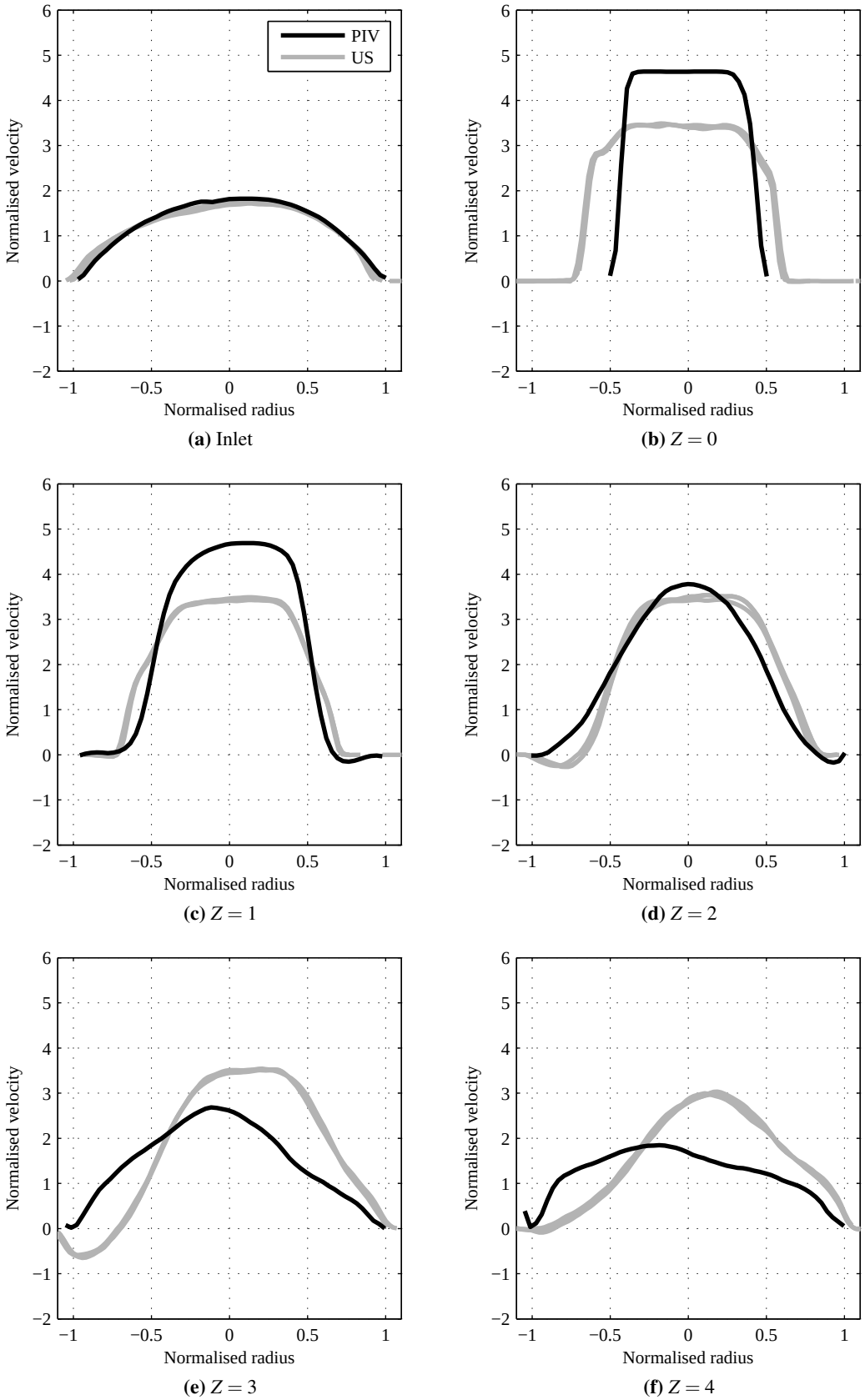

(a) Inlet **(b)** $Z = 0$

(c) $Z = 1$ **(d)** $Z = 2$

(e) $Z = 3$ **(f)** $Z = 4$

Figure B.19: *Velocity profiles at* Re_{-1} *=800 in the 50% stenosis model measured by* PIV *and* DUS

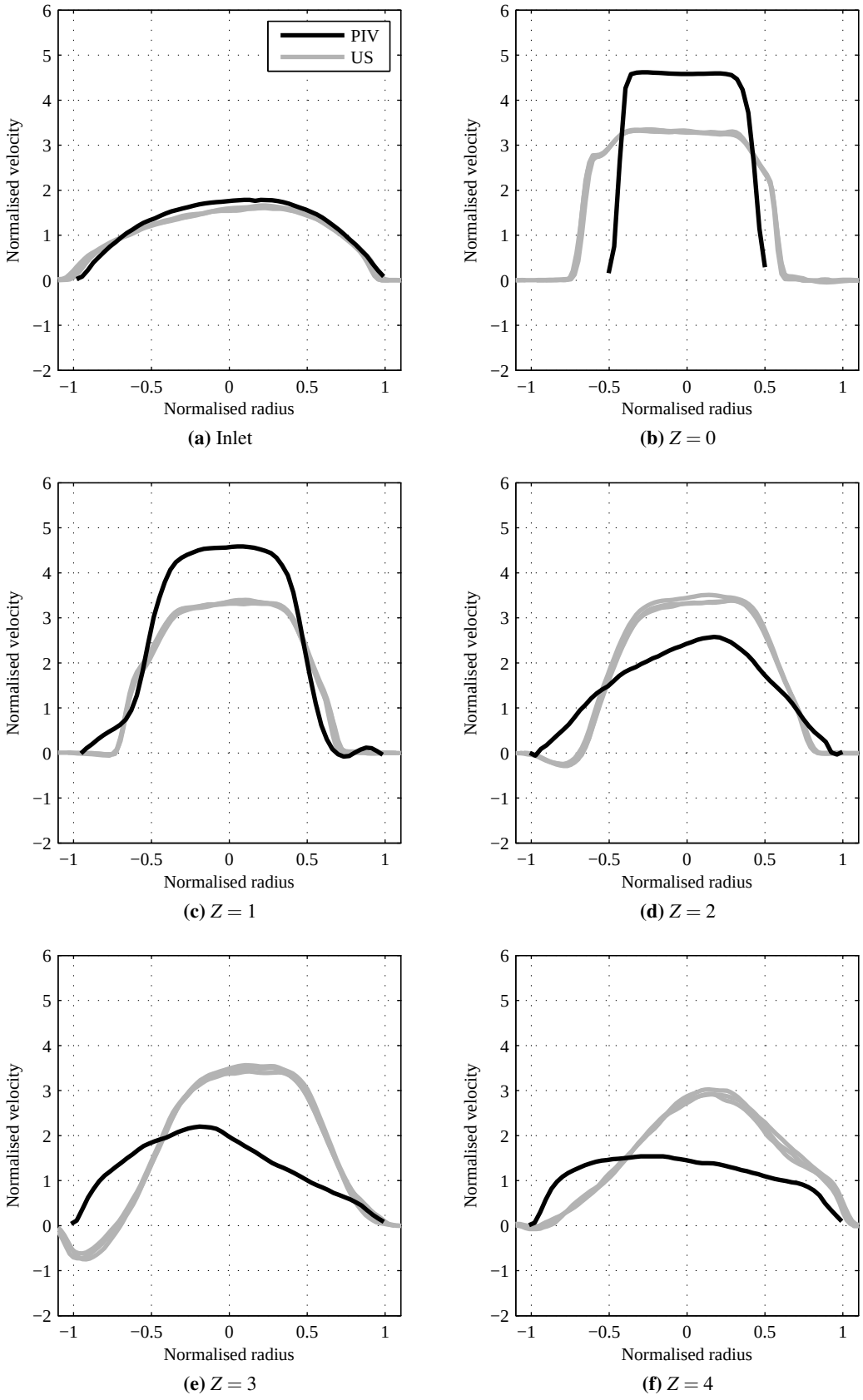

(a) Inlet **(b)** $Z = 0$

(c) $Z = 1$ **(d)** $Z = 2$

(e) $Z = 3$ **(f)** $Z = 4$

Figure B.20: *Velocity profiles at* Re_{-1} *=1000 in the 50% stenosis model measured by* PIV *and* DUS

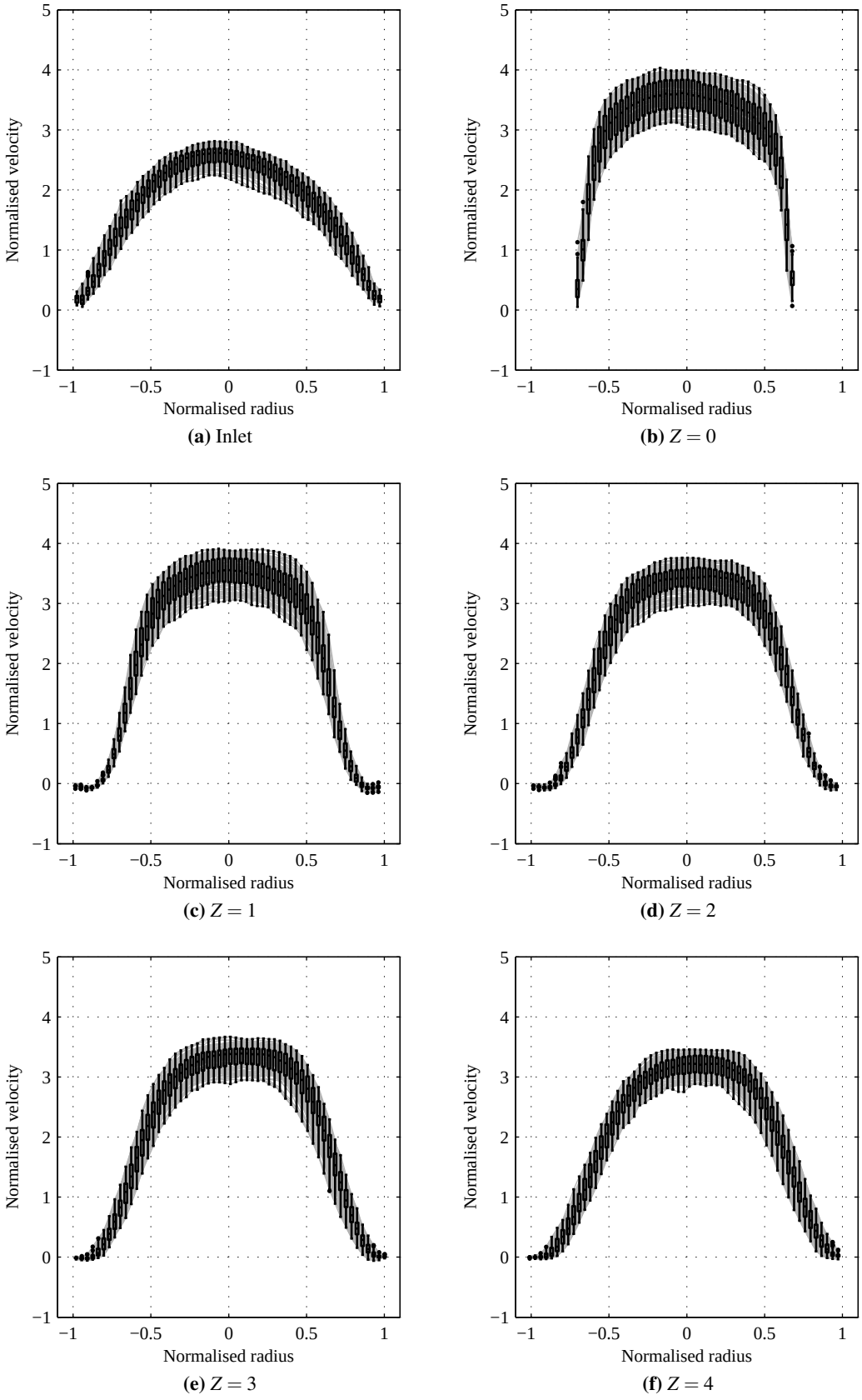

(a) Inlet **(b)** $Z = 0$

(c) $Z = 1$ **(d)** $Z = 2$

(e) $Z = 3$ **(f)** $Z = 4$

Figure B.21: *Velocity profiles at peak systole in the 30% stenosis model measured by* PIV *(*$\mathrm{Re}_{-1} = 580$*)*

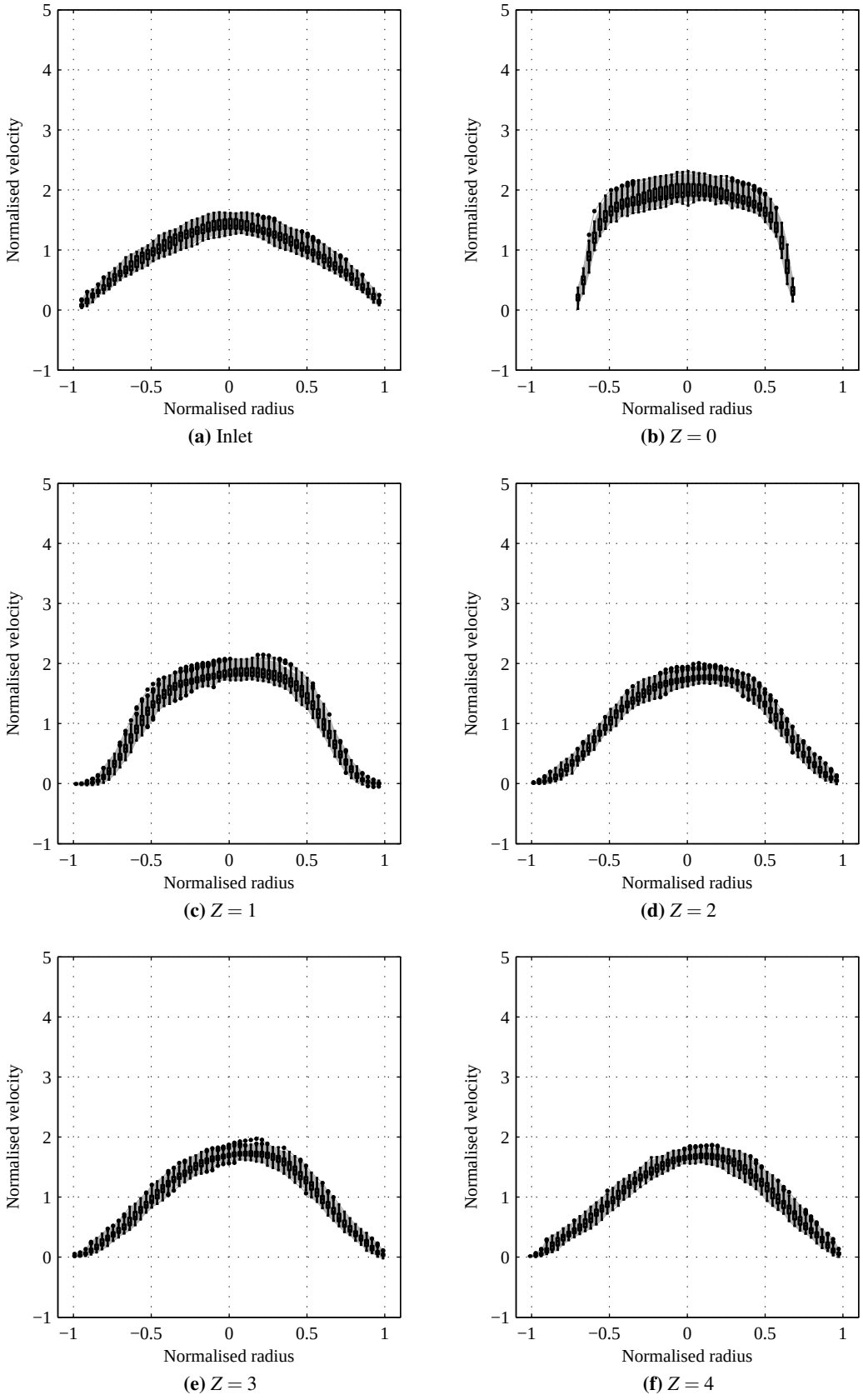

(a) Inlet **(b)** $Z = 0$

(c) $Z = 1$ **(d)** $Z = 2$

(e) $Z = 3$ **(f)** $Z = 4$

Figure B.22: *Velocity profiles at end diastole in the 30% stenosis model measured by* PIV *(*$\mathrm{Re}_{-1} = 260$*)*

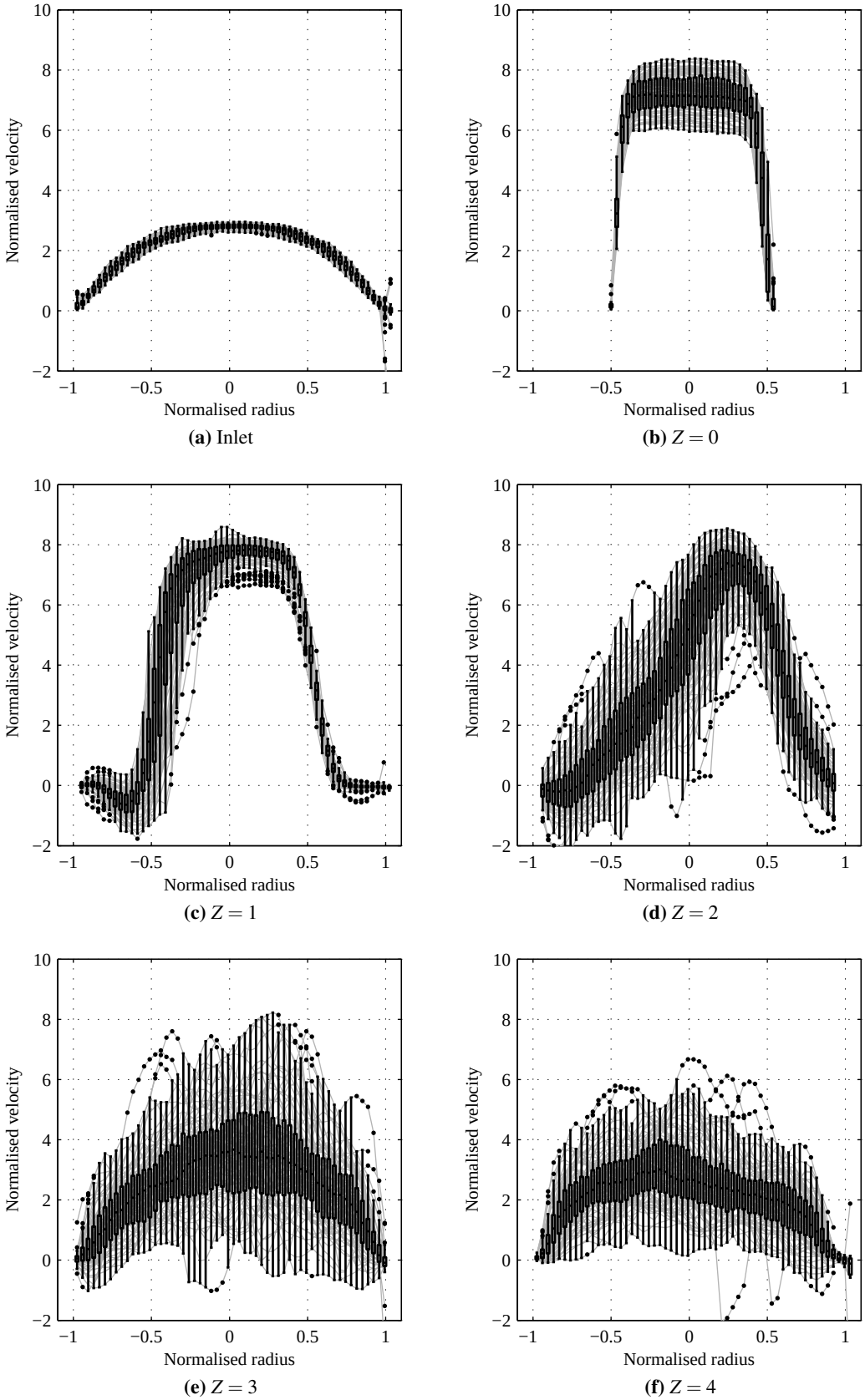

(a) Inlet **(b)** $Z = 0$

(c) $Z = 1$ **(d)** $Z = 2$

(e) $Z = 3$ **(f)** $Z = 4$

Figure B.23: *Velocity profiles at peak systole in the 50% stenosis model measured by* PIV *(*$\mathrm{Re}_{-1} = 580$*)*

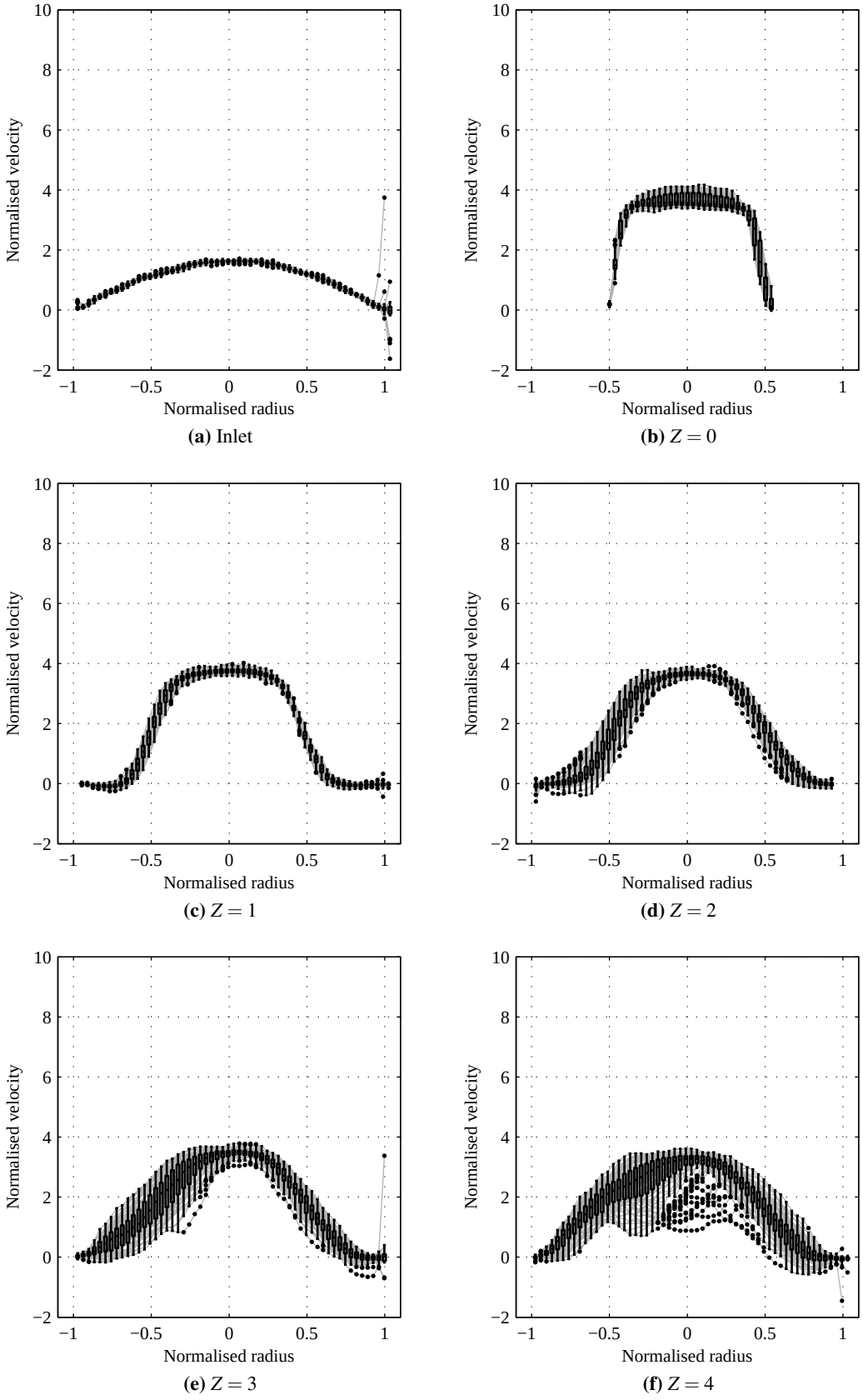

(a) Inlet **(b)** $Z = 0$

(c) $Z = 1$ **(d)** $Z = 2$

(e) $Z = 3$ **(f)** $Z = 4$

Figure B.24: *Velocity profiles at end diastole in the 50% stenosis model measured by* PIV *(*$\mathrm{Re}_{-1} = 260$*)*

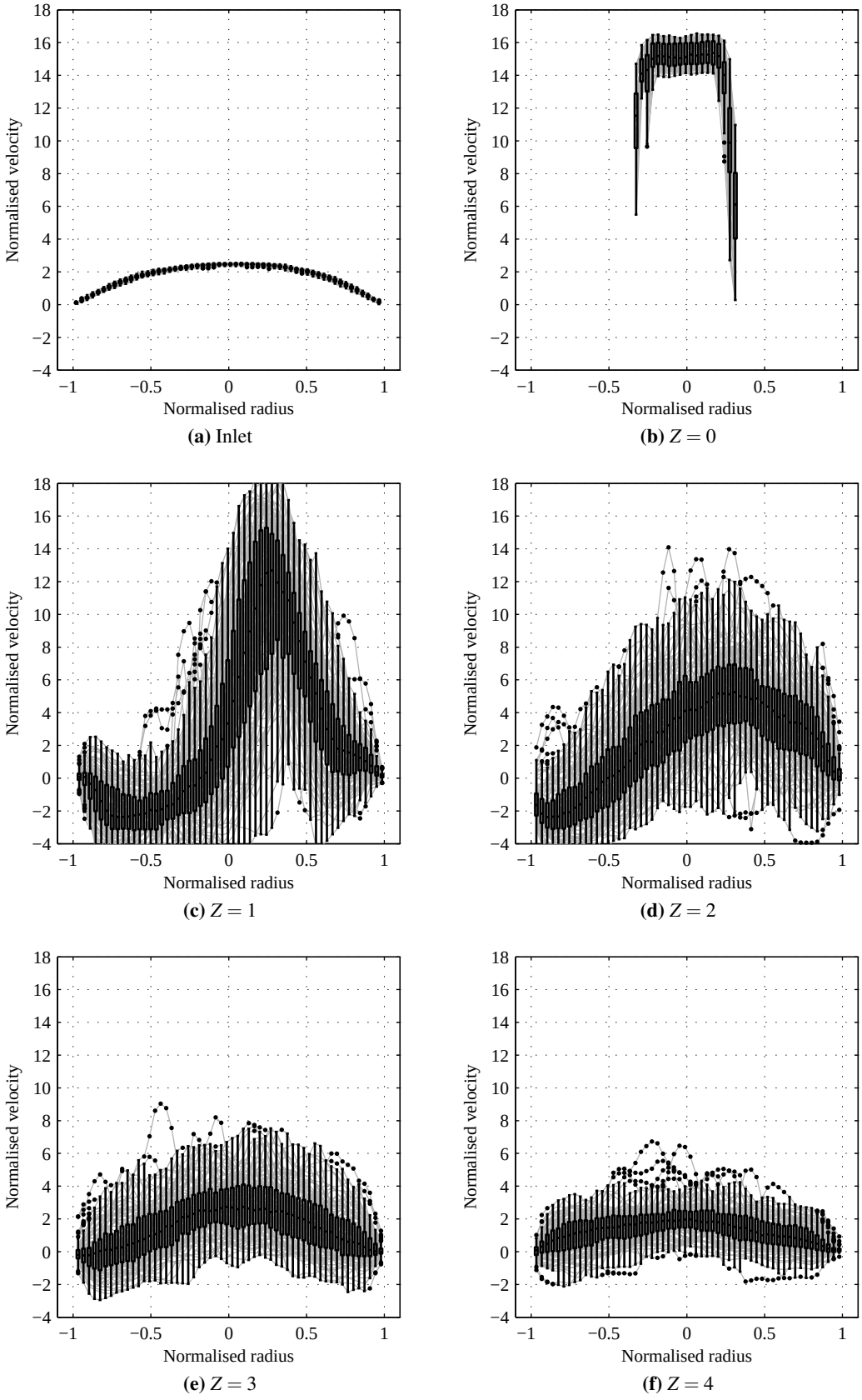

(a) Inlet **(b)** $Z = 0$ **(c)** $Z = 1$ **(d)** $Z = 2$ **(e)** $Z = 3$ **(f)** $Z = 4$

Figure B.25: *Velocity profiles at peak systole in the 70% stenosis model measured by* PIV *(*$\mathrm{Re}_{-1} = 470$*)*

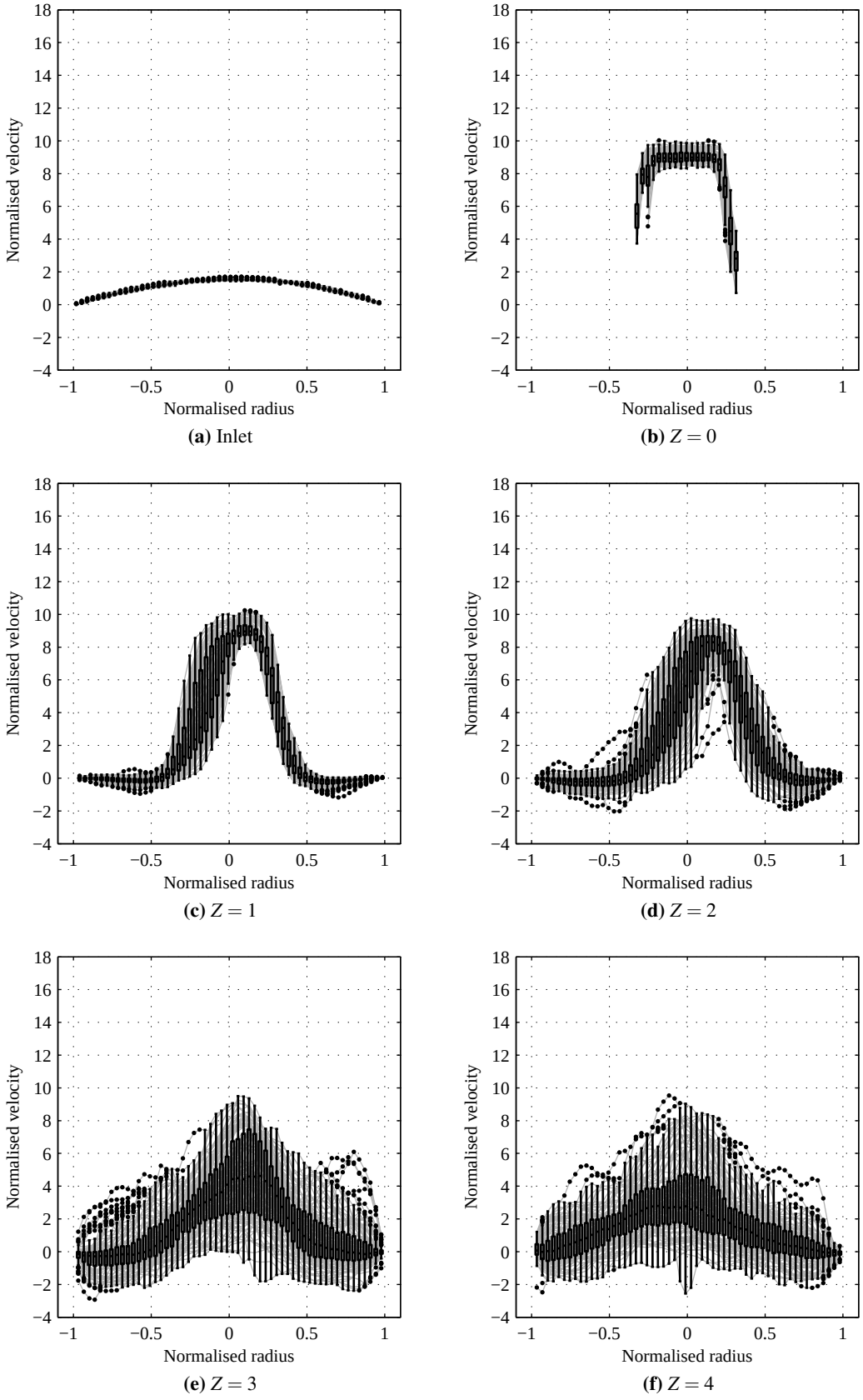

(a) Inlet **(b)** $Z = 0$

(c) $Z = 1$ **(d)** $Z = 2$

(e) $Z = 3$ **(f)** $Z = 4$

Figure B.26: *Velocity profiles at end diastole in the 70% stenosis model measured by* PIV *(*$\mathrm{Re}_{-1} = 250$*)*

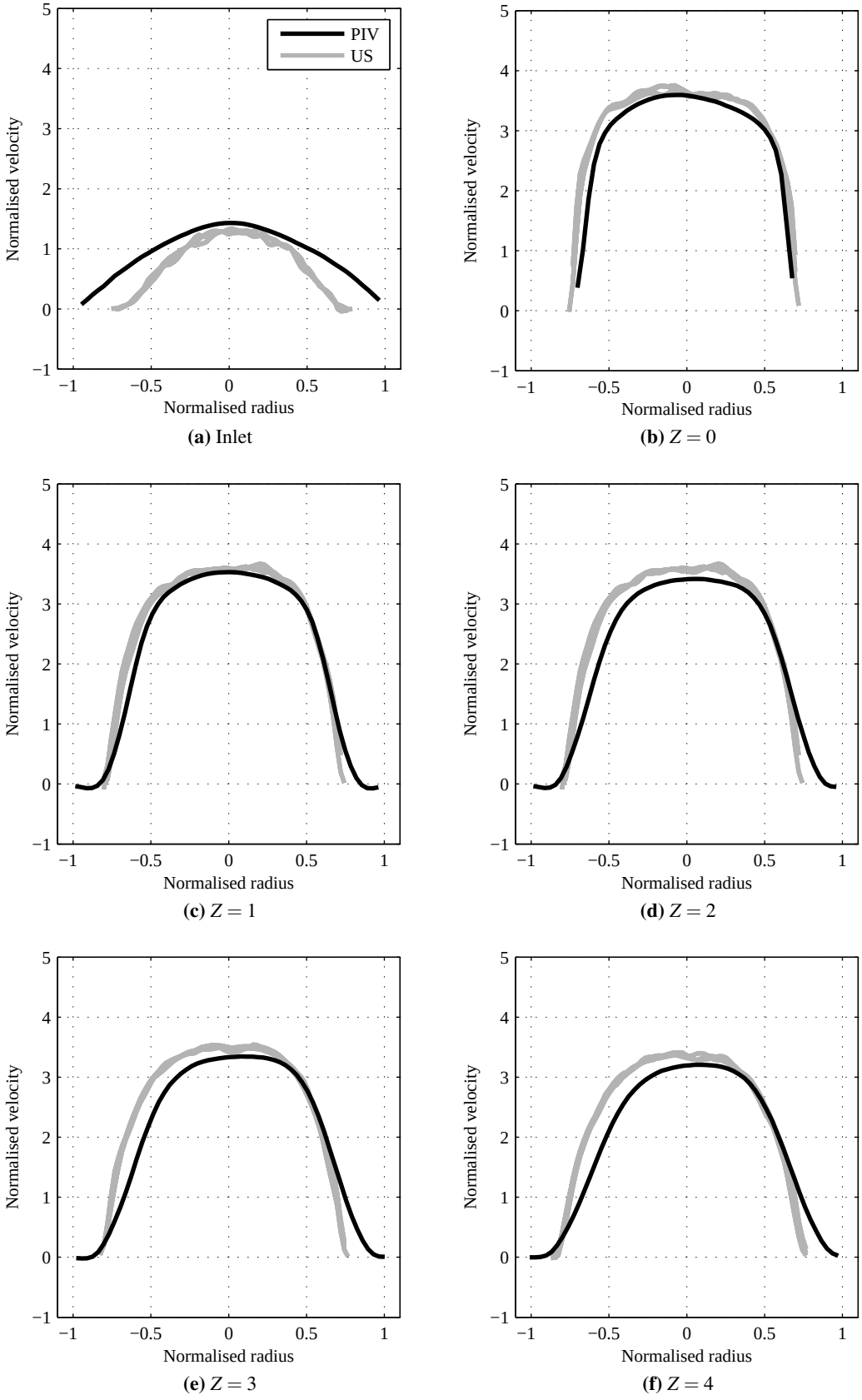

(a) Inlet **(b)** $Z = 0$ **(c)** $Z = 1$ **(d)** $Z = 2$ **(e)** $Z = 3$ **(f)** $Z = 4$

Figure B.27: *Velocity profiles at peak systole in the 30% stenosis model measured by* PIV *and* DUS *(*$\mathrm{Re}_{-1} = 580$*)*

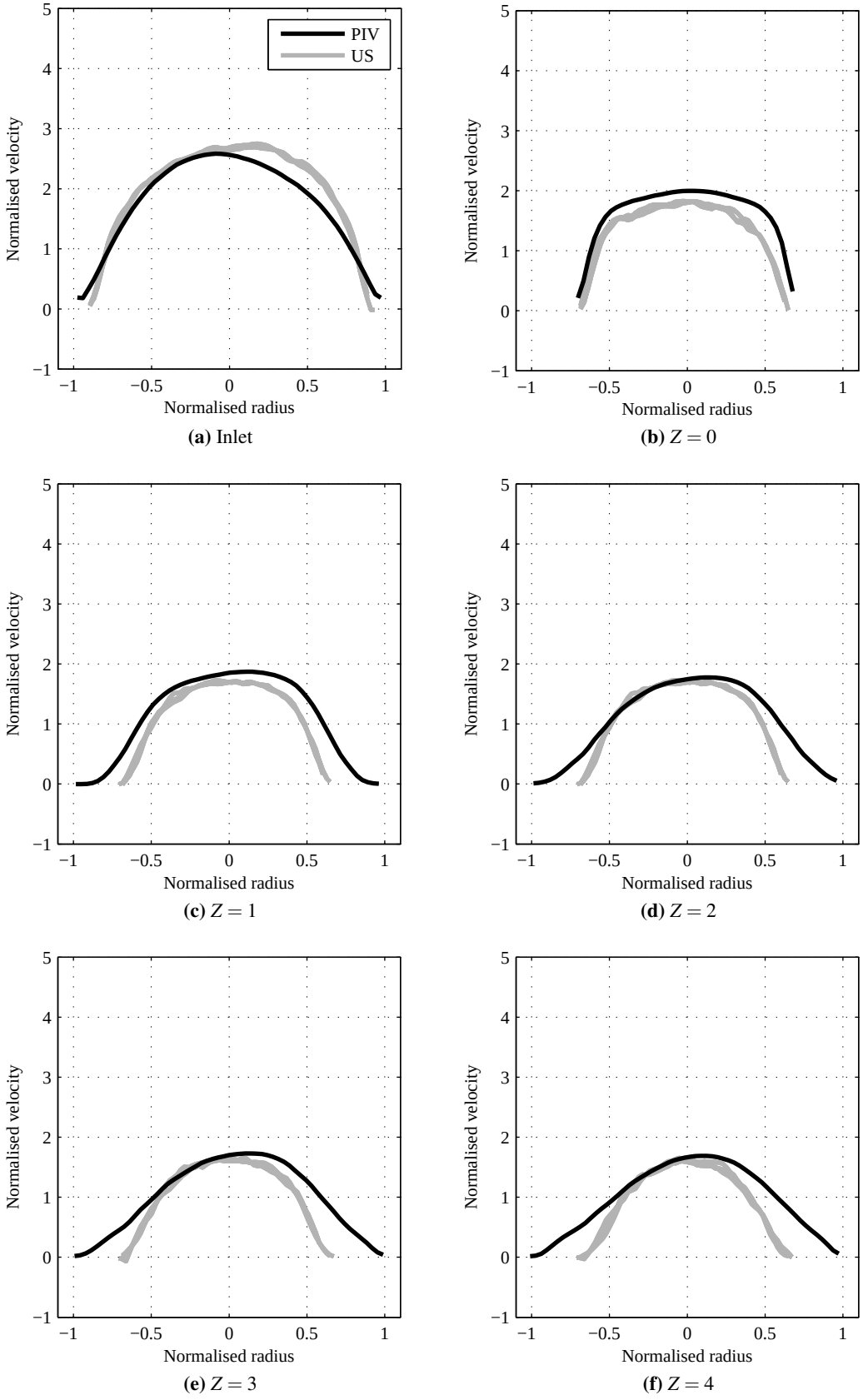

(a) Inlet **(b)** $Z = 0$

(c) $Z = 1$ **(d)** $Z = 2$

(e) $Z = 3$ **(f)** $Z = 4$

Figure B.28: *Velocity profiles at end diastole in the 30% stenosis model measured by* PIV *and* DUS *(*$\mathrm{Re}_{-1} = 260$*)*

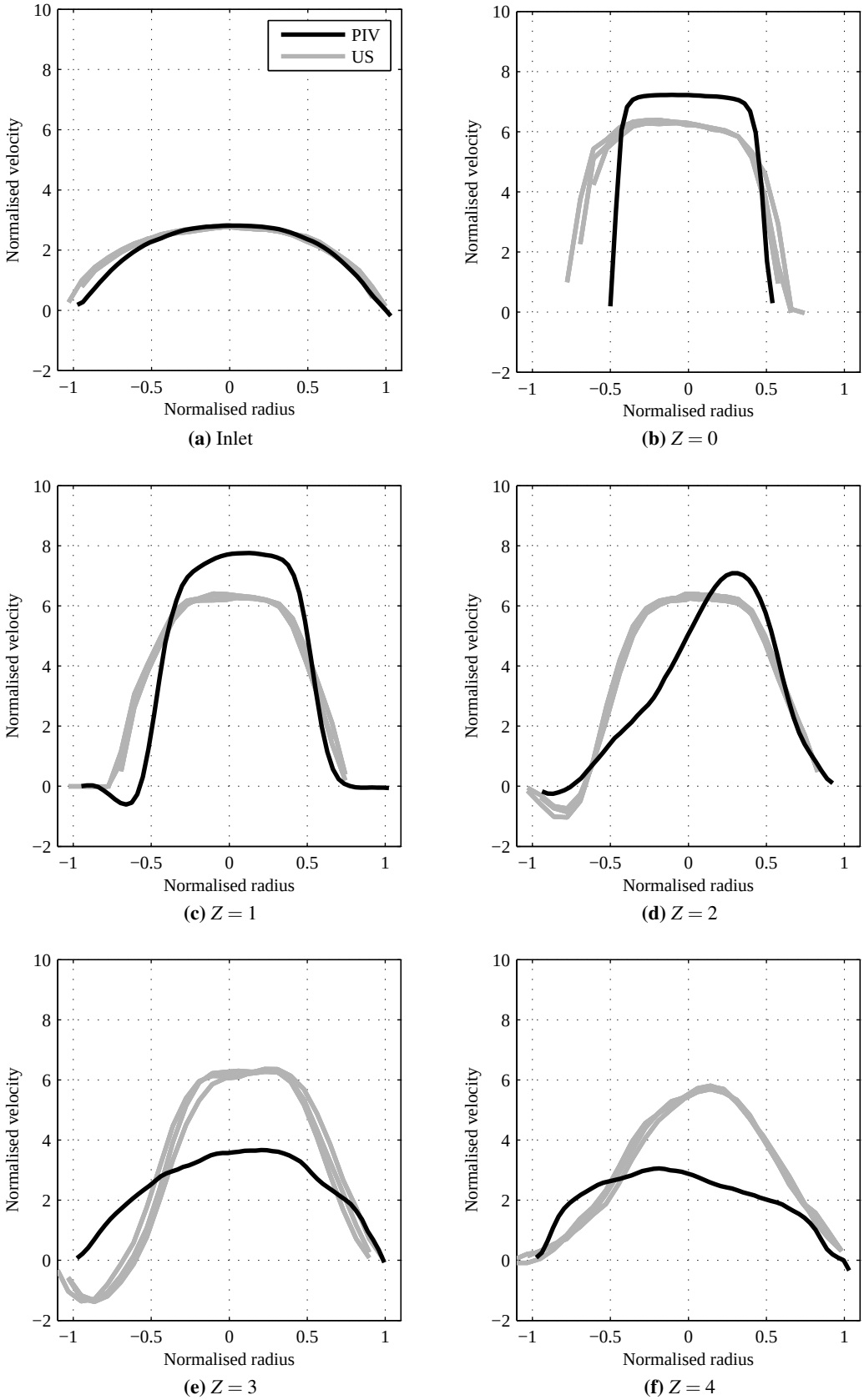

(a) Inlet **(b)** $Z = 0$ **(c)** $Z = 1$ **(d)** $Z = 2$ **(e)** $Z = 3$ **(f)** $Z = 4$

Figure B.29: *Velocity profiles at peak systole in the 50% stenosis model measured by* PIV *and* DUS *(*$\mathrm{Re}_{-1} = 580$*)*

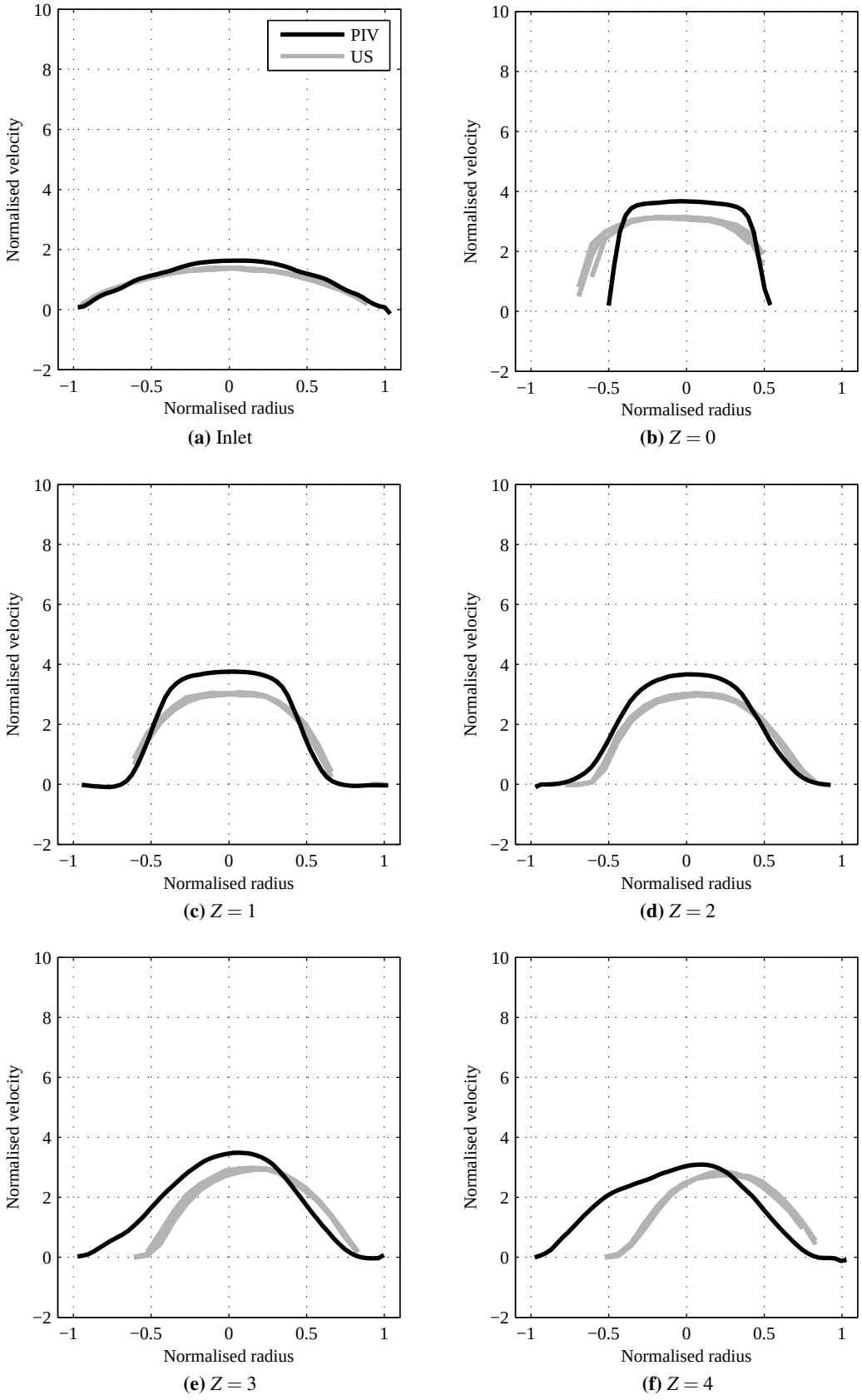

(a) Inlet **(b)** $Z = 0$

(c) $Z = 1$ **(d)** $Z = 2$

(e) $Z = 3$ **(f)** $Z = 4$

Figure B.30: *Velocity profiles at end diastole in the 50% stenosis model measured by* PIV *and* DUS *(*$\mathrm{Re}_{-1} = 260$*)*

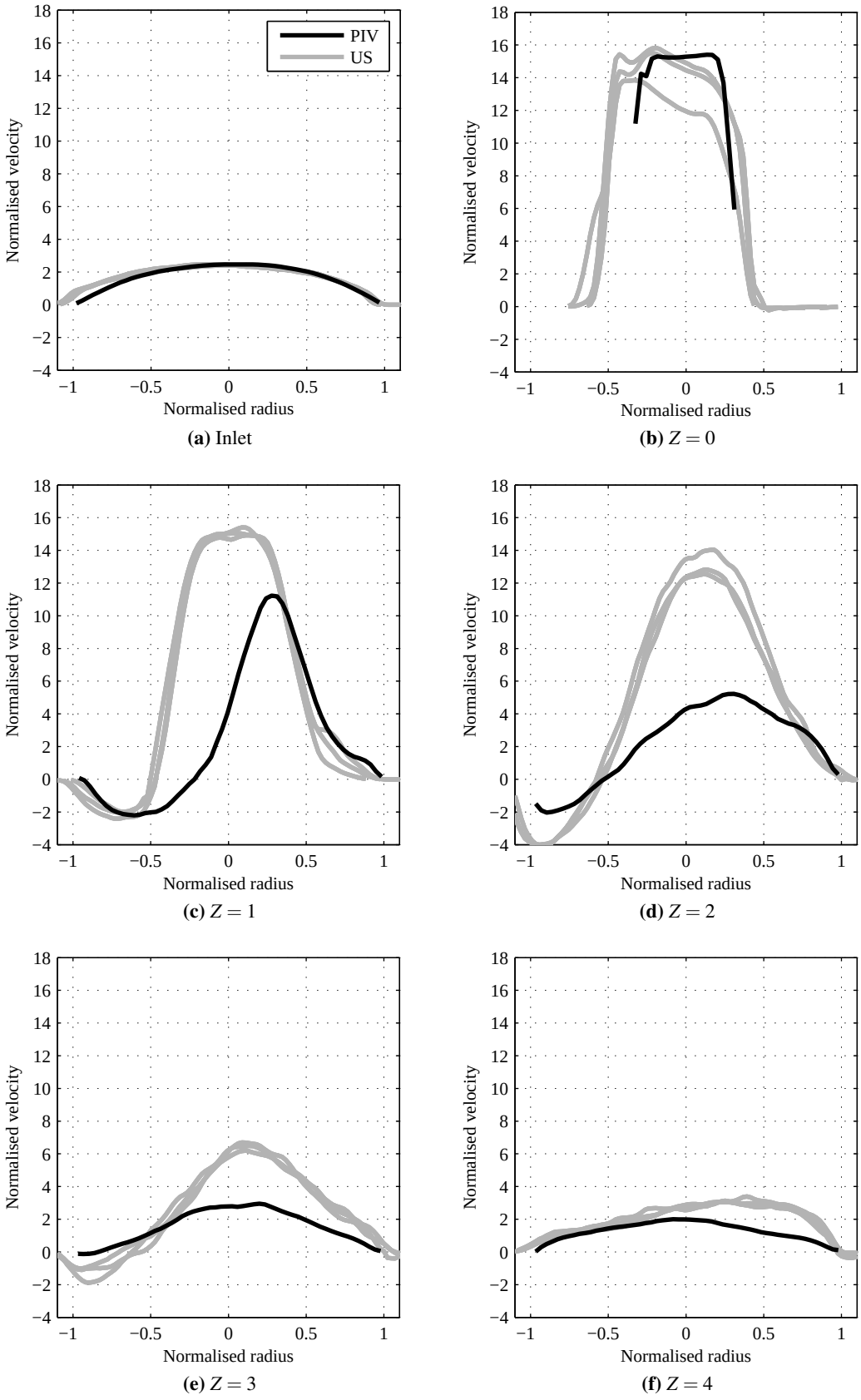

(a) Inlet **(b)** $Z = 0$ **(c)** $Z = 1$ **(d)** $Z = 2$ **(e)** $Z = 3$ **(f)** $Z = 4$

Figure B.31: *Velocity profiles at peak systole in the 70% stenosis model measured by* PIV *and* DUS *(*$\mathrm{Re}_{-1} = 470$*)*

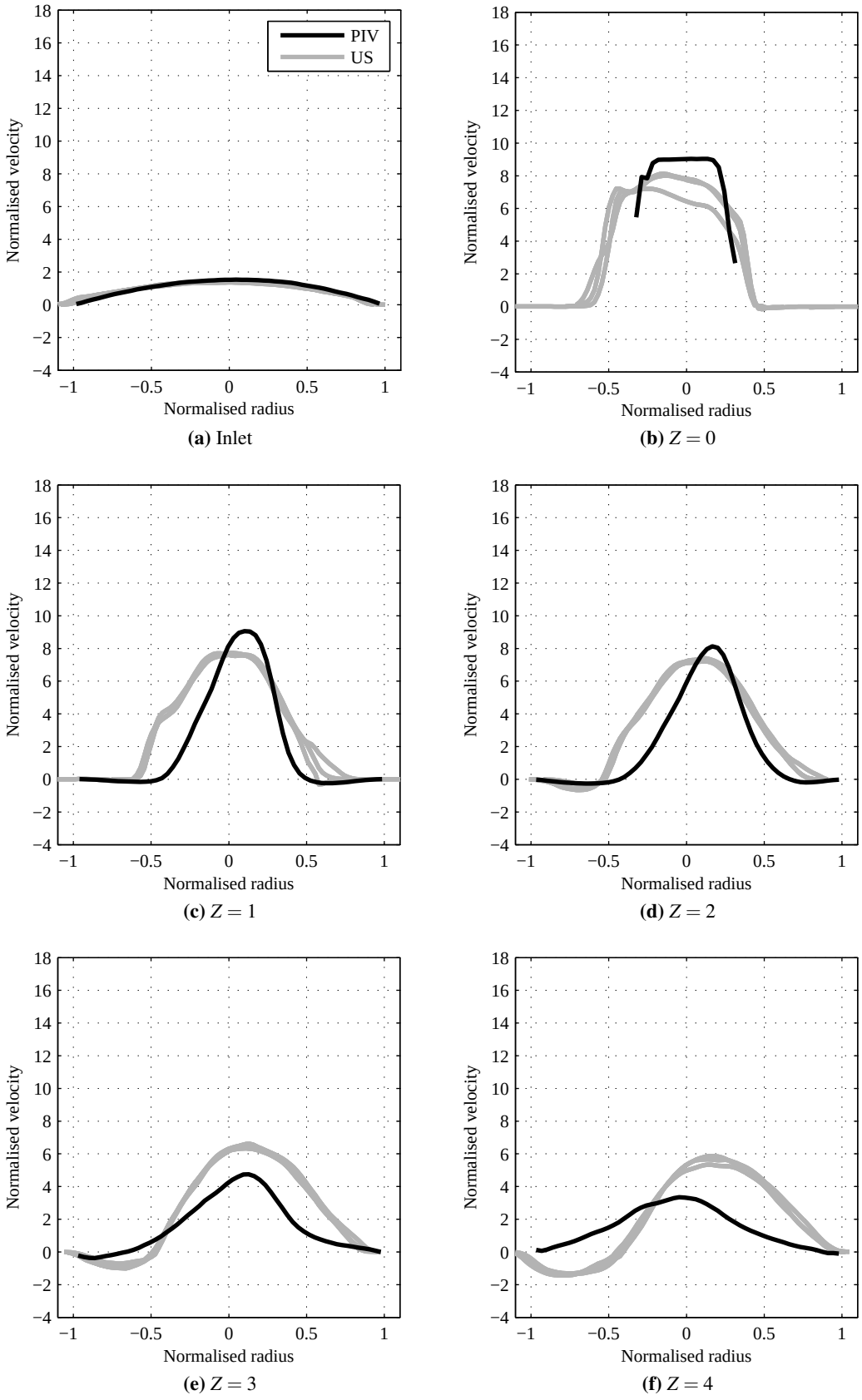

(a) Inlet **(b)** $Z = 0$

(c) $Z = 1$ **(d)** $Z = 2$

(e) $Z = 3$ **(f)** $Z = 4$

Figure B.32: *Velocity profiles at end diastole in the 70% stenosis model measured by* PIV *and* DUS *(*$\mathrm{Re}_{-1} = 250$*)*

References

Adrian, R. (1991), 'Particle imaging techniques for experimental fluid mechanics', *Annual Review of Fluid Mechanics* **23**, 261–304.

Adrian, R. (2005), 'Twenty years of particle image velocimetry', *Experiments in Fluids* **39**(2), 159 – 169.

Ahmed, S. & Giddens, D. (1983*a*), 'Flow disturbance measurements through a constricted tube at moderate Reynolds numbers', *Journal of Biomechanics* **16**, 955–963.

Ahmed, S. & Giddens, D. (1983*b*), 'Velocity measurements in steady flow through axisymmetric stenoses at moderate Reynolds numbers', *Journal of Biomechanics* **16**(7), 505–516.

Ahmed, S. & Giddens, D. (1984), 'Pulsatile poststenotic flow studies with laser Doppler anemometry', *Journal of Biomechanics* **17**(9), 695–705.

Alexandrov, A., Vital, D., Brodie, D., Hamilton, P. & Grotta, J. (1997), 'Grading carotid stenosis with ultrasound. An interlaboratory comparison', *Stroke* **28**, 1208–1210.

Arnold, J., Marchiori, G., Imrie, J., Burton, G., Pflugfelder, P. & Kostuk, W. (1991), 'Large artery function in patients with chronic heart failure. Studies of brachial artery diameter and hemodynamics', *Circulation* **84**, 2418–2425.

Asbury, C., Ruberti, J., Bluth, E. & Peattie, R. (1995), 'Experimental investigation of steady flow in rigid models of abdominal aortic aneurysms', *Annals of Biomedical Engineering* **23**(1), 29–39.

Ata, O. & Fish, P. (1991), 'Effect of deviation from plane wave conditions on the Doppler spectrum from an ultrasonic blood flow detector', *Ultrasonics* **29**(5), 395–403.

Avolio, A. (1980), 'Multi-branched model of the human arterial system', *Medical & Biological Engineering & Computing* **18**, 709–718.

Baker, D. (1970), 'Pulsed ultrasonic Doppler blood-flow sensing', *IEEE Transactions on Sonics and Ultrasonics* **SU-17**(3), 170–185.

Bale-Glickman, J., Selby, K., Saloner, D. & Sava{s}, . (2003), 'Experimental flow studies in exact-replica phantoms of atherosclerotic carotid bifurcations under steady input conditions', *Journal of Biomechanical Engineering* **125**(1), 38–48.

Bambi, G., Morganti, T., Ricci, S., Boni, E., Guidi, F., Palombo, C. & Tortoli, P. (2004), 'A novel ultrasound instrument for investigation of arterial mechanics', *Ultrasonics* **42**, 731 – 737.

Barbee, K., Davies, P. & Lal, R. (1994), 'Shear stress-induced reorganization of the surface topography of living endothelial cells imaged by atomic force microscopy', *Circulation Research* **74**, 163–171.

Barnett, H., Taylor, D., Eliasziw, M., Fox, A., Ferguson, G., Haynes, R., Rankin, R., Clagett, G., Hachinski, V., Sackett, D., Thorpe, K., Meldrum, H. & Spence, J. (1998), 'Benefit of carotid endarterectomy in patients with symptomatic moderate or severe stenosis. North American Symptomatic Carotid Endarterectomy Trial Collaborators', *New England Journal of Medicine* **339**, 1415–1425.

Bastos, C., Fish, P., Steel, R. & Vaz, F. (2000), 'Doppler power spectrum from a Gaussian sample volume', *Ultrasonics* **37**, 623–632.

Beaglehole, R., Irwin, A. & Prentice, A. (2004), *The world health report 2004—changing history*, World Health Organization, Geneva.

Bendick, P., Juleff, R. & Glover, J. (1997), 'Arterial adaptation to increased wall shear stress', *Vascular Surgery* **31**(2), 153 – 161.

Bluestein, D., Gutierrez, C., Londono, M. & Schoephoerster, R. (1999), 'Vortex Shedding in Steady Flow Through a Model of an Arterial Stenosis and Its Relevance to Mural Platelet Deposition', *Annals of Biomedical Engineering* **27**(6), 763–773.

Bluth, E., Stavros, A., Marich, K., Wetzner, S., Aufrichtig, D. & Baker, J. (1988), 'Carotid duplex sonography: a multicenter recommendation for standardized imaging and Doppler criteria', *Radiographics* **8**, 487–506.

Bonnefous, O. & Pesqué, P. (1986), 'Time domain formulation of pulse-Doppler ultrasound and blood velocity estimation by cross correlation', *Ultrasonic Imaging* **8**, 73–85.

Brands, P., Hoeks, A., Hofstra, L. & Reneman, R. (1995), 'A noninvasive method to estimate wall shear rate using ultrasound', *Ultrasound in Medicine and Biology* **21**(2), 171 – 185.

Brodszki, J., Gardiner, H., Eriksson, A., Stale, H. & Marsál, K. (1998), 'Reproducibility of ultrasonic fetal volume blood flow measurements', *Clinical Physiology* **18**, 479–485.

Budwig, R. (1994), 'Refractive index matching methods for liquid flow investigations', *Experiments in Fluids* **17**(5), 350–355.

Caro, C., Fitz-Gerald, J. & Schroter, R. (1971), 'Atheroma and arterial wall shear. Observation, correlation and proposal of a shear dependent mass transfer mechanism for atherogenesis', *Proceedings of the Royal Society of London B Biological Scienceencess* **177**, 109–159.

Caro, C., Pedley, T., Schroter, R. & Seed, W. (1978), *The mechanics of the circulation*, Oxford University Press, Oxford, UK.

Cassanova, R. & Giddens, D. (1978), 'Disorder distal to modeled stenoses in steady and pulsatile flow', *Journal of Biomechanics* **11**, 441–453.

Cezeaux, J. & van Grondelle, A. (1997), 'Accuracy of the inverse Womersley method for the calculation of hemodynamic variables', *Annals of Biomedical Engineering* **25**, 536–546.

Cheng, C., Helderman, F., Tempel, D., Segers, D., Hierck, B., Poelmann, R., van Tol, A., Duncker, D., Robbers-Visser, D., Ursem, N., van Haperen, R., Wentzel, J., Gijsen, F., van der Steen, A., de Crom, R. & Krams, R. (2007), 'Large variations in absolute wall shear stress levels within one species and between species', *Atherosclerosis* **195**, 225–235.

Cheng, C., Parker, D. & Taylor, C. (2002), 'Quantification of wall shear stress in large blood vessels using Lagrangian interpolation functions with cine phase-contrast magnetic resonance imaging', *Annals of Biomedical Engineering* **30**(8), 1020–1032.

Cloft, H., Murphy, K., Prince, M. & Brunberg, J. (1996), '3D gadolinium-enhanced MR angiography of the carotid arteries', *Magnetic Resonance Imaging* **14**, 593–600.

Culebras, A., Kase, C., Masdeu, J., Fox, A., Bryan, R., Grossman, C., Lee, D., Adams, H. & Thies, W. (1997), 'Practice guidelines for the use of imaging in transient ischemic attacks and acute stroke. A report of the Stroke Council, American Heart Association', *Stroke* **28**, 1480–1497.

Daigle, R., Stavros, A. & Lee, R. (1990), 'Overestimation of velocity and frequency values by multielement linear array Dopplers', *Journal of Vascular Technology* **14**(5), 203–213.

Dammers, R., Stifft, F., Tordoir, J., Hameleers, J., Hoeks, A. & Kitslaar, P. (2003), 'Shear stress depends on vascular territory: comparison between common carotid and brachial artery', *Journal of Applied Physiology* **94**, 485–489.

Dammers, R., Tordoir, J., Hameleers, J., Kitslaar, P. & Hoeks, A. (2002), 'Brachial artery shear stress is independent of gender or age and does not modify vessel wall mechanical properties', *Ultrasound in Medicine and Biology* **28**, 1015–1022.

Davies, K. & Humphrey, P. (1993), 'Complications of cerebral angiography in patients with symptomatic carotid territory ischaemia screened by carotid ultrasound', *Journal of Neurology, Neurosurgery and Psychiatry* **56**, 967–972.

Davies, P. (1995), 'Flow-mediated endothelial mechanotransduction', *Physiological Review* **75**, 519–560.

di Mario, C., Bom, N., Li, W. & van der Steen, A. (1999), Clinical diagnostic ultrasound, *in* G. Baxter, P. Allan & P. Morley, eds, 'Intravascular echography', Blackwell Science Ltd, Edinburgh, UK, chapter 15, pp. 208–217.

Elgersma, O., van Leersum, M., Buijs, P., van Leeuwen, M., van de Schouw, Y., Eikelboom, B. & van der Graaf, Y. (1998), 'Changes over time in optimal duplex threshold for the identification of patients eligible for carotid endarterectomy', *Stroke* **29**, 2352–2356.

European Carotid Surgery Trial Collaborators (1998), 'Randomised trial of endarterectomy for recently symptomatic carotid stenosis: final results of the MRC European Carotid Surgery Trial (ECST)', *Lancet* **351**(9113), 1379–87.

Evans, D. (1982), 'Some aspects of the relationship between instantaneous volumetric blood flow and continuous wave Doppler ultrasound recordings–III. The calculation of Doppler power spectra from mean velocity waveforms, and the results of processing these spectra with maximum, mean, and RMS frequency processors', *Ultrasound in Medicine and Biology* **8**, 617–623.

Evans, D. & McDicken, W. (2000), *Doppler ultrasound: physics, instrumentation and signal processing*, 2nd edn, John Wiley & Sons, Chichester, UK.

Fatemi, R. & Rittgers, S. (1994), 'Derivation of shear rates from near-wall LDA measurements under steady and pulsatile flow conditions', *Journal of Biomechanical Engineering* **116**, 361–368.

Fillinger, M., Baker, R., Zwolak, R., Musson, A., Lenz, J., Mott, J., Bech, F., Walsh, D. & Cronenwett, J. (1996), 'Carotid duplex criteria for a 60% or greater angiographic stenosis: variation according to equipment', *Journal of Vascular Surgery* **24**, 856–864.

Fish, P. (1986), *Physical principles of medical ultrasound*, Ellis Horwood, Chichester, chapter Doppler methods, pp. 338–376.

Fish, P. (1991), 'Nonstationarity broadening in pulsed Doppler spectrum measurements', *Ultrasound in Medicine and Biology* **17**(2), 147–155.

Fishbane, P., Gasiorowicz, S. & Thornton, S. (1996), *Physics for scientists and engineers*, Prentice Hall, New Jersey, USA.

Flaherty, J., Pierce, J., Ferrans, V., Patel, D., Tucker, W. & Fry, D. (1972), 'Endothelial nuclear patterns in the canine arterial tree with particular reference to hemodynamic events', *Circulation Research* **30**, 23–23.

Flaud, P., Bensalah, A. & Peronneau, P. (1997), 'Deconvolution process in measurement of arterial velocity profiles via an ultrasonic pulsed Doppler velocimeter for evaluation of the wall shear rate', *Ultrasound in Medicine and Biology* **23**, 425–436.

Forsberg, F., Morvay, Z., Nandkumar, R., Deane, C. & Needleman, L. (2000), 'Shear rate estimation using a clinical ultrasound scanner', *Journal of Ultrasound in Medicine* **19**, 323 – 327.

Forsting, M. & Wanke, I. (2003), 'Funeral for a friend', *Stroke* **34**, 1324–1332.

Franklin, D., Schlegel, W. & Rushmer, R. (1961), 'Blood flow measured by Doppler frequency shift of back-scattered ultrasound', *Science* **134**, 564–5.

Fraser, K. (2007), Computational estimation of haemodynamics and tissue stresses in abdominal aortic aneurysms, PhD thesis, University of Edinburgh.

Fraser, K., Meagher, S., Blake, J., Easson, W. & Hoskins, P. (2008), 'Characterization of an abdominal aortic velocity waveform in patients with abdominal aortic aneurysm', *Ultrasound in Medicine and Biology* **34**, 73–80.

Frayne, R., Holdsworth, D., Gowman, L., Rickey, D., Drangova, M., Fenster, A. & Rutt, B. (1992), 'Computer-controlled flow simulator for MR flow studies', *Journal of Magnetic Resonance Imaging* **2**, 605–612.

Friedman, M., Deters, O., Bargeron, C., Hutchins, G. & Mark, F. (1986), 'Shear dependent thickening of the human arterial intima', *Atherosclerosis* **60**(2), 161–171.

Friedman, M., Hutchins, G., Bargeron, C., Deters, O. & Mark, F. (1981), 'Correlation betweeen intimal thickness and fluid shear in human arteries', *Atherosclerosis* **39**, 425 – 436.

Gach, H. & Lowe, I. (1998), 'Characterization of flow emerging from a stenosis using MRI', *Magnetic Resonance in Medicine* **40**(4), 559–70.

Gach, H. & Lowe, I. (2000), 'Measuring Flow Reattachment Lengths Downstream of a Stenosis Using MRI', *Journal of Magnetic Resonance Imaging* **12**, 939–948.

Gerada, M., Struijk, P., Stewart, P., Guerriero, S., Melis, G. & Wladimiroff, J. (2006), 'Comparison between color Doppler cineloop- and conventional spectral Doppler-derived maximum velocity and flow in the umbilical vein', *Ultrasound in Obstetrics and Gynecology* **28**, 156–161.

Gerber, B., Rosen, B., Mahesh, M., Araujo, L., Sutton, M. S. J. & Lima, J. (2004), Physical principles of cardiovascular imaging, *in* M. Sutton & J. Rutherford, eds, 'Clinical cardiovascular imaging', Elsevier Saunders, Philadelphia, Pennsylvania, USA, chapter 1, pp. 1–76.

Giddens, D., Zarins, C. & Glagov, S. (1993), 'The role of fluid mechanics in the localization and detection of atherosclerosis', *Journal of Biomechanical Engineering - Transactions of the ASME* **115**, 588 – 594.

Gnasso, A., Carallo, C., Irace, C., Spagnuolo, V., Novara, G. D., Mattioli, P. & Pujia, A. (1996), 'Association Between Intima-Media Thickness and Wall Shear Stress in Common Carotid Arteries in Healthy Male Subjects', *Circulation* **94**(12), 3257–3262.

Hankey, G., Warlow, C. & Sellar, R. (1990), 'Cerebral angiographic risk in mild cerebrovascular disease', *Stroke* **21**, 209–222.

Heijenbrok-Kal, M., Buskens, E., Nederkoorn, P., van der Graaf, Y. & Hunink, M. (2006), 'Optimal peak systolic velocity threshold at duplex us for determining the need for carotid endarterectomy: a decision analytic approach', *Radiology* **238**, 480–488.

Hoeks, A., Hennerici, M. & Reneman, R. (1991), 'Spectral composition of Doppler signals', *Ultrasound in Medicine and Biology* **17**, 751–760.

Hoeks, A., Samijo, S., Brands, P. & Reneman, R. (1995), 'Noninvasive determination of shear-rate distribution across the arterial lumen', *Hypertension* **26**, 26–26.

Holdsworth, D., Norley, C., Frayne, R., Steinman, D. & Rutt, B. (1999), 'Characterization of common carotid artery blood-flow waveforms in normal human subjects', *Physiological Measurement* **20**(3), 219 – 240.

Holdsworth, D., Rickey, D., Drangova, M., Miller, D. & Fenster, A. (1991), 'Computer-controlled positive displacement pump for physiological flow simulation', *Medical & Biological Engineering & Computing* **29**, 565–570.

Hoskins, P. (1990), 'Measurement of arterial blood flow by Doppler ultrasound', *Clinical Physics and Physiological Measurement* **11**, 1–26.

Hoskins, P. (1994*a*), 'Choice of moving target for a string phantom: I. Measurement of filament backscatter characteristics', *Ultrasound in Medicine and Biology* **20**(8), 773–780.

Hoskins, P. (1994*b*), The {bbs} string phantom, *in* P. Hoskins, S. Sherriff & J. Evans, eds, 'Testing of Döppler ultrasound equipment', Stephen Austin and Sons Ltd, Hereford, pp. 65–73.

Hoskins, P. (1996), 'Accuracy of maximum velocity estimates made using Doppler ultrasound systems', *British Journal of Radiology* **69**, 172–177.

Hoskins, P. (1997), 'Peak velocity estimation in arterial stenosis models using colour vector Doppler', *Ultrasound in Medicine and Biology* **23**, 889–897.

Hoskins, P. (1999), 'A review of the measurement of blood velocity and related quantities using Doppler ultrasound', *Proceedings of the Institute of Mechanical Engineers [H]* **213**, 391–400.

Hoskins, P. (2007), 'Simulation and validation of arterial ultrasound imaging and blood flow', *Ultrasound in Medicine & Biology*.

Hoskins, P., Anderson, T. & McDicken, W. (1989), 'A computer controlled flow waveform phantom for generation of physiological Doppler waveforms', *Physics in Medicine and Biology* **34**(11), 1709–1717.

Hoskins, P., Fish, P., Pye, S. & Anderson, T. (1999), 'Finite beam-width ray model for geometric spectral broadening', *Ultrasound in Medicine and Biology* **25**, 391–404.

Hoskins, P., Fleming, A., Stonebridge, P., Allan, P. & Cameron, D. (1994), 'Scan-plane vector maps and secondary flow motions in arteries', *European Journal of Ultrasound* **1**, 159–169.

Hughes, P. & How, T. (1993), 'Quantitative measurement of wall shear rate by pulsed Doppler ultrasound', *Journal of Medical Engineering and Technology* **17**, 58–64.

Hughes, P. & How, T. (1994), 'Pulsatile velocity distribution and wall shear rate measurement using pulsed Doppler ultrasound', *Journal of Biomechanics* **27**, 103–110.

Humphrey, J. (2002), *Cardiovascular solid mechanics: cells, tissues, and organs*, Springer-Verlag, New York.

Hunink, M., Polak, J., Barlan, M. & O'Leary, D. (1993), 'Detection and quantification of carotid artery stenosis: efficacy of various Doppler velocity parameters', *American Journal of Roentgenology* **160**, 619–625.

Jensen, J. (1993), 'Range/velocity limitations for time-domain blood velocity estimation', *Ultrasound in Medicine and Biology* **19**, 741–749.

Jensen, J. (1996), *Estimation of blood velocities using ultrasound*, Cambridge University Press, Cambridge.

Kamiya, A. & Togawa, T. (1980), 'Adaptive regulation of wall shear stress to flow change in the canine carotid artery', *American Journal of Physiology* **239**, H14–H21.

Kasai, C., Namekawa, K., Koyano, A. & Omoto, R. (1985), 'Real-time two-dimensional blood flow imaging using an autocorrelation technique', *IEEE Transactions on Sonics and Ultrasonics* **SU-32**(3), 458–464.

Keller, H., Meier, W., Anliker, M. & Kumpe, D. (1976*a*), 'Noninvasive measurement of velocity profiles and blood flow in the common carotid artery by pulsed Doppler ultrasound', *Stroke* **7**, 370–377.

Keller, H., Meier, W., Yonekawa, Y. & Kumpe, D. (1976*b*), 'Noninavasive angiography for the diagnosis of carotid artery disease using Doppler ultrasound (carotid artery Doppler)', *Stroke* **7**, 354–363.

Köhler, U., Marshall, I., Robertson, M., Long, Q., Xu, X. & Hoskins, P. (2001), 'MRI measurement of wall shear stress vectors in bifurcation models and comparison with CFD predictions', *Journal of Magnetic Resonance Imaging* **14**, 563–573.

Koller, A. & Kaley, G. (1990), 'Endothelium regulates skeletal muscle microcirculation by a blood flow velocity-sensing mechanism', *American Journal of Physiology* **258**, H916–H920.

Koller, A., Sun, D. & Kaley, G. (1993), 'Role of shear stress and endothelial prostaglandins in flow- and viscosity-induced dilation of arterioles in vitro', *Circulation Research* **72**, 1276–1284.

Kornet, L., Hoeks, A., Lambregts, J. & Reneman, R. (2000), 'Mean wall shear stress in the femoral arterial bifurcation is low and independent of age at rest', *Journal of Vascular Research* **37**, 112–122.

Ku, D. & Giddens, D. (1987), 'Laser Doppler anemometer measurements of pulsatile flow in a model carotid bifurcation', *Journal of Biomechanics* **20**, 407–421.

Ku, D., Giddens, D., Phillips, D. & Strandness, D. (1985*a*), 'Hemodynamics of the normal human carotid bifurcation: in vitro and in vivo studies', *Ultrasound in Medicine and Biology* **11**(1), 13–26.

Ku, D., Giddens, D., Zarins, C. & Glagov, S. (1985*b*), 'Pulsatile flow and atherosclerosis in the human carotid bifurcation. Positive correlation between plaque location and low oscillating shear stress', *Arteriosclerosis, Thrombosis and Vascular Biology* **5**(3), 293–320.

Kuntz, K., Polak, J., Whittemore, A., Skillman, J. & Kent, K. (1997), 'Duplex ultrasound criteria for the identification of carotid stenosis should be laboratory specific', *Stroke* **28**, 597–602.

Langille, B. & O'Donnell, F. (1986), 'Reductions in arterial diameter produced by chronic decreases in blood flow are endothelium-dependent', *Science* **231**(4736), 405–407.

Li, M. (2006), Numerical simulation of blood flow and vessel wall stresses in stenosed arteries, Master's thesis, University of Edinburgh.

Libby, P. & Aikawa, M. (2002), 'Stabilization of atherosclerotic plaques: New mechanisms and clinical targets', *Nature Medicine* **8**(11), 1257–1262.

Ling, S. & Atabek, H. (1972), 'A nonlinear analysis of pulsatile flow in arteries', *Journal of Fluid Mechanics* **55**, 493.

Loree, H., Kamm, R., Stringfellow, R. & Lee, R. (1992), 'Effects of fibrous cap thickness on peak circumferential stress in model atherosclerotic vessels', *Circulation Research* **71**(4), 850–858.

Lou, Z., Yang, W.-J. & Stein, P. (1993), 'Errors in the estimation of arterial wall shear rates that result from curve fitting of velocity profiles', *Journal of Biomechanics* **26**(4/5), 383 – 390.

Loudon, C. & Tordesillas, A. (1998), 'The use of the dimensionless Womersley number to characterize the unsteady nature of internal flow', *Journal of Theoretical Biology* **191**, 63–78.

Lusis, A. (2000), 'Atherosclerosis', *Nature* **407**, 233–241.

Mackey, W., Khabbaz, K., Bojar, R. & O'Donnell, T. (1996), 'Simultaneous carotid endarterectomy and coronary bypass: perioperative risk and long-term survival', *Journal of Vascular Surgery* **24**, 58–64.

Maier, S., Meier, D., Boesiger, P., Moser, U. & Vieli, A. (1989), 'Human abdominal aorta: comparative measurements of blood flow with MR imaging and multigated Doppler US', *Radiology* **171**, 487–492.

Marshall, I., Papathanasopoulou, P. & Wartlolowska, K. (2004), 'Carotid flow rates and flow division at the bifurcation in healthy volunteers', *Physiological Measurement* **25**(3), 691–697.

McDicken, W. (1986), 'A versatile test-object for the calibration of ultrasonic Doppler flow instruments', *Ultrasound in Medicine and Biology* **12**, 245–249.

Meagher, S., Poepping, T., Ramnarine, K., Black, R. & Hoskins, P. (2007), 'Anatomical flow phantoms of the nonplanar carotid bifurcation, part II: experimental validation with Doppler ultrasound', *Ultrasound in Medicine and Biology* **33**, 303–310.

Melling, A. (1997), 'Tracer particles and seeding for particle image velocimetry', *Measurement, Science and Technology* **8**(12), 1406–1416.

Mitchell, G., Parise, H., Vita, J., Larson, M., Warner, E., Keaney, J., Keyes, M., Levy, D., Vasan, R. & Benjamin, E. (2004), 'Local shear stress and brachial artery flow-mediated dilation: the Framingham Heart Study', *Hypertension* **44**, 134–139.

Moore, J. & Ku, D. (1994), 'Pulsatile velocity measurements in a model of the human abdominal aorta under simulated exercise and postprandial conditions', *Journal of Biomechanical Engineering - Transactions of the ASME* **116**, 337 – 346.

Murray, C. (1926), 'The Physiological Principle of Minimum Work: I. The Vascular System and the Cost of Blood Volume', *Proceedings of the National Academy of Science* **12**, 207–214.

Murray, I. (2004), Development of a Doppler tissue imaging test object for routine quality assurance and research, Master's thesis, University of Edinburgh.

Narrow, T., Yoda, M. & Abdel-Khalik, S. (2000), 'A simple model for the refractive index of sodium iodide aqueous solutions', *Experiments in Fluids* **28**(3), 282–283.

Nederkoorn, P., Mali, W., Eikelboom, B., Elgersma, O., Buskens, E., Hunink, M., Kappelle, L., Buijs, P., Wüst, A., van der Lugt, A. & van der Graaf, Y. (2002), 'Preoperative diagnosis of carotid artery stenosis: accuracy of noninvasive testing', *Stroke* **33**, 2003–2008.

Nederkoorn, P., van der Graaf, Y. & Hunink, M. (2003), 'Duplex ultrasound and magnetic resonance angiography compared with digital subtraction angiography in carotid artery stenosis: a systematic review', *Stroke* **34**, 1324–1332.

Nguyen, T., Biadillah, Y., Mongrain, R., Brunette, J., Tardif, J.-C. & Bertrand, Q. (2004), 'A method for matching the refractive index and kinematic viscosity of a blood analog for flow visualization in hydraulic cardiovascular models', *Journal of Biomechanical Engineering* **126**(4), 529–535.

Nichols, W. & O'Rourke, M. (1990), *McDonald's blood flow in arteries*, 3rd edn, Edward Arnold, London.

Nogueira, J., Lecuona, A. & Rodriguez, P. (1997), 'Data validation, false vectors correction and derived magnitudes calculation on PIV data', *Measurement Science and Technology* **8**(12), 1493–1501.

Olufsen, M., Peskin, C., Kim, W., Pedersen, E., Nadim, A. & Larsen, J. (2000), 'Numerical simulation and experimental validation of blood flow in arteries with structured-tree outflow conditions', *Annals of Biomedical Engineering* **28**, 1281–1299.

Oshinski, J., Ku, D., Mukundan, S., Loth, F. & Pettigrew, R. (1995), 'Determination of wall shear stress in the aorta with the use of MR phase velocity mapping', *Journal of Magnetic Resonance Imaging* **5**(6), 640–647.

Overbeck, J., Beach, K. & Strandness, D. (1992), 'Vector Doppler: accurate measurement of blood velocity in two dimensions', *Ultrasound in Medicine and Biology* **18**, 19–31.

Oyre, S., Pedersen, E., Ringgard, S., Boesiger, P. & Paasle, W. (1997), 'In vivo wall shear stress measured by magnetic resonance velocity mapping in the normal human abdominal aorta', *European Journal of Vascular and Endovascular Surgery* **13**, 263 – 271.

Oyre, S., Ringgaard, S., Kozerke, S., Paaske, W., Erlandsen, M., Boesiger, P. & Pedersen, E. (1998*a*), 'Accurate noninvasive quantitation of blood flow, cross-sectional lumen vessel area and wall shear stress by three-dimensional paraboloid modeling of magnetic resonance imaging velocity data', *Journal of the American College of Cardiology* **32**(1), 128–134.

Oyre, S., Ringgaard, S., Kozerke, S., Paaske, W., Scheidegger, M., Boesiger, P. & Pedersen, E. (1998*b*), 'Quantitation of circumferential subpixel vessel wall position and wall shear stress by multiple sectored three-dimensional paraboloid modeling of velocity encoded cine MR', *Magnetic Resonance in Medicine* **40**(5), 645–55.

Pao, R. (1961), *Fluid mechanics*, John Wiley & Sons, Inc., New York.

Pedersen, E., Agerbaek, M., Kristensen, I. & Yoganathan, A. (1997), 'Wall shear stress and early atherosclerotic lesions in the abdominal aorta in young adults', *European Journal of Vascular and Endovascular Surgery* **13**, 443 – 451.

Poepping, T., Nikolov, H., Rankin, R., Lee, M. & Holdsworth, D. (2002), 'An in vitro system for Doppler ultrasound flow studies in the stenosed carotid artery bifurcation', *Ultrasound in Medicine and Biology* **28**, 495–495.

Prasad, A. (2000), 'Particle image velocimetry', *Current Science* **79**(1), 51 – 60.

Raffel, M., Willert, C. & Kompenhans, J. (1998), *Particle image velocimetry: a practical guide*, Springer, London.

Ramnarine, K., Nassiri, D., Hoskins, P. & Lubbers, J. (1998), 'Validation of a new blood-mimicking fluid for use in Doppler flow test objects', *Ultrasound in Medicine and Biology* **24**, 451–459.

Reese, J. & Thompson, D. (1998), 'Shear stress in arterial stenoses: a momentum integral model', *Journal of Biomechanics* **31**, 1051 – 1057.

Reneman, R., Arts, T. & Hoeks, A. (2006), 'Wall shear stress - an important determinant of endothelial cell function and structure - in the arterial system in vivo. Discrepancies with theory', *Journal of Vascular Research* **43**(3), 251–269.

Richardson, P. (2002), 'Biomechanics of plaque rupture: progress, problems, and new frontiers', *Annals of Biomedical Engineering* **30**, 524–536.

Robinson, M., Sacks, D., Perlmutter, G. & Marinelli, D. (1988), 'Diagnostic criteria for carotid duplex sonography', *American Journal of Roentgenology* **151**, 1045–1049.

Rothwell, P., Pendlebury, S., Wardlaw, J. & Warlow, C. (2000), 'Critical appraisal of the design and reporting of studies of imaging and measurement of carotid stenosis', *Stroke* **31**, 1444–1450.

Ryval, J., Straatman, A. & Steinman, D. (2004), 'Two-equation turbulence modeling of pulsatile flow in a stenosed tube', *Journal of Biomechanical Engineering* **126**, 625–635.

Samijo, S., Willigers, J., Barkhuysen, R., Kitslaar, P., Reneman, R., Brands, P. & Hoeks, A. (1998), 'Wall shear stress in the human common carotid artery as function of age and gender', *Cardiovascular Research* **39**, 515–522.

Samijo, S., Willigers, J., Brands, P., Barkhuysen, R., Reneman, R., Kitslaar, P. & Hoeks, A. (1997), 'Reproducibility of shear rate and shear stress assessment by means of ultrasound in the common carotid artery of young human males and females', *Ultrasound in Medicine and Biology* **23**, 583–590.

Schlichting, H. (1987), *Boundary-layer theory*, 7th edn, McGraw-Hill, New York.

Sherwin, S. & Blackburn, H. (2005), 'Three-dimensional instabilities and transition of steady and pulsatile axisymmetric stenotic flows', *Journal of Fluid Mechanics* **533**, 297–327.

Shortland, A. & Cochrane, T. (1989), 'Doppler spectral waveform generation in vitro: an aid to diagnosis of vascular disease', *Ultrasound in Medicine and Biology* **15**, 737–748.

Silber, H., Ouyang, P., Bluemke, D., Gupta, S., Foo, T. & Lima, J. (2005), 'Why is flow-mediated dilation dependent on arterial size? Assessment of the shear stimulus using phase-contrast magnetic resonance imaging', *American Journal of Physiology: Heart, Circulation and Physiology* **288**, H822–H828.

Sivanesan, S., How, T., Black, R. & Bakran, A. (1999), 'Flow patterns in the radiocephalic arteriovenous fistula: an in vitro study', *Journal of Biomechanics* **32**(9), 915–925.

Slager, C., Wentzel, J., Gijsen, F., Schuurbiers, J., van der Wal, A., van der Steen, A. & Serruys, P. (2005*a*), 'The role of shear stress in the generation of rupture-prone vulnerable plaques', *Nature Clinical Practice Cardiovascular Medicine* **2**, 401–407.

Slager, C., Wentzel, J., Gijsen, F., Thury, A., van der Wal, A., Schaar, J. & Serruys, P. (2005*b*), 'The role of shear stress in the destabilization of vulnerable plaques and related therapeutic implications', *Nature Clinical Practice Cardiovascular Medicine* **2**, 456–464.

Smith, M., Long, D., Damiano, E. & Ley, K. (2003), 'Near-wall micro-PIV Reveals a hydrodynamically relevant endothelial surface layer in venules in vivo', *Biophysical Journal* **85**(1), 637–645.

Spencer, M. & Reid, J. (1979), 'Quantitation of carotid stenosis with continuous-wave (C-W) Doppler ultrasound', *Stroke* **10**, 326–330.

Steel, R., Fish, P., Ramnarine, K., Criton, A., Routh, H. & Hoskins, P. (2003), 'Velocity fluctuation reduction in vector Doppler ultrasound using a hybrid single/dual-beam algorithm', *IEEE Transactions on Ultrasonics, Ferroelectronics and Frequency Control* **50**, 89–89.

Steinberg, D. (2002), 'Atherogenesis in perspective: hypercholesterolemia and inflammation as partners in crime', *Nature Medicine* **8**, 1211–1217.

Steinman, D. (2002), 'Image-based computational fluid dynamics modeling in realistic arterial geometries', *Annals of Biomedical Engineering* **30**, 483–497.

Steinman, D., Vinh, B., Ethier, C., Ojha, M., Cobbold, R. & Johnston, K. (1993), 'A numerical simulation of flow in a two-dimensional end-to-side anastomosis model', *Journal of Biomechanical Engineering* **115**, 112–118.

Stroev, P., Hoskins, P. & Easson, W. (2007), 'Distribution of wall shear rate throughout the arterial tree: a case study', *Atherosclerosis* **191**, 276–280.

Stroud, J., Berger, S. & Saloner, D. (2000), 'Influence of stenosis morphology on flow through severely stenotic vessels: implications for plaque rupture', *Journal of Biomechanics* **33**, 443 – 455.

Struijk, P., Stewart, P., Fernando, K., Mathews, V., Loupas, T., Steegers, E. & Wladimiroff, J. (2005), 'Wall shear stress and related hemodynamic parameters in the fetal descending aorta derived from color Doppler velocity profiles', *Ultrasound in Medicine and Biology* **31**(11), 1441–1450.

Sveen, J. (2004), 'An introduction to MatPIV v.1.6.1'.

Taylor, C., Cheng, C., Espinosa, L., Tang, B., Parker, D. & Herfkens, R. (2002), 'In vivo quantification of blood flow and wall shear stress in the human abdominal aorta during lower limb exercise', *Annals of Biomedical Engineering* **30**, 402–408.

Taylor, C., Hughes, T. & Zarins, C. (1998), 'Finite element modeling of the three-dimensional pulsatile flow in the abdominal aorta: Relevance to atherosclerosis', *Annals of Biomedical Engineering* **26**, 975 – 987.

Teirlinck, C., Bezemer, R., Kollmann, C., Lubbers, J., Hoskins, P., Ramnarine, K., Fish, P., Fredeldt, K. & Schaarschmidt, U. (1998), 'Development of an example flow test object and comparison of five of these test objects, constructed in various laboratories', *Ultrasonics* **36**, 653–660.

Thompson, R., Trudinger, B. & Cook, C. (1985), 'Doppler ultrasound waveforms in the fetal umbilical artery: quantitative analysis technique', *Ultrasound in Medicine and Biology* **11**, 707–718.

Tortoli, P., Michelassi, V., Bambi, G., Guidi, F. & Righi, D. (2003), 'Interaction between secondary velocities, flow pulsation and vessel morphology in the common carotid artery', *Ultrasound in Medicine and Biology* **29**, 407–415.

Tortoli, P., Morganti, T., Bambi, G., Palombo, C. & Ramnarine, K. (2006), 'Noninvasive simultaneous assessment of wall shear rate and wall distension in carotid arteries', *Ultrasound in Medicine and Biology* **32**, 1661–1670.

van der Hulst, H. (1981), *Light scattering by small particles*, Dover Publications, Inc, New York, USA.

Varghese, S., Frankel, S. & Fischer, P. (2007*a*), 'Direct numerical simulation of stenotic flows. Part 1. Steady flow', *Journal of Fluid Mechanics* **582**, 253–280.

Varghese, S., Frankel, S. & Fischer, P. (2007*b*), 'Direct numerical simulation of stenotic flows. Part 2. Pulsatile flow', *Journal of Fluid Mechanics* **582**, 281–318.

Vieli, A., Moser, U., Maier, S., Meier, D. & Boesiger, P. (1989), 'Velocity profiles in the normal human abdominal aorta: a comparison between ultrasound and magnetic resonance data', *Ultrasound in Medicine and Biology* **15**, 113–119.

Walker, J. & Naylor, A. (2006), 'Ultrasound based measurement of Ścarotid stenosis> 70%Š: an audit of UK practice', *European Journal of Vascular & Endovascular Surgery* **31**(5), 487–490.

Watts, D., Sutcliffe, C., Morgan, R., Meagher, S., Wardlaw, J., Connell, M., Bastin, M., Marshall, I., Ramnarine, K., Hoskins, P. & Black, R. (2007), 'Anatomical flow phantoms of the nonplanar carotid bifurcation, part I: computer-aided design and fabrication', *Ultrasound in Medicine and Biology* **33**, 296–302.

Weaver, J., Evans, A. & Walder, D. (1969), 'The effect of increased fibrinogen content on the viscosity of blood', *Clinical Science* **36**, 1–10.

Westerweel, J. (1993), Digital Particle Image Velocimetry, PhD thesis, Technische Universiteit Delft.

Westerweel, J. (1997), 'Fundamentals of digital particle image velocimetry', *Measurement, Science and Technology* **8**(12), 1379–1392.

Womersley, J. (1955), 'Method for the calculation of velocity, rate of flow and viscous drag in arteries when the pressure gradient is known', *Journal of Physiology* **127**, 553 – 563.

Wootton, D. & Ku, D. (1999), 'Fluid mechanics of vascular systems, diseases, and thrombosis', *Annual Reviews Biomedical Engineering* **1**, 299–299.

Wu, S., Ringgaard, S., Oyre, S., Hansen, M., Rasmus, S. & Pedersen, E. (2004), 'Wall shear rates differ between the normal carotid, femoral, and brachial arteries: an in vivo MRI study', *Journal of Magnetic Resonance Imaging* **19**, 188–193.

Yongchareon, W. & Young, D. (1979), 'Initiation of turbulence in models of arterial stenoses', *Journal of Biomechanics* **12**(3), 185–96.

Yusuf, S., Zucker, D., Peduzzi, P., Fisher, L., Takaro, T., Kennedy, J., Davis, K., Killip, T., Passamani, E. & Norris, R. (1994), 'Effect of coronary artery bypass graft surgery on survival: overview of 10-year results from randomised trials by the Coronary Artery Bypass Graft Surgery Trialists Collaboration', *Lancet* **344**, 563–570.

Zamir, M. (2005), *The physics of coronary blood flow*, Springer, New York, NY, USA.

Zarins, C., Giddens, D., Bharadvaj, B., Sottiurai, V., Mabon, R. & Glagov, S. (1983), 'Carotid bifurcation atherosclerosis. Quantitative correlation of plaque localization with flow velocity profiles and wall shear stress', *Circulation Research* **53**(4), 502–514.

Zarins, C., Zatina, M., Giddens, D., Ku, D. & Glagov, S. (1987), 'Shear stress regulation of artery lumen diameter in experimental atherogenesis', *Journal of Vascular Surgery* **5**, 413–420.